



UNIVERSITÀ
DEGLI STUDI
DI PADOVA

Sede Amministrativa: Università degli Studi di Padova

Dipartimento di Ingegneria Industriale

CORSO DI DOTTORATO DI RICERCA IN INGEGNERIA INDUSTRIALE

CURRICOLO: MATERIALI

CICLO XXXII

Enhancement of alloys formability by electroplastic effect

Tesi redatta con il contributo finanziario della Fondazione Cariparo

Direttore della Scuola: Ch.mo Prof. Paolo Colombo

Coordinatore d'indirizzo: Prof. Enrico Bernardo

Supervisore: Prof.ssa Irene Calliari

Dottorando: Claudio Gennari

Acknowledgements

The present work will not have been possible without the help of a myriad of people, say thanks to all of them would be quite impossible, so I will spend a few words to the ones who helped me more during this years of ~~pains and agonies~~ joys and achievements.

I will be eternally grateful to my parents and to all the members of my family who believe in me and were always there when I needed.

I would like to acknowledge all my research group, starting from Marco Breda who helped me rediscovering my love for this subject. I would say thank you to Luca Pezzato, without whom I would never be able to survive the infinite burocraZy of University of Padua, and Pietro Giovanni Cerchier that lightened the mood of the lab with his ~~stupid~~ superclever jokes and the usual Christmas song. Thanks to Alessio Settimi, Mattia Lago and Denise Hanoz that were always there when any help was needed.

Thanks to Professor Manuele Dabalà and Professor Katya Brunelli who were always there when I needed any enlightenment or advice. Professor Stefania Bruschi and his research team who helped with the mechanical tests. Professor Michele Forzan and Professor Renato Gobbo for their invaluable help regarding the electrical stuff and finally, thanks to all the other Professors I forgot to mention.

A special thanks goes to my supervisor Professor Irene Calliari who believed in me and gave me the opportunity of this PhD.

My last and most important thank you goes to Elena, my partner in crime and in life, it is impossible to describe the patience, the help and the support she gave me during this period, I would definetly be lost without her.

ABSTRACT

This thesis summarizes the results obtained during the PhD research period in Industrial Engineering at the Industrial Engineering Doctorate School of University of Padua. The research project was mainly focused on the effect of the electrical current on the plastic deformation and on the microstructure of different metal alloys known as *Electroplastic Effect* (EPE).

The research project was conducted in collaboration with the Metallurgy, Mechanical and Electrical Engineering groups of the Industrial Engineering Department of University of Padua.

This thesis is organized in five different chapters. The first chapter deals with the state of the art of the Electroplastic Effect, starting from the first scientific papers and then focusing mainly on the various theories that try to explain the phenomenon. In the second chapter, already performed researches at University of Padua are reported. The third chapter focuses on the experimental apparatus used during the research period. Fourth chapter is focused on the experimental results obtained using continuous and pulsed direct current on four types of high technological interest metal alloys (pure aluminum, titanium grade five, an experimental TWIP steel and four grades of duplex stainless steels). The fifth chapter deals with electropulsed treatment on a super duplex stainless steel. It has been decided to include two appendixes that contributed to the scientific training of the candidate. Appendix A reports the results concerning the influence of small volume fraction and different morphologies of secondary phases on the *ductile-to-brittle* (DBT) transition of a UNS S32205 duplex stainless steels. Finally, appendix B describes the influence of cold rolling on the laser weldability of UNS S32750 duplex stainless steel.

Most of the research activities were carried out in the laboratories of the Metallurgy group, the Electrical Engineering group and the Mechanical

Engineering group of the Industrial Engineering Department of University of Padua. Specifically, tensile tests were carried out at the Precision Manufacturing Laboratory under the supervision of Professor Stefania Bruschi and Professor Andrea Ghiotti, electrical measurements were performed at the Laboratory of Electroheating of Padova (LEP) under the supervision of Professor Michele Forzan and Professor Renato Gobbo, finally, the characterization of the samples were performed at the metallurgy laboratories supervised by Professor Irene Calliari and Professor Manuele Dabalà. Some activities were conducted outside the University of Padua in collaboration with other institutions. In particular laser welding and phase quantification by means of electromagnetic measurements were carried out thanks to Professor Istvan Mészáros of the Department of Materials Science and Engineering of the Budapest University of Technology and Economics and finally, impact toughness tests were conducted at the Quality Control Laboratories of Acciaierie Valbruna S.p.A. under the guidance of Engineer Enrico Piva.

This research work helped to improve the knowledge on the electroplasticity phenomenon, in particular for a specific class of steels in which two phases with different metallurgical characteristics are present.

SOMMARIO

Il presente elaborato riassume i risultati ottenuti durante il periodo di ricerca necessario al conseguimento del titolo di Dottore di Ricerca in Ingegneria Industriale presso la Scuola di Dottorato dell'Università degli Studi di Padova. Il progetto di ricerca consiste nello studio dell'effetto della corrente elettrica sulla deformazione plastica e sulla stabilità microstrutturale di diverse leghe metalliche conosciuto come *Effetto Elettroplastico (EPE)*.

Il progetto di ricerca è nato all'interno del Dipartimento di Ingegneria Industriale dell'Università degli Studi di Padova in seguito ad una collaborazione tra il gruppo di Metallurgia, Ingegneria Meccanica e Ingegneria Elettrica.

La tesi è suddivisa in cinque capitoli. Il primo capitolo tratta dello stato dell'arte del fenomeno dell'elettroplasticità, a partire dai primi articoli scientifici che ne hanno parlato per poi focalizzarsi principalmente sulle possibili spiegazioni del fenomeno. Nel secondo capitolo sono esposti i lavori già effettuati all'interno dell'Università di Padova prima dell'inizio del percorso di Dottorato. Il terzo capitolo riassume le apparecchiature utilizzate durante il periodo di ricerca. Il quarto capitolo espone i risultati ottenuti utilizzando corrente continua e pulsata su quattro categorie di leghe metalliche di elevato interesse tecnologico (alluminio commercialmente puro, una lega di Titanio grado cinque, un acciaio inossidabile TWIP e quattro acciai inossidabili bifasici). Nel quinto capitolo viene studiato l'effetto di trattamenti elettro-pulsati su un acciaio inossidabile bifasico. In appendice sono riportati due lavori che esulano dal progetto di ricerca ma che si sono ritenuti utili nella formazione scientifica del candidato. L'appendice A riporta uno studio sull'influenza della morfologia di una piccola frazione volumetrica di fasi secondarie sulla transizione duttile fragile di un acciaio inossidabile bifasico UNS S32205. L'appendice B tratta

invece l'influenza della deformazione plastica a freddo sulla saldabilità tramite laser di un acciaio inossidabile bifasico UNS S32750.

La maggior parte delle attività di ricerca sono state effettuate presso i laboratori del gruppo di Metallurgia, del gruppo di Ingegneria Elettrica e del gruppo di Tecnologia Meccanica del Dipartimento di Ingegneria Industriale (DII) dell'Università degli Studi di Padova. Nello specifico le prove di trazione sono state eseguite presso il laboratorio di Precision Manufacturing sotto la supervisione della Professoressa Stefania Bruschi e del Professor Andrea Ghiotti, le misure elettriche sono state eseguite presso il Laboratorio di Electroheating di Padova (LEP) sotto la guida del Professor Michele Forzan e del Professor Renato Gobbo, mentre la caratterizzazione è stata eseguita presso i laboratori di metallurgia supervisionati dalla Professoressa Irene Calliari e dal Professor Manuele Dabalà. Alcune attività sono state svolte in collaborazione con altre istituzioni, in particolare le saldature laser e la quantificazione delle fasi per mezzo di misure elettromagnetiche grazie al Professor Istvan Mészáros del Dipartimento di Scienza e Ingegneria dei Materiali della Budapest University of Technology and Economics e le prove di resilienza presso il laboratorio Controllo Qualità delle Acciaierie Valbruna S.p.A. di Vicenza sotto la guida dell'Ingegnere Enrico Piva.

Il presente lavoro di ricerca ha contribuito ad aumentare la conoscenza del fenomeno dell'elettroplasticità, in particolare per una determinata classe di acciai in cui sono presenti due fasi con diverse caratteristiche metallurgiche.

Table of contents

Acknowledgements.....	i
ABSTRACT.....	ii
SOMMARIO.....	iv
Table of contents.....	vi
1. CHAPTER 1.....	1
1.1. INTRODUCTION.....	1
1.2. EAF history.....	7
1.3. Electroplastic effect theories	17
1.3.1. Electron Wind Force	18
1.3.2. Magnetoplasticity.....	20
1.3.3. Heterogeneous atomic scale joule heating	25
1.3.4. Dissolution of metallic bonds.....	27
1.4. Electrically assisted manufacturing processes	29
1.4.1. Forging process	30
1.4.2. Rolling process	30
1.4.3. Drawing process.....	31
1.4.4. Deep drawing process.....	32
1.4.5. Embossing process.....	32
1.4.6. Blanking process	33
1.4.7. Incremental forming process.....	34
1.4.8. Friction stir welding process	34
1.4.9. Pressure welding process	35
1.4.10. Cutting process.....	36
1.5. Electropulsing treatments	37
1.5.1. Grain refinement and recrystallisation	39
1.5.2. Phase transitions and grains refinement	40
1.5.3. Texture evolution and oriented microstructure	43
1.6. References.....	46
2. CHAPTER 2.....	63
2.1. INTRODUCTION.....	63
2.2. Stacking Fault Energy	63

2.3.	Investigated materials and methodology	67
2.4.	Austenitic stainless steel AISI 316L	70
2.5.	C11000 Copper.....	72
2.6.	Aluminum alloy 1050 H24	73
2.7.	Ferritic stainless steel AISI 430	75
2.8.	Discussions	76
2.9.	Conclusions	84
2.10.	References.....	86
3.	CHAPTER 3.....	89
3.1.	INTRODUCTION.....	89
3.2.	Power suppliers	89
3.2.1.	Commercially available power supply.....	89
3.2.2.	Pulsed power supply	90
3.3.	Scanning electron microscope	93
3.4.	Transmission electron microscope.....	94
3.5.	Optical microscope.....	95
3.6.	X-ray diffraction.....	95
3.6.1.	Siemens D500.....	95
3.6.2.	Bruker D8	96
3.6.3.	Spider X portable residual stresses diffractometer	97
3.7.	Corrosion tests	99
3.8.	Tensile test machine	100
3.9.	Thermal infrared camera.....	101
3.10.	References.....	102
4.	CHAPTER 4.....	103
4.1.	INTRODUCTION.....	103
4.2.	Titanium.....	103
4.2.1.	Titanium alloys.....	105
4.2.2.	Materials and methods.....	110
4.2.3.	As received material	112
4.2.4.	Electrically assisted tensile tests.....	113
4.2.5.	Thermal tensile test.....	114
4.2.6.	Comparisons.....	115

4.2.7.	Concluding remarks	121
4.3.	Twinning induced plasticity stainless steel	122
4.3.1.	Materials and methods.....	126
4.3.2.	As received material	128
4.3.3.	Electrically assisted tensile tests.....	129
4.3.4.	Thermal tensile tests	131
4.3.5.	Comparisons.....	132
4.3.6.	Concluding remarks	140
4.4.	Aluminum AA1050 H24.....	142
4.4.1.	Materials and methods.....	143
4.4.2.	As received material	147
4.4.3.	Thermal regimes.....	148
4.4.4.	Tensile tests	150
4.4.5.	X-ray diffraction and TEM.....	153
4.4.6.	Concluding remarks	156
4.5.	Duplex stainless steels	157
4.5.1.	Materials and methods.....	162
4.5.2.	As received materials	164
4.5.3.	Temperature and current regimes.....	166
4.5.4.	Tensile behaviour	172
4.5.5.	Discussions.....	176
4.5.6.	Concluding remarks	179
4.5.7.	Materials and methods.....	180
4.5.8.	As received material	181
4.5.9.	Thermal regimes.....	182
4.5.10.	Pulsed current tensile tests	185
4.5.11.	Discussions.....	188
4.5.12.	Concluding remarks	189
4.6.	References.....	190
5.	CHAPTER 5.....	197
5.1.	INTRODUCTION.....	197
5.2.	Duplex stainless steel UNS S32750	198
5.2.1.	Materials and methods.....	201

5.2.2. As received material	204
5.2.3. Results.....	205
5.2.4. Discussions.....	218
5.2.5. Concluding remarks	220
5.3. References.....	221
APPENDIX A.....	231
INTRODUCTION	231
Materials and methods	232
Results and discussions	234
Microstructure.....	234
Impact toughness: ductile to brittle transition	236
Fracture behavior.....	238
Lateral expansion.....	242
Conclusions	245
References	246
APPENDIX B	249
INTRODUCTION	249
Materials and methods	251
Results and discussions	254
Microstructure.....	254
Microhardness.....	259
Corrosion pitting temperature (CPT)	260
Eddy currents.....	265
Conclusions	267
References	268

CHAPTER 1

Electroplastic Effect

1.1. INTRODUCTION

Deformation of metallic alloys is rarely done at room temperature because of higher force needed to form them and their limited formability. It is therefore necessary to increase the temperature, usually above the recrystallization temperature, in order to reduce the energy needed and to retard the failure of the workpiece, hence increasing its formability limit. This can be achieved in different ways, the most commons are conventional heating, induction heating, in which the increase in temperature of the workpiece is done by a magnetic field that induces eddy current in the workpiece and finally by resistive heating, in which the temperature increase is due to the collisions of the electrons that flow through the workpiece with the ions constituting the crystal structure, commonly known as joule heating.

In the recent years a novel metal manufacturing technique called *Electrically Assisted Forming* or *Manufacturing* (EAF/EAM) has demonstrated to have the ability to enhance the forming limit of the material and, at the same time, to reduce the flow stress needed for the deformation, as well as springback. The effects induced by the applied electrical current during or after the deformation are caused by the so called *Electroplastic Effect* (EPE). This type of metal forming is very interesting in the case of metallic materials that show high mechanical strength and limited formability such as titanium or magnesium. An example of the benefits of EAF on Ti 6Al 4V alloy can be seen in Figure 1.1. It is clear that with EAF can be achieved higher deformation before reaching failure of the material in comparison with the traditional forming technique (forging in this case).

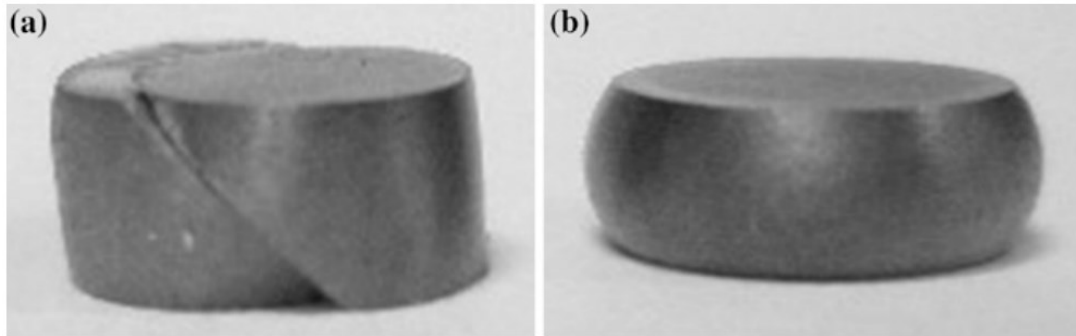


Figure 1.1 Titanium grade 5 subjected to traditional forging (a) and EAF (b). Higher deformation can be achieved without reaching failure with EAF (b) compared to the traditional forming processes [1].

Another example of EAF can be seen in Figure 1.2 in which higher deformation were achieved when forging AZ31 magnesium alloy compared to the traditional technique.

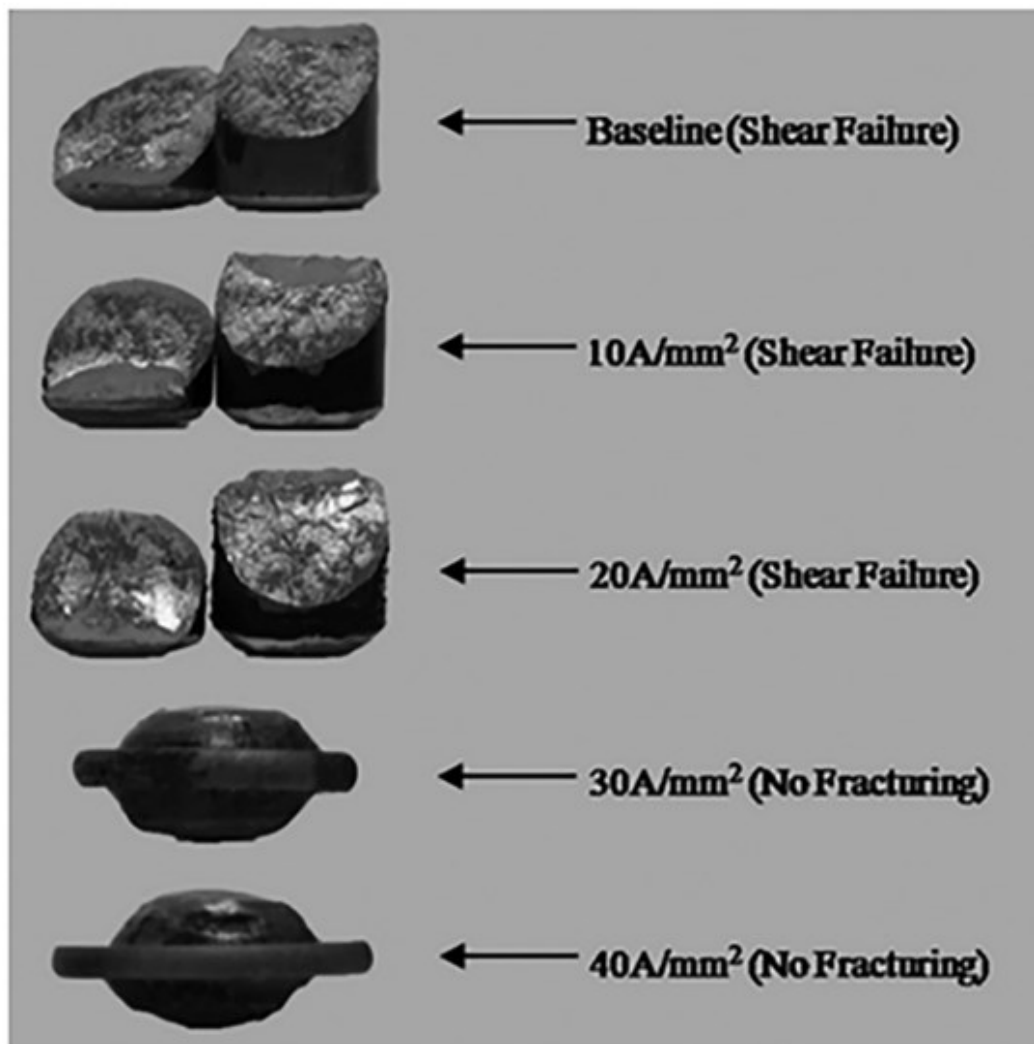


Figure 1.2 Impression die forging of magnesium AZ31 without current (top) and with different current densities applied [2].

In order to implement EAF on traditional forming industrial plants, special considerations have to be done. First of all the need of an electrical generator capable of achieving current density needed in order for the EPE to onset. Secondly special care must be taken in designing the connectors to deliver a stable electrical contact to the workpiece, which can be tricky when it comes to all the manufacturing processes in which the workpiece is not still such as rolling, drawing etc. Thirdly, all machines must be insulated from the electrical current in order to reduce electric shock risks for the people around and to confine the current flow to the workpiece. Taking into account all the above and the cost-benefits analysis, higher product quality and performance can be obtained with this manufacturing technique. One of the limitations of EAM is the high electrical current needed which limits the maximum cross section of the workpiece that can be manufactured.

Electropulsed treatments (EPT) are the processes in which the electrical current is applied to the workpiece after the deformation. An example of the benefits that EPT can produce is depicted in Figure 1.3. Springback is a key concern when it comes to metal bending, and the elimination of the issue is not so straightforward, involving mathematical models or trial and error.

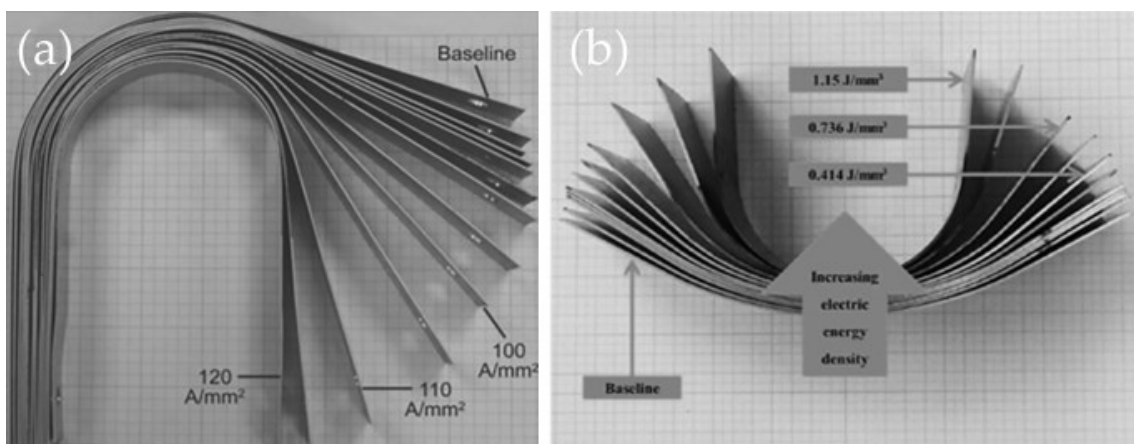


Figure 1.3 Springback elimination in AA6111 alloy (a) and high strength steel (b) after electropulsed treatment after deformation [3,4].

Performing an electroplastic treatment after the bending process can reduce or even eliminate springback in aluminum alloy AA6111 and high

strength steel as can be seen Figure 1.3 (a) and (b) respectively. Electroplastic treatment can also be applied to modify the microstructure of the workpiece. Spheroidization of pearlitic microstructure achieved depending on the current density applied after severe wire drawing is shown in Figure 1.4 [5].

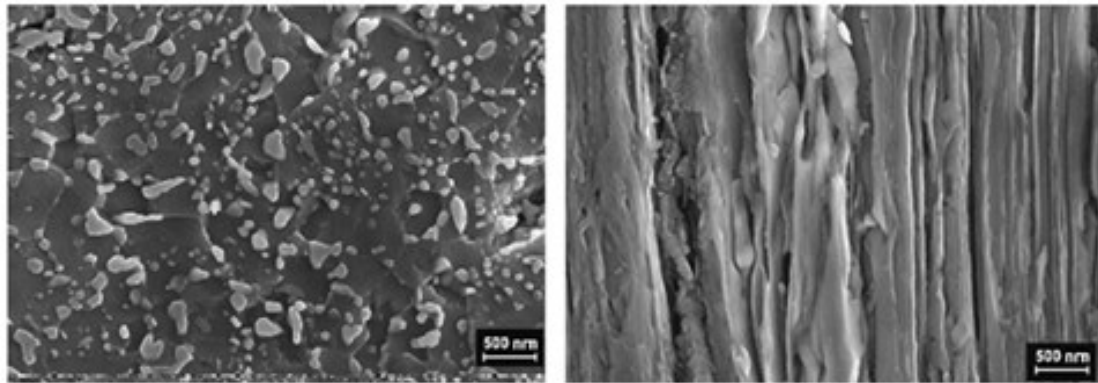


Figure 1.4 Pearlite spheroidization after electropulsed treatment (a) after cold drawing. (b) Prior pearlitic microstructure [5].

High energy electrical pulses can also aid to heal microcracks and retard fracture thanks to the mechanism illustrated in Figure 1.5 [6].

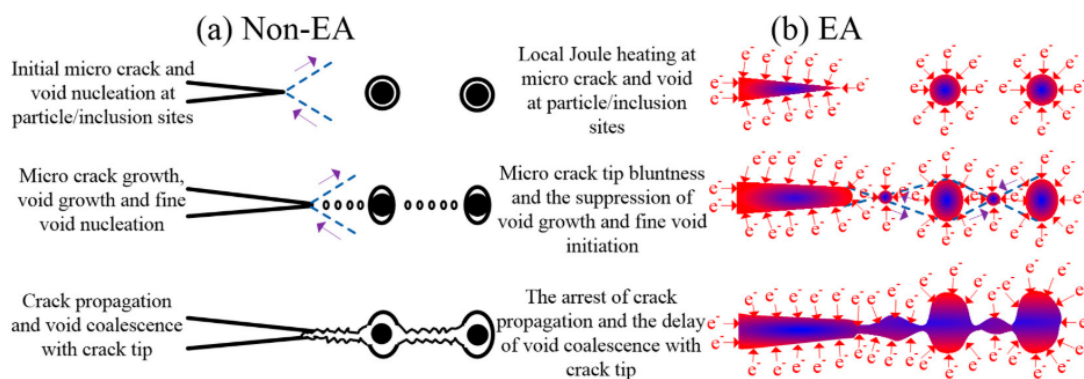


Figure 1.5 Expected mechanism of crack propagation, void nucleation, growth and coalescence: (a) non-EA and (b) EA configuration [6].

As stated before, one of the key issues in order to utilize EAF is the setup of the system as well as the design of the electrical generator. A schematic of an EAF test setup can be seen in Figure 1.6.

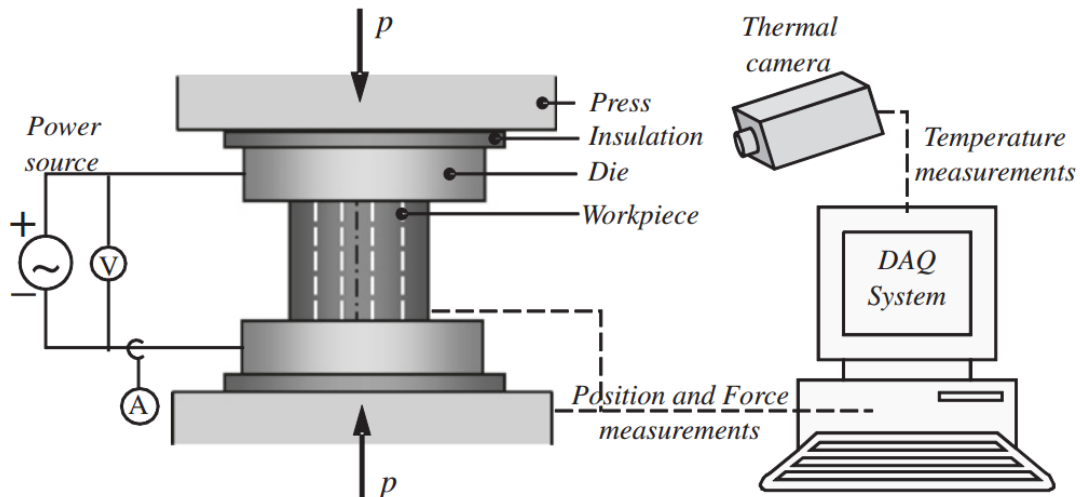


Figure 1.6 Schematic of an EAF test setup [1].

The power supply has to be able to shape the current in different ways in order to be suitable for different materials. The key features of the electrical generator must be:

- High power capacity
- Adequate current capacity for the process (current density \times expected cross-sectional area)
- High-dynamic controller to deal with current transient suppression

Some potential power supply designs could be:

- *Battery-based system.* This is an expandable *Direct-Current* (DC) system that can scale up to practically any power level. It should be integrated with a current controller
- *Isolated-gate bipolar transistor (IGBT) system.* This is a high-power, high efficiency, fast-switching device and can be used for current modulation.
- *Power metal-oxide-semiconductor field-effect transistor (power MOSFET) based system.* This is typically for lower-voltage (not necessarily lower power) applications.
- *Silicon-controlled rectifier (SCR).* Also termed a thyristor, this device is typically used to control high-current, high-voltage applications,

and can be rapidly switched for high-dynamic behavior, which makes this type of power supply good for the EAF application.

1.2. EAF history

First investigations of electricity on dislocations go back in the mid-fifties in Russia, followed by work of United States researchers in the last decades of the twentieth century. Electroplasticity studies are nowadays conducted in a lot of universities all across the world, even though the main research groups are located in the US and in Russia .

First documented observation on the influence of an electrical field on the deformation of a material is the work conducted by Machlin et al. [7] in 1959. They observed a decrease in the yield stress and an increase in elongation at rupture during three point bend test of sodium chloride brittle rock salt, and a reduction of the strain hardening coefficient during compression; both test under 6 kV potential. Later on, Nabarro discussed the electric characteristic of dislocations and the effect of electric and magnetic field on them in his book in 1967 [8]. The first theoretical study on the influence of electrical current on moving dislocations was conducted by Kravchenko in 1967 [9]. He proposed a mechanism by which the electric current perturbs the system of electrons in the crystal. The absorption of the elastic-wave energy by the electrons gives way to a stimulated energy transfer to the perturbing field, provided the electron drift velocity exceeds the phase velocity of the elastic wave. The energy is transferred by Cerenkov radiation: the probability of emission of a quantum by the electron becomes larger than the absorption probability. In the case of a dislocation moving with constant speed, the phase velocity of the elastic-perturbation waves is the dislocation velocity. It then became possible to aid dislocation motion without any external mechanical force. Troitskii and his team in 1969 [10] focused on the study of the effect of electrical current on different metallic materials. They studied the deformation under pulsed current (pulse duration $\sim 10^{-4}$ s and intensities between 600 A and 4800 A) of a very wide variety of metallic alloys such as zinc, lead, indium and tin finding that electrical current

lowered the flow stress. One of the main key concerns was to understand whether the EPE was due purely to undetectable joule heating inside the material or if it was an athermal effect due to the electron flow. In 1978 Klimov et al. [11] observed the presence of another effect than joule heating, concluding that an athermal effect had to be present. In the same year an interesting article was published by Okazaki, Kagawa and the young Hans Conrad which then built and lead a specialized team in electroplasticity at the University of North Carolina starting from the nineties [12]. They studied the effect of discharging current from capacitor on pure titanium, pure iron, pure tin and pure lead wires during tensile tests. They didn't observe a substantial increase in the temperature of the specimens under applied electric current, but they noted that the highest effect of electricity in order of materials follows the one of the normal-to-superconducting transition temperature, suggesting that it may reflect similar types of electron-dislocation interactions. Later on (1980) they studied a possible explanation concerning the skin and pinch effect due to the transient electrical current [13] concluding that those effects are negligible in comparison to the measured stress drop, confirming the presence of an effect on top of joule heating. It was thanks to Fiks in 1981 [14] that a thorough evaluation of the interaction between conducting electrons and dislocation confirmed the presence of an increase diffusion rate due to the electrons on the latter, even though it should have been one order of magnitude lower than the experimental results. The same year Bolko et al. [15] proposed the concept of "*electron wind*" in order to explain the force exerted on the moving dislocations by the electrical current. They applied a single pulse of DC on single crystal spheres of copper, gold and tungsten and measured the change in contact area which should be caused by the movement of dislocation loops. They found that an electron wind force was present, and its direction depended on the polarity of the current applied. Interestingly, Goldman et al. [16] observed no EPE in lead in its superconductive state (cooled down to 4.2 K), which could confirm

the scattering electron nature of the EPE in the material as pointed out later by Troitskii in 1984 [17]. A comprehensive overview on the EPE was published in 1986 by Sprecher, Mannan and Conrad [18] in which they studied the EPE on a wide variety of metallic materials with different crystal structure (Al, Cu, Ni, Fe, Nb, W, and Ti). They confirmed the presence of the electron wind force and suggested that the electrons could also influence the *Stacking Fault Energy* (SFE) of the alloys. Moving forward, in 1991 an interesting article was published by Kopanev [19] in which a current density threshold for the EPE to occur was introduced. He found that increasing degree of plastic deformation prior to applying electrical current reduces the current density needed to the onset of the EPE. Not much progresses have been made in the next years until 1995 when Molotskii and Fleurov published an article entitled "*Magnetic effects in electroplasticity of metals*" [20]. They observed a discrepancy in the calculated effect of the electron wind on the stress drop during deformation and the actual measured value, concluding that electron wind alone cannot be the only responsible for the EPE. They suggested that the induced magnetic field due to the current flow can help dislocations to depin from weak obstacles increasing their mobility. The model assumes that in the dislocation core dangling paramagnetic bonds are present. The magnetic field induced transition between the singlet to triplet state of the pinning bonds can considerably facilitate depinning. This model works quite well with materials that possess face centered cubic crystal structure; the dislocations mobility is hindered by the presence of forest of dislocations that act as a weak pinning point. In the case of body centered cubic materials dislocations have to overcome the Peierls-Nabarro barriers which are not weak obstacles. In the same year Davies and Ogwu [21] proposed to use high electrical voltage pulses in order to increase the ductility of brittle intermetallic compounds. A new point of view emerged in the paper published by Roschupkin and Bataronov in 1996 [22]. Since previous theories didn't explain all the aspect of the EPE, they suggested that:

- A nonequilibrium group of dislocations is formed in the process of plastic deformation (retarded dislocation accumulation, group accumulation in slip lines, etc.). A current pulse causes them to be unloaded, which is accompanied by a microplastic deformation. The biggest part of the observed jump in deformation occurs due to the internal stress energy accumulated during preliminary plastic deformation, and the current pulse acts only as an initiator of unloading and therefore may be insignificant in the level of the equivalent interaction.
- The accumulation of new nonequilibrium groups also requires plastic deformation, which is the nature of the time for formation of the nonequilibrium groups in which the current pulse does not affect the plastic deformation. Here the hardening processes increase that time with increasing overall deformation such that only the first n current pulses are effective, where each arrival is able to bring out nonequilibrium dislocation groups.

In 2000 Hans Conrad published a lot of papers regarding the EPE [23–25]. One of the most interesting is the one that investigated the influence of electrical current on the solid state phase transformations in metals (e.g., intermetallic compound formation and growth in diffusion couples, precipitation, crystallization of amorphous alloys and recrystallization and grain growth of cold worked metals) [24]. He observed an increased atomic flux due to electromigration and, concerning metallic alloys, an increase in nucleation rate during recrystallization and aging rather than the lowering of the activation barrier of the phenomenon.

In 1998 a research group from Tsinghua University in China lead by Guoyi Tang started to investigate the EPE from an industrial application point of view. They investigated the feasibility of an electroplastic drawing process on austenitic stainless steel [26]. An in depth study on electroplastic drawing on

austenitic stainless steel AISI 304 L was published in 2000 [27]. Tang et al. found an improved surface finish, a diminishing of the drawing force, a lower amount of strain induced martensite and, more interestingly, the possibility to skip some in-between annealing steps. Investigation of EPE on indentation have been conducted by Livesey et al. in 2001 on a 3.25 wt.% silicon steel [28] finding a relationship between the decrease in hardness with respect to the current used during microhardness tests.

Starting from roughly the year 2000 the interest in the electroplastic field increased and a lot of research groups from all around the world began to investigate the possible industrial application of the phenomenon. Inspired by the work of Conrad, Levitin and Loskutov from Zaporozhye National Technical University in Ukraine [29] were able to increase the fatigue life of titanium alloy up to 50% by conducting an electropulsed treatment prior to the fatigue test. In 2004 an overview of the studies into the effect of weak magnetic fields on the structure and mechanical properties of nonmagnetic solids of various nature was published by Golovin of the Tambov State University [30]. Regarding the possible explanation of the EPE, Golovin backed up the hypothesis of Molotskii and Fleurov [20], moreover he looked at the EPE under the point of view of plastic flow as a chemical reaction proceeding in a crystal [31,32], focusing on the spin-dependent dislocation depinning from obstacles.

The following year a research group from US Army Research Laboratory and the Department of Mechanical Engineering of the Johns Hopkins University in Baltimore [33] performed a finite element analysis on previously published researches on electroplasticity (e.g. Okazaki, Troitskii, Conrad etc.). Their conclusions were the following:

- It is not necessary to invoke an electroplastic deformation mechanism to explain the deformation of metals subjected to electromagnetic (EM) loading. The observed load drop during current pulse is due to the joule heat generated, rate of thermal

expansion, the shape of the current pulse applied, and the area under the pulse shape.

- Thermo-viscoplastic material response functions should be used for describing coupled EM/mechanical loading.
- The time scale for EM diffusion into a solid metal cylinder is in the order of fractions of a millisecond as compared to thermal time scales, which are four orders larger. The EM diffusion time scale is determined by the magnitude of the electrical conductivity. Heat conduction and the Lorentz forces are not critical for the particular time scales in this problem

They were the first group of researchers that proposed the idea that there were no EPE and that it was all due to joule heating.

EPE could help to improve the formability of difficult to form metallic alloys, one of which is magnesium alloy. Much papers have been published on magnesium alloys regarding rolling, tensile tests, texture development, severe plastic deformation and solution treatment, mainly by research groups located in China. Electroplastic rolling of magnesium AZ31, AZ61 and AZ91 sheet is a promising forming technique that showed to improve the ductility of the alloys, promoting dynamic recrystallization and reducing twins in the microstructure [34–36]. Interesting investigation was carried out by Guoyi et al. [35–38], they have studied the influence of high intensity and high frequency electrical pulses on the solution treatment, on the corrosion resistance and on the drawability of magnesium alloys AZ31 and AZ61. Phase transformation from $\beta \rightarrow \alpha$ took place in just 4 s under electropulse treatment. Conversely, no transformation has been observed in the case of the conventional heat treatment, not to mention the better corrosion resistance of the former in seawater in comparison with the latter.

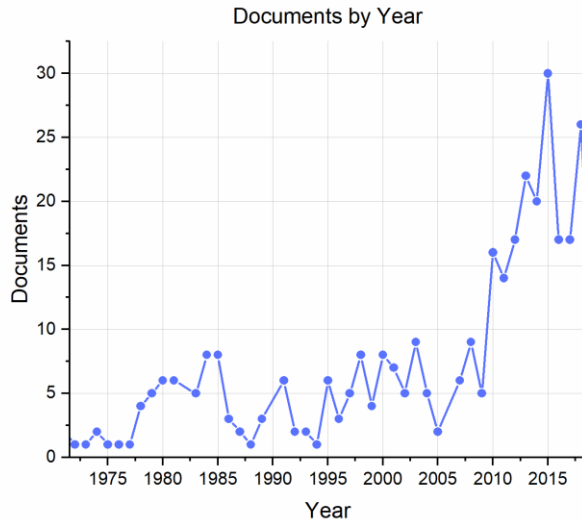


Figure 1.7 Documents by year published in the electroplastic field

Within the next years much documents were published (Figure 1.7) to establish how electricity affected the mechanical behavior (e.g., rolling, drawing, cutting, forging etc.) of metallic alloys (aluminum, magnesium, titanium, nickel, steel etc.) among different researchers and universities across the world (Figure 1.8).

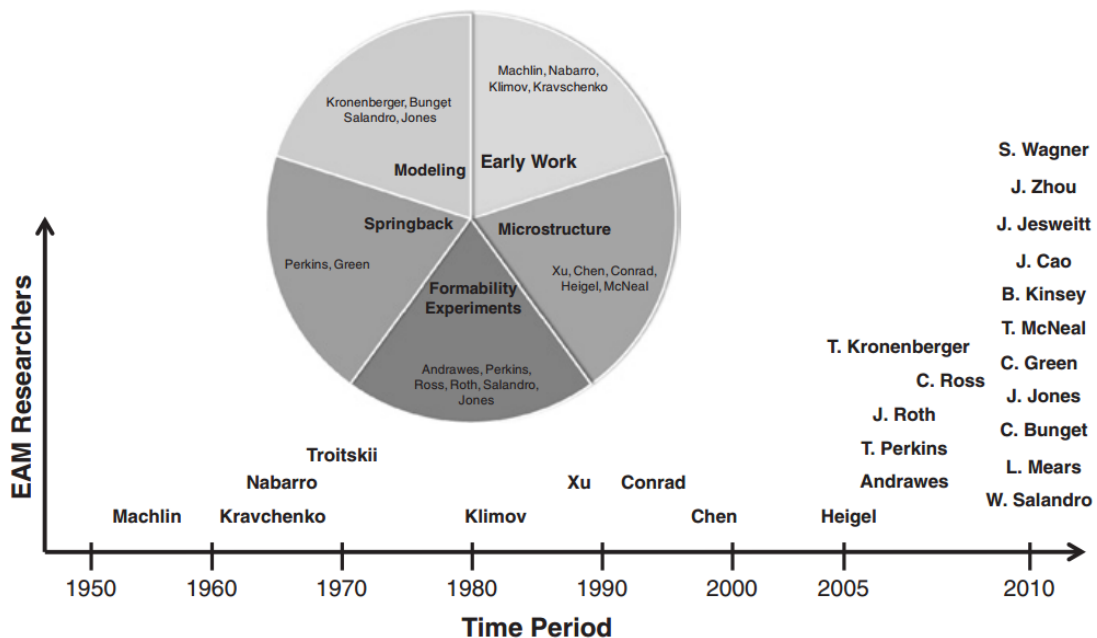


Figure 1.8 Timeline and research topics in the field of electroplasticity among researchers [39].

The most prolific author in the electroplastic field is Stolyarov from the Russian Academy of Science in Moscow. He focused the studies on the

influence of EPE on shape memory alloys, more specifically on nickel titanium alloys. He investigated phase transformations, tensile tests, rolling and severe plastic deformation as well [40–45].

In 2010 Kukudzhanov et al. [46] performed a study on the current distribution inside a material with ordered structural defects (i.e., cylindrical microvoids and plane microcracks). They observed that in correspondence of the defects and depending on their nature, there was an increase in joule heating which could lead to local melting if the current density was high enough. This could explain the increase in formability observed during electrically assisted forming processes because of crack healing.

Another author that contributed a lot in the field of electroplasticity is Wesley Salandro from Clemson University. He focused on the modeling of EPE by conducting experiments on light alloys, mainly aluminum, during tensile test, bending, forging and so on, finally publishing a book entitled *“Electrically assisted Forming (Modeling and Control)”* [1,39,47–54].

In 2011 Baranov et al. [55] were the first to study the EPE during cutting operations, being able to reduce the cutting time by 10% to 12%. Other works on electroplastic machining on a variety of metallic materials were then published confirming the reduction in cutting time and cutting force and the increase of surface finish of the workpiece [56–60].

Moving forward to 2013 Kinsey et al. [61] investigated the EPE during electromagnetic forming by means of Kolsky bar test at high strain rate (10^3 s^{-1}) on austenitic stainless steel AISI 304 and Titanium alloy grade five (Ti 6Al 4V). They observed a decrease in the flow stress for current density up to 100 A/mm^2 for titanium and 180 A/mm^2 for AISI 304 that could be related only to the increase in temperature because of the electrical current. They didn't observe any contribution of the current to the fracture strain or the strain hardening coefficient concluding that it could be possible that, due to the high strain rate, the electricity couldn't increase further dislocation mobility because they

exceeded the limit for the viscous drag of dislocation in the lattice structure. In the same year Magargee et al. published a paper on the EPE on a biphasic brass 70/30 (continuous direct current during tensile test) [62]. They observed a correlation between the flow stress reduction and the grain size as well as the increase in joule heating. They also observed cavitation in correspondence of some grain boundaries which they attributed to the low stacking fault energy of dislocations in f.c.c. metals. Such dislocations dissociate into partials and suppress the recovery and recrystallization processes up to the temperature where strain-induced grain boundary pre-melting occurs. Another possible explanation was the reduction of the virtual melting point of the metal because of an increase in vacancy concentration. It is interesting to point out that the increase in temperature for the smaller grain size brass means that there could be higher scattering of electrons due to the higher extent of grain boundaries increasing the joule heating effect. Magargee et al. were able to predict the behavior of commercially pure titanium under electrically assisted uniaxial tensile test with continuous electrical current [63]. Probably the most interesting discovery done by Magargee was the existence of an electric current density threshold related to the resistivity of the alloy in order for the EPE to onset [64]. He introduced the concept of "*current density sensitivity*" which is the rate-of-change of thermal softening with respect to effective current density. In Figure 1.9 it can be seen that not only higher levels of electric current must be used to induce thermal softening for low melting point metals (compared to high melting point metals) but also more care must be taken to ensure that the current density falls within the range of effective current density sensitivity.

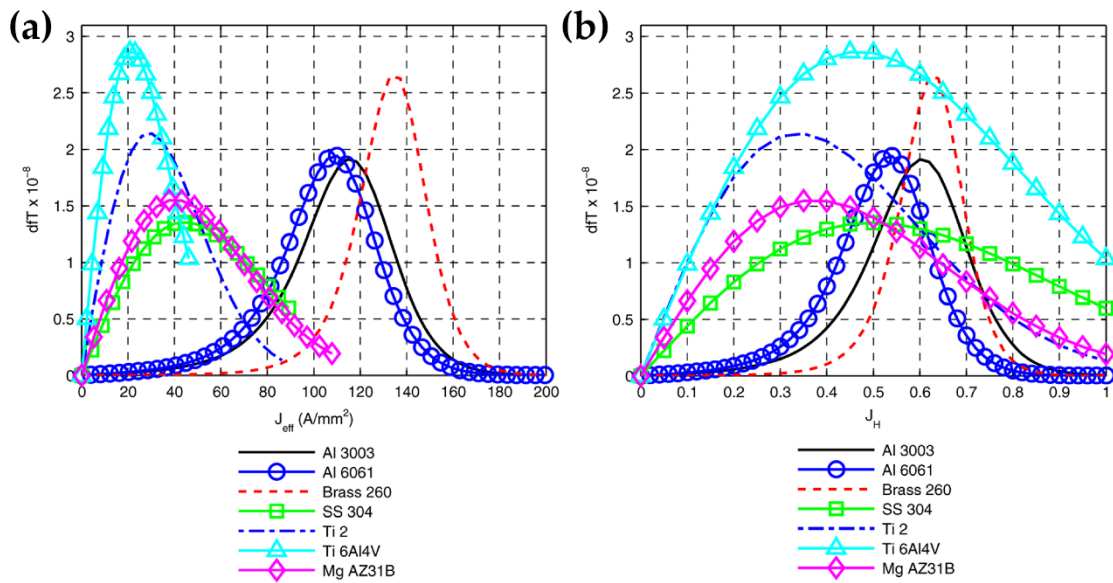


Figure 1.9 Current density sensitivity as a function of current density (a) and current density sensitivity as a function of homologous current density (ratio of effective current density normalized by current density needed to induce melting of the metal) (b) [64].

EPE raised a lot of interest in the field of sheet bending of difficult to form materials and high strength alloys because of the ability to reduce cracks formation on the outer fibers of the sheet the bending force and, more important, the elimination of the springback effect which is a big concern in sheet forming [47,65–67].

In the last years a lot of papers have been published on the EPE, focusing mainly on rolling, drawing, machining, texture development on light alloys (i.e., magnesium, aluminum and titanium) and some high strength steels (i.e., DP 980 and TRIP steels) and duplex stainless steels [68-85].

In conclusion a lot of interest is arising in the EPE in the recent years because of the challenge in understanding the phenomenon that could lead to improvement and easier way to form very high strength alloys that are by nature very difficult to form.

1.3. Electroplastic effect theories

A theory that can well describe the EPE in toto is very difficult to form because of the multiscale nature of the phenomenon. Since its discovery a lot of researchers developed theories to explain how electrical current can affect the microstructure or the behavior of a metallic alloy. In order to unravel this mystery, it is important to understand what a metal is. At microscopic level metallic materials are held together by a particular chemical bond called metallic bond. It consists of an electrostatic attractive force that arises between the positively charged metallic ions and the cloud of conduction electrons. It can be described as a delocalization of the electron cloud among a structure of charged ions. This particular type of bond is different from others chemical bonds, accounting for the peculiar characteristic of metallic alloys such as strength, ductility, thermal and electrical properties etc. Because of this, it is legit that electrical current flowing through the metal could affect its physical and chemical properties. Since its discovery a lot of researcher tried to explain how EPE works and some contrasting theories have also been developed (electron wind force theory is quite controversial).

The main aspects that have been attributed to the EPE are the following:

- *Electron wind force*: momentum transfer between the flow of electron due to the electrical current to the dislocations which reduces the flow stress and increase dislocation mobility aiding plastic flow [9,18,20]
- *Magnetoplasticity*: the induced magnetic field due to the electrical current interacts with dislocations aiding their depinning from weak obstacles and favoring their motion [8,86]
- *Heterogeneous atomic scale joule heating*: the electrical resistivity of a metallic alloy is influenced by its composition, grain size, plastic deformation, inclusions, stacking faults, voids and so on. During

plastic deformation dislocations are formed and interact with each others causing regions of higher dislocation density in correspondence of twin and grain boundaries, stacking fault, precipitates etc. This will cause an increase in electrical resistivity which could lead to hot spots within the metal leading to higher localized resistive heating, hence thermal softening

- *Dissolution of metallic bonds:* metallic bonds are held together by the sharing of electrons of the electron cloud. An excess of electrons due to electrical current could cause a weakening of the metallic bond which can lead to easier deformation due to bond dissolution and reformation during plastic flow [87]

1.3.1. *Electron Wind Force*

Electron wind force theory arises from the study of *Electromigration*. Electromigration is atomic diffusion driven by an electric field as current passes through a metal. It has been studied as a potential failure mechanism for thin film connectors in circuits [88]. Failure of electronic connector is due to the electron wind force, because the collisions of flowing electrons with ions core results in mass diffusion toward the grounded side of the connector [89].

In the case of dislocations, when applied electrical current, they experience a force. This force can be written as follow:

$$f_{ew} = B_e v_e \tag{1.1}$$

where B_e is a constant that describes the electron to dislocation interaction and v_e is the average drift velocity of the electrons. The force described in 1.1 is related to the effective stress τ_{eq} , generated by the electron current density j , and with the Burgers vector b of the dislocation through the relationship $f_{ew} = \tau_{eq} b$.

The drift velocity of the electrons is defined and can be calculated using the following relationship:

$$v_e = \frac{j}{n_e e_0} \quad (1.2)$$

where n_e is the electron density and e_0 is the electron charge. Knowing all of these we can rewrite the effective stress as:

$$\tau_{ew} = C_{ew}^{theor} j \quad (1.3)$$

defining:

$$C_{ew}^{theor} = \frac{B_e}{n_e b e_0} \quad (1.4)$$

Taking for example parameters $B_e=0.8 \times 10^{-10}$ Ns/cm² at 4.2 K [90], $n_e=8.33 \times 10^{22}$ cm⁻³, $b=2.56 \times 10^{-8}$ cm in the case of pure copper, equation 1.4 results in $C_{ew}^{theor}=2.3 \times 10^{-9}$ MPa/(A/cm²), which is four order of magnitude less than the experimental value $C_{ew}^{exp}=2.8 \times 10^{-5}$ MPa/(A/cm²), a consistent discrepancy can be observed for other metallic materials as well. One possible explanation is that the direction of moving dislocations depends on the direction of the applied stress and, moreover, by the sign of the dislocations. Zuev et al. [91] proposed a relationship to evaluate the average drift velocity of dislocations taking into account the direction of electron flow and the sign of dislocation:

$$v_+ - v_- = 2 \frac{f_{ew}}{B} = 2 \frac{B_e}{B} \frac{j}{n_e e_0} \quad (1.5)$$

Where B is the total viscous drag of the dislocations. $B=2.5 \times 10^{-8}$ Ns/cm² and $n_e=1.33 \times 10^{23}$ cm⁻³ as calculated by Lavrentev et al. [92]. Considering a current density of $j=7.5 \times 10^3$ A/cm² and $B_e=3.6 \times 10^{-5}$ Ns/cm² we obtain $v_+ - v_- = 0.01$ cm/s which is in good agreement with experimental data [91].

1.3.2. Magnetoplasticity

This theory was proposed by Molotskii and Fleurov in 1995, later backed up and elegantly investigated by Golovin [20,30]. Previous studies of interaction between dislocation and magnetic field found that dislocation path length L increased with the square of the magnetic field B and in proportion to the duration of the exposure to the magnetic field and reached several hundred micrometers. Interestingly, the direction of motion of dislocations did not change as the field changed polarity, so the effect was not due to ponderomotive forces caused by the magnetic field and to the vortex electric field that arises when a magnetic field is switched on or when a sample is placed in it [93]. Similar results were obtained by the same research group on different materials (CsI, InSb, LiF) [90-100] and in Zn and Al [104,105]. A summary of the results are showed in Figure 1.10.

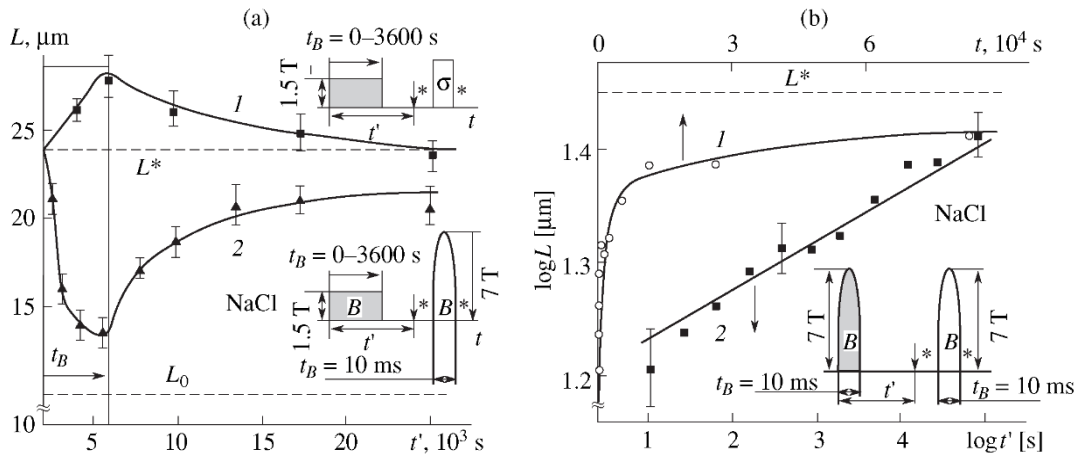


Figure 1.10 Regularities of magnetic field-stimulated depinning of dislocations in various materials. (a) Dependence of the path length L of edge dislocations on magnetic field and exposure time t_B for NaCl crystals with a Ca concentration of (1, 1') 0.5, (2, 2') 1, (3, 3') 10, and (4, 4') 100 ppm obtained (1–4) from the $L(B)$ dependence and (1'–4') from the $L(t_B)$ dependence; (5) the proportion of starting dislocations; insets show the concentration dependence of L for $B = 0.5$ T and the diagram representing the experiment; L_0 is the path length in etchant. (b) (1) Dislocation path lengths in Al normalized to the average distance between dislocations $\lambda = \sqrt{\rho_0}$, where ρ_0 is their average density, and (2) proportion of starting dislocations as functions of the duration t_B of exposure to a magnetic field $B = 1.2$ T. Inset shows the consecutive order of procedures: arrow means production of dislocations, asterisk stands for etching, and B means exposure to a magnetic field; $T = 293$ K.

Estimations show that the force exerted on dislocations by a magnetic field is several orders of magnitude less than the internal stresses, let alone the starting dislocation stresses. In [106], a great number of dislocation paths

($N > 10^3$) were measured in different widely separated (> 1 mm) regions of a crystal and it was found that the quantity of shifted dislocations and their mean path lengths were the same in the four equivalent crystallographic directions (for the f.c.c. structure) and were independent of the magnetic field direction (provided the dislocation lines were perpendicular to this direction). It follows that dislocations move in the random field of internal stresses and a magnetic field only lowers the height of barriers to dislocation motion.

Regarding metallic materials, it was known that dislocation cores contain paramagnetic centers not only in covalent crystals, where it is clear that these centers are associated with dangling bonds, but also in ionic, metallic, and ionic covalent crystals, where electrons are captured by jogs, kinks, and other specific features of cores. Therefore, in these macroscopic diamagnetic materials, paramagnetic centers (localized electrons, holes, triplet excitons, ion radicals) are always present and can be involved in exchange interaction. Plastic flow can be seen as a chemical reaction proceeding inside the crystal. Intensive plastic deformation or relaxation of the structure due to internal stresses causes the formation, motion, interaction, annihilation, and other dislocation-related mechanism inside the crystal, which can be treated as chemical reactions between various reagents (Figure 1.11).

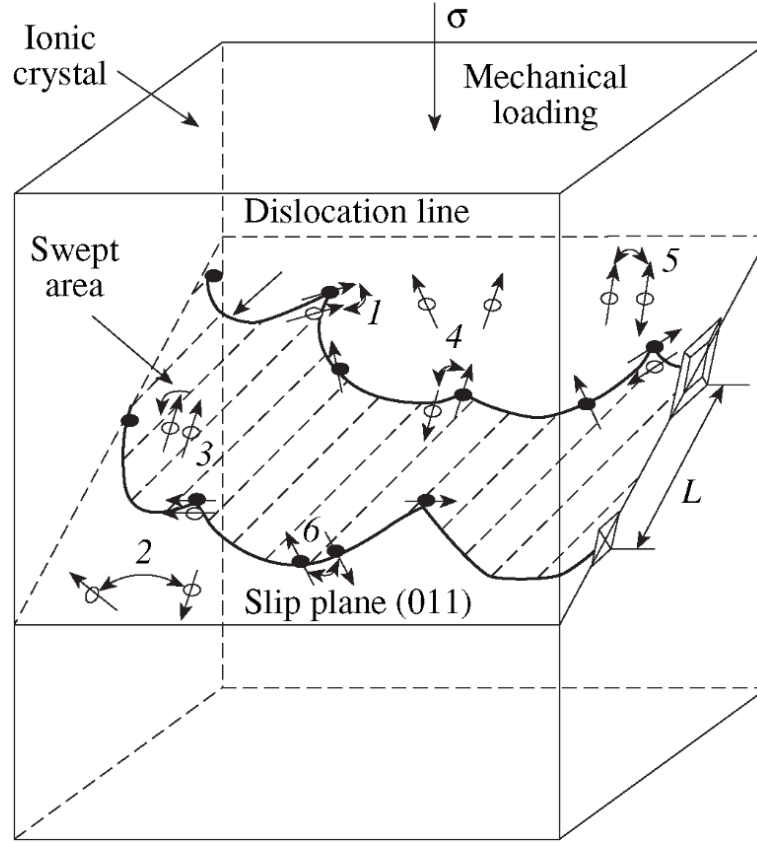


Figure 1.11 Plastic deformation as solid-state chemical reactions between structural defects: (1, 2, 3) monomolecular reactions of dislocation break-away from an obstacle, decay of a complex of point defects, and its reorientation, respectively; and (4, 5, 6) bimolecular reactions of dislocation pinning, formation of a complex of point defects, and recombination of paramagnetic centers in a dislocation core, respectively [30].

When forced against an obstacle by stresses, a dislocation makes many attempts to overcome it, with the attempt frequency being determined by the phonon frequencies ($f_{ph}=10^6-10^{13}$ Hz) and the natural frequencies of vibration of the dislocation structure [107]:

$$f_n = (n/2\pi\lambda)\sqrt{12\gamma/m} \quad (1.6)$$

$$\approx (0.4n/\lambda)\sqrt{G_s/\rho} \approx n(10^8 \div 10^9) \text{ Hz}$$

where γ is the linear stress, m is the effective linear mass of the dislocation line, G_s is the shear modulus, ρ is the density, and n is the harmonic number. As a consequence of that, a dislocation makes millions of attempts before it succeeds in overcoming a barrier. In Figure 1.12 it is represented the motion of dislocation through a random network of obstacles in a slip plane as a repeating cycle.

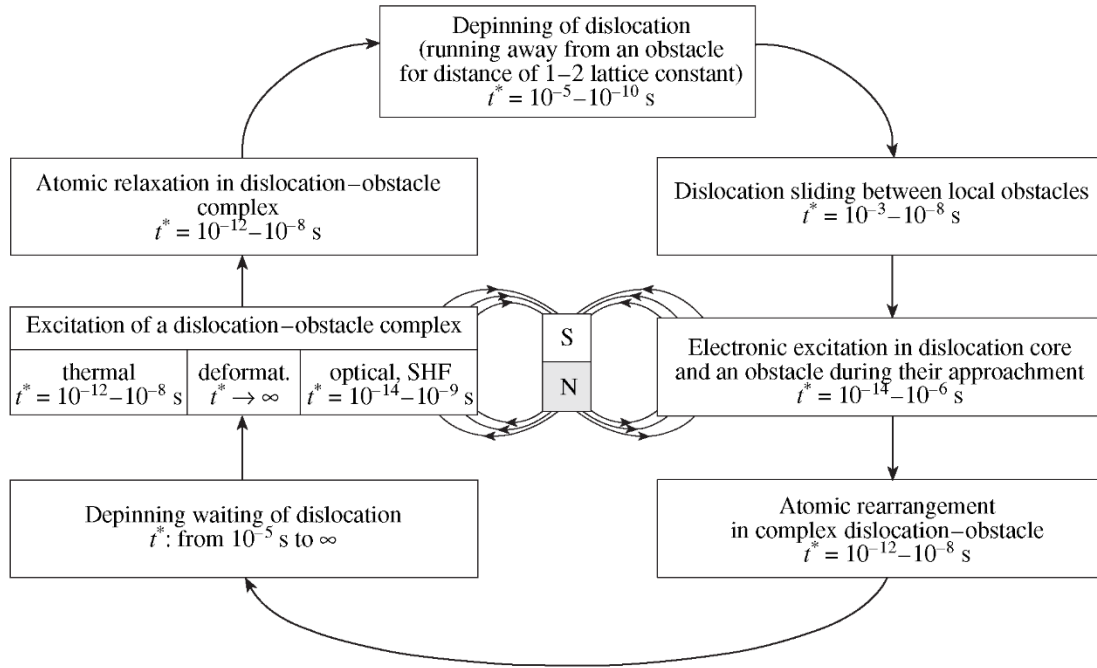


Figure 1.12 Main stages of one cycle of dislocation motion through a random network of local obstacles and their characteristic times. A magnetic field can affect only short-lived excited states of electrons in interacting defects [30].

During these short-lived excitations, spin conversion can occur under the action of a magnetic field, favoring the depinning from the weak obstacles. A schematic diagram of the steps from singlet to triplet states that allow dislocations to overcome weak obstacles is presented in Figure 1.13.

Magnetoplasticity could be one mechanism by which EPE works, it will be very difficult to take into account everything that happens during plastic deformation in a material that presents a lot of heterogeneities (i.e. dislocations substructure, precipitates, secondary phases, grain boundaries, phase boundaries etc.).

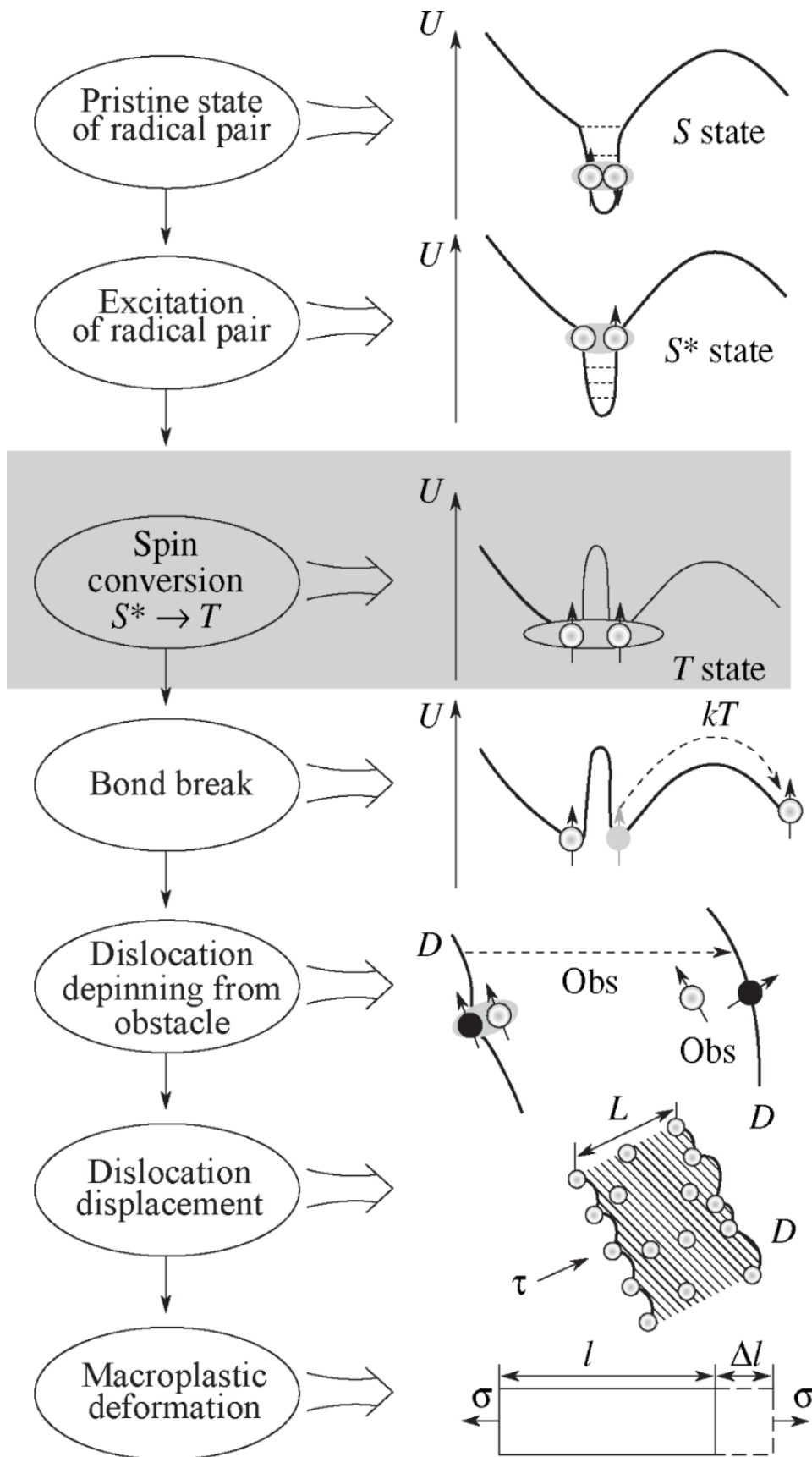


Figure 1.13 Schematic diagram of different stages of MPE associated with acceleration of dislocation depinning due to an MF. D stands for dislocation, L is its path length, Obs stands for obstacle, τ and σ are applied stresses, and l and Δl are the length of a sample and its change due to deformation, respectively; (1, 2) elastic and exchange parts of interaction between defects in a crystal, respectively [30].

1.3.3. Heterogeneous atomic scale joule heating

It is documented in the work by Fan et al. [62] the occurrence of grain boundary melting during electrically assisted tension with continuous electrical current of 70/30 brass (Figure 1.14).

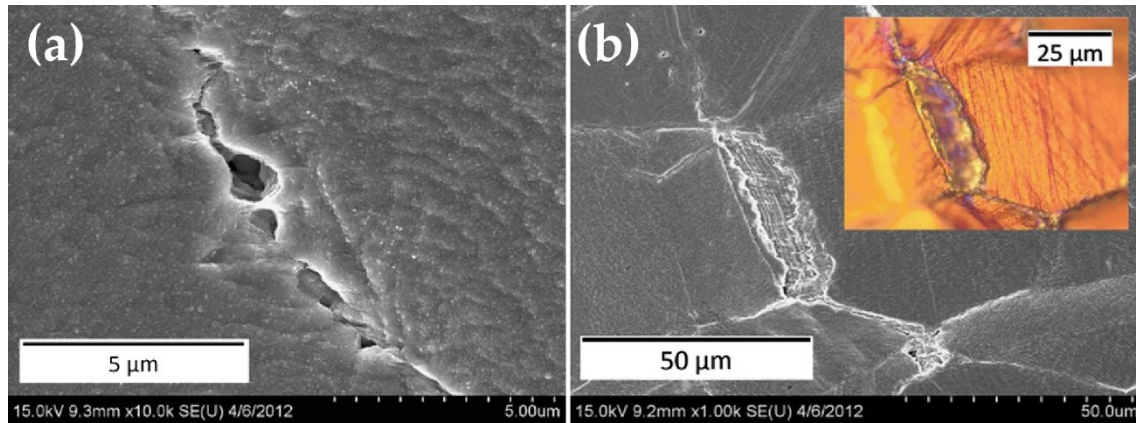


Figure 1.14 Observation of intergranular cavitation and local necking across grain boundary after electrically-assisted tension test (using a current density of 150 A/mm^2) (a), SEM image of local grain boundary melting (with corresponding optical microscope image) (b) [62].

Heterogeneities (e.g., secondary phases, grain boundaries, phase boundaries, dislocation network etc.) inside the material will affect the local resistivity modifying the current distribution within the microstructure. Zhao et al. [108] modelled the current distribution of an electrical pulse in a nanocrystalline material. They found a gradient of current density around grain boundaries, especially at triple points, moreover the relative orientation of the grain boundaries with respect the current density plays an important role. Grain boundaries oriented orthogonal to the electron flow could cause higher current density compared to orientation along the macro current flow. As a result, electrical current is heterogeneously distributed based on the angle between the macro current and the grain boundaries (Figure 1.15).

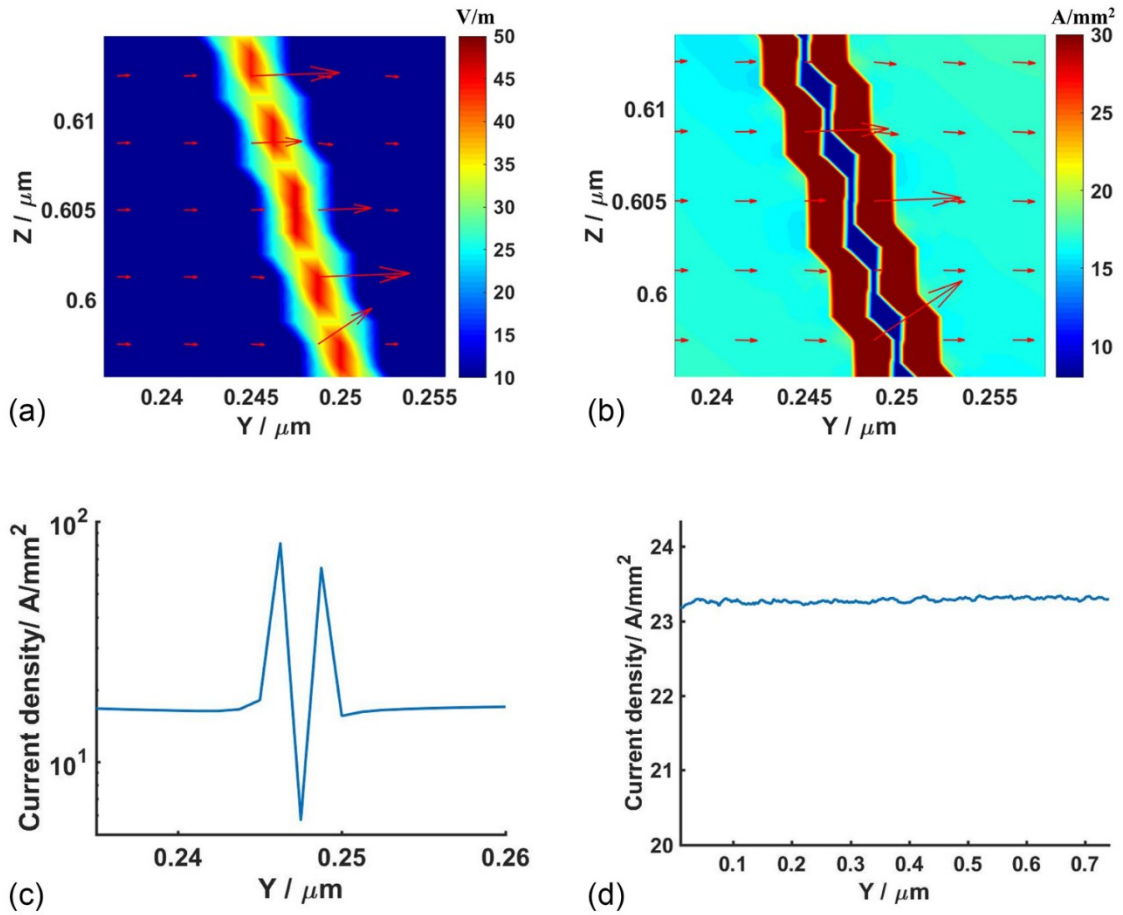


Figure 1.15 (a) The electric field intensity, (b) the current density around a simulated grain boundary, (c) current density plot along the dashed line shown in (b), and (d) overall current density of the micro simulation region in the y direction. The arrows indicate the directions of the electric field and current [108].

The uneven distribution of electrical current will affect the heating rate as well. Heating rate of grain boundaries is higher compared to that of the grain interior which causes a temperature gradient inside the grain (Figure 1.16).

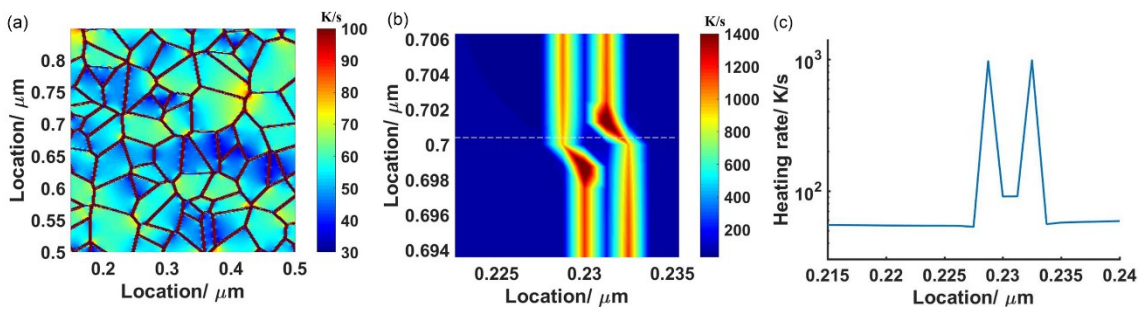


Figure 1.16 (a) Heating rate distribution in the grain structure; (b) localized resistive heating rate near a grain boundary; (c) heating rate plot along the dashed line shown in (b) [108].

The temperature gradient is been affected by the thermal diffusivity of the material, the grain size itself and the magnitude of the macro current density (i.e., higher macro current density results in higher heating rate which can

enhance the temperature gradient due to the time it takes to conduct the heat). Higher joule heating in correspondence of region with higher current density could be one of the causes for the EPE.

1.3.4. *Dissolution of metallic bonds*

In order to create an excess of electrons within the material it is necessary that some sort of electron stagnation must be present. This is an interesting theory recently proposed by Ruszkiewicz et al. published in a 2018 paper entitled *“Investigation of Heterogeneous Joule Heating as the Explanation for the Transient Electroplastic Stress Drop in Pulsed Tension of 7075-T6 Aluminum”* [109]. They multiscale modeled electrical current distribution inside a 7075 T6 aluminum alloys as a function of local electrical resistivity taking into account the precipitates and the extent of grain boundaries. They found that microscale joule heating is unable to fully account for the EPE. In their paper they proposed a new theory called *“Electron Stagnation Theory”*. The application of electric current to a metal will result in an increased number of electrons in the electron cloud proportional to the applied current density. The electrons will move at a drift velocity with emphasized directionality toward ground. As the electrons move through the metal, they will encounter precipitates, grain boundaries, dislocations, and other obstacles, all acting as impediments to electron flow. Electrons flowing toward a precipitate of increased electrical resistivity will be forced to flow around the precipitate, similar to water flowing around a rigid body within its flow. At the central point where the water contacts the rigid body there is a stagnation point, where the velocity of the water reaches zero and the water behind slows down. A similar phenomenon may happen with electrons moving past obstacles. However, electrons do not flow in a straight line; instead, they move about in random patterns until colliding with an obstacle or other electrons, which redirect their path. This will

result in electron stagnation points on the precipitate resulting in increased electron density, likely with an emphasis on the left side of the obstacle if ground is on the right side of the specimen/obstacle, shown in Figure 1.17.

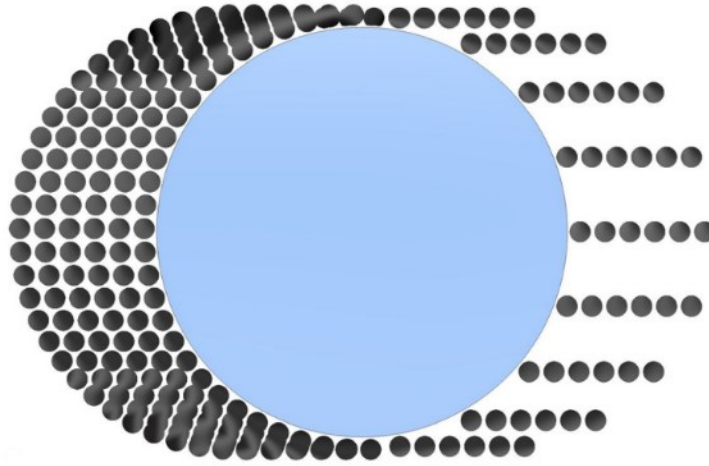


Figure 1.17 Increased electron density at an obstacle due to electron stagnation, the large circle represents an obstacle, the smaller circles represent electrons [109].

This increased electron density will reduce sharing of electrons by ion cores near the impeding edges of the precipitate. If there is an electron near the stagnation point, it will be hit with continuous collisions of electrons as they reach the stagnation point, resulting in an increased electron density and dissolution or weakening of bonds. A similar reaction would occur when electrons encounter dislocations or other small obstacles; the increased electrical resistivity will force the electrons to move around the obstacle causing stagnation points on the obstacle and increased electron density.

As dislocations encounter voids, interstitials and precipitates, dislocation loops may form around the obstacle leading to an effectively larger stagnation zone around the obstacle.

This effect would be magnified at grain boundaries as increased dislocation tangles and lattice misalignment will lead to increased electron stagnation and a greater electron density on the impeding side of the grain boundary. Due to the length of grain boundaries, the stagnation regions will be larger resulting in a greater electron density than a single obstacle such as

precipitate. As such, it is expected that dislocation motion resistance will be lowest at grain boundaries.

Electron stagnation theory is a promising new way that could be able to explain the electropalstic effect.

1.4. Electrically assisted manufacturing processes

Potential application for electroplasticity in manufacturing processes have been widely investigated in the last few decades because of its promising effect on material ductility. Main processes for which EAM is suggested lie in the field of bulk deformation such as sheet metal forming, forging, rolling and drawing. Other processes have been recently investigated like metal joining and material removal processes. A brief scheme of the actual applications of the EPE is presented in Figure 1.18.

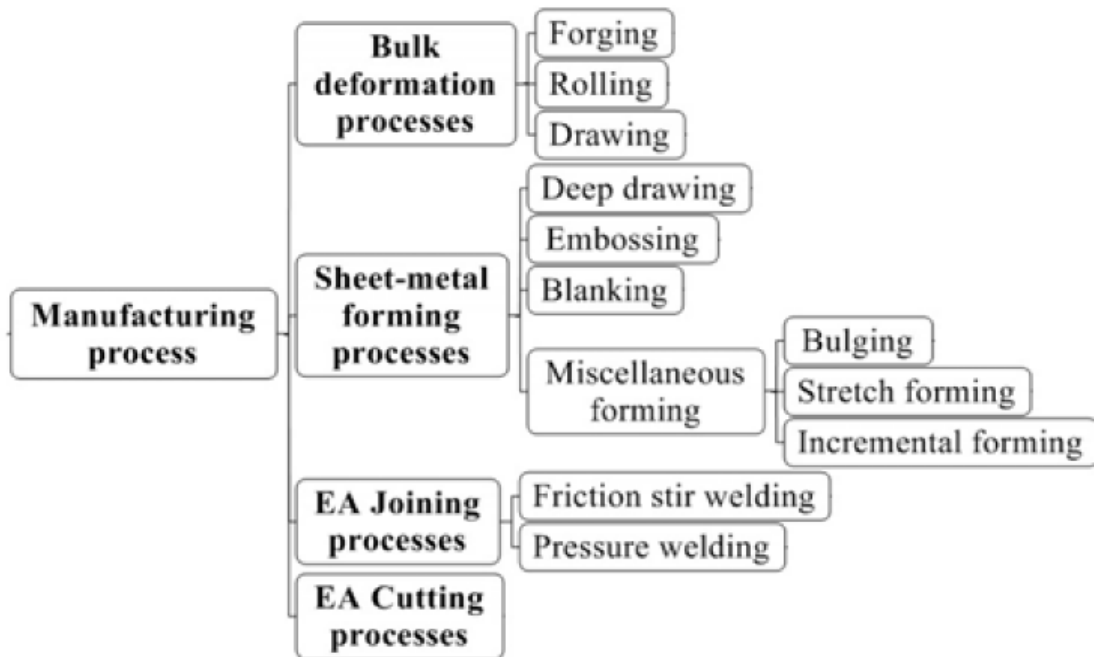


Figure 1.18 Schematic of electrically assisted manufacturing processes [110].

1.4.1. Forging process

Decrease in force needed for forging process and increase in ductility of certain alloys have been observed by some researchers [2,111]. The application of electroplasticity in the forging process could be done taking into account that the current density will vary during the process due to the change in cross section. A schematic of a forging process can be seen in Figure 1.19.

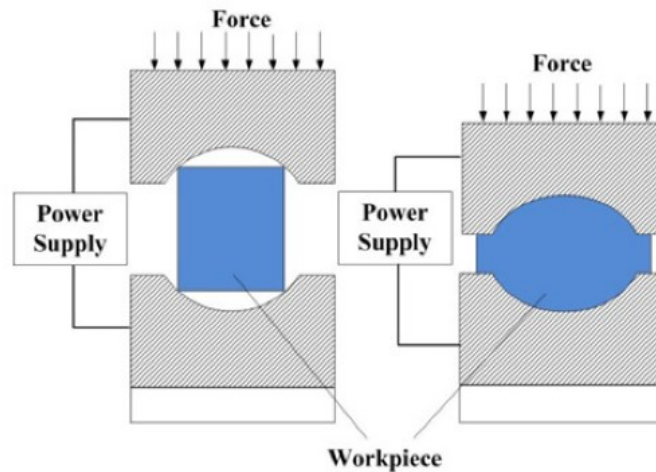


Figure 1.19 Schematic of a close die electrically assisted forging process [110].

1.4.2. Rolling process

Electrically assisted rolling process are widely investigated in the recent years. Magnesium alloys, nickel titanium based shape memory alloys, aluminum and titanium alloys have been subjected to electroplastic rolling and micro rolling [112–114]. In Figure 1.20 is showed a schematic of an electrically assisted rolling process. Care must be taken when designing the electrical rolling contact in order to avoid inconvenient high voltage electrical discharge that could damage both the workpiece and the rollers.

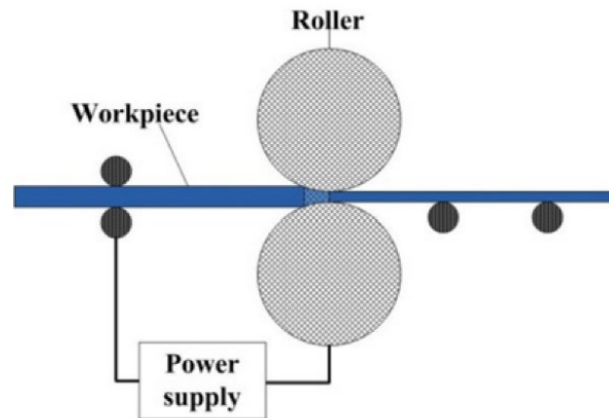


Figure 1.20 Schematic of an electrically assisted rolling process [114].

1.4.3. Drawing process

Electrically assisted drawing process is very promising because of the relatively small and constant cross section of the material deformed and the relatively easy way to deliver current to the workpiece. It has been studied since the first year after the discovery of the EPE, focusing mainly on difficult to form material such as tungsten [115,116]. Austenitic stainless steel, cast iron and copper showed a decrease in the drawing force and a better surface quality than conventional drawing, sparing also a few annealing steps [27,117–121]. Reduced production cycle and better product quality can be achieved with electroplastic drawing. In Figure 1.21 a schematic of an electroplastic drawing process is presented.

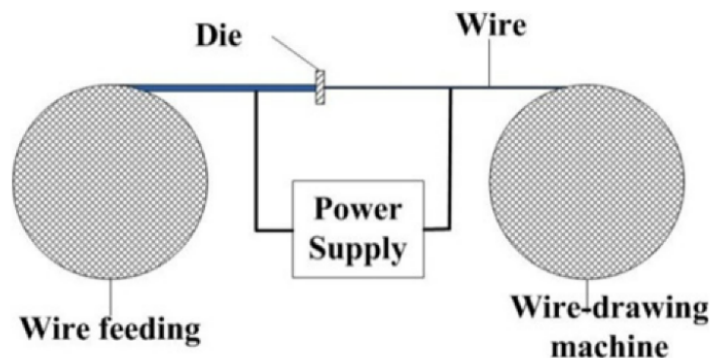


Figure 1.21 Schematic of an electrically assisted drawing process [27].

1.4.4. Deep drawing process

As observed by Wang et al. [122] lower resistance to deformation, better plasticity, improved ductility, dynamic recrystallized grains at low temperature, and low energy consumption are the advantages of the EA deep drawing process. He was able to enhance the drawability of AZ31 magnesium alloy cup and lowering the temperature needed for recrystallization to 200 °C rather than 350 °C of the conventional drawing. Figure 1.22 depicts a schematic of an electrically assisted deep drawing apparatus.

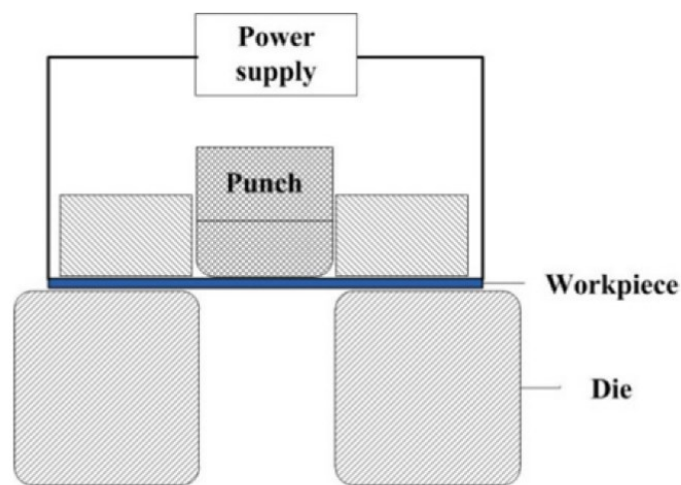


Figure 1.22 Schematic of an electrically assisted deep drawing process [122].

1.4.5. Embossing process

In Figure 1.23 it is showed an electrically assisted embossing process. It was proposed by Mai et al. [123] to fabricate micro channel on an austenitic stainless steel 316L at 110 °C. As for the other electrically assisted processes, reduced die pressure and more precise geometric features were obtained in comparison with the conventional embossing process.

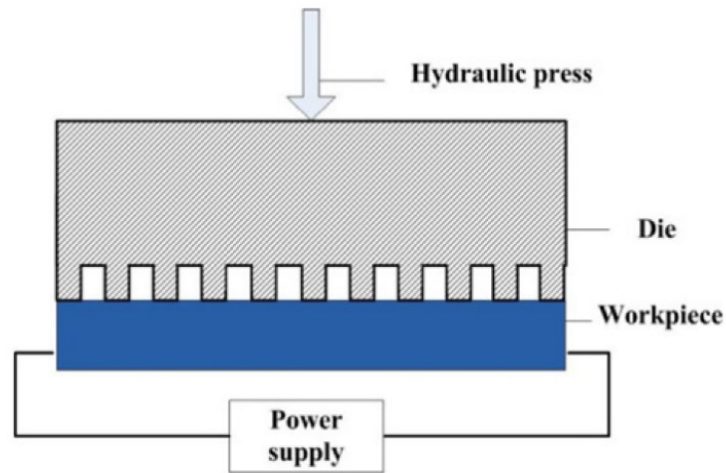


Figure 1.23 Schematic of an electrically assisted embossing process [123].

1.4.6. Blanking process

Electrically assisted blanking was proposed by Kim et al. [124] in order to form ultra-high strength steel (one single electric pulse during blanking operation). The process proved to reduce the blanking force by 85% and 20% compared, respectively, with conventional cold blanking and resistive heating blanking performed at the same temperature reached by the electrically assisted blanking (175 °C). Schematic of the process is presented in Figure 1.24.

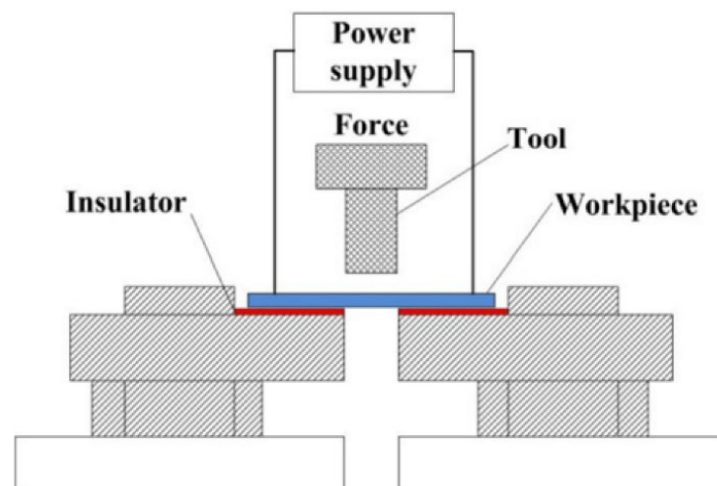


Figure 1.24 Schematic of an electrically assisted blanking process [124].

1.4.7. Incremental forming process

During incremental forming, only a small portion of the entire workpiece is subjected to deformation. It is, therefore, possible to apply a current density during the process and exploit the benefits of electroplastic effect. Asghar et al. [125] were able to deform at 47 °C titanium grade 5 alloys which is usually formed at temperature of 900 °C (Figure 1.25). Shape distortion and forming forces were reduced when applying a pulsed current in comparison with the traditional incremental forming processes. Thanks to the small cross section higher current density can be achieved without very onerous investment in the electric apparatus.

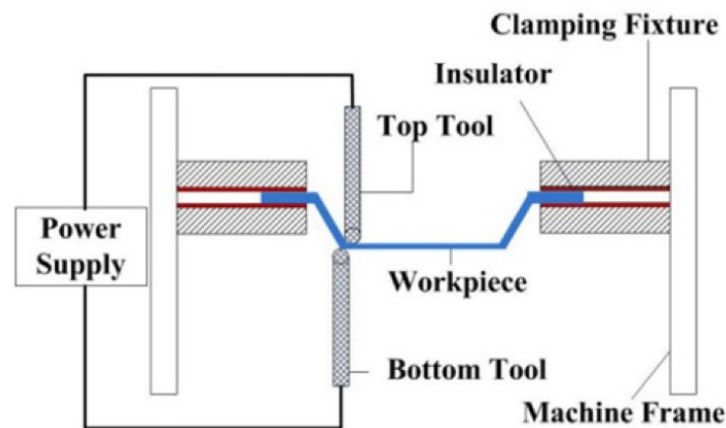


Figure 1.25 Schematic of an electrically assisted incremental forming process [126].

1.4.8. Friction stir welding process

Friction stir welding is a novel joining process that has been investigated a lot in the last decades. Friction stir welding is limited by the very high forces needed to joint high strength materials, but it is very versatile in the case of light alloys. Applying electrical current (continuous or pulsed) during friction stir welding it is possible to reduce the force in the Z axis, the tool wear, the power consumption and increase the weld speed as reported in [127–129]. Schematic of an electrically assisted friction stir welding process is shown in Figure 1.26.

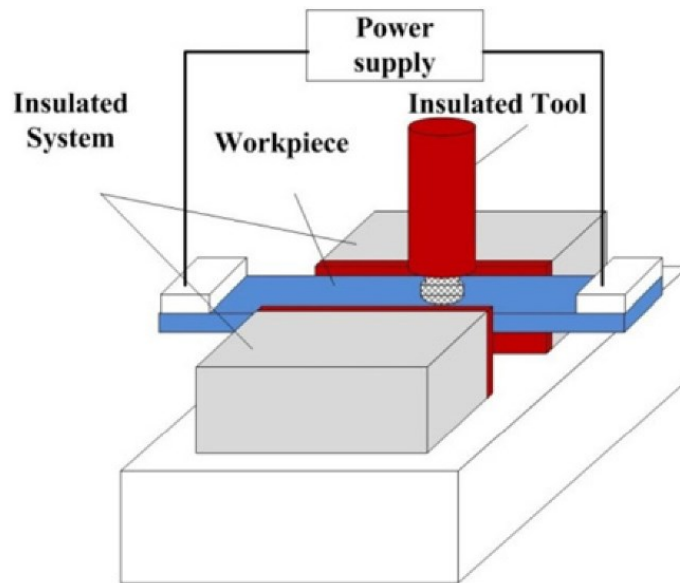


Figure 1.26 Schematic of an electrically assisted friction stir welding process [129].

1.4.9. Pressure welding process

It is suggested by Xu et al. [130] the electrically assisted pressure welding in Figure 1.27. They were able to pressure weld thin films of austenitic stainless steel 316L at 75 °C and 20 A/mm² of current density, increasing the bonding area from approximately 90 μm of the conventional process to 280 μm in the case of electrically assisted pressure welding.

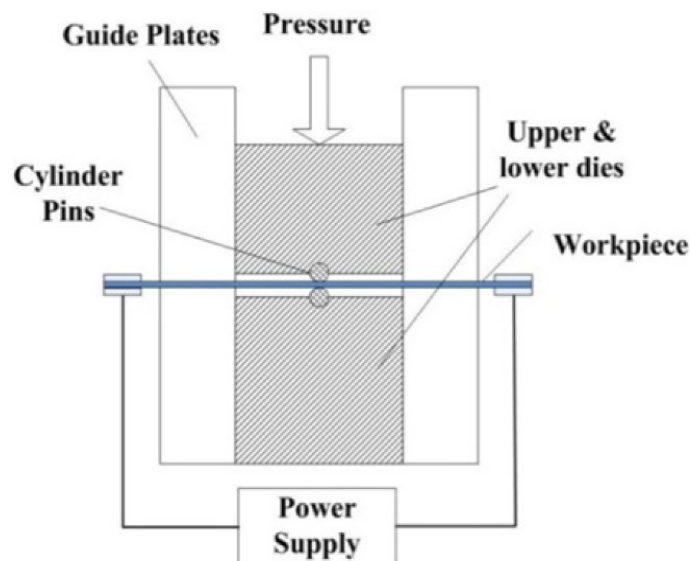


Figure 1.27 Schematic of an electrically assisted pressure welding process [130].

1.4.10. *Cutting process*

Baranov et al. [55] studied the electropalstic cutting process on a wide variety of material (i.e., copper, steel, duralumin, and cast iron). He applied pulsed current and measured the drilling force and speed. Decrease of friction force by 25-30% and decrease in processing time up to 12% were obtained in comparison with the traditional cutting process. Different morphologies of the chip were also found. Schematic of an electrically assisted cutting process is shown in Figure 1.28.

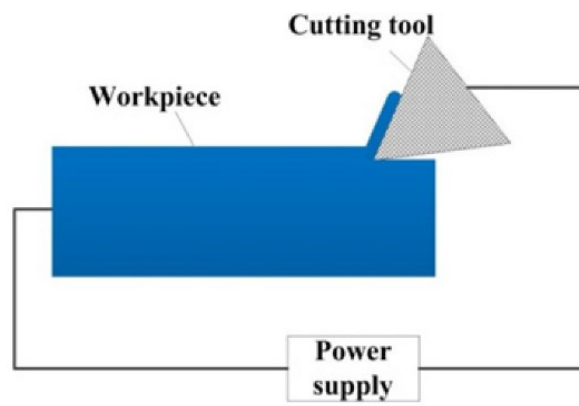


Figure 1.28 Schematic of an electrically assisted cutting process [55].

1.5. Electropulsing treatments

Conversely to the electrically assisted forming, in which electrical current is applied during the deformation, *Electropulsing Treatment* (EPT) is a new microstructure strengthening approach that uses high density and short duration electric current pulses applied to a bulk material. It has been observed that EPT was able to form an ultra-fined grain during phase transformation and recrystallisation, to change orientation and texture and to influence shape and distribution of secondary phase's particles during solid state transformation and solidification of metallic alloys. It has been reported that EPT was also able to heal microcracks within the material [131,132]

Some effect of EPT on some metallic alloys are depicted in Figure 1.29 [5,38,133–137].

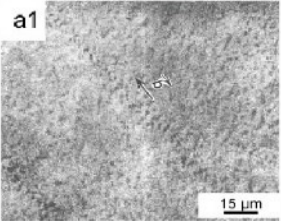
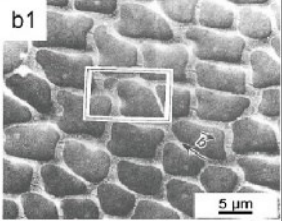
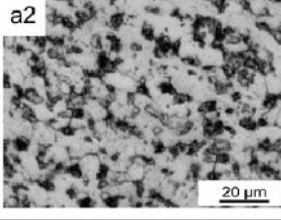
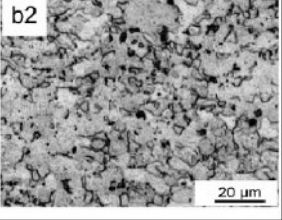
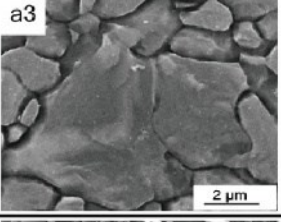
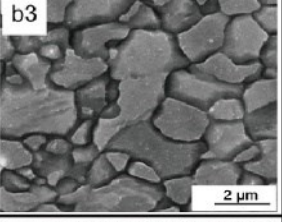
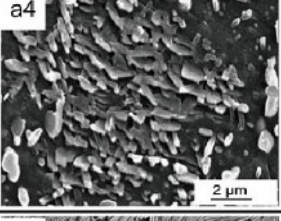
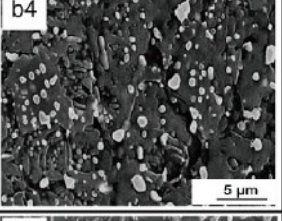
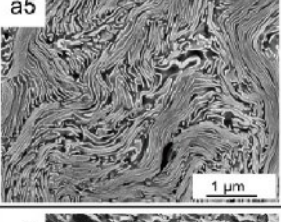
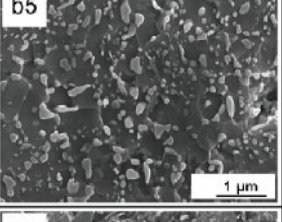
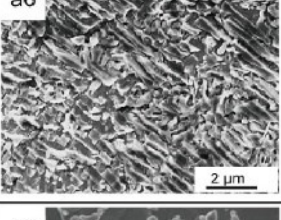
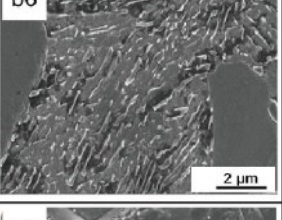
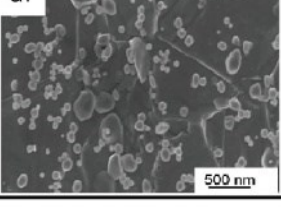
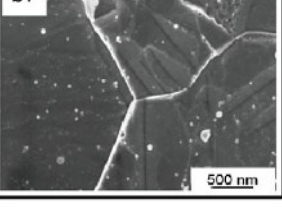
Typical metal materials		Untreated by EPT	Treated by EPT	References
Copper alloy	brass	a1 	b1 	[133]
		a2 	b2 	[134]
Magnesium alloy	AZ 31	a3 	b3 	[135]
	AZ 91	a4 	b4 	[38]
iron steel	pearlitic steel (0.8% C)	a5 	b5 	[5]
	TRIP (0.14% C)	a6 	b6 	[136]
	316L stainless steel	a7 	b7 	[137]

Figure 1.29 Microstructure of some metallic alloys before EPT (a1-a7) and after EPT (b1-b7) [138].

1.5.1. Grain refinement and recrystallisation

In his work Conrad et al. [24] performed an electropulsing heat treatment with current density of 800 A/mm² and a frequency of 2 Hz to cold drawn copper wire during annealing at 265 °C. Grain refinement at lower temperature compared with the conventional heat treatment was observed, and grain growth at slightly higher temperature (275 °C). They supposed that the electrical current enhanced the nucleation rate of the new forming grains. Grain refinement was observed also by other researchers (Figure 1.29 a1, b1). They were able to achieve a grain size smaller than 10 µm after fatigue stressing copper. Even smaller grain size (41 nm) and 200 °C reduction in the recrystallisation temperature was achieved for NiTi shape memory alloys subjected to EPT [139]. EPT on a titanium alloy TA15 (Ti 6Al 2Zr 1Mo 1V) with current density $j = 4.8 \div 5.4 \times 10^3 \text{ A/mm}^2$ completely recrystallized the alloy [140]. Similar results were obtained (5 µm average grain size, Figure 1.29 a2-b2) on a titanium grade five alloy (Ti 6Al 4V) with a current density $j = 5.06 \div 5.26 \times 10^3 \text{ A/mm}^2$ [141]. Change in the misorientation angle between grains from *Low Angle Grain Boundaries* (LAGBs) to *High Angle Grain Boundaries* (HAGBs) is a symptom of recrystallization since recrystallized structure show higher volume fraction of HAGBs. An effect of EPT on magnesium alloys AZ31 and AZ91 are showed in Figure 1.29 a3-b3, a4-b4. Besides the obvious grain refinement, a change in the misorientation angle between grains denoted the recrystallization of the entire microstructure (misorientation between 2°-15° before EPT to misorientation higher than 15° after the treatment) [135,142]. Nanocrystallized γ -iron grains (15 nm) were obtained in a 22Mn 5B steel after EPT with current density of 890 A/mm² and duration ranging from 60 ms to 180 ms [143]. It was supposed that the mechanism by which EPT were able to produce such a small grain size is that of reducing thermodynamic barriers and increasing nucleation rates of the phase. EPT were also applied to a variety of

steels (i.e., eutectoidic, TRIP, AISI 316L austenitic stainless steel and clean steel, Figure 1.29 a5-a7, b5-b7) [144]. Spheroidization of cementite in the pearlitic structure have been observed and a similar effect on the secondary phase particles in the case of the austenitic stainless steel AISI 316L. The appearance of bands in the microstructure of the TRIP steel was observed. It was proposed that the electrical pulses acted as an additional free energy hence, more interfaces can be generated leading to fragmentation of cementite particles. In Figure 1.30 it is proposed the mechanism by which electrical current induced cementite fragmentation with respect to different pearlitic orientation.

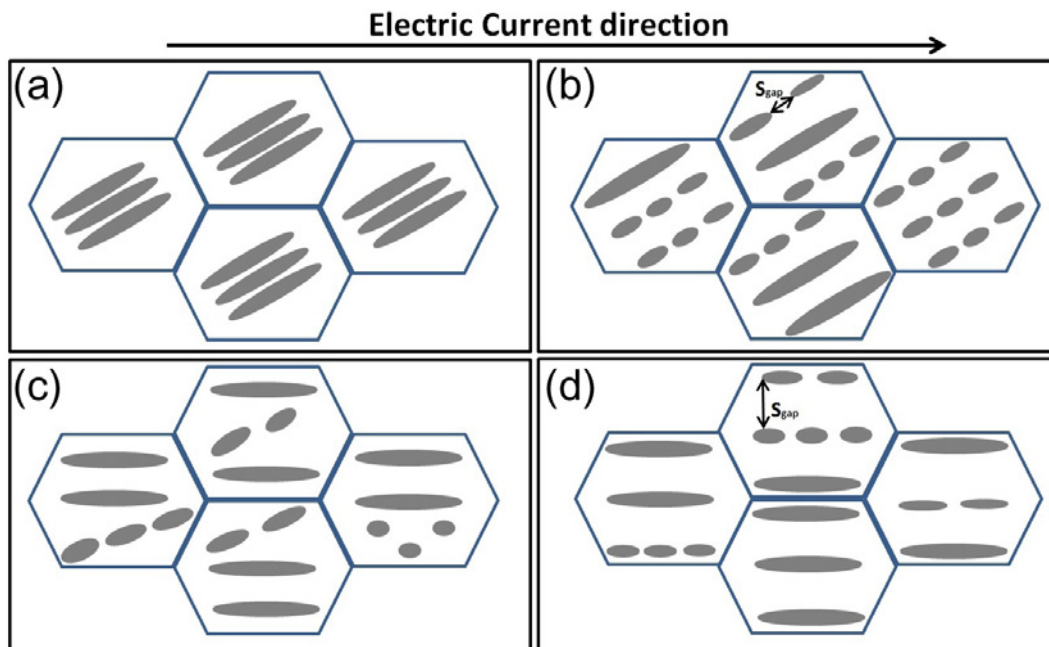


Figure 1.30 Schematic diagram of the influence of electrical current on various configuration of pearlitic microstructure [145].

1.5.2. Phase transitions and grains refinement

As previous study have observed [146], EPT is able to form ultra-fine grain structure and nanostructure. Extended theoretical researches have been done concerning the role of electrical current on interfaces of different resistivity phases, the interface diffusion in an electric field and the augmented diffusion of chemical species under an electric field known as electromigration

[88,147,148]. Lu et al. [149] reported an enhancement of stabilization of metastable phase due to its lower resistivity compared to the matrix. He supposed that EPT accelerated the precipitation of σ phase according to the eutectoidic reaction of decomposition of ferrite $\delta \rightarrow \gamma + \sigma$, stabilizing it even at temperature at which it should resolubilize.

A possible mechanism by which EPT is able to induce *Ultra Fine Grain* (UFG) and nanostructures is depicted in Figure 1.31.

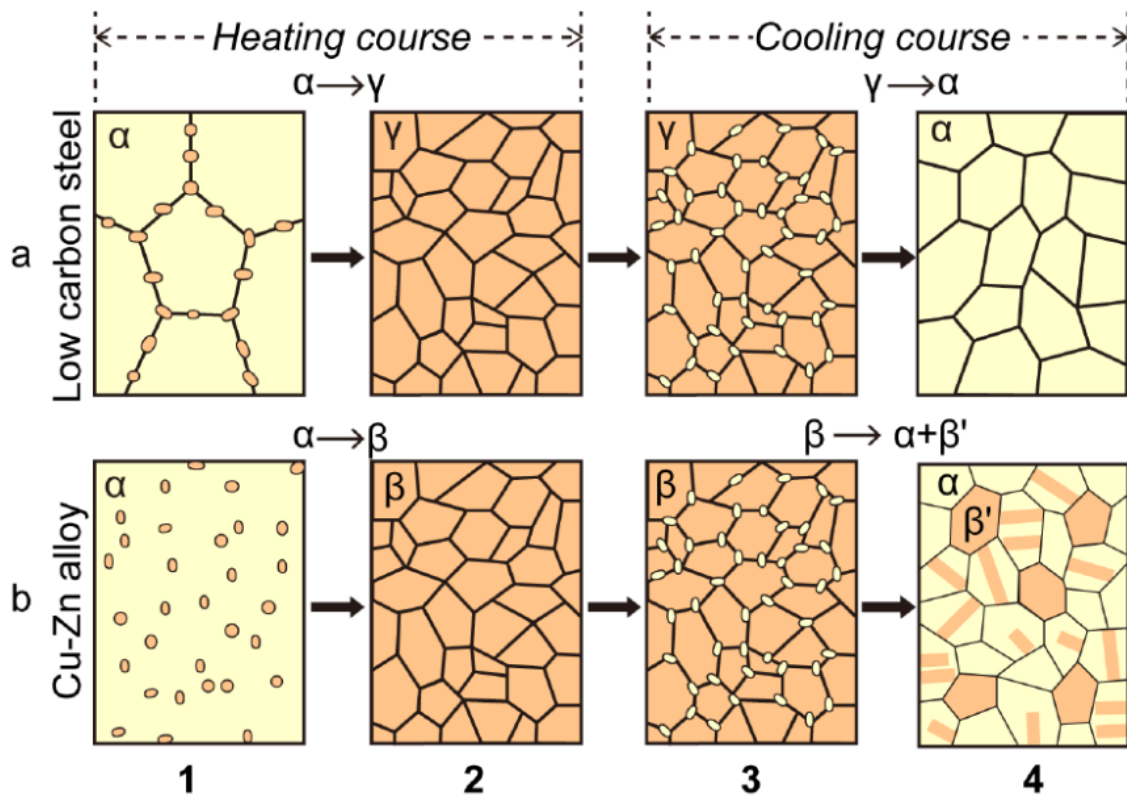


Figure 1.31 Schematic diagram of phase transition and ultra-fine grains: (a) low-carbon steel [150]; (b) Cu-Zn alloy [151]: (1) nucleation of γ or β phase, (2) grain growth of γ and β phase, (3) formation of α phase nucleation and (4) formation of ultra-fine grains and twin structure of α phase and β' phase [138].

α -Fe phase with some perlite in between α grains can be seen in Figure 1.31 (a), it will then transform in a fully austenitic microstructure together with transformation from $\alpha \rightarrow \beta$ and β' phase in brass (Figure 1.31b).

Formation of β equiaxed grain in a titanium grade five alloy after short duration EPT was observed by Ye et al. [152]. Similar results were obtained by Song et al. regarding TiAl alloy [153]. They were able to reduce the grain size and change the morphology from 1000 μm lamellae to approximately 40 μm

equiaxed grain. It was proposed by Zhou et al. [153] that the possible EPT mechanism on grain refinement and recrystallization is that of lowering the thermodynamic barriers for recrystallization and increasing the nucleation rate.

From a thermodynamic point of view, comparing the conventional heat treatment with the EPT, it must be present an additional term regarding the Gibbs free energy that decreases the apparent temperature of solid state transformations.

Li et al. [154] observed a lowering of the Gibbs free energy formation of strain induced martensite in the case of electrically assisted tensile deformation of austenitic stainless steel AISI 304 (Figure 1.32).

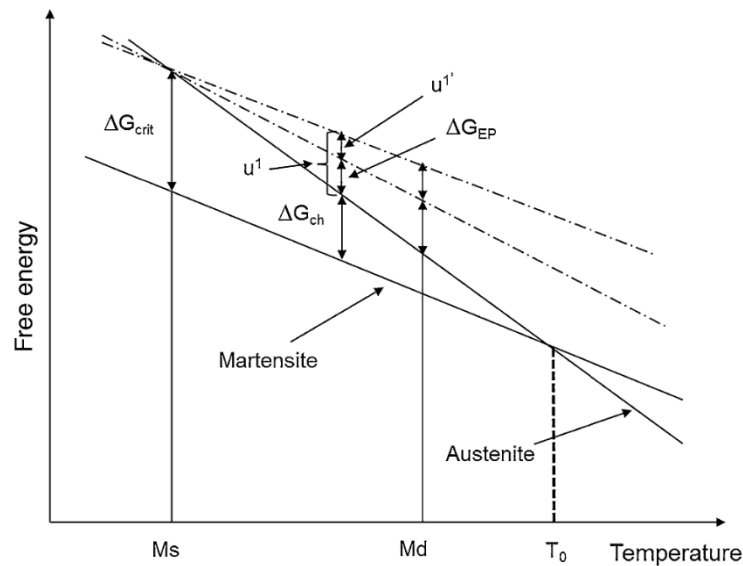


Figure 1.32 Gibbs free energy vs temperature of strain induced martensitic transformation [154].

If the temperature during deformation lies between M_s and M_d (respectively martensite start and the temperature at which 50% of martensite is formed when strained to 30%) the additional energy needed for the formation of *Strain Induced Martensite* (SIM) is the one caused by the internal strain energy u^l due to dislocation pile ups at strong barriers. Without pulsed current the internal strain energy for SIM formation can be described by:

$$u^l = \Delta G_{crit} - \Delta G_{chem} \quad (1.7)$$

In the case of an EPT an additional term proposed in [150] is used and is defined by:

$$\Delta G_{EP} = -N\Delta W_{EP} \quad (1.8)$$

where N is the number of martensitic nuclei, ΔW_{EP} is an energy change due to the distribution change of the current in the formation of martensitic nuclei, which is given by [150,155]:

$$\Delta W_{EP} = \mu g \xi(\sigma_1, \sigma_2) \Delta V C_d^2 \quad (1.9)$$

where μ is a magnetic susceptibility, g is a geometric factor, ΔV is the volume of a nucleus and C_d is an effective current density. $\xi(\sigma_1, \sigma_2)$ is a factor that depends on the electrical properties of the nucleus and the matrix, where σ_1 is the conductivity of the martensitic phase and σ_2 is the conductivity of austenitic phase. $\xi(\sigma_1, \sigma_2)$ is expressed as [150,155]:

$$\xi(\sigma_1, \sigma_2) = \frac{\sigma_2 - \sigma_1}{\sigma_1 + 2\sigma_2} \quad (1.10)$$

As a result, internal strain energy required for the martensitic transformation in the case of electropulsing treatment can be described by:

$$u^{l'} = \Delta G_{crit} - \Delta G_{chem} - \Delta G_{EP} \quad (1.11)$$

Therefore, if the term ΔG_{EP} is positive, the total internal strain energy $u^{l'}$ needed for the martensitic transformation is lower than that without electropulsing u^l .

1.5.3. *Texture evolution and oriented microstructure*

An interesting effect observed after EPT is the change in the texture and orientation of microstructure. Rahnema et al. [156] investigated the effect of EPT on the microstructure of a duplex austenitic-ferritic steel (not to be confused with duplex stainless steel). They observed crystal rotation during EPT conducted at room temperature with current densities up to

1.018×10^7 A/mm² along the direction of lower electrical resistivity of the grains probably because of the increase diffusion coefficient of phase boundaries due to electromigration. Regarding the dependence of the crystal orientation with respect the current density, Wang et al. [157] observed an increase in nucleation rate of Cu-Zn alloy when there were misalignment between the electrical current flow and the rolling direction. They also observed a random nucleation of recrystallized grain during EPT but with consistent orientation depending on the direction of the current flow.

A similar effect have been previously shown in Figure 1.30 were it can be observed higher cementite fragmentation during EPT if the interface has some sort of angularity between the direction of the electrical current [145]. One way to explain this phenomenon is the tendency of a system to lower its free energy and proceed towards equilibrium. In the case of a current flowing in a microstructure where phases with different electrical resistivity are present, its tendency is to distribute itself according to Kirchoff law, and to break the interphases that possess higher electrical resistivity (cementite sheets into cementite particles). The total resistivity is therefore lowered according to:

$$R = \frac{\rho L}{S} = \frac{\rho L}{S_{gap}} \quad (1.12)$$

where ρ is the electrical resistivity, L is the total length of the sample, S is the cross-section area and S_{gap} is the gap area between the fragmented plates, respectively.

It could be interesting to exploit this EPT feature in materials where their formability is related to its texture, such as magnesium alloys.

Cold rolled AZ91 magnesium alloy show a very strong {0001} texture. During electropulsed induced recrystallization an evolution of the texture was observed as shown in Figure 1.33. The new recrystallized grains possess strong rolling direction oriented texture {10 $\bar{1}$ 0}.

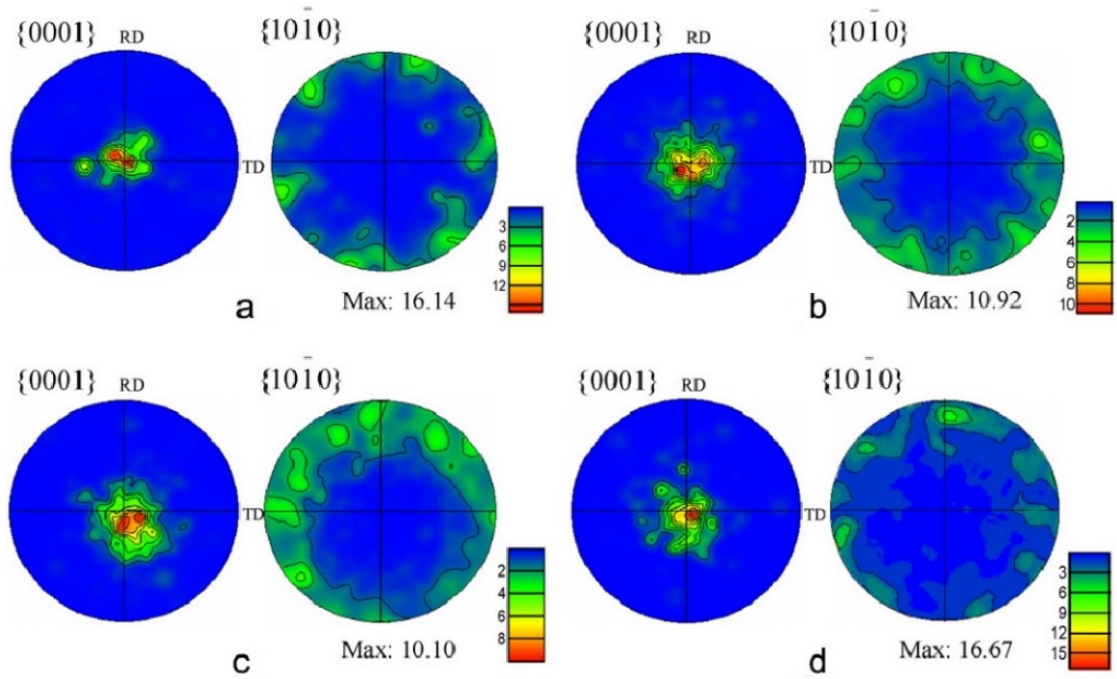


Figure 1.33 $\{0001\}$ and $\{10\bar{1}0\}$ pole figures of the AZ91 alloy after EPT: (a) cold-rolled sample; (b) 100 Hz-EPT; (c) 110 Hz-EPT; (d) 133 Hz-EPT [158].

1.6. References

- [1] Salandro, W.A.; Bunget, C.; Mears, L. "*Thermo-Mechanical Investigations of the Electroplastic Effect*", In Proceedings of the **ASME 2011 International Manufacturing Science and Engineering Conference, Volume 1**; ASME, (2011); pp. 573–582.
- [2] Jones, J.J.; Mears, L.; Roth, J.T. "*Electrically-Assisted Forming of Magnesium AZ31: Effect of Current Magnitude and Deformation Rate on Forgeability*", **J. Manuf. Sci. Eng.** (2012), Volume 134, pp.034504.
- [3] Green, C.R.; Mcneal, T.A.; Roth, J.T.; Erie, P.S.; Colledge, T.B. "*Springback elimination for al-6111 alloys using electrically-assisted manufacturing (EAM)*", **Trans. North Am. Manuf. Res. Inst.** (2009).
- [4] Kim, M.-S.; Vinh, N.T.; Yu, H.-H.; Hong, S.-T.; Lee, H.-W.; Kim, M.-J.; Han, H.N.; Roth, J.T. "*Effect of electric current density on the mechanical property of advanced high strength steels under quasi-static tensile loads*", **Int. J. Precis. Eng. Manuf.** (2014), Volume 15, pp.1207–1213.
- [5] Samuel, E.I.; Bhowmik, A.; Qin, R. "*Accelerated spheroidization Induced by high Intensity electric pulse In a severely deformed eutectoid steel*", **J. Mater. Res.** (2010), Volume 25, pp.1020–1024.
- [6] Wang, X.; Sánchez Egea, A.; Xu, J.; Meng, X.; Wang, Z.; Shan, D.; Guo, B.; Cao, J. "*Current-Induced Ductility Enhancement of a Magnesium Alloy AZ31 in Uniaxial Micro-Tension Below 373 K*", **Materials (Basel)**. (2018), Volume 12, pp.111.
- [7] Machlin, E.S. "*Applied voltage and the plastic properties of "brittle" rock salt*", **J. Appl. Phys.** (1959), Volume 30, pp.1109–1110.
- [8] Nabarro, F.N.R. *Theory of Crystal Dislocations*; Oxford University Press: Oxford, (1967);
- [9] Kravchenko, V.Y. "*Effect of directed electron beam on moving dislocations*", **Sov. Phys. JETP** (1967), Volume 24, pp.1135–1142.
- [10] Troitskii, O.A. "*Electromechanical effect in metals*", **Pis'ma Zhurn Experim Teor.**

Fiz (1969), Volume 10, pp.18.

- [11] Klimov, K.M.; Novikov, I.I. "The "electroplastic effect"", **Strength Mater.** (1984), Volume 16, pp.270–276.
- [12] Okazaki, K.; Kagawa, M.; Conrad, H. "A study of the electroplastic effect in metals", **Scr. Metall.** (1978), Volume 12, pp.1063–1068.
- [13] Okazaki, K.; Kagawa, M.; Conrad, H. "An evaluation of the contributions of skin, pinch and heating effects to the electroplastic effect in titanium", **Mater. Sci. Eng.** (1980), Volume 45, pp.109–116.
- [14] Fiks, V.B. "Interaction of conduction electrons with single dislocations in metals", **J. Exp. Theor. Phys.** (1981), Volume 53, pp.1209–1211.
- [15] Bolko, I.; Geguzin, E.; Klinchuk, I. "Drag of dislocations by an electron wind in metals", **Zhurnal Eksp. i Teor. Fiz.** (1981), Volume 54, pp.1156–1158.
- [16] Goldman, P.D.; Motowidlo, L.R.; Galligan, J.M. "The absence of an electroplastic effect in lead at 4.2K", **Scr. Metall.** (1981), Volume 15, pp.353–356.
- [17] Troitskii, O.A. "The electroplastic effect in metals", **Dislocations Solids. 8 Basic Probl. Appl.** (1984), Volume 1, pp.497–540.
- [18] Sprecher, A.F.; Mannan, S.L.; Conrad, H. "Overview no. 49 On The Mechanisms For The Electroplastic Effect In Metals", **Acta Metall.** (1986), Volume 34, pp.1145–1162.
- [19] Kopanev, A.A. "The nature of the electroplastic effect in metals", **Strength Mater.** (1991), Volume 23, pp.55–59.
- [20] Molotskii, M.I.; Fleurov, V. "Magnetic effect in electroplasticity of metals", **Phys. Rev.** (1995), Volume 52, pp.829–834.
- [21] Davies, T.J.; Ogwu, A.A. "A possible route to improving the ductility of brittle intermetallic compounds", **J. Alloys Compd.** (1995), Volume 228, pp.105–111.
- [22] Roschupkin, A.M.; Bataronov, I.L. "Physical basis of the electroplastic deformation of metals", **Russ. Phys. J.** (1996), Volume 39, pp.230–236.
- [23] Conrad, H. "Influence of an electric or magnetic field on the liquid–solid transformation in materials and on the microstructure of the solid", **Mater. Sci. Eng.**

- A (2000), Volume 287, pp.205–212.
- [24] Conrad, H. "*Effects of electric current on solid state phase transformations in metals*", **Mater. Sci. Eng. A** (2000), Volume 287, pp.227–237.
- [25] Conrad, H. "*Electroplasticity in metals and ceramics*", **Mater. Sci. Eng. A** (2000), Volume 287, pp.276–287.
- [26] Tang, G.; Zheng, M.; Zhu, Y.; Zhang, J.; Fang, W.; Li, Q. "*The application of the electro-plastic technique in the cold-drawing of steel wires*", **J. Mater. Process. Technol.** (1998), Volume 84, pp.268–270.
- [27] Tang, G.; Zhang, J.; Zheng, M.; Zhang, J.; Fang, W.; Li, Q. "*Experimental study of electroplastic effect on stainless steel wire 304L*", **Mater. Sci. Eng. A** (2000), Volume 281, pp.263–267.
- [28] Livesey, S.; Duan, X.; Priestner, R.; Collins, J. "*An electroplastic effect in 314% silicon steel*", **Scr. Mater.** (2001), Volume 44, pp.803–809.
- [29] Levitin, V.; Loskutov, S.. "*The effect of a current pulse on the fatigue of titanium alloy*", **Solid State Commun.** (2004), Volume 131, pp.181–183.
- [30] Golovin, Y.I. "*Magnetoplastic effects in solids*", **Phys. Solid State** (2004), Volume 46, pp.789–824.
- [31] Al'shits, V.I.; Darinskaya, E. V.; Petrzhik, E.A. "*In situ investigation of the magnetoplastic effect in NaCl crystals by the continuous etching method*", **Sov. physics. Solid state** (1991), Volume 33, pp.1694–1699.
- [32] Molotskii, M.I. "*Possible mechanism of the magnetoplastic effect*", **Sov. physics. Solid state** (1991), Volume 33, pp.1760–1761.
- [33] Bilyk, S.R.; Ramesh, K.T.; Wright, T.W. "*Finite deformations of metal cylinders subjected to electromagnetic fields and mechanical forces*", **J. Mech. Phys. Solids** (2005), Volume 53, pp.525–544.
- [34] Xu, Z.; Tang, G.; Tian, S.; Ding, F.; Tian, H. "*Research of electroplastic rolling of AZ31 Mg alloy strip*", **J. Mater. Process. Technol.** (2007), Volume 182, pp.128–133.
- [35] Jiang, Y.; Tang, G.; Guan, L.; Wang, S.; Xu, Z.; Shek, C.; Zhu, Y. "*Effect of*

- electropulsing treatment on solid solution behavior of an aged Mg alloy AZ61 strip*", **J. Mater. Res.** (2008), Volume 23, pp.2685–2691.
- [36] Jiang, Y.; Tang, G.; Shek, C.; Liu, W. "Microstructure and texture evolution of the cold-rolled AZ91 magnesium alloy strip under electropulsing treatment", **J. Alloys Compd.** (2011), Volume 509, pp.4308–4313.
- [37] Wang, S.; Tang, G.; Xu, Z.; Xin, Y.; Guan, L. "Corrosion behavior of the electroplastic rolled AZ31 magnesium alloy in simulated sea water", **Mater. Sci. Technol.** (2010), Volume 3.
- [38] Jiang, Y.; Tang, G.; Shek, C.; Zhu, Y.; Xu, Z. "On the thermodynamics and kinetics of electropulsing induced dissolution of β -Mg₁₇Al₁₂ phase in an aged Mg–9Al–1Zn alloy", **Acta Mater.** (2009), Volume 57, pp.4797–4808.
- [39] Salandro, W.A.; Jones, J.J.; Bunget, C.; Mears, L.; Roth, J.T. *Electrically Assisted Forming*; Springer Series in Advanced Manufacturing; Springer International Publishing: Cham, (2015); ISBN 978-3-319-08878-5.
- [40] Tilak, T.K.; Jayaprakasam, S.; Padmanabhan, K.A.; Misochenko, A.A.; Stolyarov, V. V.; J.V., T.K.; Jayaprakasam, S.; Padmanabhan, K.A.; Misochenko, A.A.; Stolyarov, V. V.; et al. "On the tensile behaviour of coarse and ultrafine grained NiTi", **Mater. Charact.** (2019), Volume 149, pp.41–51.
- [41] Stolyarov, V. "Features of Electroplastic Effect in Alloys with Martensite Transformation", **Acta Metall. Sin. (English Lett.** (2018), Volume 31, pp.1305–1310.
- [42] Stolyarov, V. V "Influence of structure refinement on electroplastic effect in shape memory TiNi alloys", **Mater. Phys. Mech.** (2015), Volume 24, pp.218–223.
- [43] Stolyarov, V. V "Deformation Behavior of Ultrafine-Grained Materials Under Tension with Current", **Russ. Phys. J.** (2015), Volume 58, pp.803–807.
- [44] Stolyarov, V. V "Role of structure refinement and electropulse current in the mechanical behavior of shape memory alloy", **J. Mach. Manuf. Reliab.** (2015), Volume 44, pp.704–709.
- [45] Potapova, A.A.; Resnina, N.N.; Stolyarov, V. V "Shape memory effects in TiNi-

- based alloys subjected to electroplastic rolling*", **J. Mater. Eng. Perform.** (2014), Volume 23, pp.2391–2395.
- [46] Kukudzhanov, V.N.; Kolomiets-Romanenko, A. V. "*Study of the influence of electric current dynamical action on mechanical properties of materials with ordered structure of defects*", **Mech. Solids** (2010), Volume 45, pp.465–475.
- [47] Salandro, W.A.; Bunget, C.; Mears, L.; Wesley, A.S.; Bunget, C.; Mears, L.; Salandro, W.A.; Bunget, C.; Mears, L. "*Modeling and Quantification of the Electroplastic Effect When Bending Stainless Steel Sheet Metal*", In Proceedings of the **ASME 2010 International Manufacturing Science and Engineering Conference, Volume 1**; ASME, (2010); pp. 581–590.
- [48] Salandro, W.A.; Bunget, C.; Mears, L. "*Electroplastic Modeling of Bending Stainless Steel Sheet Metal Using Energy Methods*", **J. Manuf. Sci. Eng.** (2011), Volume 133, pp.041008.
- [49] Salandro, W.A.; Bunget, C.J.; Mears, L. "*Several Factors Affecting the Electroplastic Effect During an Electrically-Assisted Forming Process*", **J. Manuf. Sci. Eng.** (2011), Volume 133, pp.064503.
- [50] Salandro, W.A.; Bunget, C.J.; Mears, L. "*A thermal-based approach for determining electroplastic characteristics*", **Proc. Inst. Mech. Eng. Part B J. Eng. Manuf.** (2012), Volume 226, pp.775–788.
- [51] Bunget, C.; Salandro, W.; Mears, L.; Roth, J.T. "*Energy-based modeling of an electrically-assisted forging process*", **Trans. North Am. Manuf. Res. Inst. SME** (2010), Volume 38, pp.647–654.
- [52] Salandro, W.A.; Bunget, C.; Mears, L. "*Modeling the Electroplastic Effect During Electrically-Assisted Forming of 304 Stainless Steel*", **Proc. Asme Int. Manuf. Sci. Eng. Conf. 2012** (2012), pp.93–102.
- [53] Salandro, W.; Roth, J. "*Formation of 5052 aluminum channels using electrically-assisted manufacturing (eam)*", In Proceedings of the **ASME 2009 International Manufacturing Science and Engineering Conference**; (2009); pp. 1–10.
- [54] Salandro, W.A.; Jones, J.J.; Mcneal, T.A.; Roth, J.T.; Erie, P.S.; Hong, S.; Smith,

- M.T. "Formability of Al 5xxx Sheet Metals Using Pulsed Current for Various Heat Treatments", **J. Manuf. Sci. Eng.** (2010), Volume 132, pp.1–11.
- [55] Baranov, S.A.; Staschenko, V.I.; Sukhov, A. V; Troitskii, O.A.; Tyapkin, A. V "Electroplastic Metal Cutting", **Russ. Electr. Eng.** (2011), Volume 82, pp.477–479.
- [56] Xu, Z.; Wang, H.; Sun, Z.; Ye, Y.; Tang, G. "Effect of electropulsing-assisted turning process on AISI 5120 cementation steel", **Mater. Sci. Technol. (United Kingdom)** (2017), Volume 33, pp.1454–1460.
- [57] Hameed, S.; González Rojas, H.A.; Sánchez Egea, A.; Alberro, A.N. "Electroplastic cutting influence on power consumption during drilling process", **Int. J. Adv. Manuf. Technol.** (2016), Volume 87, pp.1835–1841.
- [58] Sánchez Egea, A.; González Rojas, H.A.; Montilla Montaña, C.A.; Kallewaard Echeverri, V. "Effect of electroplastic cutting on the manufacturing process and surface properties", **J. Mater. Process. Technol.** (2015), Volume 222, pp.327–334.
- [59] Sánchez Egea, A.; González-Rojas, H.A.; Montilla-Montaña, C.A.; Kallewaard-Echeverri, V. "Turning Process Assisted in situ by Short Time Current Pulses", **Procedia Eng.** (2015), Volume 132, pp.507–512.
- [60] Jones, E.; Jones, J.J.; Mears, L. "Empirical Modeling of Direct Electric Current Effect on Machining Cutting Force", In Proceedings of the **ASME 2013 International Manufacturing Science and Engineering Conference**; (2016); pp. 1–7.
- [61] Kinsey, B.; Cullen, G.; Jordan, A.; Mates, S. "Investigation of electroplastic effect at high deformation rates for 304SS and Ti – 6Al – 4V", **CIRP Ann. - Manuf. Technol.** (2013), Volume 62, pp.279–282.
- [62] Fan, R.; Magargee, J.; Hu, P.; Cao, J. "Materials Science & Engineering A Influence of grain size and grain boundaries on the thermal and mechanical behavior of 70 / 30 brass under electrically-assisted deformation", **Mater. Sci. Eng. A** (2013), Volume 574, pp.218–225.
- [63] Magargee, J.; Morestin, F.; Cao, J. "Characterization of Flow Stress for Commercially Pure Titanium Subjected to Electrically Assisted Deformation", **J. Eng. Mater. Technol.** (2013), Volume 135, pp.041003.

- [64] Magargee, J.; Fan, R.; Cao, J. "*Analysis and Observations of Current Density Sensitivity and Thermally Activated Mechanical Behavior in Electrically-Assisted Deformation*", **J. Manuf. Sci. Eng.** (2013), Volume 135, pp.061022.
- [65] Sánchez Egea, A.; González Rojas, H.A.; Celentano, D.J.; Travieso-Rodríguez, J.A.; Llumà i Fuentes, J. "*Electroplasticity-assisted bottom bending process*", **J. Mater. Process. Technol.** (2014), Volume 214, pp.2261–2267.
- [66] Chu, X.R.; Wang, L.; Lin, S.X.; Yue, Z.M.; Gao, J. "*Experimental Investigation on Formability of AZ31B Magnesium Alloy V-Bending Under Pulse Current*", **Acta Metall. Sin. (English Lett.)** (2018), Volume 31, pp.1249–1257.
- [67] Li, X.; Zhou, Q.; Zhao, S.; Chen, J. "*Effect of pulse current on bending behavior of ti6al4v alloy*", **Procedia Eng.** (2014), Volume 81, pp.1799–1804.
- [68] Gennari, C.; Pezzato, L.; Simonetto, E.; Gobbo, R.; Forzan, M.; Calliari, I. "*Investigation of Electroplastic Effect on Four Grades of Duplex Stainless Steels*", **Materials (Basel)**. (2019), Volume 12, pp.1911.
- [69] Xu, H.; Liu, X.; Zhang, D.; Zhang, X. "*Minimizing serrated flow in Al-Mg alloys by electroplasticity*", **J. Mater. Sci. Technol.** (2019), Volume 35, pp.1108–1112.
- [70] Park, J.-W.; Jeong, H.-J.; Jin, S.-W.; Kim, M.-J.; Lee, K.; Kim, J.J.; Hong, S.-T.; Han, H.N. "*Effect of electric current on recrystallization kinetics in interstitial free steel and AZ31 magnesium alloy*", **Mater. Charact.** (2017), Volume 133, pp.70–76.
- [71] Wang, X.; Xu, J.; Shan, D.; Guo, B.; Cao, J. "*Effects of specimen and grain size on electrically-induced softening behavior in uniaxial micro-tension of AZ31 magnesium alloy: Experiment and modeling*", **Mater. Des.** (2017), Volume 127, pp.134–143.
- [72] Xu, X.; Zhao, Y.; Wang, X.; Zhang, Y.; Ning, Y. "*Effect of rapid solid-solution induced by electropulsing on the microstructure and mechanical properties in 7075 Al alloy*", **Mater. Sci. Eng. A** (2016), Volume 654, pp.278–281.
- [73] Kuang, J.; Low, T.S.E.; Niezgoda, S.R.; Li, X.; Geng, Y.; Luo, A.A.; Tang, G. "*Abnormal texture development in magnesium alloy Mg-3Al-1Zn during large strain electroplastic rolling: Effect of pulsed electric current*", **Int. J. Plast.** (2016), Volume 87, pp.86–99.

- [74] Kuang, J.; Li, X.; Zhang, R.; Ye, Y.; Luo, A.A.; Tang, G. "Enhanced rollability of Mg 3Al 1Zn alloy by pulsed electric current: a comparative study", **Mater. Des.** (2016), Volume 100, pp.204–216.
- [75] Jiang, T.; Peng, L.; Yi, P.; Lai, X. "Flow behavior and plasticity of Ti-6Al-4V under different electrically assisted treatments", **Mater. Res. Express** (2016), Volume 3.
- [76] Lin, S.X.; Chu, X.R.; Bao, W.K.; Gao, J.; Ruan, L.Q. "Experimental investigation of pulse current on mechanical behaviour of AZ31 alloy", **Mater. Sci. Technol.** (2015), Volume 31, pp.1131–1138.
- [77] Jiang, Y. bin; Guan, L.; Tang, G. yi; Cheng, B.; Liu, D. bo "Microstructure and texture evolution of Mg-3Zn-1Al magnesium alloy during large-strain electroplastic rolling", **Int. J. Miner. Metall. Mater.** (2015), Volume 22, pp.411–416.
- [78] Jeong, H.J.; Park, J. won; Jeong, K.J.; Hwang, N.M.; Hong, S.T.; Han, H.N. "Effect of Pulsed Electric Current on TRIP-Aided Steel", **Int. J. Precis. Eng. Manuf. - Green Technol.** (2019), Volume 6, pp.315–327.
- [79] Sánchez Egea, A.; Peiró, J.J.; Signorelli, J.W.; González Rojas, H.A.; Celentano, D.J. "On the microstructure effects when using electropulsing versus furnace treatments while drawing inox 308L", **J. Mater. Res. Technol.** (2019), Volume 8, pp.2269–2279.
- [80] Zhao, Z.; Wang, G.; Hou, H.; Zhang, Y.; Wang, Y. "The effect of pulsed current on the shear deformation behavior of Ti-6Al-4V alloy", **Sci. Rep.** (2018), Volume 8, pp.1–9.
- [81] Gennari, C.; Bruschi, S.; Forzan, M.; Calliari, I. "Electrical assisted uniaxial tensile test on UNS S32205, UNS S32304 and UNS S32750 duplex stainless steels", In Proceedings of the **EUROMAT**; Thessalonikki, (2017).
- [82] Li, X.; Wang, F.; Li, X.; Zhu, J.; Tang, G. "Mg–3Al–1Zn alloy strips processed by electroplastic differential speed rolling", **Mater. Sci. Technol. (United Kingdom)** (2017), Volume 33, pp.215–219.
- [83] Jeong, H.J.; Kim, M.J.; Park, J.W.; Yim, C.D.; Kim, J.J.; Kwon, O.D.; Madakashira, P.P.; Han, H.N. "Effect of pulsed electric current on dissolution of Mg

- 17 Al 12 phases in as-extruded AZ91 magnesium alloy", **Mater. Sci. Eng. A** (2017), Volume 684, pp.668–676.
- [84] Wu, W.; Xue, T.; Si, C. "Effect of Dislocation Magnification and Solute Atoms Concentration Variation on the Electroplastic Effect of 2024 Aluminum Alloy", **Sci. Adv. Mater.** (2017), Volume 9, pp.1468–1475.
- [85] Zhao, Z.; Wang, G.; Hou, H.; Han, B.; Zhang, Y.; Zhang, N. "Influence of High-Energy Pulse Current on the Mechanical Properties and Microstructures of Ti-6Al-4V Alloy", **J. Mater. Eng. Perform.** (2017), Volume 26, pp.5146–5153.
- [86] Molotskii, M.I. "Theoretical basis for electro- and magnetoplasticity", **Mater. Sci. Eng. A** (2000), Volume 287, pp.248–258.
- [87] Antolovich, S.D.; Conrad, H. "The Effects of Electric Currents and Fields on Deformation in Metals, Ceramics, and Ionic Materials: An Interpretive Survey", **Mater. Manuf. Process.** (2004), Volume 19, pp.587–610.
- [88] Ho, P.S.; Kwok, T. "Electromigration in metals", **Reports Prog. Phys.** (1989), Volume 52, pp.301–348.
- [89] Psyk, V.; Risch, D.; Kinsey, B.L.; Tekkaya, A.E.; Kleiner, M. "Electromagnetic forming - A review", **J. Mater. Process. Technol.** (2011), Volume 211, pp.787–829.
- [90] Jassby, K.M.; Vreeland, T. "Dislocation mobility in pure copper at 4.2°K", **Phys. Rev. B** (1973), Volume 8, pp.3537–3541.
- [91] Zuev, L.B.; Gromov, V.E.; Kurilov, V.F.; Gurevich, L.I. "Mobility of dislocations in zinc single crystals under the action of current pulses", **Sov. Phys. Dokl.** (1978), Volume 33, pp.199.
- [92] Lavrentev, F.F.; Salita, O.P.; Vladimirova, V.L. "Dislocation Mobility in the {1122} $\langle 1123 \rangle$ Slip System of Zinc Single Crystals", **Phys. Status Solidi** (1968), Volume 29, pp.569–574.
- [93] Al'shits, V.I.; Darinskaya, E. V; Perekalina, T.M.; Urusovskaya, A.A. "The motion of dislocations in NaCl crystals under the action of a constant magnetic field", **Fiz. Tverd. Tela** (1987), Volume 29, pp.467–471.
- [94] Alshits, V.I.; Darinskaya, E. V.; Koldaeva, M. V.; Petrzhik, E.A. "Magnetoplastic

- effect: Basic properties and physical mechanisms*", **Crystallogr. Reports** (2003), Volume 48, pp.768–795.
- [95] Alshits, V.; Darinskaya, E.; Petrzhik, E.. "Effects of magnetic fields on the dislocation unlocking from paramagnetic centers in non-magnetic crystals", **Mater. Sci. Eng. A** (1993), Volume 164, pp.322–326.
- [96] Darinskaya, E. V.; Petrzhik, E.A.; Erofeeva, S.A. "Dislocation motion in InSb crystals under a magnetic field", **J. Phys. Condens. Matter** (2002), Volume 14, pp.12883–12886.
- [97] Darinskaya, E. V; Petrzhik, E.A.; Erofeev, S.A.; Kisel', V.P. "Magnetoplastic effect in InSb", **J. Exp. Theor. Phys. Lett.** (1999), Volume 70, pp.309–313.
- [98] Darinskaya, E.V.; Petrzhik, E.A.; Erofeeva, S.A.; Kisel, V.P. "Magnetoplastic Effect in Compound Semiconductors", **Solid State Phenom.** (2009), Volume 69–70, pp.503–506.
- [99] Al'shits, V.I.; Darinskaya, E. V "Magnetoplastic effect in LiF crystals and longitudinal spin relaxation", **JETP Lett.** (1999), Volume 70, pp.761–766.
- [100] Al'shits, V.I.; Darinskaya, E. V; Mikhina, E.Y.; Petrzhik, E.A. "On the nature of the influence of an electric current on the magnetically stimulated microplasticity of Al single crystals", **JETP Lett.** (1998), Volume 67, pp.832–838.
- [101] Al'shits, V.I.; Darinskaya, E. V; Kazakova, O.L. "Influence of the concentration of Ca impurity on the magnetic threshold of the magnetoplastic effect in NaCl crystals", **Phys. Solid State** (1998), Volume 40, pp.70–73.
- [102] Al'shits, V.I.; Darinskaya, E. V; Kazakova, O.L.; Mikhina, E.Y.; Petrzhik, E.A. "Magnetoplastic effect and spin-lattice relaxation in a dislocation-paramagnetic-center system", **JETP Lett.** (1996), Volume 63, pp.668–673.
- [103] Alshits, V.I.; Darinskaya, E.V.; Kazakova, O.L.; Mikhina, E.Y.; Petrzhik, E.A. "Magnetoplastic effect in non-magnetic crystals and internal friction", **J. Alloys Compd.** (1994), Volume 211–212, pp.548–553.
- [104] Al'shits, V.I.; Darinskaya, E. V; Petrzhik, E.A.; Caffrey, J.F. "Magnetoplastic effect in aluminum single-crystals", **Sov. physics. Solid state** (1992), Volume 34, pp.81–

83.

- [105] Al'shits, V.I.; Darinskaya, E. V; Gektina, I. V; Lavrent'ev, F.F. "*Investigation of Magnetoplastic Effect in Zinc Single Crystals*", **Kristallografiya** (1990), Volume 35, pp.1014–1016.
- [106] Golovin, Y.I.; Morgunov, R.B.; Zhulikov, S.E. "*The role of internal mechanical stresses in dislocation motion stimulated by magnetic field*", **Crystallogr. Reports** (1998), Volume 43, pp.640–644.
- [107] Nowick, A.S. *Anelastic relaxation in crystalline solids*; Elsevier, (2012); Vol. 1; ISBN 0323143318.
- [108] Zhao, J.; Wang, G.X.; Dong, Y.; Ye, C. "*Multiscale modeling of localized resistive heating in nanocrystalline metals subjected to electropulsing*", **J. Appl. Phys.** (2017), Volume 122.
- [109] Ruszkiewicz, B.J.; Mears, L.; Roth, J.T. "*Investigation of Heterogeneous Joule Heating as the Explanation for the Transient Electroplastic Stress Drop in Pulsed Tension of 7075-T6 Aluminum*", **J. Manuf. Sci. Eng.** (2018), Volume 140, pp.091014.
- [110] Nguyen-Tran, H.D.; Oh, H.S.; Hong, S.T.; Han, H.N.; Cao, J.; Ahn, S.H.; Chun, D.M. "*A review of electrically-assisted manufacturing*", **Int. J. Precis. Eng. Manuf. - Green Technol.** (2015), Volume 2, pp.365–376.
- [111] Ross, C.D.; Kronenberger, T.J.; Roth, J.T. "*Effect of dc on the Formability of Ti–6Al–4V*", **J. Eng. Mater. Technol.** (2009), Volume 131, pp.031004.
- [112] Ng, M.K.; Fan, Z.; Gao, R.X.; Smith, E.F.; Cao, J. "*Characterization of electrically-assisted micro-rolling for surface texturing using embedded sensor*", **CIRP Ann. - Manuf. Technol.** (2014), Volume 63, pp.269–272.
- [113] Zhu, R.F.; Tang, G.Y.; Shi, S.Q.; Fu, M.W. "*Effect of electroplastic rolling on the ductility and superelasticity of TiNi shape memory alloy*", **Mater. Des.** (2013), Volume 44, pp.606–611.
- [114] Zhu, R.; Tang, G.; Shi, S.; Fu, M. "*Effect of electroplastic rolling on deformability and oxidation of NiTiNb shape memory alloy*", **J. Mater. Process. Technol.** (2013),

Volume 213, pp.30–35.

- [115] Pasechnik, N.V.; Zarapin, A.Y.; Chichenev, N.A. "The rolling equipment of new generation for manufacturing the precise strips from difficultly deformed materials", **Shuiyun Gongcheng/Port & Waterw. Eng.** (1998), Volume n 11, pp.58–64.
- [116] Troitskii, O.A.; Spitsyn, V.I.; Sokolov, N. V.; Ryzhkov, V.G. "Application of high-density current in plastic working of metals", **Phys. Status Solidi** (1979), Volume 52, pp.85–93.
- [117] Yao, K.-F.; Wang, J.; Zheng, M.; Yu, P.; Zhang, H. "A research on electroplastic effects in wire-drawing process of an austenitic stainless steel", **Scr. Mater.** (2001), Volume 45, pp.533–539.
- [118] Tang, G.; Zhang, J.; Yan, Y.; Zhou, H.; Fang, W. "The engineering application of the electroplastic effect in the cold-drawing of stainless steel wire", **J. Mater. Process. Technol.** (2003), Volume 137, pp.96–99.
- [119] Zimniak, Z.; Radkiewicz, G. "The electroplastic effect in the cold-drawing of copper wires for the automotive industry", **Arch. Civ. Mech. Eng.** (2008), Volume 8, pp.173–179.
- [120] Stashenko, V.I.; Troitskii, O.A.; Novikova, N.N. "Electroplastic drawing of a cast-iron wire", **J. Mach. Manuf. Reliab.** (2009), Volume 38, pp.182–184.
- [121] Stashenko, V.I.; Troitskii, O.A.; Novikova, N.N. "Electroplastic drawing medium-carbon steel", **J. Mach. Manuf. Reliab.** (2009), Volume 38, pp.369–372.
- [122] Wang, S.Z. Effect of Electric Pulses on Drawability and Corrosion Property of AZ31 Magnesium Alloy, Tsinghua University, (2009).
- [123] Mai, J.; Peng, L.; Lai, X.; Lin, Z. "Electrical-assisted embossing process for fabrication of micro-channels on 316L stainless steel plate", **J. Mater. Process. Technol.** (2013), Volume 213, pp.314–321.
- [124] Kim, W.; Yeom, K.H.; Thien, N.T.; Hong, S.T.; Min, B.K.; Ik Oh, S.; Kim, M.J.; Han, H.N.; Lee, H.W. "Electrically assisted blanking using the electroplasticity of ultra-high strength metal alloys", **CIRP Ann. - Manuf. Technol.** (2014), Volume 63, pp.273–276.

- [125] Asghar, J.; Reddy, N. V. "*Importance of Tool Configuration in Incremental Sheet Metal Forming of Difficult to Form Materials using Electro-Plasticity*", In Proceedings of the **Proceedings of the World Congress on Engineering**; (2013); Vol. III, pp. 1–5.
- [126] Jones, J.J.; Mears, L. "*A Process Comparison of Simple Stretch Forming Using Both Conventional and Electrically-Assisted Forming Techniques*", In Proceedings of the **ASME 2010 International Manufacturing Science and Engineering Conference, Volume 1**; ASME, (2010); pp. 623–631.
- [127] Ferrando, W.A. *The concept of electrically assisted friction stir welding (EAFSW) and application to the processing of various metals*; NAVAL SURFACE WARFARE CENTER CARDEROCK DIV BETHESDA MD SURVIVABILITY ..., (2008);
- [128] Pitschman, M.; Dolecki, J.W.; Johns, G.W.; Zhou, J.; Roth, J.T. "*Application of Electric Current in Friction Stir Welding*", In Proceedings of the **ASME 2010 International Manufacturing Science and Engineering Conference, Volume 1**; ASME, (2010); pp. 185–189.
- [129] Potluri, H.; Jones, J.J.; Mears, L. "*Comparison of Electrically-Assisted and Conventional Friction Stir Welding Processes by Feed Force and Torque*", (2013), pp.V001T01A055.
- [130] Xu, Z.T.; Peng, L.F.; Yi, P.Y.; Lai, X.M. "*Study on a Novel Electrical-Assisted Pressure Welding Process of Thin Metallic Foils*", **Appl. Mech. Mater.** (2012), Volume 271–272, pp.147–151.
- [131] Hosoi, A.; Yano, T.; Morita, Y.; Ju, Y. "*Quantitative evaluation of the displacement distribution and stress intensity factor of fatigue cracks healed by a controlled high-density electric current field*", **Fatigue Fract. Eng. Mater. Struct.** (2014), Volume 37, pp.1025–1033.
- [132] Qin, R.; Su, S. "*Thermodynamics of crack healing under electropulsing*", **J. Mater. Res.** (2002), Volume 17, pp.2048–2052.
- [133] Xiao, S.H.; Guo, J.D.; Wu, S.D.; He, G.H.; Li, S.X. "*Recrystallization in fatigued copper single crystals under electropulsing*", **Scr. Mater.** (2002), Volume 46, pp.1–6.

- [134] Song, H.; Wang, Z.J. "Microcrack healing and local recrystallization in pre-deformed sheet by high density electropulsing", **Mater. Sci. Eng. A** (2008), Volume 490, pp.1–6.
- [135] Liu, Y.; Fan, J.; Zhang, H.; Jin, W.; Dong, H.; Xu, B. "Recrystallization and microstructure evolution of the rolled Mg-3Al-1Zn alloy strips under electropulsing treatment", **J. Alloys Compd.** (2015), Volume 622, pp.229–235.
- [136] Rahnama, A.; Qin, R.S. "The effect of electropulsing on the interlamellar spacing and mechanical properties of a hot-rolled 0.14% carbon steel", **Mater. Sci. Eng. A** (2015), Volume 627, pp.145–152.
- [137] Lu, W.J.; Zhang, X.F.; Qin, R.S. "Stability of precipitates under electropulsing in 316L stainless steel", **Mater. Sci. Technol.** (2015), Volume 31, pp.1530–1535.
- [138] Sheng, Y.; Hua, Y.; Wang, X.; Zhao, X.; Chen, L.; Zhou, H.; Wang, J.; Berndt, C.C.; Li, W. "Application of High-Density Electropulsing to Improve the Performance of Metallic Materials: Mechanisms, Microstructure and Properties", **Materials (Basel)**. (2018), Volume 11, pp.185.
- [139] Zhu, R.; Jiang, Y.; Guan, L.; Li, H.; Tang, G. "Difference in recrystallization between electropulsing-treated and furnace-treated NiTi alloy", **J. Alloys Compd.** (2016), Volume 658, pp.548–554.
- [140] Wang, Z. jin; Song, H. "Effect of high-density electropulsing on microstructure and mechanical properties of cold-rolled TA15 titanium alloy sheet", **J. Alloys Compd.** (2009), Volume 470, pp.522–530.
- [141] SONG, H.; WANG, Z. jin; GAO, T. jun "Effect of high density electropulsing treatment on formability of TC4 titanium alloy sheet", **Trans. Nonferrous Met. Soc. China (English Ed.** (2007), Volume 17, pp.87–92.
- [142] Guan, L.; Tang, G.; Jiang, Y.; Chu, P.K. "Texture evolution in cold-rolled AZ31 magnesium alloy during electropulsing treatment", **J. Alloys Compd.** (2009), Volume 487, pp.309–313.
- [143] Ma, B.; Zhao, Y.; Ma, J.; Guo, H.; Yang, Q. "Formation of local nanocrystalline structure in a boron steel induced by electropulsing", **J. Alloys Compd.** (2013),

Volume 549, pp.77–81.

- [144] Qin, R.S.; Rahnama, A.; Lu, W.J.; Zhang, X.F.; Elliott-Bowman, B. "Electropulsed steels", **Mater. Sci. Technol.** (2014), Volume 30, pp.1040–1044.
- [145] Rahnama, A.; Qin, R.S. "Electropulse-induced microstructural evolution in a ferritic-pearlitic 0.14% C steel", **Scr. Mater.** (2015), Volume 96, pp.17–20.
- [146] Zhang, W.; Sui, M.; Zhou, Y.; He, G.; Guo, J.; Li, D. "Electropulsing-induced evolution of microstructures in materials", **Acta Metall. Sin.** (2003), Volume 39, pp.1009–1018.
- [147] Klinger, L.; Levin, L.; Srolovitz, D.J. "Interface Diffusion under an Electric Field. Interface Evolution", **Mater. Sci. Forum** (1996), Volume 207–209, pp.109–112.
- [148] Dolinsky, Y.; Elperin, T. "Thermodynamics of phase transitions in current-carrying conductors", **Phys. Rev. B** (1993), Volume 47, pp.14778.
- [149] Lu, W.J.; Zhang, X.F.; Qin, R.S. "Electropulsing-induced strengthening of steel at high temperature", **Philos. Mag. Lett.** (2014), Volume 94, pp.688–695.
- [150] Zhou, Y.; Zhang, W.; Wang, B.; He, G.; Guo, J. "Grain refinement and formation of ultrafine-grained microstructure in a low-carbon steel under electropulsing", **J. Mater. Res.** (2002), Volume 17, pp.2105–2111.
- [151] Zhou, Y.; Zhang, W.; Wang, B.; Guo, J. "Ultrafine-grained microstructure in a Cu-Zn alloy produced by electropulsing treatment", **J. Mater. Res.** (2003), Volume 18, pp.1991–1997.
- [152] Ye, X.; Thtse, Z.; Tang, G.; Song, G. "Retraction notice to Effect of electroplastic rolling on deformability, mechanical property and microstructure evolution of Ti-6Al-4V alloy strip", **Mater. Charact.** (2017), Volume 132, pp.467.
- [153] Zhou, Y.; Guo, J.; Zhang, W.; He, G. "Influence of electropulsing on nucleation during phase transformation", **J. Mater. Res.** (2002), Volume 17, pp.3012–3014.
- [154] Li, X.; Wang, S.; Zhao, S.; Ding, W.; Chen, J.; Wu, G. "Effect of Pulse Current on the Tensile Deformation of SUS304 Stainless Steel", **J. Mater. Eng. Perform.** (2015), Volume 24, pp.5065–5070.
- [155] Qin, R.S.; Zhou, B.L. "Effect of electric current pulses on grain size in castings", **Int.**

J. Non-Equilibrium Process. (1998), Volume 11, pp.77–86.

- [156] Rahnama, A.; Qin, R. "Room temperature texturing of austenite/ferrite steel by electropulsing", **Sci. Rep.** (2017), Volume 7, pp.1–6.
- [157] Wang, X.; Dai, W.; Ma, C.; Zhao, X. "Effect of electric current direction on recrystallization rate and texture of a Cu-Zn alloy", **J. Mater. Res.** (2013), Volume 28, pp.1378–1385.
- [158] Jiang, Y.; Guan, L.; Tang, G.; Shek, C.; Zhang, Z. "Influence of electropulsing treatment on microstructure and mechanical properties of cold-rolled Mg-9Al-1Zn alloy strip", **Mater. Sci. Eng. A** (2011), Volume 528, pp.5627–5635.

CHAPTER 2

Preliminary studies

2.1. INTRODUCTION

In this chapter preliminary studies on EPE performed at University of Padua are presented.

As reported in chapter one, EPE has been observed in materials that have different crystal structure, thermal conductivity, electrical resistivity, grain size as well as during various deformation methods. In literature it has been found that EPE is more likely to occur in *Body Centered Cubic* (b.c.c.) material rather than *Face Centered Cubic* (f.c.c.) [1]. The mechanism by which EPE work on plastic deformation have been dealt in chapter one, and most hypothesizes the direct interaction between electrical current and dislocations.

Concerning dislocation dynamic, very important metallurgical parameter is the *Stacking Fault Energy* (SFE), hence it is likely that EPE could be connected with the SFE of the material or, in case of a multiphase material, that of the constituting phases.

2.2. Stacking Fault Energy

The passage of a total dislocation through a crystalline lattice leaves the perfection of the lattice undisturbed. Each atom is shifted from one normal position in the lattice to an adjacent normal position. However, the energy of the system can sometimes be lowered if a total dislocation splits into a partial dislocation Figure 2.2.

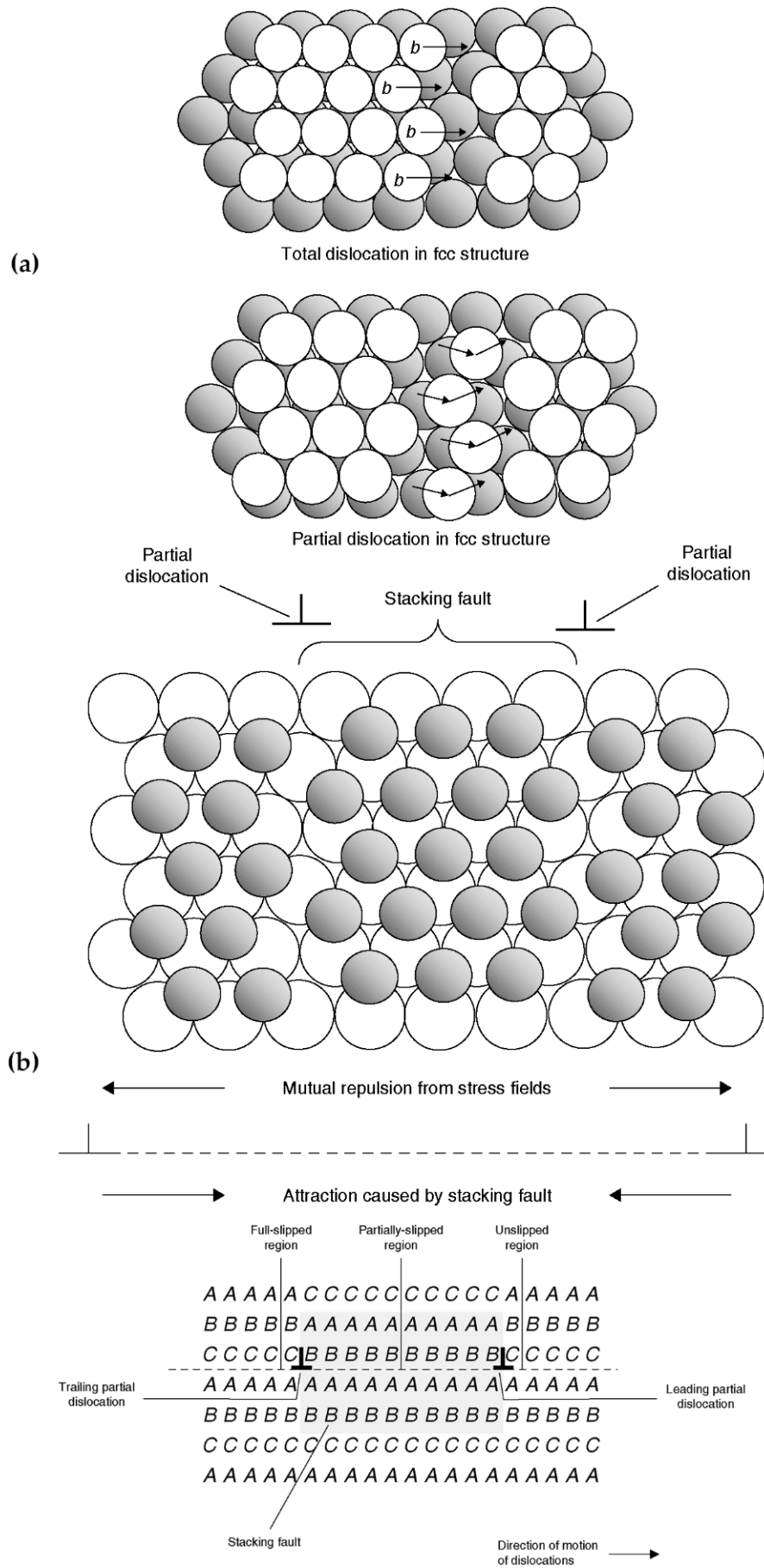


Figure 2.1 Concept of partial dislocation (a), stacking fault and extended dislocation (b) [2].

It takes less energy if the total dislocation splits into two partial dislocations that can move in a zig-zag path through the valley between atoms, rather than having to climb over an atom. Instead of an atom moving directly from its lattice position to a new position, indicated by the tip of the arrow of the Burgers vector, it can move first to an intermediate vacant site and then again to the final site. Thus, two short jumps are made instead of one longer one, which requires less energy. However, the passage of a partial dislocation leaves behind a planar region of crystalline imperfection. The planar imperfection produced by the passage of a partial dislocation is called a stacking fault, as illustrated in Figure 2.2. In an f.c.c. structure, the stacking sequence changes from the normal ABCABC to ABAB, which is the stacking sequence for the hcp structure. Passage of the second partial dislocation restores the normal ABCABC stacking sequence. These partial dislocations are often referred to as Schottky partials. The two partial dislocations that are separated by the faulted area are known as an extended dislocation. The total energy of a perfect lattice is lower than one with a stacking fault. Thus, a stacking fault has an energy associated with it. The difference in energy between a perfect lattice and one with a stacking fault is known as the stacking fault energy (SFE). Equilibrium occurs between the repulsive energy of the two partials and the surface energy of the fault. The larger the separation between the partial dislocations, the smaller is the repulsive force between them. On the other hand, the surface energy associated with the stacking fault increases with the distance between the two partial dislocations. In general, if the separation between the partial dislocations is small, the metal is said to have a high SFE. If the separation is large, the metal would have a low SFE. For example, the separation in aluminum (high SFE) is on the order of an atomic spacing, while that of copper (low SFE) is approximately twelve atomic spacings.

Stacking fault energy plays a role in determining deformation textures in f.c.c. and h.c.p. metals. Stacking faults also influence plastic deformation characteristics. Metals with wide stacking faults (low SFE) strain harden more

rapidly and twin more readily during annealing than those with narrow stacking faults (high SFE). In Table 2.1 are summarized the values of SFE for some metals and alloys.

Table 2.1 Approximate SFE of various materials

Metal	SFE [mJ/m ²]
Brass	<10
Austenitic stainless steel	<10
Silver	20-25
Gold	50-75
Copper	80-90
Nickel	130-200
Aluminum	200-250

SFE is also correlated to the electron-to-atom ratio (i.e., the ratio between the valence electron and the ions) among other properties [3] as can be seen in Figure 2.2.

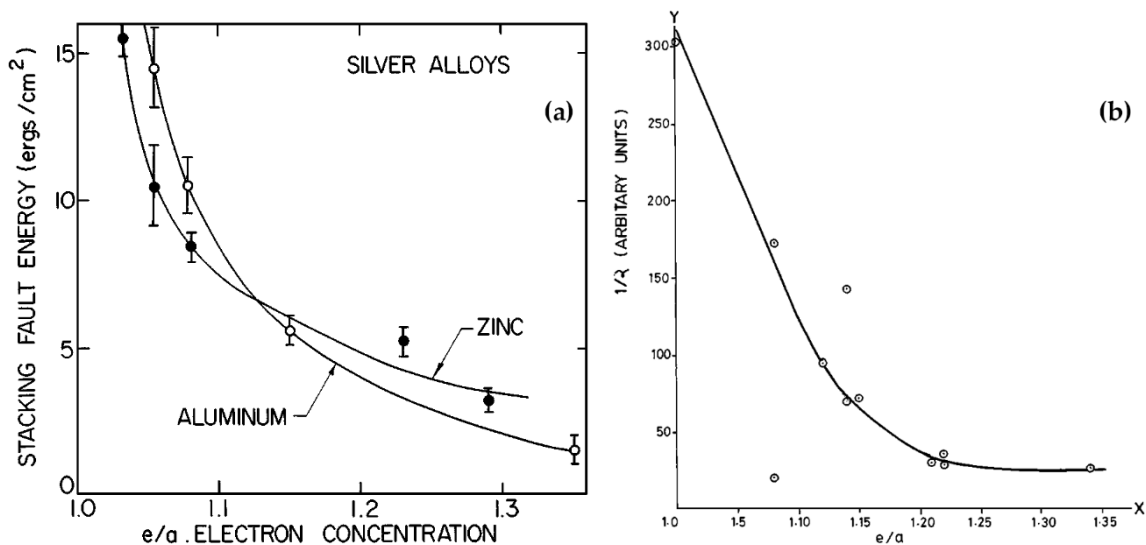


Figure 2.2 Variation of stacking fault energy with e/a ratio of silver alloys (a) [4] and variation of the stacking fault probability with e/a ratio in copper alloys [5].

SFE also influences the atomic mobility during annealing, leading high-SFE materials to preferentially recover rather than recrystallize since dislocations rearrangements are less hindered [6].

2.3. Investigated materials and methodology

In order to verify any dependence of the insurgence of EPE from the SFE, various metallic alloys with different crystal structure and SFE have been tested. The tested materials and their SFEs are summarized in Table 2.2.

Table 2.2 SFE of the investigated materials.

Metal	SFE [mJ/m ²]
Austenitic stainless steel AISI 316L	~40
Ferritic stainless steel AISI 430	-
Copper C11000	~90
Aluminum AA1050 H24	~200

All the materials were in sheet form with thickness ranging from 1 mm to 1.2 mm. They were strained until fracture by mean of an MTS tensile test machine modified in order to deliver electrical current to the specimen during the test. A schematic of the tensile test machine setup can be seen in Figure 2.3.

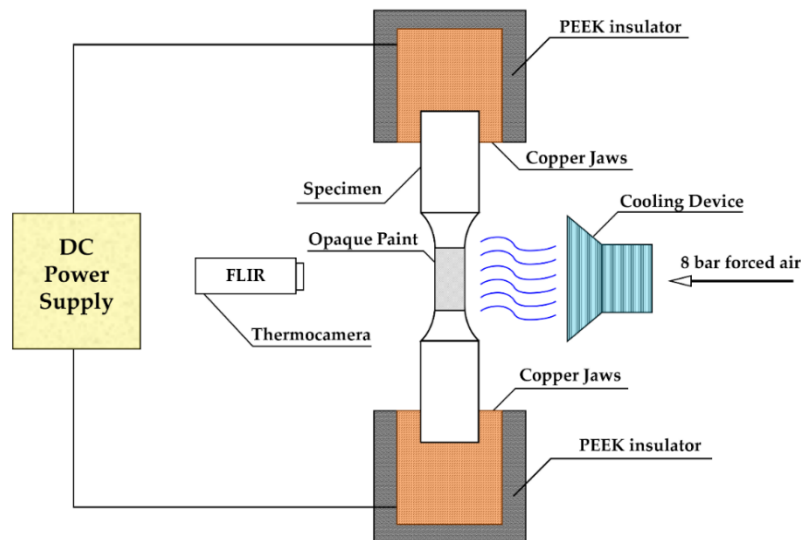


Figure 2.3 Schematic of electrically assisted tensile test MTS machine setup.

The power supply is able to deliver 6000 A at 10 V in current control with an accuracy of 1 A. The insulation from the MTS frame was made by mean of copper jaws embedded in PEEK. In order to limit specimen joule heating, forced air at a pressure of 8 bar was blown for all the duration of the tests. The temperature measurements were performed through a FLIR A40 infrared thermal camera with an accuracy of 1 °C. The gauge length of the specimen was coated with an opaque painting in order to stabilize its emissivity to 0.8. Thermal tests were performed at the same temperature reached by the electrical test in order to separate the contribution of the electrical current from that of the temperature. The temperature and the current densities used for the different materials are summarized in Table 2.3.

Table 2.3 Material resistivity, current density and temperature reached during the tests.

Material	Electrical resistivity [Ω·cm]	Current density [A/mm ²]	Temperature [°C]	Homologous temperature (T _H)
AISI 316L	7.54x10 ⁻⁵	5	75	0.21
		10	145	0.25
		15	270	0.33
		20	490	0.46
AISI 430	5,87x10 ⁻⁵	5	40	0.21
		10	100	0.25
		15	200	0.32
		17.5	300	0.38
		20	400	0.45
C11000	1.70x10 ⁻⁶	21	450	0.48
		4	30	0.22
		17	40	0.23
		33	60	0.25
		50	100	0.28
AA1050-H24	2.80x10 ⁻⁶	67	200	0.35
		5	25	0.32
		10	25	0.32
		25	40	0.34
		30	45	0.34
		35	55	0.36
		45	70	0.37
55	115	0.42		
65	165	0.47		

It has been calculated the homologous temperature because it allows to compare the dependence of the mechanical properties with respect the temperature for alloys that present different melting temperature. Homologous temperature is defined as follow

$$T_H = \frac{T_i}{T_m} \quad (2.1)$$

where T_i is the test temperature and T_m is the melting temperature of the alloy, both expressed in Kelvin. Upper limit for the current density was defined in order to not overcome $0.5 \times T_h$. Higher temperature involve different dislocation dynamic mechanism and higher diffusional contributions on deformation mechanism making the interpretation of the results much more complicated. The thermal regimes of the different materials are depicted in

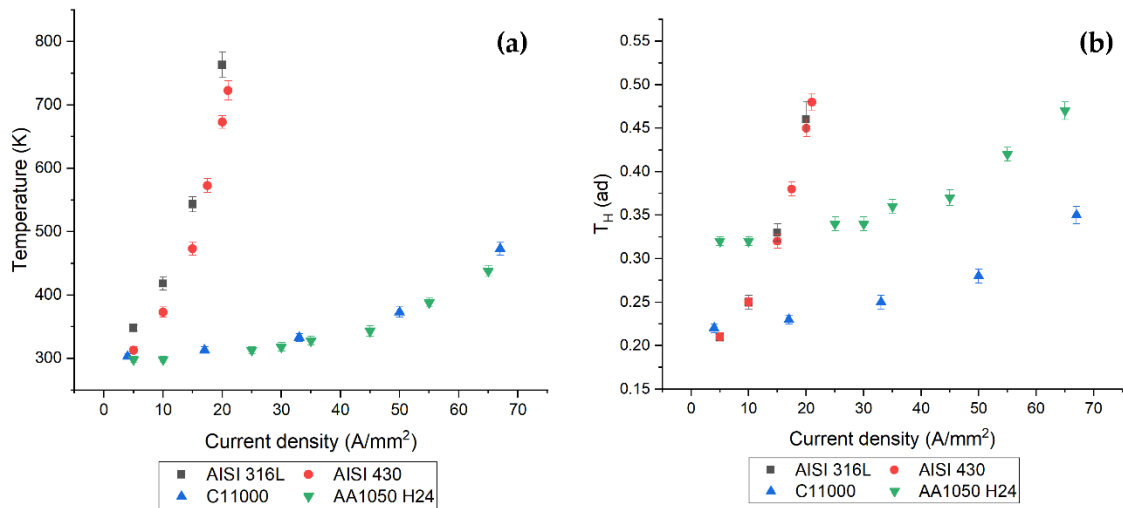


Figure 2.4 Thermal regimes of tested materials: (a) Temperature vs Current density, (b) Homologous Temperature vs Current density.

Since austenitic stainless steel AISI 316L suffer from SIM precipitation due to *Transformation Induced Plasticity* (TRIP) all materials were strained with a deformation rate of 10^{-2} s^{-1} in order to prevent the phenomenon and to compare the results obtained from the different alloys.

From the tensile test curves it has been extrapolated the *Ultimate Tensile Strength* (UTS) and the relative variation with respect the thermal test

$$UTS_{rel} = \frac{UTS_{el}}{UTS_{th}} \quad (2.2)$$

where UTS_{el} is the UTS of the electrical test while UTS_{th} is the UTS of the relative thermal test.

Relative fracture strain, on the other hand, has been calculated as follow:

$$\varepsilon_{rel} = \frac{\varepsilon_{test}}{\varepsilon_{baseline}} \quad (2.3)$$

Where ε_{test} is the fracture strain of the considered condition and $\varepsilon_{baseline}$ is the fracture strain of the room temperature test.

2.4. Austenitic stainless steel AISI 316L

The material was tested using continuous current densities ranging from 5 to 20 A/mm², since the adopted cooling device did not allow for the application of higher current densities because of the high electrical resistivity and low thermal conductivity of the steel. Among the tested materials, AISI 316L possesses the lowest SFE value, and the performed electrical and thermal tests caused a reduction of the mechanical properties in comparison with the baseline.

A clear difference between the tests performed in current regime and the thermal counterparts can be seen, showing that electricity affected the steel properties mainly by worsening the fracture strain (Figure 2.5). On the other hand, the UTS reduction in current regime compared to the thermal ones was not significant up to 10 A/mm² ($T_H = 0.25$) and reached a maximum of 40 MPa at the highest current density (20 A/mm², $T_H = 0.46$). The observed behaviour is in agreement with a previous study on AISI 304L austenitic stainless steel [7], where a material softening as a consequence of the current application has been noted, but for which the thermal comparisons have not been performed.

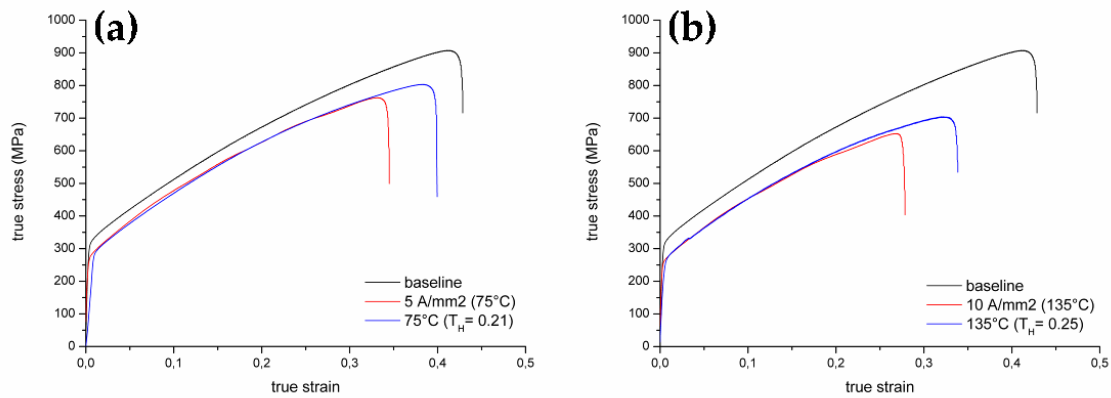


Figure 2.5 Comparison between thermal, electrical and baseline flow stress curves of AISI 316L (a) 5 A/mm² and (b) 10 A/mm².

In AISI 316L, the same overall behaviour was observed in the entire experimental current density range (Figure 2.6); thermal and electrical curves always stand below the baseline and the elongations obtained in the current regime were always lower than the thermal counterparts. The strain at fracture was increasingly worsened as the current density increased and, even if the material exhibited a softening in terms of mechanical strength, no enhancements in formability in comparison with the baseline were observed. However, besides the possible contribution of SFE on EPE, the absence of an electrical effect can also be ascribed to the presence of an activation threshold for EPE, as noted by Conrad and Magargee [8,9]. Indeed, in the case under study, the applied currents were not enough to overcome such limit and the employed current densities only caused a reduction in the material flow properties.

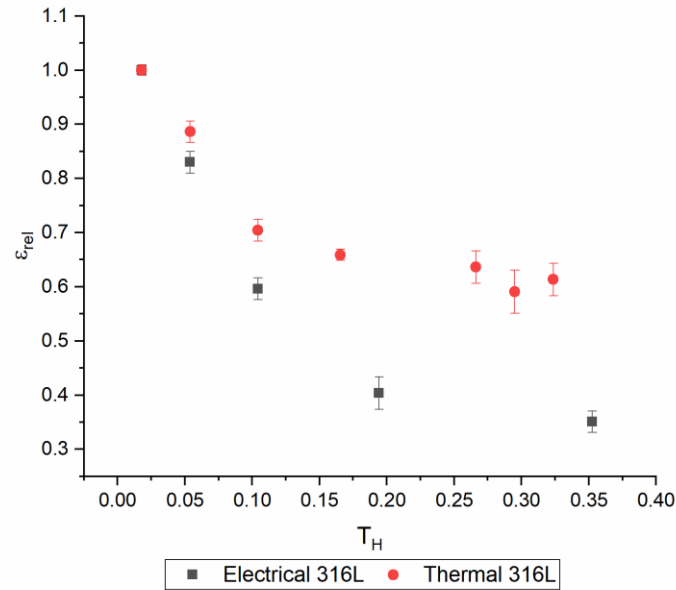


Figure 2.6 Relative variation of true strain in austenitic stainless steel AISI 316L as a function of the homologous temperature.

2.5. C11000 Copper

The lower electrical resistivity and higher thermal conductivity of copper compared to austenitic stainless steel AISI 316L permitted the application of higher current densities (up to 65 A/mm²), without excessive specimens heating during the electrically-assisted tensile tests. For this intermediate SFE metal, significant thermal variations with respect to room temperature were not observed when relatively low current densities were applied, and the testing temperatures were maintained around 40 °C ($T_H = 0.23$ at 20 A/mm²). Despite the low temperatures, however, a slight worsening of the copper properties compared to the baseline was observed in the low current density range, both in electrical and thermal regimes. On the other hand, when the applied current overcame 20 A/mm², the fracture strain in the electrically-assisted tests were reduced in comparison with the thermal counterparts (Figure 2.7), but no significant variations in UTS were observed. Even in this case, thermal and electrical curves always stand below the baseline, denoting a similar material softening if compared to the room temperature behavior.

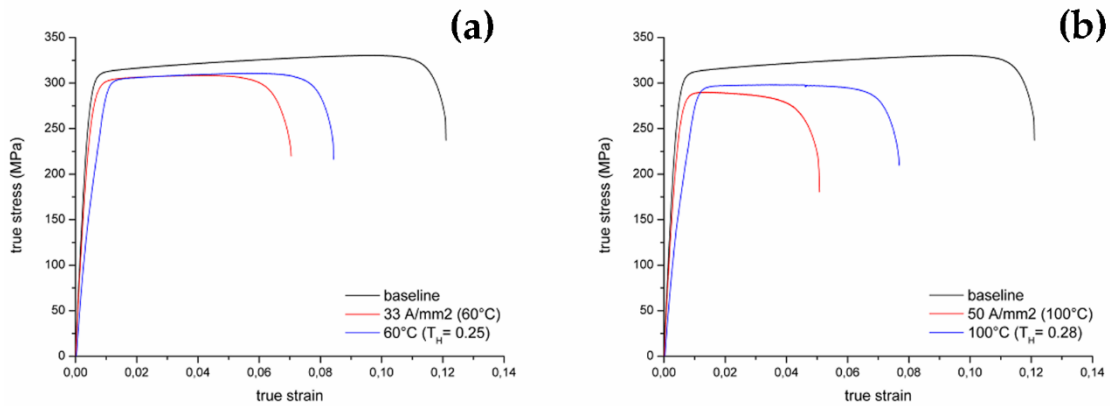


Figure 2.7 Comparison between thermal, electrical and baseline flow stress curves of C11000 Copper (a) 33 A/mm² and (b) 50 A/mm².

2.6. Aluminum alloy 1050 H24

The lower electrical resistivity of the high SFE aluminum alloy permitted to strain the material adopting current densities from 5 to 65 A/mm², as for the copper. In this material, conversely to what happened in copper and steel, the application of electricity caused a progressive enhancement in the fracture strain as the current was increased, reaching a peak in formability at 25 A/mm² (Figure 2.8). Moreover, in this low current density range, electricity also increased the UTS of aluminum respect to the baseline, whereas the thermal tests revealed a slight material softening. However, a trend inversion in the achievable fracture strain was observed for current densities higher than 25 A/mm², and aluminum exhibited a progressive reduction in total elongation. In particular, over 45 A/mm² ($T_H = 0.37$), the material behavior was similar to that of the other tested f.c.c. materials, showing a decrease in formability compared to the thermal counterparts. In this regard, a substantial electrical-to-thermal difference in elongation was registered at 65 A/mm² (Figure 2.8), although for this material the elongation is supposed to increase when the temperature is raised up to 200°C [10], as confirmed by the thermal tests.

In the experimental current density range, aluminum exhibited a clearly different behavior in comparison to the other f.c.c. materials (Figure 2.9),

highlighting a real effectiveness of electricity when relatively low current densities were applied, even if its electro-plastic threshold reported in literature is slightly higher and of the same order of magnitude to that of steel and copper [8,9]. However, this favorable effect of electricity was only present for current densities lower and equal to 25 A/mm², whereas the solely thermal straining was found to be more effective in improving the material workability when homologous temperatures over 0.4 were involved.

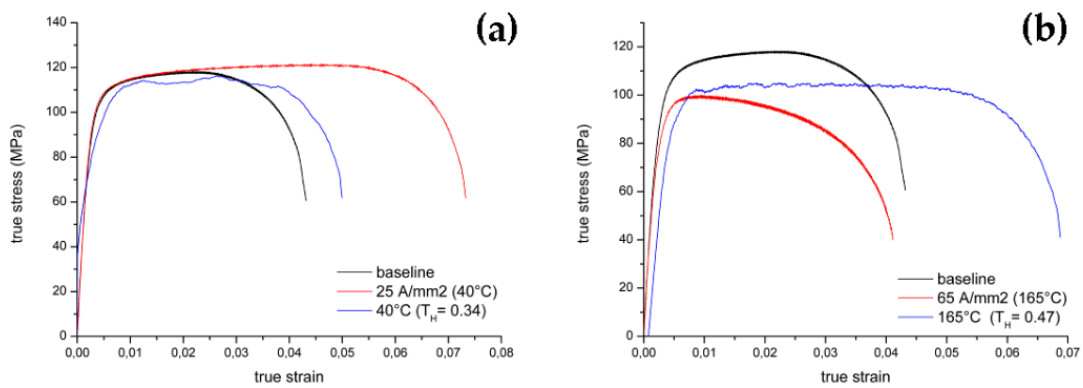


Figure 2.8 Comparison between thermal, electrical and baseline flow stress curves of Aluminum 1050 H24 (a) 25 A/mm² and (b) 65 A/mm².

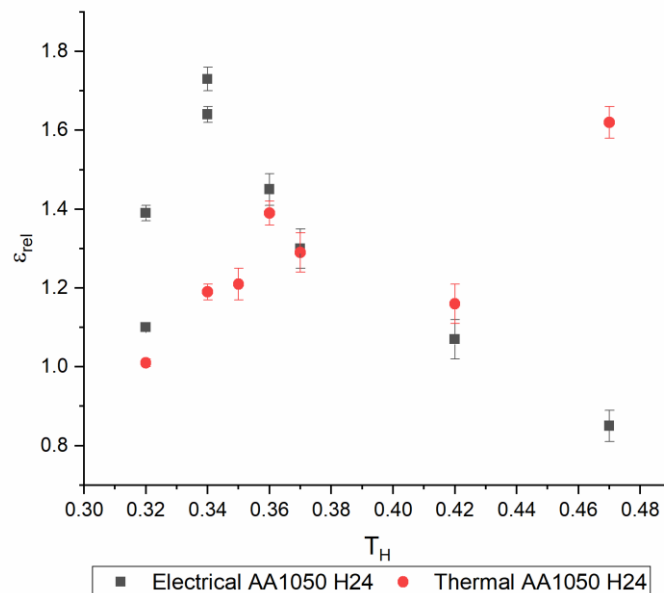


Figure 2.9 Relative variation of true strain in AA1050-H24 as a function of the homologous temperature.

2.7. Ferritic stainless steel AISI 430

In the case of AISI 430, the high electrical resistivity, the low thermal conductivity and the type of cooling device did not allow the use of such high current densities as for copper or aluminum, nevertheless it was possible to reach higher current density compared to the austenitic stainless steel (i.e., up to 21 A/mm²). It has to be mentioned that deformation mechanism in b.c.c. materials are rather different compared to f.c.c. ones. The plasticity of b.c.c. metals, especially at low temperature, is controlled by the rate of the dislocation transitions over the Peierls barriers by mean of creation and separation of the kink pairs, rather than by dislocation depinning from impurities [11], while in f.c.c. dislocations are more or less always free to move and plasticity is suppressed upon reaching “forest” dislocation [12].

Electricity caused an unavoidable temperature rise (partially limited by the cooling device) that modified the material mechanical response by reducing the elongation at rupture and by lowering the UTS. Compared to the base material flow stress curve (baseline), any enhancement in formability was not observed and the employed current densities caused a progressive reduction in mechanical properties. Therefore, owing to not negligible workpieces heating, EPE cannot be clearly observed by solely consider the test performed in current regime.

Two examples of thermal and current true stress-strain curves are reported in Figure 2.10. Comparing thermal and electrical results, it can be noted that electricity acted on the material properties by mainly influencing the fracture strain, whereas UTS was not substantially affected; in any case, the flow properties were always reduced if compared to the baseline, as observed for the previous materials. As can be seen from Figure 2.11, where relative strain is plotted against the registered temperature, this behavior was observed

in the entire experimental current density range, denoting an effective contribution of electricity in improving formability of the steel.

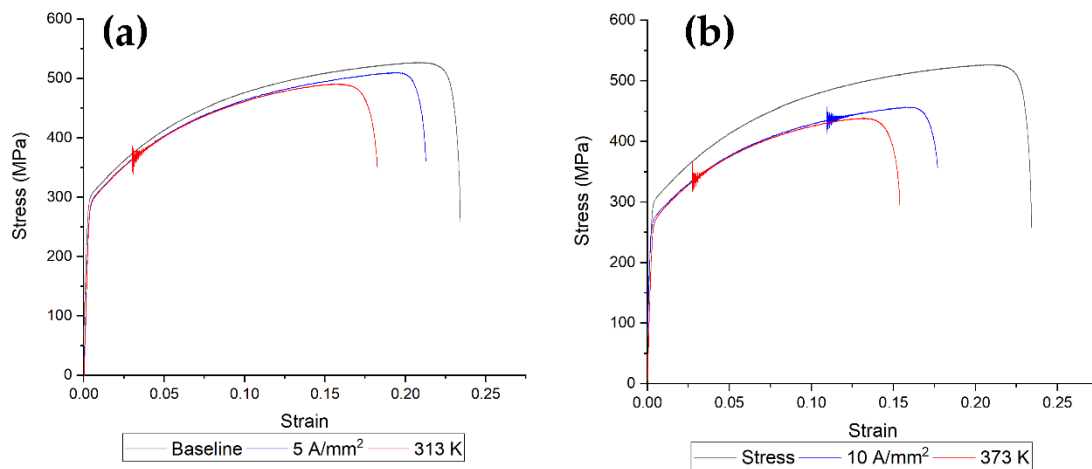


Figure 2.10 Comparison between thermal, electrical and baseline flow stress curves of ferritic stainless steel AISI 430 (a) 5 A/mm² and (b) 10 A/mm².

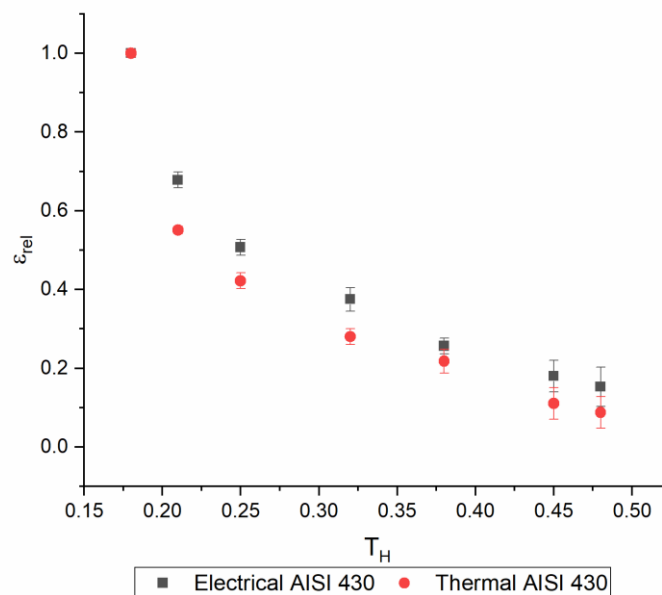


Figure 2.11 Relative variation of true strain in ferritic stainless steel AISI 430 as a function of the homologous temperature.

2.8. Discussions

Among the tested materials, EPE in uniaxial tensile deformation only occurred in the high-SFE aluminum, and in less extent in the ferritic stainless steel AISI 430, denoting a possible contribution of this metallurgical parameter

on electroplasticity in metals. The results showed that, as the current densities (and the testing temperatures) were increased, the low- and intermediate-SFE materials exhibited a decreasing trend in the relative variation of total elongation within the entire experimental current-density range (Figure 2.12), and the overall mechanical properties in electrically-assisted tension were always pejorative compared to both the baselines and the thermal counterparts. On the contrary, aluminum showed very favorable enhancements in elongation when relatively low current densities were applied (Figure 2.12) and, up to 10 A/mm², the employed cooling device permitted to maintain the thermal regime close to room temperature (Figure 2.4), thus avoiding excessive specimens heating. In aluminum, the greatest improvement in strain was registered at 25 A/mm² whereas, for higher current densities, the elongations were reduced in comparison with the thermal counterparts. Furthermore, over 45 A/mm², aluminum started to behave similarly to the other materials, exhibiting a worsening in fracture strain compared to the corresponding thermal test (Figure 2.8).

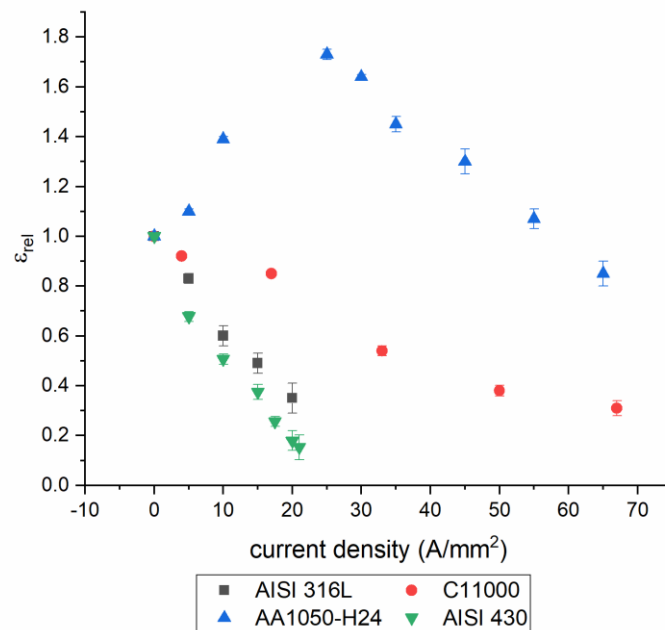


Figure 2.12 Relative variation of tested material fracture strain as a function of the current density.

Regarding the mechanical strength, a material softening in comparison to the thermal tests was observed in the stainless steel under current application, which exhibited a progressive UTS decrease in the entire experimental current-density range, reaching a reduction of approximately 10% at the maximum current density (Figure 2.13). Conversely, no noticeable variations between electrical and thermal UTSs were registered either for AISI 430 and for copper, being the obtained values very close each other and within the experimental error (Figure 2.13). On the other hand, the UTS of aluminum showed a trend similar to that of its elongation, exhibiting improvements up to 25 A/mm² and a progressive reduction when such current density was overcome, also underlining a further worsening compare to the baseline over 45 A/mm² (Figure 2.13).

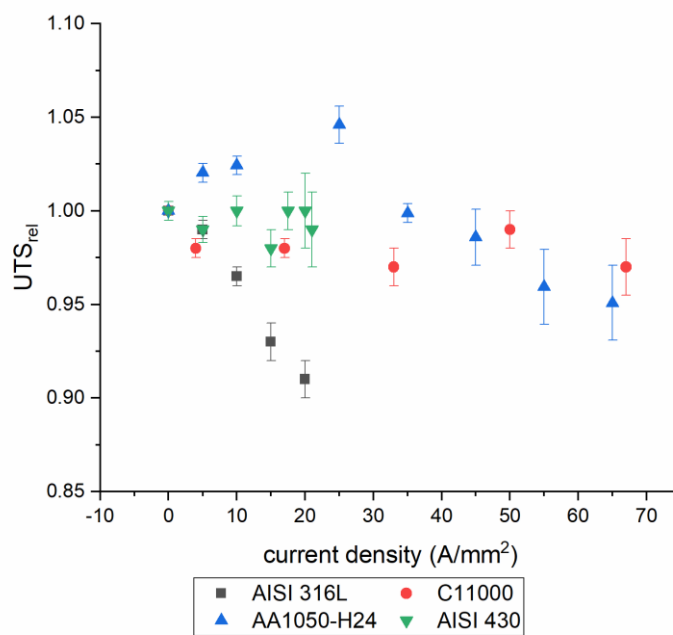


Figure 2.13 Relative variation of tested materials UTS as a function of the current density.

In any case, the performed experimental tests revealed the presence of an extra-effect added to that of temperature, especially in elongation, which in turn opposed (medium and low SFE) and eased (high SFE) the formability of the materials. In AISI 316L (low SFE), the negative effect of electricity was strongly pronounced as the current density was increased, whereas in copper (medium

SFE) the decrease in formability was quite smoothed and tended to reach a plateau when high current densities were involved. On the contrary, for AA1050-H24 (high SFE), electricity led to a considerable improvement in the material formability that, however, was only present when relatively low current densities were applied. AISI 430 as well shows an improvement in fracture strain at every current density tested, but in less extent compared to AA1050-H24.

In EPE, the variables involved are several, belonging to physical/metallurgical properties and testing condition. Nevertheless, fixing the deformation mode (tension) a comparison among the tested materials can be performed by taking into account their SFE, also considering that copper and aluminum possess comparable electrical resistivity (Table 2.3) but exhibited very different behaviors in the low current-density range (Figure 2.12 and Figure 2.13). Moreover, it must be noticed that aluminum possesses a considerably lower melting point compared to that of copper and stainless steel, which may have some implications if heating is involved, since straining this material at room temperature equals to deform it closely to the end-boundary of its cold-working regime.

The experimental results revealed a clear splitting of the materials behaviour as a function of their SFE, especially if fracture strain is considered (Figure 2.12), which can therefore be considered a representative parameter in contributing to EPE. The passage of continuous current within the tested materials altered their mechanism of deformation, owing to both the presence of scattering electrons and the increase in temperature caused by localized resistive heating. In electrically-assisted tension of austenitic stainless steel and copper an additional term to the thermally-activated deformation mechanism seemed to be present in controlling dislocations dynamics, probably allowing for the overcoming of some long-range barriers and acting as a further thermal contribution. A possible explanation for the premature fracture of AISI 316L

and C11000 could be ascribed to the premature reaching of critical dislocation density at cell walls without altering the stress needed to reach such a situation. As a support to this hypothesis scanning electron micrography performed on AISI 316L exhibited a minor number of slip bands within the grains in the proximity of the fracture surface compared to its thermal counterpart (Figure 2.14) [13].

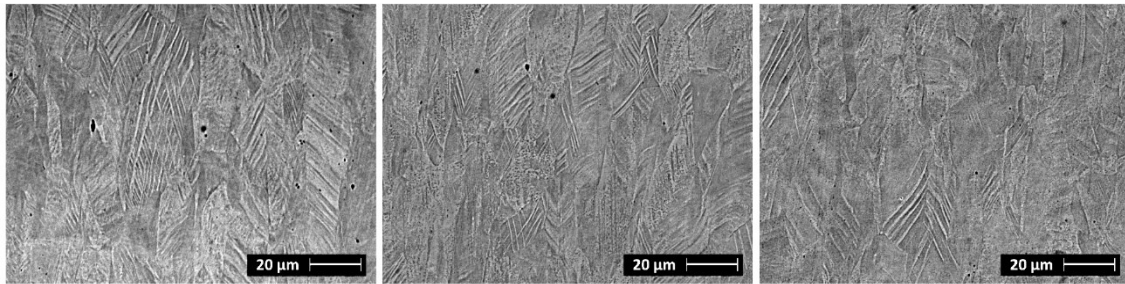


Figure 2.14 Scanning electron micrograph in backscattered electrons near fracture surface of AISI 316L: base material (left), thermal test at 75 °C (middle) and continuous current test at 5 A/mm² at 75°C (right).

Partial suppression of band formation could be due to localized resistive heating which enhance dislocation mobility.

On the other hand, in aluminum, electricity locally rise the temperature toward considerably high values, thus favoring important diffusional contribution, such as those governing recovery. At high temperatures, recovery in aluminum is facilitated, since dislocations motion is less hindered owing to its high SFE [6]. In this material, the observed improvements can be explained considering that the localized resistive heating induced by current may have affected its mechanical behaviour by easing recovery and allowing for the annihilation of existing dislocations. Similar consideration can be done to the ferritic stainless steel, taking into account the different deformation mechanism in which the electrical current probably lowered the energy needed for the dislocations to overcome the Peierls barrier, thus leading to higher dislocation mobility and increasing the chance for dislocation annihilation leading to recovery. Therefore, new dislocations were generated in the partially recovered microstructure, thus permitting the material to withstand greater deformations before the final rupture and enhancing the fracture strain. Thus, the high SFE

value of aluminum and ferritic stainless steel may be considered responsible of the observed behaviour, favoring recovery when localized resistive heating occur, and this correlation between EPE and SFE can also justify the observed behaviors of copper and AISI 316L, possessing both considerably lower SFEs. However, the low melting point of aluminum implies that such recovery conditions are readily reached for lower current densities respect to the intermediate-SFE copper (which possesses a similar electrical resistivity), leading aluminum in a favorable position for the occurrence of EPE (at least in tension).

The role of SFE in EPE suggested from the results obtained in the present work must be considered valid if uniaxial tension is performed, since literature data from tensile and compressive tests on same materials revealed different behaviour when continuous current is applied [14,15], highlighting a strong contribution of the deformation mode on EPE. In fact, besides the material type, it must be considered that the mechanisms of deformation in tension and compression are dissimilar. In compression, the cross sections are continually increased, and the deformation causes cracks and micro-voids to be either reduced or closed. Conversely, tensile deformation eases the expansion of such defects, causing necking to occur and an excessive heating due to localized increase in current density that leads to higher joule heating. Therefore, the effect of current on the maximum achievable deformation can be significantly different. As confirmed by literature, EPE has been found to be not very effective in tension, whereas extraordinary results have been obtained in compression of Magnesium, Titanium and Aluminum alloys, making *electrically assisted manufacturing* (EAM) very suitable in forging operations [14]. Actually, if taken as pure metals, Al, Mg and Ti are all high-SFE materials arranged in close-packed structures (f.c.c. and h.c.p.), and the addition of alloying elements to these materials lowers their SFE that, however, remains considerably higher

than that of copper or austenitic steels, validating the hypothesis of a role of SFE in EPE.

Nevertheless, together with SFE and deformation mode, a further contribution of the microstructure must be taken into account in analyzing EPE, in terms of number of phases, crystal structure, grain size and precipitation-hardening conditions. Extraordinary improvements in compressed titanium has been revealed on grade Ti 6Al 4V [14], which possesses a biphasic microstructure consisting of h.c.p. and b.c.c. whereas no favorable effect has been observed in compressing pure titanium subjected to the same current densities [16,17]. Conversely, straining pure titanium in uniaxial tension has led to considerable enhancements in formability [17], while the electrically-assisted tension tests on grade Ti 6Al 4V only revealed slight improvements [15]. These results on pure and alloyed titanium, both of them possessing a high SFE, clearly denote a direct interaction among EPE and the involved variables (i.e. SFE, deformation mode and microstructure). Furthermore, EPE has been also found to occur in a biphasic 60/40 brass (f.c.c. + b.c.c.) [14,15], which is considered to be a low-SFE material if this property is measured in the copper-based phase, but which possesses two phases having different SFEs. In this latter case, the presence of a b.c.c. high-SFE phase in the brass may have contribute to alter the material behaviour by inducing the observed little EPE. Moreover, even the grain size may have some effects on the extent of EPE [18], since a coarser copper microstructure has been found to favorably contribute to EPE, being the observed total elongation greater to that of the corresponding thermal tests, owing to localized heating effects. Finally, the different hardening conditions of the aluminum alloys reported in literature [14,15] may have further altered the materials response in electrically-assisted deformation, explaining the observed differences in formability. Therefore, a combination of several variables must be considered in studying EPE and thermal comparisons

are mandatory in order to reveal a real effectiveness of the EAM experiments during continuous current application.

As a final note, it is stressed that a further effect of electricity in the elastic regime was noted in each tested material, resulting in a more or less pronounced elastic stiffening in the electric tests compared to the thermal counterparts (Figure 2.5, 2.7 and 2.8). In AISI 316L, this variation was slightly visible and within the experimental errors, but such stiffening was clearly present in copper at any current density (Figure 2.7) and in aluminum for densities overcoming 55 A/mm² (Figure 2.8).

2.9. Conclusions

An analysis of EPE in three f.c.c. materials and one b.c.c. having different SFE was performed (AISI 316L stainless steel, AISI 430 ferritic stainless steel, C11000 copper and A1050-H24 aluminum alloy). The results obtained from electrically-assisted uniaxial tension (current regime) were compared to those performed at room temperature (baselines) and to those conducted at the corresponding temperature reached upon current application. As was noted in the experiments, the passage of electricity through the materials changed their response to uniaxial plastic deformation in comparison to both baselines and thermal tests, denoting a further (positive or negative) effect on the mechanical response ascribable to SFE.

Among the tested materials, EPE during tensile deformation was found to occur only in aluminum and ferritic stainless steel AISI 430, the two materials with the highest SFE. However, the increase in formability was only registered in the low current-density range for the aluminum, where the material experienced the maximum increase in total elongation compared to the baseline (173% at 25 A/mm²); conversely, higher densities led to a progressive worsening in its strain at fracture. Ferritic stainless steel AISI 430 showed an increase in fracture strain for all the current densities employed but not as much as aluminum. The increase in total elongation is only with respect the thermal counterpart while, for aluminum, it exceeded even the baseline. On the other hand, copper (intermediate-SFE) and austenitic stainless steel (low-SFE) always exhibited a progressive reduction in mechanical properties as the current density was increased, and their formability was always reduced respect to baselines and thermal tests.

From the obtained results and from the analysis of literature data, both SFE and deformation mode can be accounted as playing an important role in the occurrence of EPE under continuous current application and, among the

effects inducing EPE, it seemed that the localized resistive heating could be the most effective one in leading to EPE in high-SFE materials. Indeed, resistive heating within the microstructure can locally shift the thermal regimes toward those temperatures at which recovery is determinant in controlling dislocation dynamics, thus permitting the annihilation of defects and dislocation and easing the formation of defect-free areas in which new dislocation can be generated by plastic deformation. However, the presence of others EPE related phenomena (electron wind force, excess of electrons and electron stagnation theory) cannot be neglected. On the contrary, in low and intermediate SFE materials it seemed that electricity enhanced dislocations mobility by only allowing an anticipate reaching of the forests dislocation in comparison to what observed in thermal regime, thus acting as a further contribution to thermally-activated mechanisms and leading to a premature failure of the material in terms of total elongation.

Nevertheless, it must be noticed that the description of EPE within metals is not a straightforward process, since several material-related variables can affect in different extent the variation in formability of the materials. Among these, the presence of a biphasic microstructure, the grain size, the thermo-mechanical history of the material and their mutual correlation must be considered in studying EPE, and the effect of temperature risings caused by Joule heating under current application must be always verified by testing the materials in pure thermal regime.

2.10. References

- [1] Liu, X.; Lan, S.; Ni, J. "*Experimental study of Electro-Plastic Effect on Advanced High Strength Steels*", **Mater. Sci. Eng. A** (2013), Volume 582, pp.211–218.
- [2] Reed-Hill, R.E. "*Physical metallurgy principles*".
- [3] Tiwari, G.P.; Ramanujan, R. V. "*Relation between the electron to atom ratio and some properties of metallic systems*", **J. Mater. Sci.** (2001), Volume 36, pp.271–283.
- [4] Thornton, P.R.; Mitchell, T.E.; Hirsch, P.B. "*The dependence of cross-slip on stacking-fault energy in face-centred cubic metals and alloys*", **Philos. Mag.** (1962), Volume 7, pp.1349–1369.
- [5] Smallman, R.E.; Westmacott, & K.H.; Westucott, K.H. "*Stacking faults in face-centred cubic metals and alloys Stacking Faults in Face-Centred Cubic Metals and Alloyst*", (2010), pp.37–41.
- [6] Honeycombe, R.W.K. *The plastic deformation of metals*; Edward Arnold London, (1968); Vol. 231;.
- [7] Magargee, J.; Fan, R.; Cao, J. "*Analysis and Observations of Current Density Sensitivity and Thermally Activated Mechanical Behavior in Electrically-Assisted Deformation*", **J. Manuf. Sci. Eng.** (2013), Volume 135, pp.061022.
- [8] Conrad, H. "*Some effects of an electric field on the plastic deformation of metals and ceramics*", **Mater. Res. Innov.** (1998), Volume 2, pp.1–8.
- [9] Magargee, J.; Fan, R. "*Analysis and Observations of Current Density Sensitivity and Thermalily Activated Mechanicali Beiiavior in Eiectricaiiy-Assisted Deformation*", (2013), Volume 135.
- [10] Touloukian, Y.S.; Ho, C.Y. "*Properties of aluminium and aluminium alloys. thermoplastic properties*", **Res. Center, Purdue Univ. West Lafayette, IN, Rep.** (1973), Volume 2.
- [11] Molotskii, M.I. "*Theoretical basis for electro- and magnetoplasticity*", **Mater. Sci. Eng. A** (2000), Volume 287, pp.248–258.
- [12] Mclean, D. "*Dislocations and Plastic Deformation*", **Int. Mater. Rev.** (1974),

Volume 19, pp.268–268.

- [13] Breda, M.; Michieletto, F.; Beridze, E.E.E.; Gennari, C. "*Experimental Study on Electroplastic Effect in AISI 316L Austenitic Stainless Steel*", **Appl. Mech. Mater.** (2015), Volume 792, pp.568–571.
- [14] Perkins, T.A.; Kronenberger, T.J.; Roth, J.T. "*Metallic Forging Using Electrical Flow as an Alternative to Warm/Hot Working*", **J. Manuf. Sci. Eng.** (2007), Volume 129, pp.84.
- [15] Ross, C.; Roth, J.T. "*The Effects of DC Current on the Tensile Properties of Metals*", (2008), pp.363–372.
- [16] Salandro, W.A.; Bunget, C.J.; Mears, L. "*A thermal-based approach for determining electroplastic characteristics*", **Proc. Inst. Mech. Eng. Part B J. Eng. Manuf.** (2012), Volume 226, pp.775–788.
- [17] Magargee, J.; Morestin, F.; Cao, J. "*Characterization of Flow Stress for Commercially Pure Titanium Subjected to Electrically Assisted Deformation*", **J. Eng. Mater. Technol.** (2013), Volume 135, pp.041003.
- [18] Fan, R.; Magargee, J.; Hu, P.; Cao, J. "*Influence of grain size and grain boundaries on the thermal and mechanical behavior of 70/30 brass under electrically-assisted deformation*", **Mater. Sci. Eng. A** (2013), Volume 574, pp.218–225.

CHAPTER 3

Experimental set up

3.1. INTRODUCTION

This chapter briefly describes the instrumentation utilized during the PhD, focusing on the design and development of a dedicated power supply for electroplasticity tests.

3.2. Power suppliers

In order to deliver electrical current to the test machine, two different power suppliers were used. One is a commercially available while the other one had to be designed and manufactured. The need to design a pulsed power supply comes from the fact that the commercially available was only able to deliver current pulses of minimum duration of 1 ms, which is not short enough to avoid substantial joule heating. It was then necessary to develop a new power supply able to decrease the pulse duration and increase the frequency at which the pulses are delivered to the specimen.

3.2.1. *Commercially available power supply*

The commercially available power supply was manufactured by Powerel S.r.l. located in Montecchio Maggiore, Vicenza. It consists of six independent different modules capable of delivering 1000 A at 10 V each, with a maximum power of 60 kW (Figure 3.1).

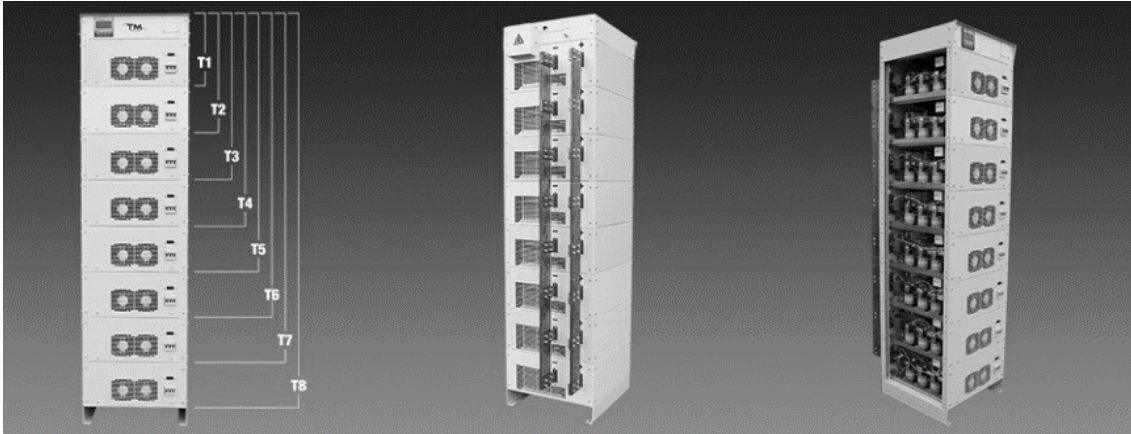


Figure 3.1 Overview of the power supply, front (left), back (center) and back without the casing (right).

It can deliver both continuous and pulsed current with a minimum pulse duration of 1 ms and a maximum pulse period of 65000 ms. The wave form is squared even at the lowest possible pulse duration.

This power supply is the one utilized to perform the electrically assisted tensile test with continuous current and the pulsed current tensile test on duplex stainless steel UNS S32750.

A key issue for electrically assisted manufacturing, as said in chapter 1, is the confinement of the electrical current to the specimen. In order to do that, special self-designed copper jaws embedded in *polyether ether kethone* (PEEK) were designed and manufactured (Figure 3.2).

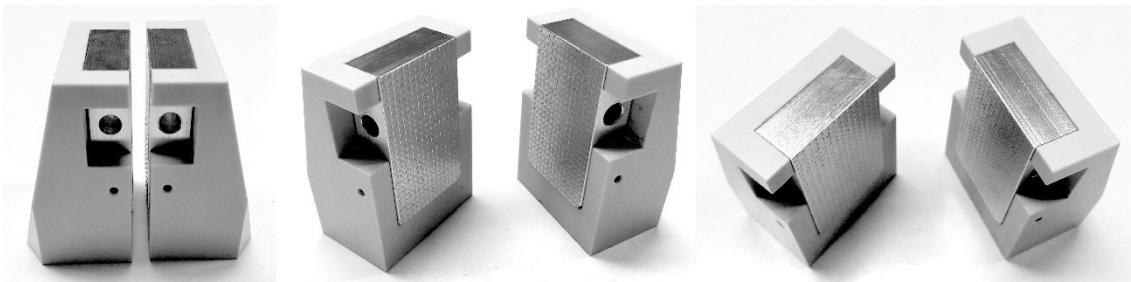


Figure 3.2 Copper embedded in PEEK jaws for electrically assisted tensile test.

3.2.2. Pulsed power supply

As previously mentioned in 3.2, a power supply (Figure 3.3) with the following specifications was needed to investigate higher current density without excessive joule heating of the workpiece:

- Current intensity variable between 500 A and 5000 A
- Current pulse duration in the order of 100 μ s according to literature
- Current frequency variable up to 60 Hz
- Uninterrupted current erogation up to approximately 200 s



Figure 3.3 Pulsed power supply.

The working principle of this current pulse generator is based on the discharge of a charged capacitor bank (C) on an electrical network characterized by an electrical resistance (R) and magnetic inductance (L). Resistance and inductance mostly depend upon the connections between the generator and the test specimen on the testing machine: no significant influence is due to the specimen. R and L have a great influence on the performance of the generator that must be designed accordingly to the electric network characteristics. The possibility to guarantee a certain number of pulses per second was the main

difficulty in the generator design. The discharge of a capacitor on an R-L circuit induces harmonic oscillation of voltage and current. In the electric network realized for the electroplasticity tests an underdamped response is expected. The use of a thyristor allows switching on the circuit to discharge the capacitor but also to switch off the circuit when the current crosses the zero value. This way, the circuit is open when the current is almost zero and the capacitor still has a significant voltage, even if its sign is opposite in comparison with the one at the starting of the process. To reduce the charging time of the capacitors and the power required by the DC supply, the bank is closed, by a secondary SCR, another time on an internal inductor to reverse its polarity before the next charging (Figure 3.4 and Figure 3.5).

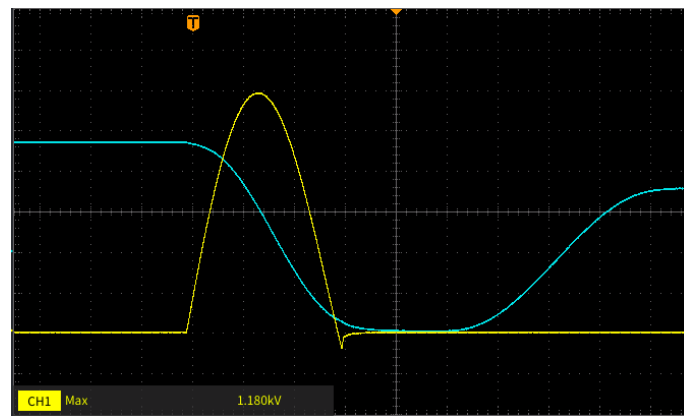


Figure 3.4 Screen capture of the oscilloscope showing the evolution over time of the electrical current delivered to the specimen (yellow line) and the evolution over time of the voltage across the capacitors (cyan line).

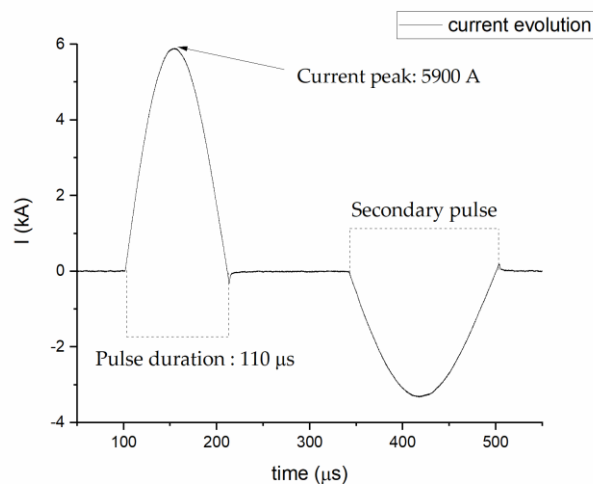


Figure 3.5 Evolution of the current during one pulse.

In Figure 3.5 it can be seen the first pulse of electrical current that passes through the specimen, while the second pulse of negative polarity current is the internal one that raises the voltage of the bank of capacitors in order to recover some energy and reduce the voltage needed to recharge them. Pulse duration is in the order of 100 μ s, one order of magnitude lower compared to the other power supply; small or negligible joule heating is expected [1]. Utilizing the same current density and considering only the pulse duration, the thermal energy delivered to the specimen is two order of magnitude lower if we compare with the continuous current power supply.

Since the working voltage and current intensity are higher in comparison with the other power supply, another jaw design is mandatory in order to avoid current discharges (Figure 3.6).

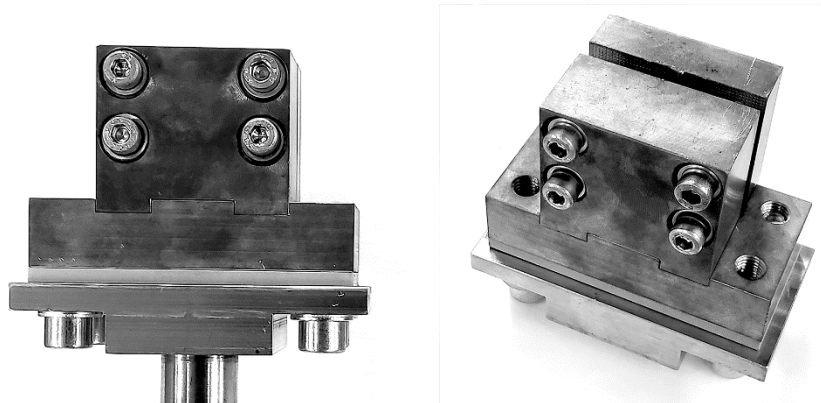


Figure 3.6 Copper jaws for electrically assisted tensile test for the pulsed power supply.

3.3. Scanning electron microscope

Characterization of the materials and the fracture surfaces were performed with a Cambridge Leica Stereoscan LEO 440 scanning electron microscope equipped with a Philips PV9800 EDS probe (Figure 3.7). The observation were conducted in secondary electron mode at an accelerating voltage of 15 kV and in backscattered mode at an accelerating voltage of 25 kV except when dealing with duplex stainless steel (accelerating voltage 29 kV).

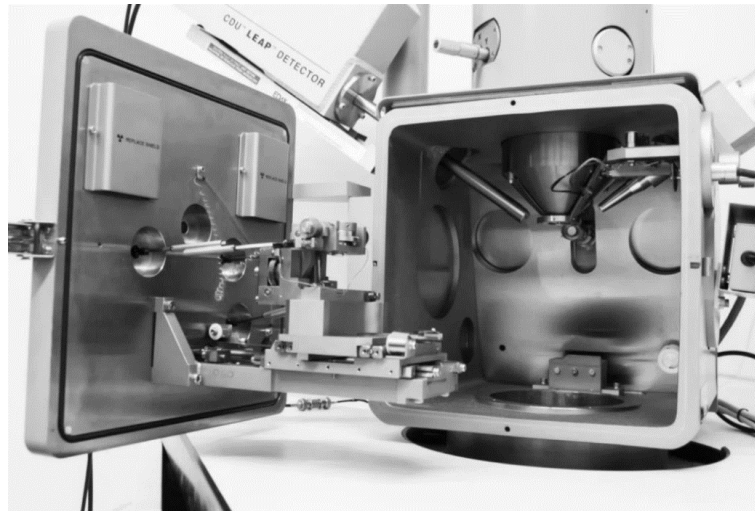


Figure 3.7 Scanning electron microscope Leica Cambridge Stereoscan Leo 440.

3.4. Transmission electron microscope

A Jeol 100 CX-II transmission electron microscope was utilized in order to compare the dislocation density and the dislocation substructure and network on aluminum specimens tested in electrically assisted tension mode. It was utilized with an accelerating voltage of 120 kV and 160 kV in bright field mode and two beam condition in order to improve dislocation contrast (Figure 3.8).

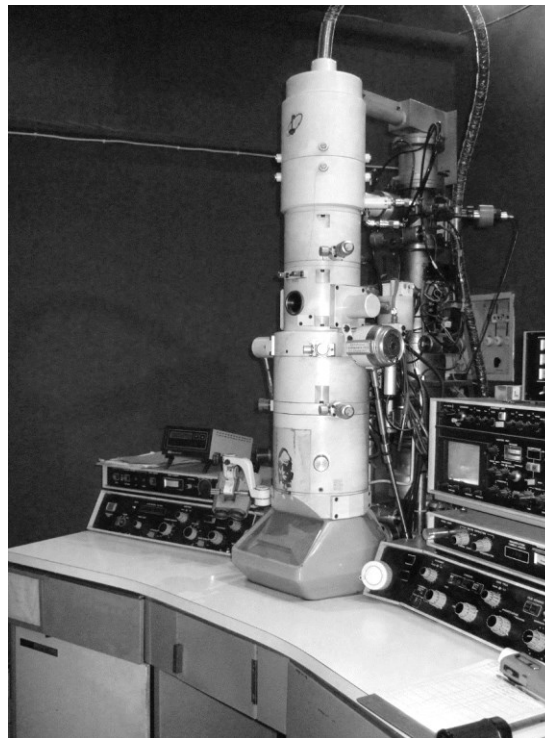


Figure 3.8 Jeol 100CX-II transmission electron microscope.

3.5. Optical microscope

A Leica DMRE optical microscope was utilized to observe the microstructure of the investigated materials. It was utilized in bright field and dark field, along with differential interference contrast (Nomarsky microscopy)



Figure 3.9 Leica DMRE optical microscopy.

3.6. X-ray diffraction

X-ray diffraction has been utilized to calculate the volume fraction of the different constituent of the materials analyzed and to perform profile fitting of the peaks. It has been also performed residual stress measurements with a portable-dedicated x ray diffractometer.

3.6.1. Siemens D500

A Siemens D500 equipped with $\text{CuK}\alpha$ radiation tube and a monochromator on the detector side have been employed to perform Rietveld refinement in order to calculate the volume fraction of the different constituent of the alloys. Scan angle depends on the alloys analyzed while scan step and counting time were 0.05° and 5 s respectively.

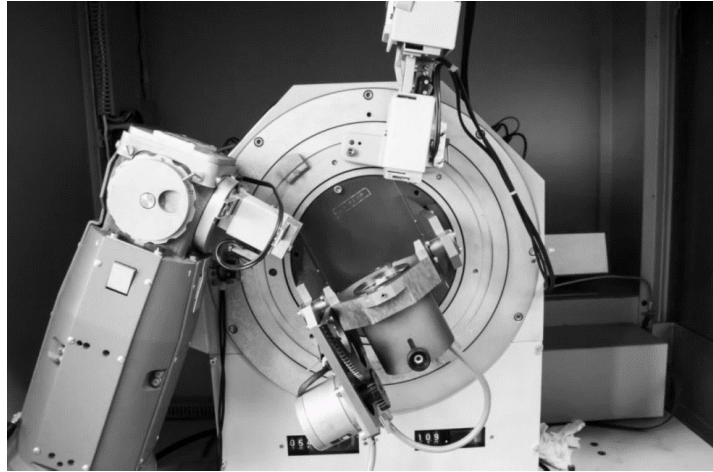


Figure 3.10 Siemens D500 x-ray diffractometer.

Luca Lutterotti freeware Maud© software have been utilized to perform Rietveld refinement on the collected data [2–4].

3.6.2. Bruker D8

A Bruker D8 x-ray diffractometer equipped with CuK α X-ray tube without monochromator was employed to perform peak shape analysis in order to evaluate microstrain, dislocation density and stacking fault in duplex stainless steel UNS S32750. Scan angle between 40° and 95° with a step size of 0.01° in order to have at least ten points over the half height of the peak and a counting time of 3 s have been utilized to perform peak shape analysis.

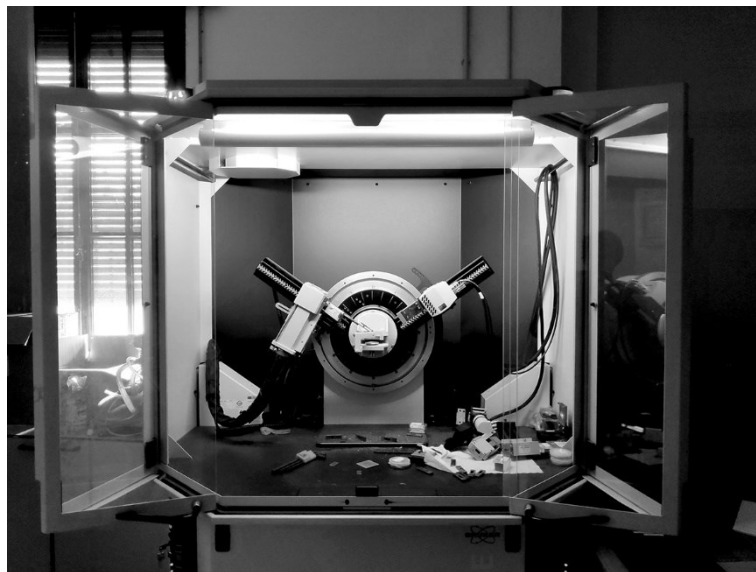


Figure 3.11 Bruker D8 x-ray diffractometer.

HighScore Plus© software by PANalytical have been utilized to analyze the collected data.

3.6.3. Spider X portable residual stresses diffractometer

Residual stresses were measured utilizing a dedicated X-ray diffractometer produced by GNR Analytical Instrument Group S.r.l.. It is able to perform residual stress measurements both on f.c.c. and b.c.c. material thanks to two goniometers equipped respectively with $\text{CuK}\alpha$ tube and $\text{CrK}\alpha$ radiation tube. It was utilized to measure residual stresses on duplex stainless steel UNS S32750 consisting of both f.c.c. phase (austenite) and b.c.c. phase (ferrite).

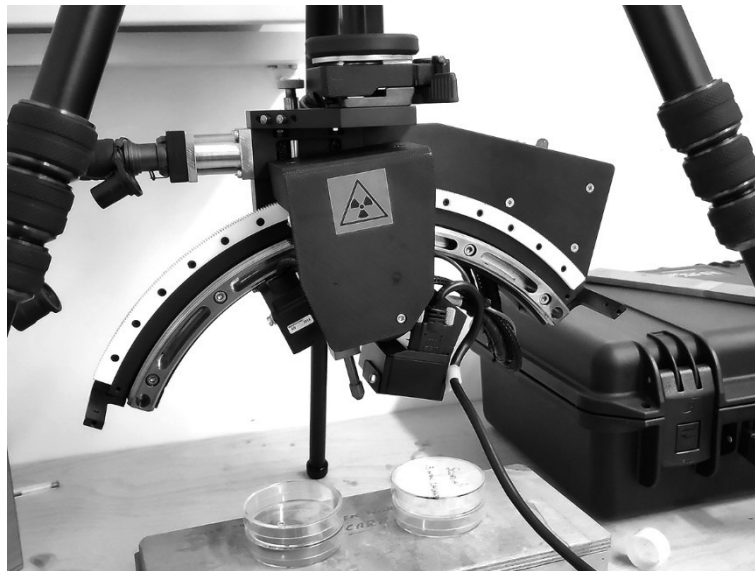


Figure 3.12 GNR Analytical Spider X x-ray diffractometer.

It uses the $\sin^2\Psi$ technique which will be briefly described below starting from the *two angle* technique.

The following equation describes the fundamental relationship between lattice spacing and the biaxial strength in the surface of the sample where the lattice spacing $d_{\phi\psi}$ is a linear function of $\sin^2 \psi$:

$$d_{\phi\psi} = \left[\left(\frac{1+\nu}{E} \right)_{(hkl)} \sigma_{\phi} d_0 \sin^2 \psi \right] - \left[\left(\frac{\nu}{E} \right)_{(hkl)} d_0 (\sigma_1 + \sigma_2) + d_0 \right] \quad (3.1)$$

where $d_{\phi\psi}$ is the spacing between the lattice planes measured in the direction defined by ϕ and ψ , d_0 is the stress-free lattice spacing, $\left(\frac{1+\nu}{E}\right)_{(hkl)}$ and $\left(\frac{\nu}{E}\right)_{(hkl)}$ are the elastic constants for the crystallographic direction normal to the lattice planes in which the strain is measured, as specified by the Miller indices (hkl) and σ_ϕ , σ_1 and σ_2 are defined as in Figure 3.13.

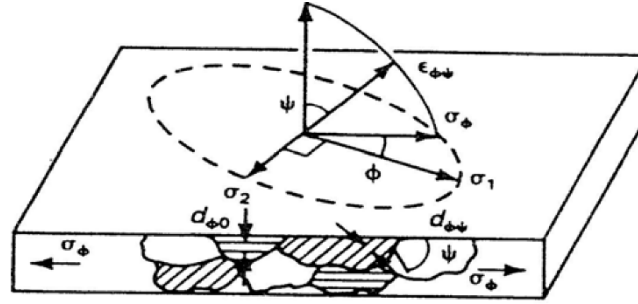


Figure 3.13 Plane stress elastic model.

As an example, Figure 3.14 shows the dependence of $d(311)$ for ψ , ranging from 0 to 45° for shot peened 5056-O aluminum having a surface stress of -148 MPa, to which a straight line has been fitted by least squares regression.

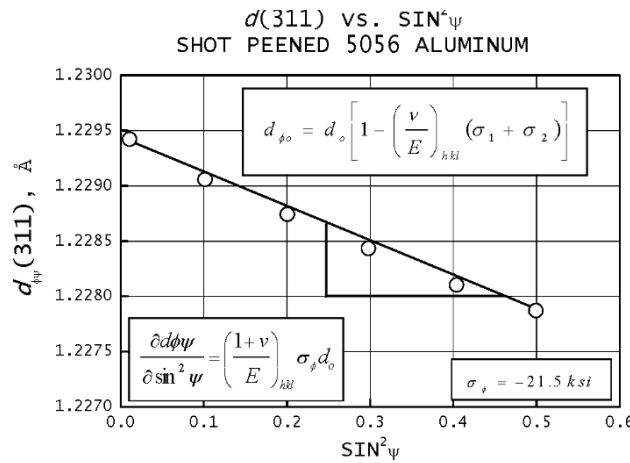


Figure 3.14 $d(311)$ versus $\sin^2 \psi$ plot for a shot peened 5056-O aluminum alloy having a surface stress of -148 MPa [5].

According to the equation 3.1 and Figure 3.14 if the lattice spacing, $d_{\phi\psi}$ is a linear function of $\sin^2 \psi$, the stress can be determined by measuring the lattice spacing for any two ψ angles. Selecting ψ angles to provide as large a range of $\sin^2 \psi$ as possible within the limitations imposed by the diffraction angle 2θ and the sample geometry maximizes sensitivity of the method. Lattice spacing is

determined precisely at two extreme values of ψ , typically 0 and 45°, and the stress is calculated using (3.2).

$$\sigma_{\phi} = \left(\frac{E}{1 + \nu} \right)_{(hkl)} \frac{1}{d_{\phi 0}} \left(\frac{\partial d_{\phi \psi}}{\partial \sin^2 \psi} \right) \quad (3.2)$$

The $\sin^2 \psi$ technique is identical to the two-angle technique, except lattice spacing is determined for multiple ψ tilts, a straight line is fitted by least squares regression (as shown for the shot peened aluminum sample in Figure 3.14), and the stress is calculated from the slope of the best fit line using (3.2). The primary advantage of the $\sin^2 \psi$ technique, considering the additional time required for data collection, is in establishing the linearity of d as a function of $\sin^2 \psi$ to demonstrate that x-ray diffraction residual stress measurement is possible on the sample of interest.

3.7. Corrosion tests

Corrosion tests were carried out through potentiodynamic polarization tests by mean of an AMEL 2549 potentiostat (Figure 3.15) and were conducted according to ASTM standard G61-86.



Figure 3.15 Potentiostat for the corrosion tests.

To measure the critical pitting temperature an AMEL 7060 potentiostat coupled with a thermostatic bath was used following the procedure described in ASTM standard G150.



Figure 3.16 Amel 7060 potentiostat.

3.8. Tensile test machine

The tensile test machine utilized in the experiment is an MTS 322 equipped with a load cell of 50 kN. Elongation data were collected through the cross head position and the load through the load cell. As previously mentioned in 3.2.1 and 3.2.2 special self-designed jaws have to be employed in order to isolate the frame of the tensile test machine from the circulating electric current, depending on the power supply.



Figure 3.17 MTS 322 tensile test machine.

3.9. Thermal infrared camera

In order to collect temperature measurements a thermal infrared camera FLIR A40 Thermovision® was utilized (Figure 3.18) along with its dedicated software FLIR Tools®. It can collect temperature data between 0 °C and 1500 °C with a sample rate adjustable up to 50 Hz.



Figure 3.18 FLIR A40 Thermovision® thermal infrared camera.

3.10. References

- [1] Sprecher, A.F.; Mannan, S.L.; Conrad, H. "*Overview no. 49 On The Mechanisms For The Electroplastic Effect In Metals*", **Acta Metall.** (1986), Volume 34, pp.1145–1162.
- [2] Lutterotti, L. "*Total pattern fitting for the combined size-strain-stress-texture determination in thin film diffraction*", **Nucl. Instruments Methods Phys. Res. Sect. B Beam Interact. with Mater. Atoms** (2010), Volume 268, pp.334–340.
- [3] Lutterotti, L.; Chateigner, D.; Ferrari, S.; Ricote, J. "*Texture, residual stress and structural analysis of thin films using a combined X-ray analysis*", **Thin Solid Films** (2004), Volume 450, pp.34–41.
- [4] Lutterotti, L.; Bortolotti, M.; Ischia, G.; Lonardelli, I.; Wenk, H.R. "*Rietveld texture analysis from diffraction images*", **Zeitschrift fur Krist. Suppl.** (2007), Volume 1, pp.125–130.
- [5] Hilley, M.E.; Larson, J.A.; Jaczak, C.F.; Ricklefs, R.E. "*Residual Stress Measurement by X-ray Diffraction-SAE J784a, Society of Automotive Engineers*", **Inc., New York, New York** (1971).

CHAPTER 4

Continuous and pulsed current

4.1. INTRODUCTION

In this chapter, electrically assisted tensile tests on different alloys under continuous and pulsed electrical current are presented. The first set of tests is conducted on a titanium grade five alloy moving on to a lab grade stainless steel grade which present the so called *Twinning Induced Plasticity* (TWIP) phenomenon. A more in-dept study on the effect of the triaxiality and rolling direction on the EPE have been performed on a pure aluminum alloy under continuous electrical current. At the end of the chapter the investigation of continuous current on four grades of duplex stainless steels and pulsed current on duplex stainless steel UNS S32750 are presented. For each material, an introduction paragraph explaining the features, the metallurgy and some application is redacted.

4.2. Titanium

Titanium is a very interesting metal due to its high mechanical properties and low density (4.51 g cm^{-3}). Its melting point is $1670 \text{ }^\circ\text{C}$ which is ideal for use in components that operate at high temperature. Some physical properties of titanium and its alloys compared to other metals are summarized in Table 4.1 [1].

Table 4.1 Physical properties of titanium.

Properties	Ti	Ti-5Al-2.5Sn	Ti-6Al-4V	Ti-3AlTi-8V-6Cr-4Mo-4Zr	7075 aluminum	17-7PH steel	4340 steel
Density, g/cm ³ (lb/in. ³)	4.540 (0.164)	4.484 (0.162)	4.429 (0.160)	4.816 (0.174)	2.796 (0.101)	7.640 (0.276)	7.833 (0.283)
Thermal conductivity, W/m · K (Btu/h · ft ² · ft · °F)	17.0 (9.8)	7.8 (4.5)	6.7 (3.9)	6.9 (4.0)	121.1 (70.0)	16.6 (9.6)	37.5 (21.7)
Electrical resistivity, μΩ · m at 21 °C (μΩ · in. at 70 °F)	0.61 (24)	1.57 (62)	1.71 (67.4)	1.52 (60)	0.06 (2.3)	0.86 (34.0)	0.22 (8.8)
Coefficient of thermal expansion, m/m · °C (10 ⁻⁶ in./in. · °F)	10.1 (5.6) (20–650 °C, or 70– 1200 °F)	9.7 (5.4) (20–650 °C, or 70– 1200 °F)	11.0 (6.09) (20–650 °C, or 70– 1200 °F)	8.8 (4.9) (20–650 °C, or 70– 1200 °F)	26.4 (14.4) (20–300 °C, or 70– 572 °F)	12.5 (6.9) (20–425 °C, or 70–800 °F)	14.8 (8.1) (20–650 °C, or 70– 1200 °F)
Specific heat, J/kg at 21 °C (Btu/lb · °F at 70 °F)	540 (0.129)	523 (0.125)	565 (0.135)	515 (0.123)	962 (0.23)	502 (0.12)	448 (0.107)
Melting range, °C (°F)	1670 (3038)	1600 (2910)	1605–1670 (2920–3040)	1650 (3000)	475–640 (890–1180)	1400–1455 (2550–2650)	1505 (2740)
Alloy type	α	α	α + β	β

Because of its high reactivity with oxygen it get coated with a very stable titanium oxide layer which enhance its corrosion resistance in oxidizing environments, on the other hand it can catch fire and cause severe damage in particular circumstances (i.e., rubbing against other metals at elevated temperatures, Figure 4.1).

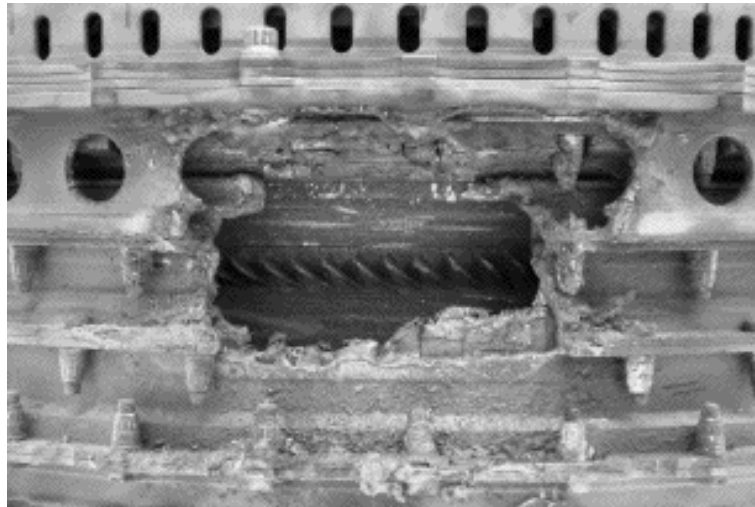


Figure 4.1 Consequences of a titanium fire in an aeroengine [2].

It is largely used in the aerospace industry because of its high specific mechanical properties and in objects that have a high end value due to its cost (six times that of aluminum and ten times that of steel).

Titanium possesses a hexagonal closed pack (h.c.p.) structure at room temperature and pressure (α-Titanium) with a *c/a* ratio of 1.587. Under applied load it can activate three different slip system: pyramidal, prismatic and basal

plane along the close-packed direction. It has an allotropic transformation at 890 °C which changes the crystal structure from h.c.p. to a b.c.c. called β -Titanium which is stable up to the melting temperature .

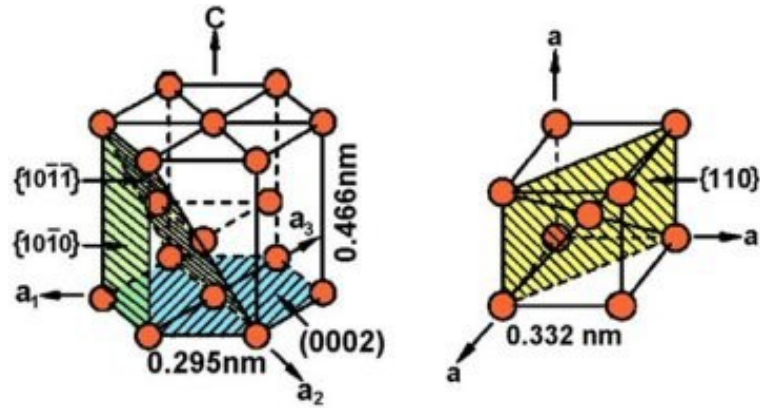


Figure 4.2 Crystal structures of titanium [3].

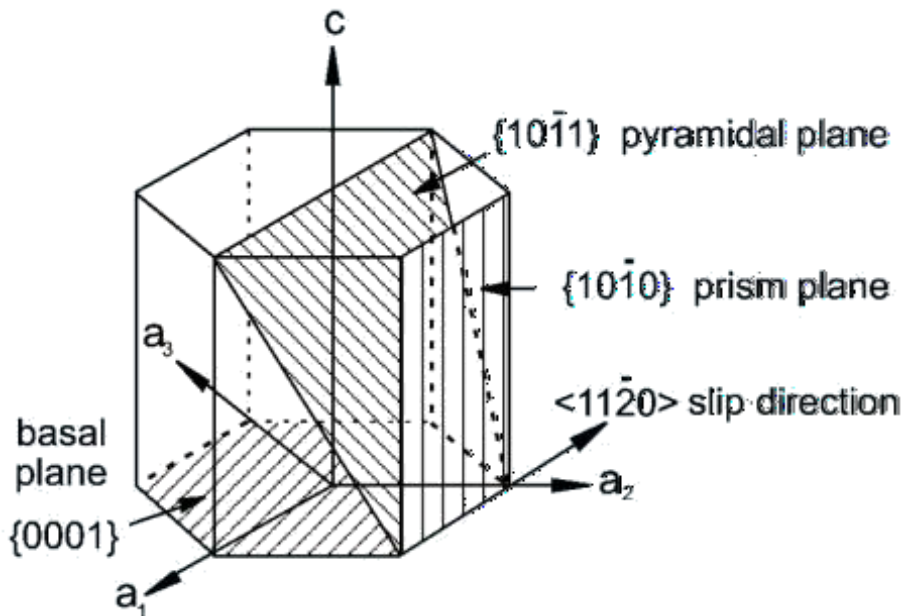


Figure 4.3 Slip system of h.c.p. titanium [3].

4.2.1. Titanium alloys

Following the Hume-Rothery rules [4–6], all elements within 0.85 to 1.15 atomic radius of titanium have a significant solubility. Elements with smaller radius than 0.59 that of the Ti (e.g. H, C, N, O) have substantial solubility in interstitial gaps (Figure 4.4).

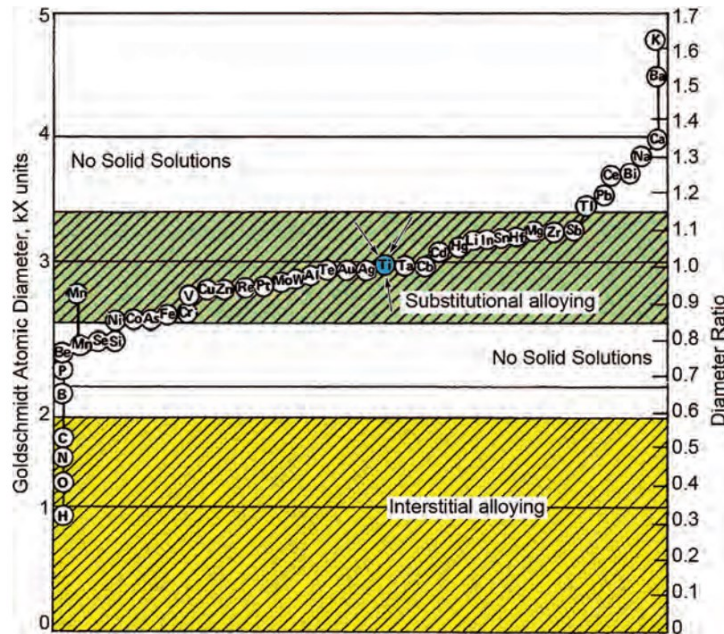


Figure 4.4 Atomic diameter referred to titanium [1].

As can be seen from Figure 4.4, the solubility gap encloses a lot of elements, hence numerous alloys can be produced.

According to their effect in stabilizing α phase or β phase, alloying elements are subdivided into α -stabilizers or β -stabilizers. Thus, Al, O, N and Ga are all α -stabilizers. Mo, V, W and Ta are all β -stabilizers. Cu, Mn, Fe, Ni, Co and H are also β -stabilizers but form the eutectoid (Figure 4.5). The eutectoid reaction is frequently sluggish (since substitutional atoms are involved) and is suppressed.

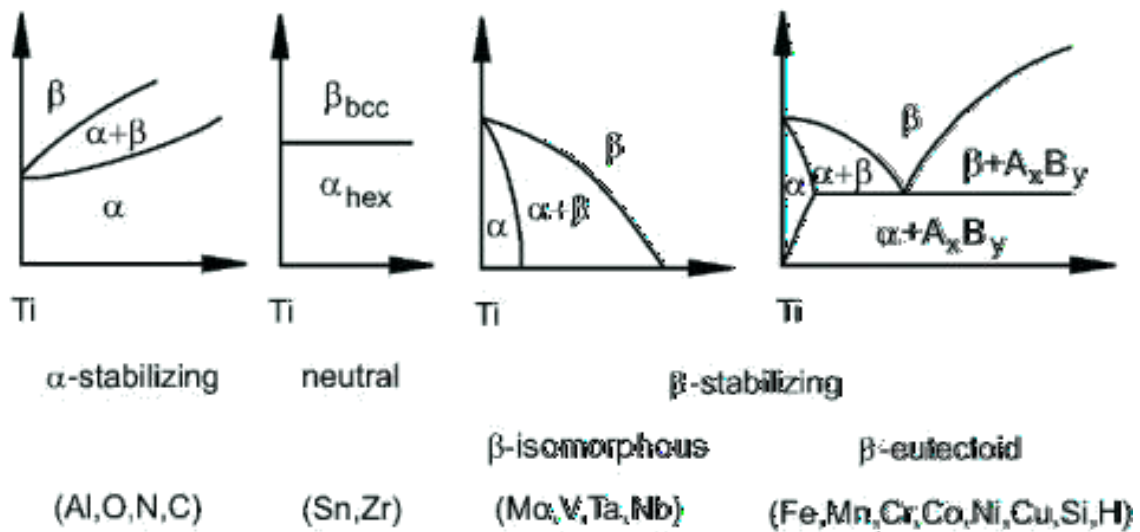


Figure 4.5 Effect of α -stabilizers and β -stabilizers elements in titanium [2].

Interstitial atoms do not fit properly and cause changes in the lattice parameters. Hydrogen is the most important one because of its high solubility. B.c.c.-Ti has three octahedral interstices per atom whereas h.c.p.-Ti has one per atom. The latter are therefore larger, so that the solubility of O, N, and C is much higher in the α phase. Titanium is capable of absorbing up to 60 at.% of hydrogen, which can also be removed by annealing in a vacuum. Hydrogen enters the tetrahedral holes which are larger in b.c.c. than h.c.p.. Thus the solubility of hydrogen is larger in β titanium. The enthalpy of solution of hydrogen in Ti is negative ($\Delta H < 0$).

Since hydrogen solubility in titanium decreases increasing temperature, titanium is a candidate material for the wall of magnetically confined fusion reactors. The hydrogen based plasma is not detrimental since at 500 °C and 1 Pa pressure, Ti does not pick up enough hydrogen for embrittlement. An additional feature is that Ti resists swelling due to neutron damage. A large enough concentration of hydrogen induces the precipitation of hydrides.

TiH_{1.5-2.0} has a Cubic-F lattice and its precipitation causes embrittlement due to a volume expansion of about 18%. There are regions of hydrostatic tension at crack tips where it forms preferentially, leading to large increases in the crack growth rate, some 50-fold during fatigue. One problem with this method of hydrogen storage is that hydride formation is accompanied by a considerable volume expansion, which in turn can embrittle the alloy. Amorphous alloys of titanium are better in this respect, since they do form hydrides and yet reversibly accommodate large quantities of hydrogen by an expansion of the nearest-neighbor distance.

4.2.1.1. Titanium α alloys

The α -alloys contain predominantly α -phase at temperatures well above 540 °C (1000 °F). A major class of α -alloy is the unalloyed commercially pure

(CP) titanium family of alloys that differ by the amount of oxygen and iron in each alloy. Alloys with higher interstitial content are higher in strength, hardness, and transformation temperature compared to high-purity alloys. Other α -alloys contain additions such as aluminum and tin (e.g., Ti 5Al 2.5Sn and Ti 6Al 2Sn 4Zr 2Mo wt.%). Generally, α -rich alloys are more resistant to high-temperature creep than α/β or β -alloys, and α -alloys exhibit little strengthening from heat treatment. These alloys are usually annealed or recrystallized to remove stresses from cold working. They have good weldability and generally inferior forgeability in comparison to α/β or β -alloys [7].

4.2.1.2. Titanium α/β -alloys

α/β -alloys contain one or more of the α and β -stabilizers. These alloys retain more β -phase after final heat treatment than the near α -alloys, and can be strengthened by solution treating and aging, although they are generally used in the annealed condition. Solution treatment is usually performed high in the α/β -phase field followed by aging at lower temperature to precipitate α -phase, giving a mixture of relatively coarse primary α - and fine α -phase in an α/β -matrix. Solution treating and aging can increase the strength of these alloys by up to 80%. Alloys with low amounts of β -stabilizer (e.g., “work-horse” Ti 6Al 4V wt.%) have poor hardenability and must be rapidly quenched for subsequent strengthening. A water quench of Ti 6Al 4V will adequately harden sections only less than 25 mm. β -stabilizers in α/β -alloys increase hardenability [7].

4.2.1.3. Titanium β alloys

β -Alloys have more β -stabilizer and less α -stabilizer than α/β -alloys. These alloys have high hardenability with the β -phase being retained completely during air cooling of thin sections and water quenching of thick

sections. β -alloys have good forgeability and good cold formability in the solution-treated condition. After solution treatment, aging is performed to transform some β -phase to α -phase. The strength level of these alloys can be greater than that of α/β -alloys, a result of finely dispersed α -particles in the β -phase. These alloys have relatively higher densities, and generally lower creep strengths than the α/β -alloys. The fracture toughness of aged β -alloys at a given strength level is generally higher than that of an aged α/β -alloy, although crack growth rates can be faster [7].

4.2.2. Materials and methods

The investigated alloys is Ti 6Al 4V α/β -titanium alloys in form of 1 mm thick sheet which composition is summarized in Table 4.2.

Table 4.2 Composition of the investigated alloy (wt.%).

Al	V	C	N	O	H	Fe	Y	Ti
6.17	4.32	0.05	0.04	0.28	0.01	0.27	0.02	Bal.

The specimens for the tensile test were obtained along the rolling direction with geometry according to ASTM E8/E8M-16a standard with some slight modification due to the sheet dimension Figure 4.6.

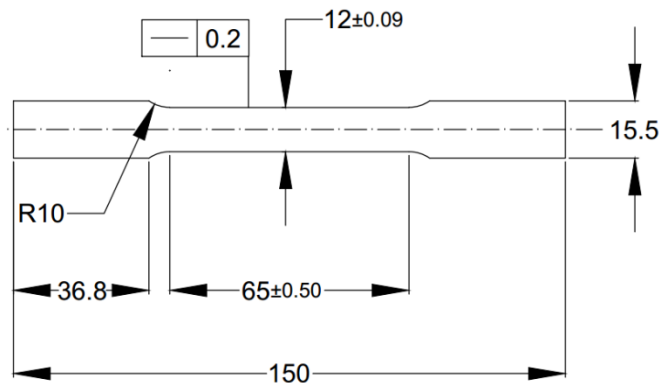


Figure 4.6 Specimens geometry.

The side of the specimen that faces the infrared thermal camera was painted with a black opaque lacquer in order to uniform the emission of the infrared radiation. Continuous current power supply Powerel S.p.a. was employed for the electrical and thermal tests. In order to separate the possible joule heating effect from that of the electrical current, thermal tests at the same temperature reached under current regime were performed. Three current densities with the related thermal regime were identified (Figure 4.7 and Table 4.3).

Table 4.3 Temperature reached at different current densities.

Current Density [A/mm ²]	Temperature [K]
5	363±11
10	533±22
15	803±33

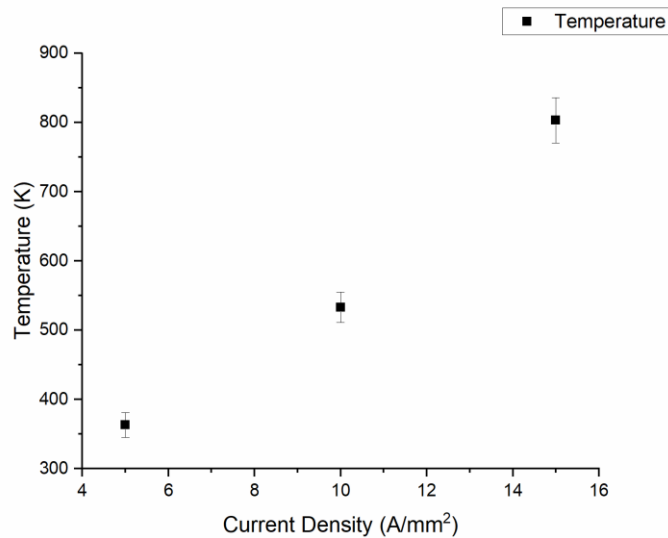


Figure 4.7 Thermal regime with respect current density utilized in the experiments.

Tensile tests were conducted on an MTS 322 tensile test machine equipped with a climatic chamber for the thermal test. Since climatic chamber is not able to reach the highest temperature recorded, it has been decided to heat the specimen through electric current and shut it off just before the start of the tensile test. Tensile tests were conducted at a strain rate of 10^{-1} s^{-1} after having observed some effect at lower strain rates (Figure 4.9) and to reduce the duration of the test. Blow air at 8 bar of pressure was used to cool the specimens and limits joule heating. Three tests for each condition have been performed, the error bars are the standard deviation of the performed tests.

Specimen characterization have been performed by mean of Siemens D500 X-ray diffractometer in order to be able to detect grain rotation and texturizing. Leica DMRE optical microscope have been utilized to investigate the microstructure of the tested samples. For revealing the microstructure, Kroll's reagent have been used (1% HF, 5% HNO₃ and 94% water in volume).

4.2.3. As received material

The material was delivered in the form a metal hot rolled and annealed sheet of 1 mm thickness with a microstructure consisting of an almost equiaxed Ti- α +Ti- β grains (Figure 4.8).

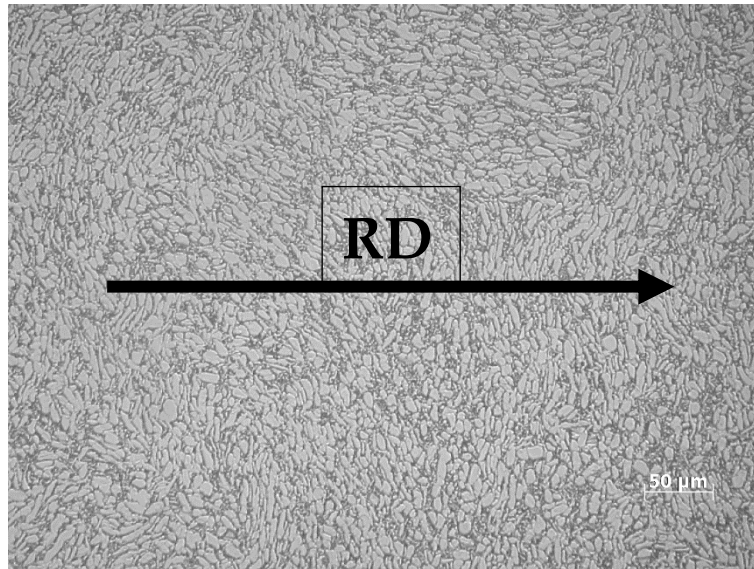


Figure 4.8 Microstructure of the as received titanium sheet, RD stands for rolling direction.

In order to have a baseline to compare the electrical test to, room temperature tensile tests at different strain rates have been performed.

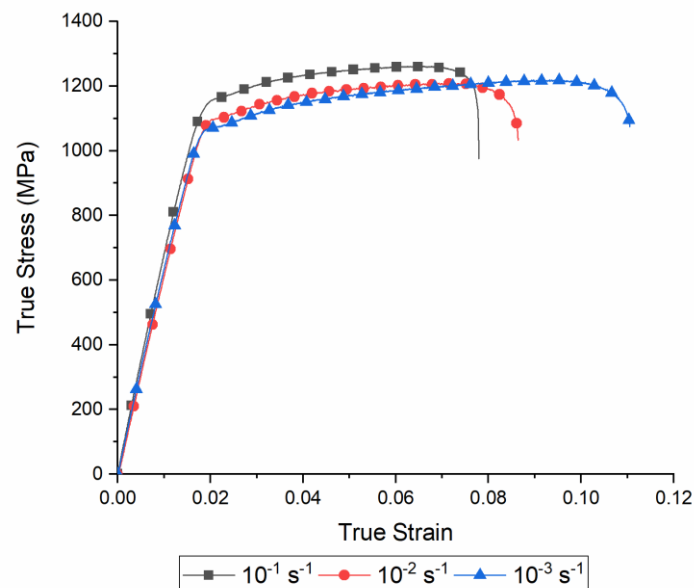


Figure 4.9 Room temperature tests at different strain rates.

As can be seen from Figure 4.9, lowering the strain rate affected yield stress (YS), uniform and fracture strain and ultimate tensile strength (UTS) as other researchers observed, denoting a strain rate sensitivity for this type of alloy [8,9]. It has been decided to conduct all the test at a strain rate of 10^{-1} s^{-1} (baseline hereafter) to reduce the test duration, to avoid any effect due to lower strain rates and to better replicate thermal tests.

4.2.4. Electrically assisted tensile tests

The flow stress curves of the tests conducted at three different current densities are depicted in Figure 4.10.

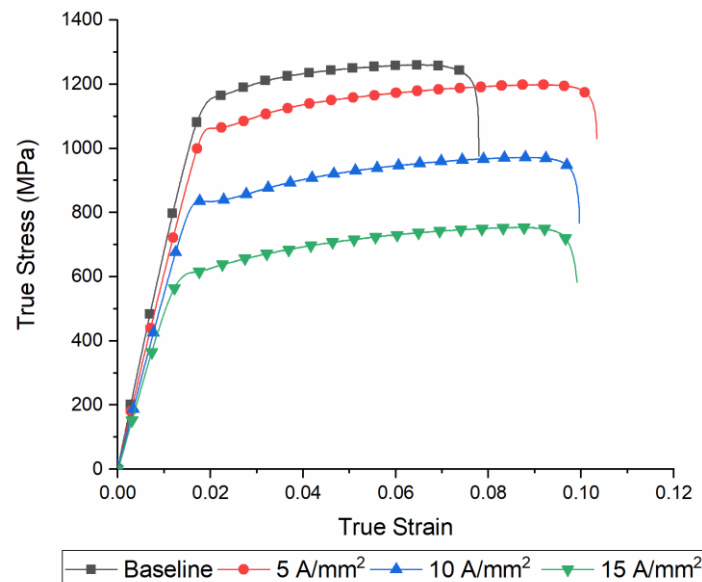


Figure 4.10 True stress-strain curves at room temperature (baseline) and at different current densities.

The tests conducted in current regime denoted an increase in the fracture strain in comparison to the baseline, while the YS and the UTS gradually decreased as the current density and the thermal regime increase. In Table 4.4 are summarized the value for the YS, UTS and fracture strain of the current density test.

Table 4.4 Mechanical properties of the baseline and the electrically assisted tensile tested specimens.

Current Density [A/mm ²]	UTS [MPa]	YS [MPa]	Fracture strain [%]
0	1161±10	1093±12	8.3±0.7
5	1083±15	1010±15	9.7±0.6
10	875±12	784±11	10.5±0.2
15	693±13	588±14	9.4±0.5

Interesting to note that even a slight increase in temperature compare to the baseline (50 K) enhanced the fracture strain of approximately 10% meaning that an increase in dislocation mobility and possibly, the activation of more than one slip system occurred.

4.2.5. Thermal tensile test

In order to see the influence of electrical current, thermal tests have been conducted at the same temperature reached by the electrical tests. The true stress-strain curves of the thermal test are depicted in Figure 4.11.

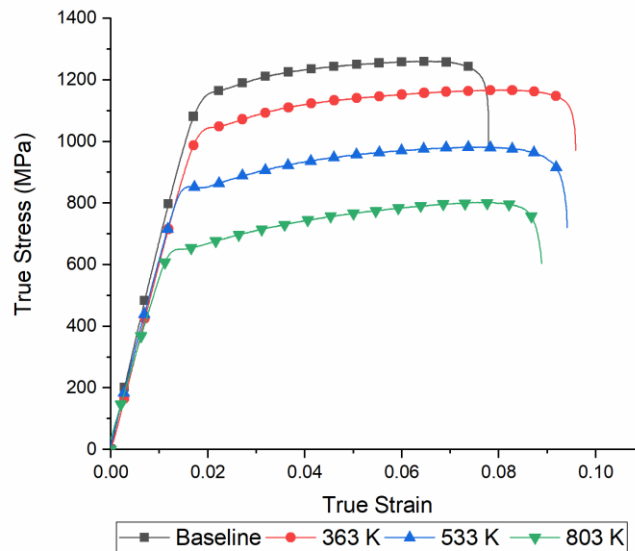


Figure 4.11 True stress-strain curves at room temperature (baseline) and at different thermal regimes.

As for the current regime tests, we can observe a gradual decrease in the YS, UTS while fracture strain was affected in less extent by the increase in

temperature. A summary of the numerical values of the YS, UTS and fracture strain are reported in Table 4.5.

Table 4.5 Mechanical properties of the baseline and the thermal tested specimens.

Temperature [K]	UTS [MPa]	YS [MPa]	Fracture strain [%]
293±1	1161±10	1093±12	8.3±0.7
363±11	1082±21	1018±22	9.8±0.2
533±22	910±15	830±25	9.7±0.3
803±33	749±29	639±36	9.3±0.4

The same trend can be observed for the fracture strain in comparison to that of the current regime.

4.2.6. Comparisons

In Figure 4.12 are presented the comparisons between the tensile tests conducted under electrical current and the related thermal counterparts, along with the room temperature test (baseline). One test per parameter have been shown as an example.

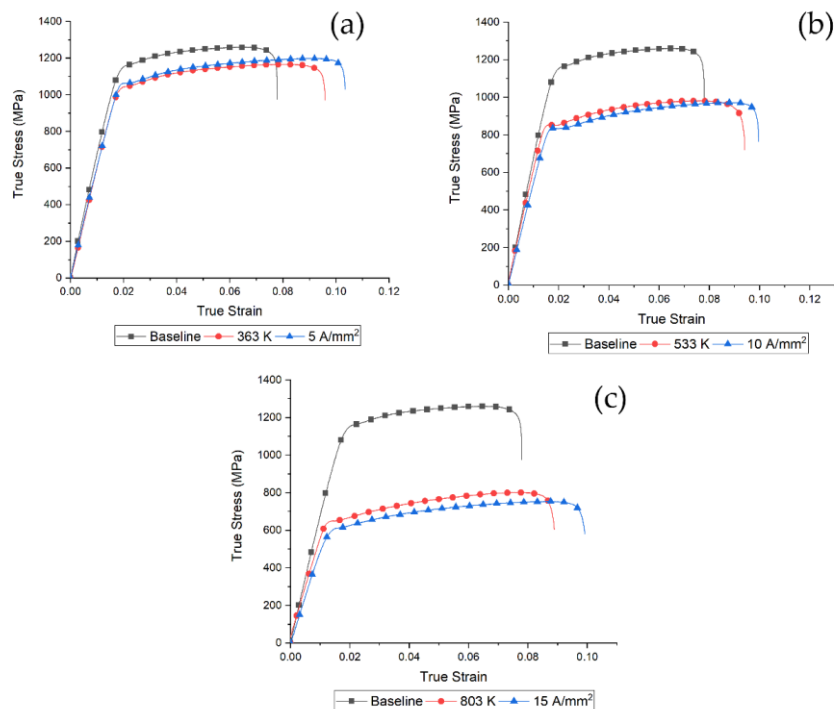


Figure 4.12 Comparison between thermal, electrical and baseline flow stress curves of (a) 5 A/mm² and 363 K, (b) 10 A/mm² and 533 K and (c) 15 A/mm² and 803 K.

From the figure above electrical tests showed a slight increase in fracture strain compared to the thermal counterpart while subtle differences can be observed for YS and UTS probably due to the difficulty in reproducing the thermal regime. In comparison with the baseline, fracture strain increases for both thermal and electrical test whilst YS and UTS gradually decrease.

In order to compare the results obtained from the electrical and the thermal tests, relative fracture strain, relative YS and relative UTS have been calculated with the following expressions:

$$\varepsilon_{rel} = \frac{\varepsilon_i}{\varepsilon_{baseline}} \quad (4.1)$$

in which ε_i refers to the fracture strain of the test and $\varepsilon_{baseline}$ is the fracture strain of the room temperature test.

$$YS_{rel} = \frac{YS_i}{YS_{baseline}} \quad (4.2)$$

Where YS_i is the yield stress of the test and $YS_{baseline}$ is the yield stress of the room temperature test.

$$UTS_{rel} = \frac{UTS_i}{UTS_{baseline}} \quad (4.3)$$

Where UTS_i is the ultimate tensile strength of the test and $UTS_{baseline}$ is the ultimate tensile strength of the room temperature test.

$$\varepsilon_{rel}^{uniform} = \frac{\varepsilon_i^{uniform}}{\varepsilon_{baseline}^{uniform}} \quad (4.4)$$

In which $\varepsilon_i^{uniform}$ is the uniform elongation of the test and $\varepsilon_{baseline}^{uniform}$ is the uniform elongation of the room temperature test.

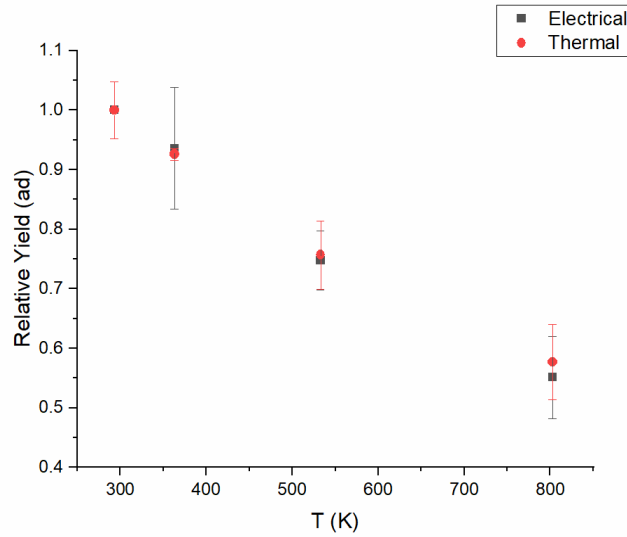


Figure 4.13 Relative YS of the electrical and thermal tests.

As can be seen from Figure 4.13 the relative yield stress of the thermal and electrical tests show the same value, with no clear effect of the electrical current on top of joule heating.

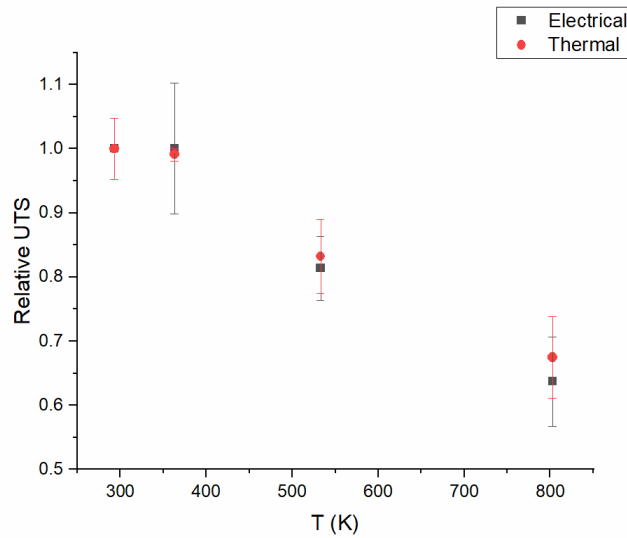


Figure 4.14 Relative UTS of the electrical and thermal tests.

Same consideration for the UTS can be made: relative UTS for electrical and thermal tests are the same, with no effect of the electrical current (Figure 4.14).

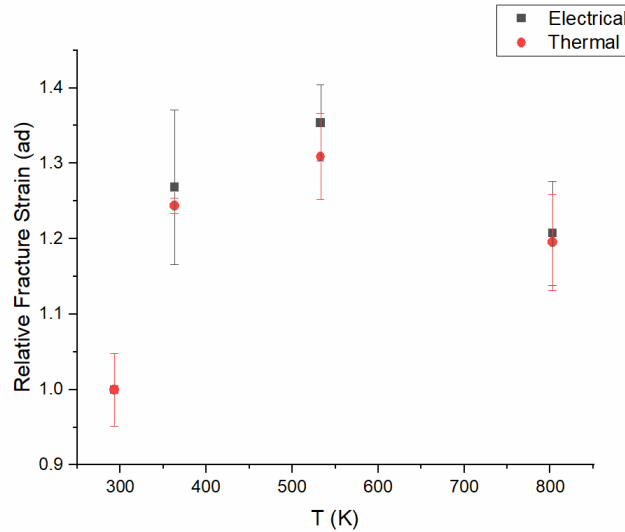


Figure 4.15 Relative fracture strain of the electrical and thermal tests.

Conversely, the test conducted at 10 A/mm² shows a slight increase in the fracture strain in comparison with the corresponding thermal test, even though it falls within the error bar. For the other current densities no differences in term of fracture strain can be noted.

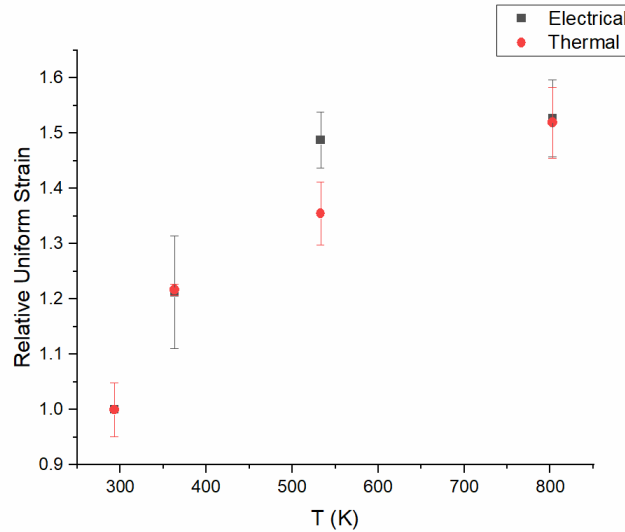


Figure 4.16 Relative Uniform strain of the electrical and thermal tests.

Even though this material doesn't show a pronounced local necking during localized plastic instability, it is better to compare uniform strain (elongation in correspondence of the UTS) rather than fracture strain. As can be seen in Figure 4.16, the trend of relative uniform strain is in accordance with

that of the fracture strain, denoting a slight increase for the material tested at 10 A/mm² in comparison with the related thermal test.

Titanium grade five stressed in uniaxial mode does not show any electroplastic effect on top of the effect of the raise in temperature, conversely to what other researchers found due to the lack of thermal comparison tests [10].

The microstructure of the tested samples under different electrical and thermal condition are depicted in Figure 4.17.

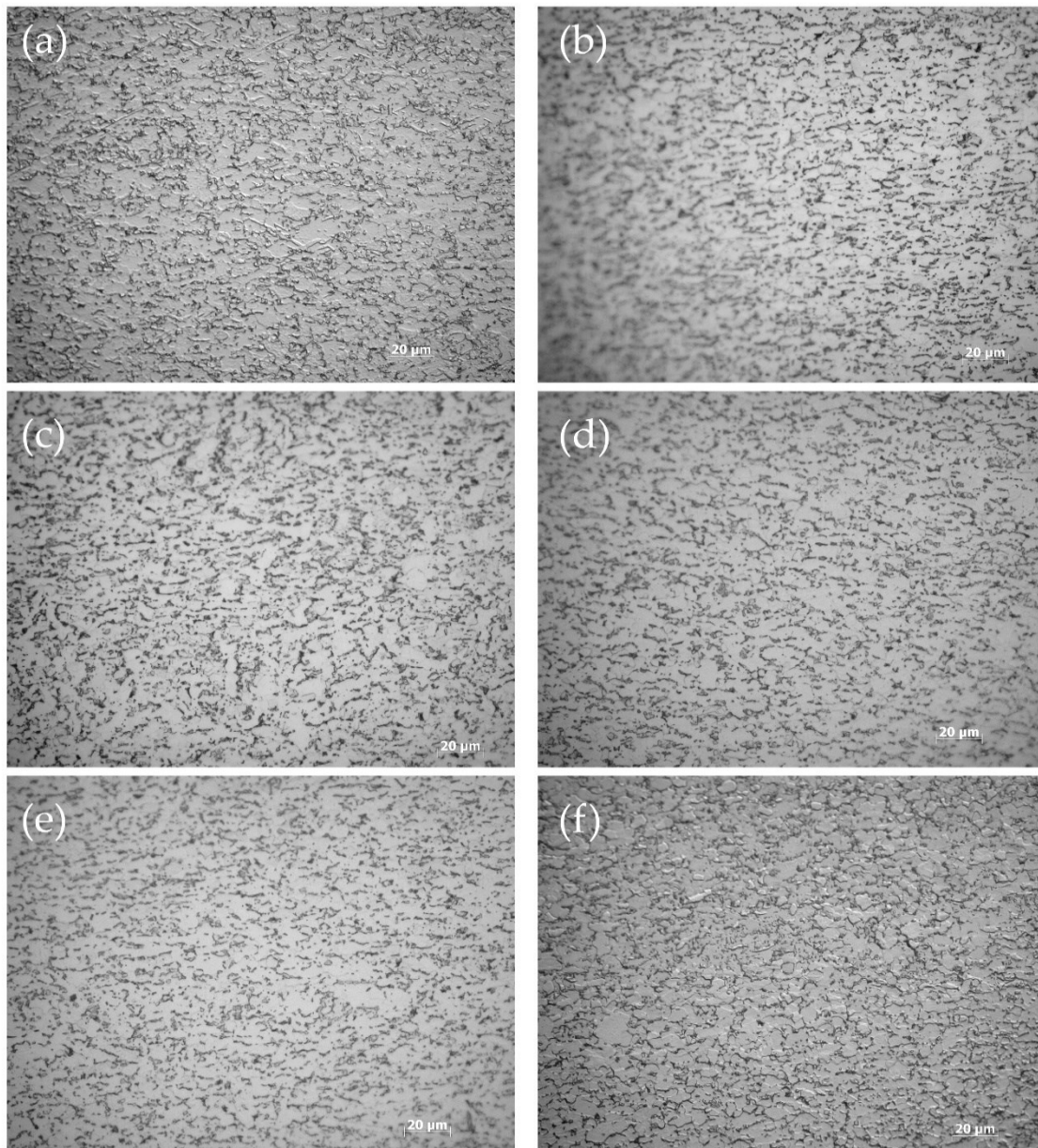


Figure 4.17 Micrographs of the deformed samples: (a) 5 A/mm², (b) 363 K, (c) 10 A/mm², (d) 533 K, (e) 15 A/mm², and (f) 803 K.

Since the material behave almost in the same manner, with no differences in terms of UTS, YS, fracture strain and uniform strain it was not expected any differences in the microstructure, as the micrographs of Figure 4.17 show. Contribution of the deformation, depending on how close to the fracture surfaces the micrographs have been taken, can be seen in Figure 4.17c and d.

X-ray diffraction pattern of the as received material along the rolling direction is showed in Figure 4.18.

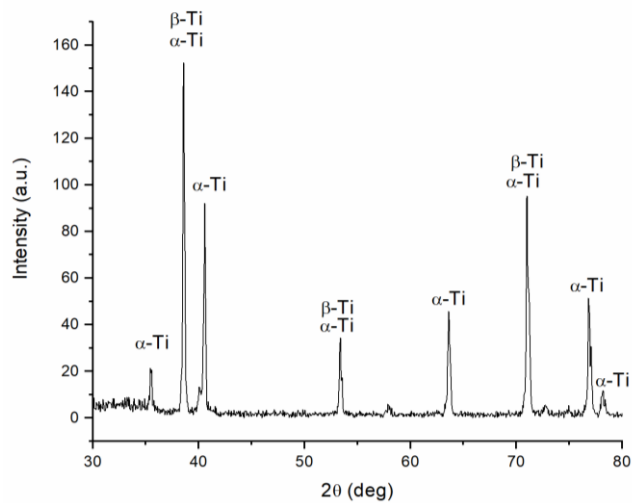


Figure 4.18 X-ray diffraction pattern of the as received material.

In order to observe any contribution from the deformation to the texture, other xrd measurements have been performed at 10 mm and at 5 mm from the fracture surfaces of the material deformed at room temperature (Figure 4.19).

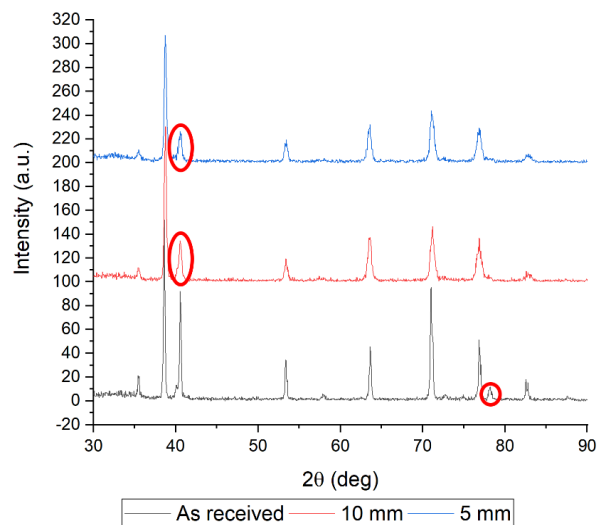


Figure 4.19 Xrd patterns of the as received materials and near the fracture surfaces after straining at room temperature.

A gradual reduction of the intensity of the peaks marked with the circle can be noted getting closer to the fracture surfaces, denoting a gradual rotation of the grain orientation due to the triaxiality of the stress in that region.

4.2.7. *Concluding remarks*

Since its high strength and difficult in forming, and its crystal structure, titanium is a good candidate to be tested for electroplastic effect.

This particular titanium grade did not show any effect of the electrical current on top of that of the raise in temperature under uniaxial load, conversely to what other researchers found due to the lack of comparison to pure thermal tests [11]. It has been observed that EPE works very good on material with hexagonal closed pack (h.c.p.) crystal structure as well as high SFE b.c.c. [12–17]. It is possible that due to the low thermal conductivity and the high electrical resistivity, using continuous current it was not possible to reach the current density threshold needed for the electroplastic effect to occur as observed by Magargee et al. [18].

In conclusion, electricity didn't affect YS, UTS, fracture strain nor uniform strain of titanium grade five in this current density range and load mode. Higher current density could be needed which can be possible to achieve only utilizing pulsed current in order to reduce joule heating.

4.3. Twinning induced plasticity stainless steel

Twinning induced plasticity (TWIP) steels are a very specific type of steel designed mainly for the automotive industry. They have very high mechanical strength and ductility which permit to greatly reduce the weight of the vehicle, its greenhouse gas emission and lowers fuel consumption. They have been developed in order to fill the empty region of the so called “banana diagram” in which are reported elongation along the vertical axis and UTS along the horizontal axis (Figure 4.20).

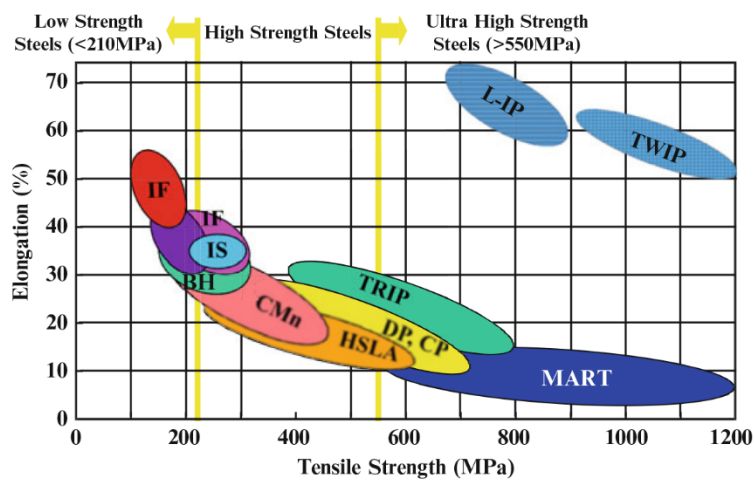


Figure 4.20 Relationship of tensile strength and elongation of various automotive steels [19].

In Figure 4.21 it can be seen the very high strength and ductility of TWIP steels in comparison with those of a titanium stabilized interstitial free steel (Ti-IF) and a typical ferritic steel. Ti-IF steels are considered one of the most formable industrial steel grades. Comparing TWIP steel with Ti-IF steel it can be seen the obvious higher uniform elongation, greater UTS, lower YS, higher strain hardening index and practically zero post uniform elongation. Some serration can be observed on the last part of the flow stress curves related to the phenomenon of *Dynamic Strain Aging* (DSA).

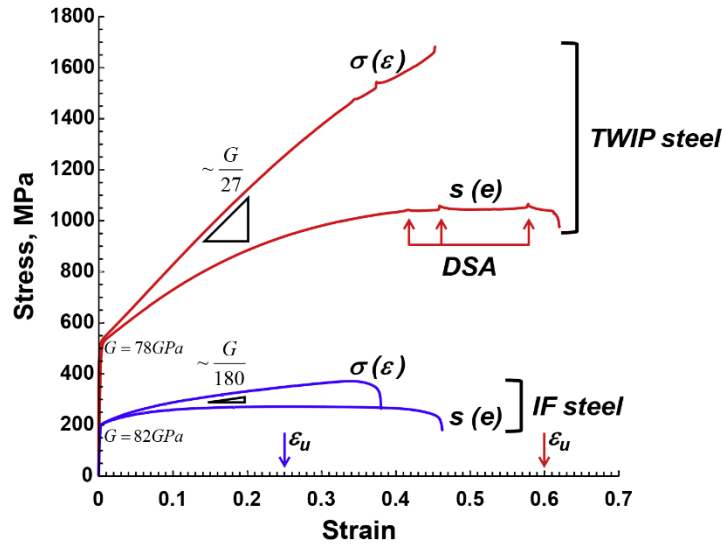


Figure 4.21 Comparison of the uniaxial tensile stress-strain curves for a Ti-stabilized interstitial-free (IF) ferritic steel (b.c.c. crystal structure) and an austenitic Fe-18%Mn-0.6%C-1.5%Al TWIP steel (f.c.c. crystal structure), illustrating a considerable difference in mechanical properties resulting from the more than six times larger strain hardening rate of the TWIP steel as compared to the IF steel [20].

The alloy content of TWIP steels is typically 15-30% Mn, 0-1% C, 0-3% Al, and 0-3% Si with small addition of Cr, Co, N, Nb, Ti and/or V. Their peculiar behaviour is driven by its *Stacking Fault Energy* (SFE) which dramatically depends on the composition.

SFE at room temperature is between 15 and 45 mJ/m², range in which twinning deformation is active. If SFE is lower than 15 mJ/m² *Transformation Induced Plasticity* (TRIP) can take place, leading to precipitation of α' or ϵ -martensite rather than twinning (Figure 4.22).

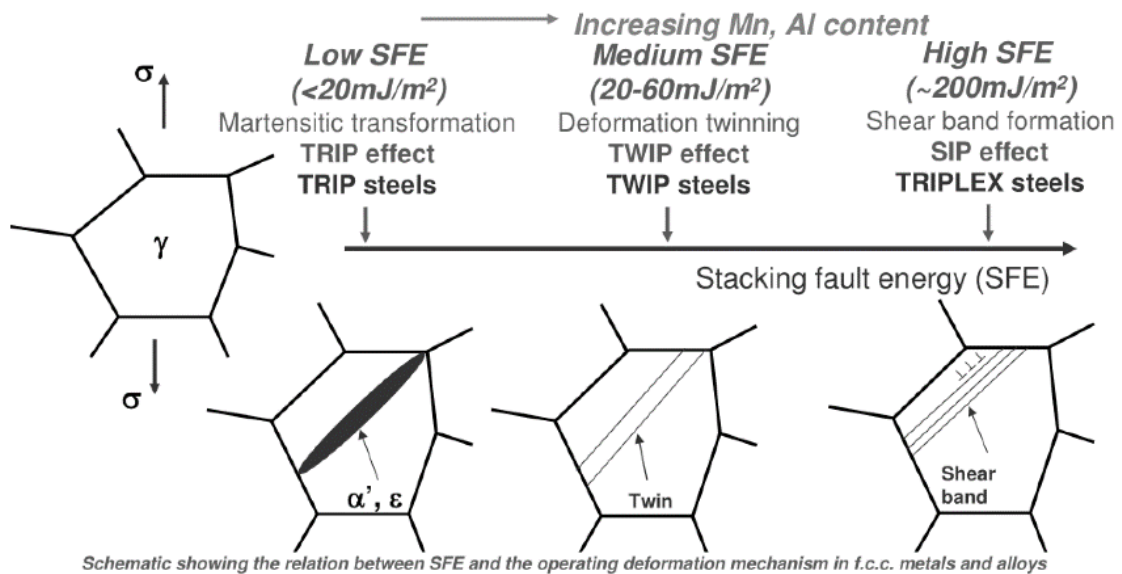


Figure 4.22 Change in deformation mechanism with respect to the SFE.

SFE plays also an important role in the deformation mechanism, lower SFE leads to higher density of strain-induced twins, which act as strong barriers to dislocation glide, and ultimately results in higher strain hardening [21].

The high strain hardening that these type of steel shows is due to the constant interaction between gliding dislocations with grain boundaries, wide stacking fault and deformation twins leading to a phenomenon called “*Dynamic Hall-Petch effect*” (Figure 4.23) that reduces the dislocation mean free path. As the stress increases, volume fraction of mechanical induced twins increases dividing grains into smaller grains reducing the glide distance of dislocation.

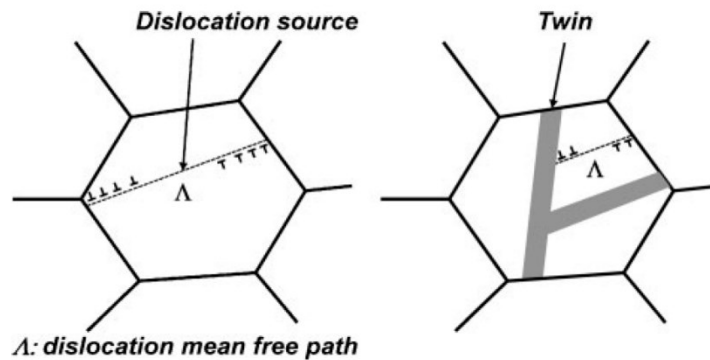


Figure 4.23 Dynamic Hall-Petch effect as strain hardening mechanism in TWIP steels (DMFP-Dislocation Mean Free Path) [22].

Deformation mechanism of TWIP steels is very controversial and despite the recent advances and the acceptance of the model of Dynamic Hall-Petch effect, there is no consensus on the fundamental mechanism of strain hardening. Low SFE is critical for increasing the dislocation density while maintaining relatively long homogeneous slip distances. Exceptional ductility and strength are explained by multistage strain hardening at first, planar dislocation slip is activated as commonly observed in low SFE alloys. With additional strain, wavy slip is promoted leading to dislocation configurations that are progressively refined as the applied stress increases. The nucleation of deformation twins requires the critical dislocation density coupled with relatively long distances available for homogeneous slip. The activation of deformation twinning raises strain hardening of the alloy even further and

therefore increases its ductility. Finally, the secondary twin system can be activated triggering intensive twin intersections that further strain harden the alloy [23]. It has to be noted that despite the key role of twins formation, the dominating deformation mode in TWIP steels is dislocation glide.

It is, therefore, interesting to investigate whether or not electrical current has any effect on this steel grades.

4.3.1. Materials and methods

The materials is a lab scale TWIP stainless steel grade delivered in form of 1 mm thickness sheet. The composition of the investigated experimental alloy is summarized in Table 4.6.

Table 4.6 Range of composition of the investigated alloy (wt.%).

C	Si	Mn	Cr	Mo	Al	Ni	Cu	Fe
0.22	0.39	16.3	13.9	0.079	0.012	0.70	0.41	Bal.

The specimens for the tensile test were obtained along the rolling direction with geometry according to ASTM E8/E8M-16a standard with reduced gauge length to 45 mm due to the sheet dimension.

The side of the specimen that face the infrared thermal camera was painted with a black opaque lacquer in order to uniform the emission of the infrared radiation. Continuous current power supply Powerel S.p.a. was employed for the electrical and thermal tests. In order to separate the joule heating effect from that of the electrical current, thermal tests at the same temperature reached under current regime were performed. Three current densities with the related thermal regime were identified (Table 4.7 and Figure 4.24).

Table 4.7 Temperature reached at different current densities.

Current Density [A/mm ²]	Temperature [K]
5	333±8
10	448±12
15	673±17

Conversely to titanium, austenitic stainless steels possess higher conductivity, therefore the temperature reached with the same current density are slightly lower. It is important to note that since the deformation mechanism of this steels grade is governed by their SFE, it is necessary to limit joule heating since SFE is also temperature dependent. Moreover, it was decided to limit the test temperature to the cold/warm regime ($<0.5 \cdot T_m$ where T_m have to be

expressed in Kelvin) in order to avoid the onset of more complicated dislocation dynamics. Taking all this into account, the maximum current density reached was 15 A/mm².

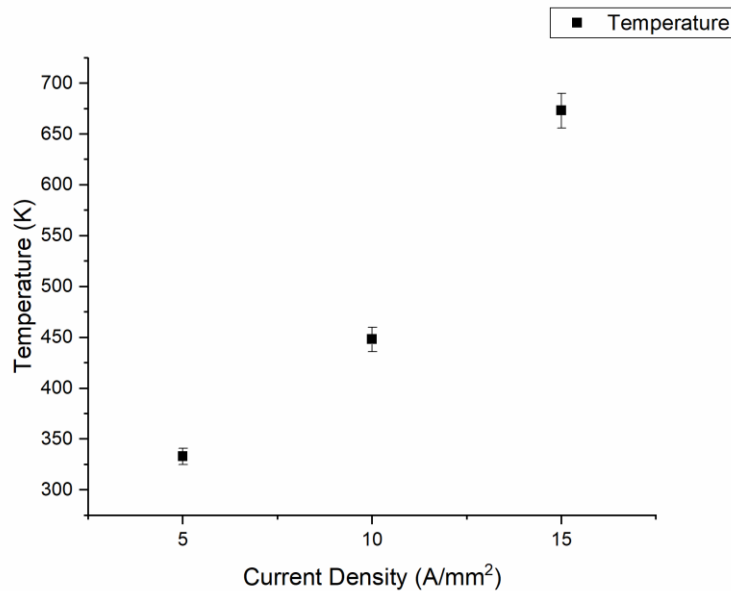


Figure 4.24 Thermal regime with respect current density utilized in the experiments.

Tensile tests were conducted on an MTS 322 tensile test machine modified for electrically assisted tensile tests. Thermal tensile tests have been conducted heating the specimens through electrical current, shutting it off just before the start of the tensile test in order to maintain the same machine setup. Tensile tests were conducted at a strain rate of 10^{-1} s^{-1} in order to avoid any possible transformation induced phenomena that could take place at lower strain rate (TRIP effect). Blow air at 8 bar of pressure was used to cool the specimen and limits joule heating. Three tests for each condition have been performed, the error bars are the standard deviation within the tests.

Characterization of the specimens were conducted through optical microscopy by means Leica DMRE optical microscopy and X-ray diffraction measurements have been performed on a Siemens D500 diffractometer. Etching solution to reveal microstructure was 10% oxalic acid in water by volume.

4.3.2. As received material

The material was delivered in a 1 mm thickness sheet of metal with microstructure showed in Figure 4.25 and Figure 4.26.

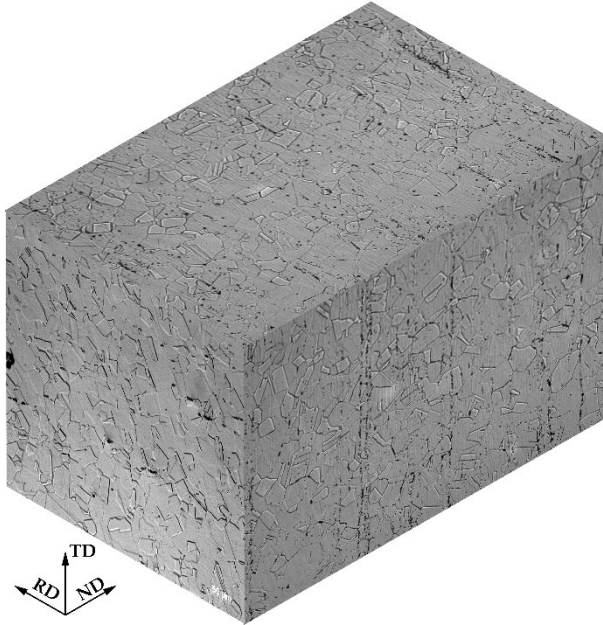


Figure 4.25 3D representation of the microstructure along the three main direction: RD rolling direction, TD transversal direction and ND normal direction.

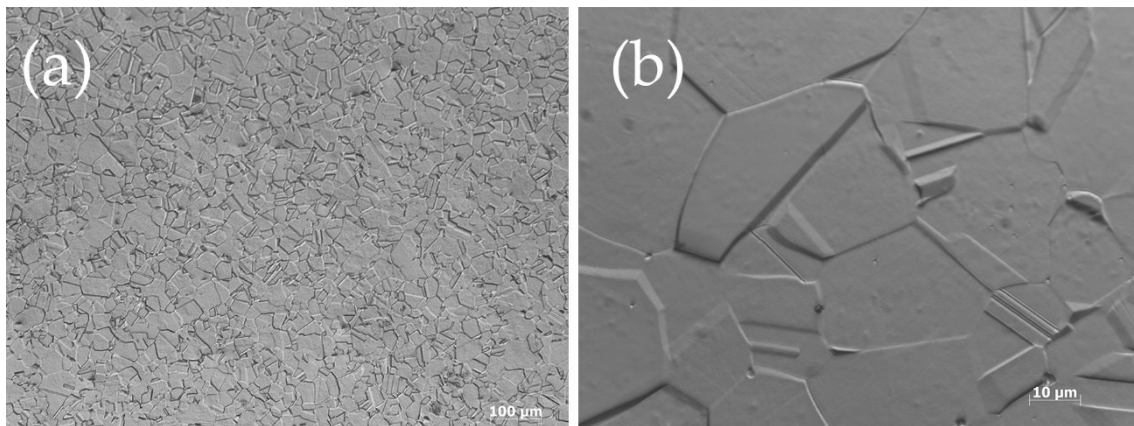


Figure 4.26 Microstructure of the as received materials (a), particular of the annealing twin (b).

The material possesses a homogeneous microstructure with equiaxed grains of mean diameter of $31 \pm 5 \mu\text{m}$ calculated on the three directions (RD, TD and ND). Dark aligned spots can be observed on the TD and RD micrographs of Figure 4.25 aligned towards the relative directions due to the electrochemical attack probably because of a residual texturization after the rolling process. On the micrographs of Figure 4.26b a lot of annealing twins are present since

materials with low SFE tends form this twins during annealing as observed by other researchers [22].

X-ray diffraction measurement on the as received material (Figure 4.27) showed a strong intensity of the $\gamma(311)$ diffraction because of the grain orientation due to the rolling process and the subsequent annealing treatment.

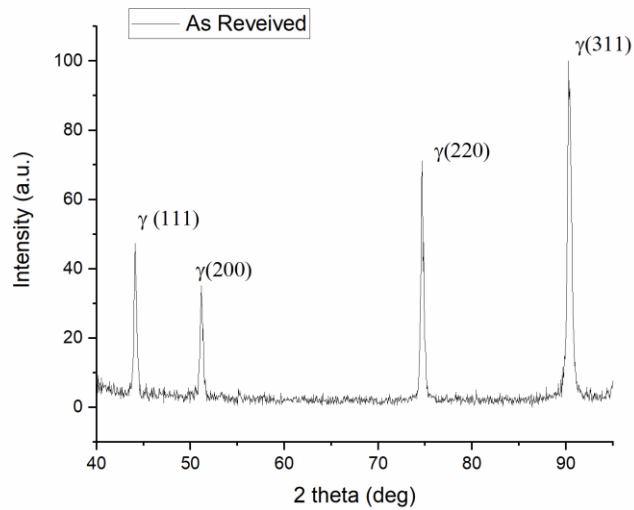


Figure 4.27 X-ray diffraction pattern of the as received material.

4.3.3. Electrically assisted tensile tests

The true stress-strain curves of the tests conducted with continuous electrical current are showed in Figure 4.28.

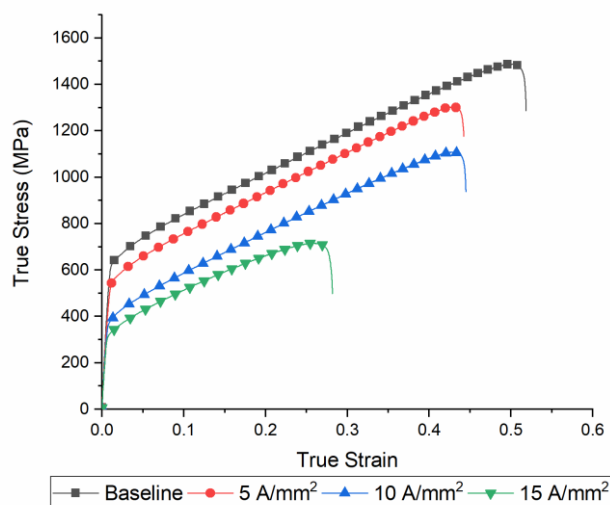


Figure 4.28 True stress-strain curves at room temperature (baseline) and at different current densities.

As displayed in Figure 4.28, as the current density increased UTS and YS decreased. It is worth noting that these steel grades does not show an extended post uniform elongation region due to their ability of strong strain harden. Interestingly, the test conducted at 5 A/mm² and 10 A/mm² show the same fracture strain despite the increase in temperature, probably because the rise in temperature from 333 K to 448 K did not involve substantial changes in the activation of secondary slip systems along with the reduction in the SFE that could lead to different twins volume fraction formation. The test at the highest current density (15 A/mm² and 673 K) showed the lowest UTS, YS and fracture strain as expected. No DSA was observed even though TWIP steels are sensitive to this phenomenon. From literature it has been found that if carbon content is between 0.2 and 0.4 weight percent, neither serration nor DSA are present in FeMnC TWIP steels [19].

Table 4.8 Mechanical properties of the baseline and the electrically assisted tensile tested specimens.

Current Density [A/mm²]	UTS [MPa]	YS [MPa]	Fracture strain [%]
0	1488±5	635±5	0.52±0.01
5	1303±12	548±15	0.44±0.02
10	1109±15	372±12	0.45±0.01
15	716±18	318±11	0.28±0.02

Numerical values of mechanical properties relative to Figure 4.28 are summarized in Table 4.8 Mechanical properties of the baseline and the electrically assisted tensile tested specimens

4.3.4. Thermal tensile tests

As for the titanium case, thermal tensile tests have been conducted in order to separate the contribution of the electrical current from that of the increase in temperature due to joule heating.

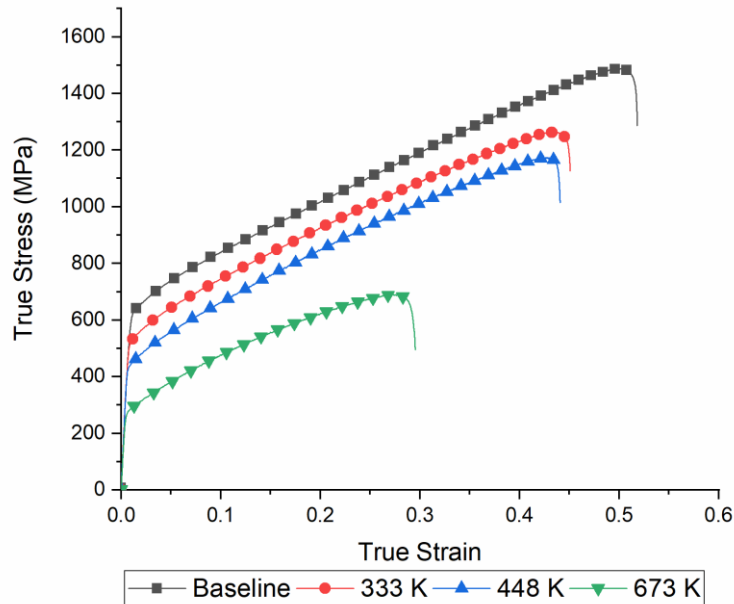


Figure 4.29 True stress-strain curves at room temperature (baseline) and at different thermal regimes.

Same consideration as for the electrically tensile tests can be made for the thermal tests. Increasing the test temperature UTS and YS gradually decreased. The lowest fracture strain was observed for the test at higher temperature, while the other thermal tests showed approximately the same fracture strain (Figure 4.29). Numerical values of the mechanical properties of the thermal tensile tests are summarized in Table 4.9.

Table 4.9 Mechanical properties of the baseline and the thermal tested specimens.

Temperature [K]	UTS [MPa]	YS [MPa]	Fracture strain [%]
293±1	1488±5	635±5	0.52±0.01
333±8	1275±18	526±21	0.46±0.02
448±12	1157±23	435±11	0.44±0.01
673±17	681±15	273±13	0.30±0.02

4.3.5. Comparisons

The comparisons between the tests conducted under electrical current and the related thermal counterparts are depicted in Figure 4.30. Only one flow stress curve per condition have been showed as representative to the tests conducted.

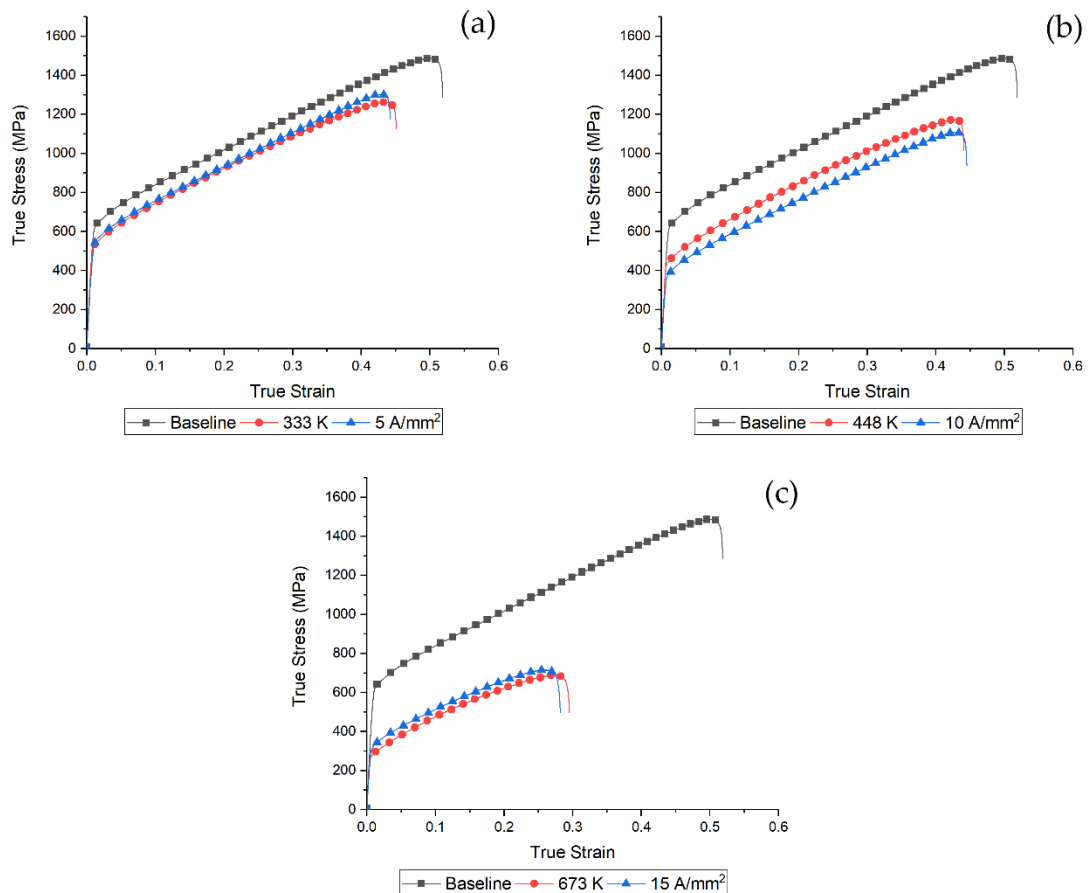


Figure 4.30 Comparison between thermal, electrical and baseline flow stress curves of (a) 5 A/mm² and 333 K, (b) 10 A/mm² and 448 K and (c) 15 A/mm² and 673 K.

Taking into account the considerations made on the previous paragraphs (4.3.3 and 4.3.4), no sensitive difference can be observed between the electrically assisted tensile test and the related thermal tests. For clearness, relative yield stress, relative ultimate tensile strength, relative fracture strain and relative uniform strain have been calculated with equations 4.1, 4.2, 4.3 and equation 4.4 and are displayed in the following figures (Figure 4.31, 4.32, 4.33 and 4.34).

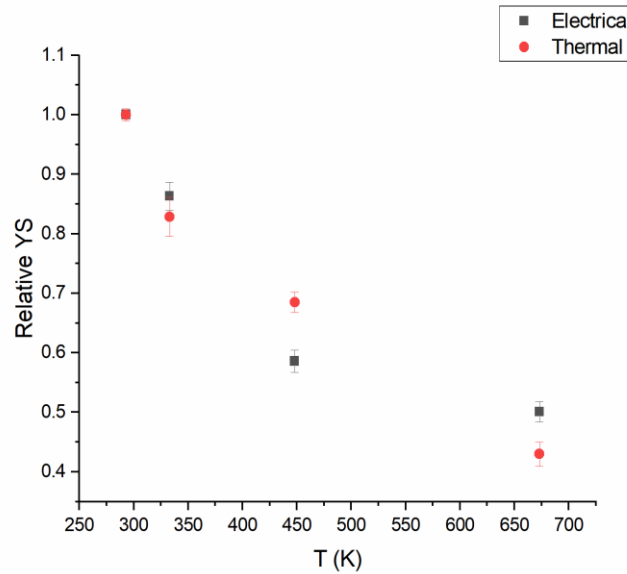


Figure 4.31 Relative YS of the electrical and thermal tests.

Figure 4.31 displays the relative YS of the tested material. As can be seen, the differences between electrical and thermal tests are subtle and probably to refer to the fact that there could be a slight difference in the thermal regime at which the specimens was subjected. Taking all this into account, the trend is the same for both sets of test and no clear differences are evident.

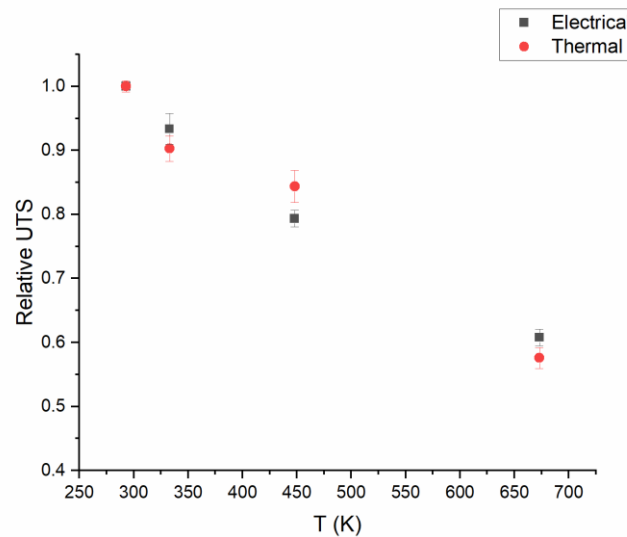


Figure 4.32 Relative UTS of the electrical and thermal tests.

Relative UTS is practically the same both for the electrical current tests and the thermal counterpart as is clearly evident in Figure 4.32.

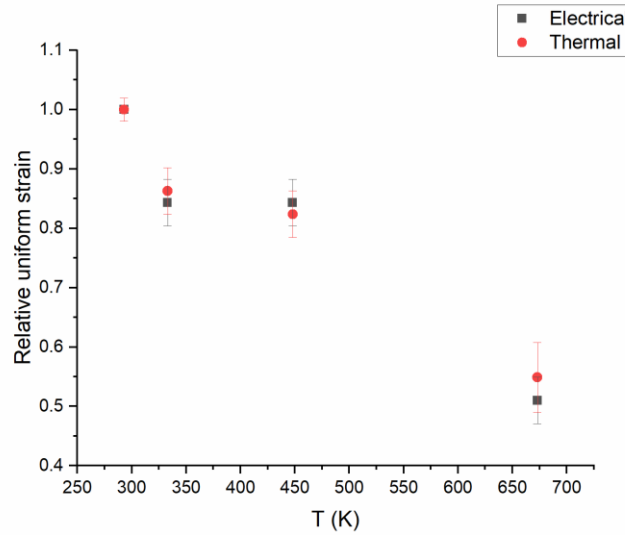


Figure 4.33 Relative uniform strain of the electrical and thermal tests.

Relative uniform strain did not show any difference between electrical and thermal tests.

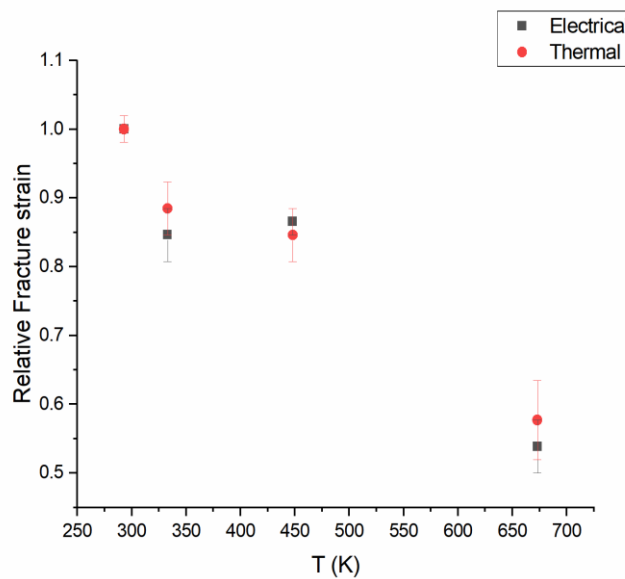


Figure 4.34 Relative fracture strain of the electrical and thermal tests.

Conversely to other metallic alloys, TWIP steels show a very small post uniform elongation, with localized necking not very pronounced. In this frame of reference it is possible to compare fracture strain between thermal and electrical tests since joule heating in correspondence of the fracture surfaces is not very pronounced. Relative fracture strain is the same within the

experimental error for both the electrical tests and the thermal counterparts (Figure 4.34).

To further characterize the tested specimens, strain hardening rate have been calculated and are displayed in Figure 4.35 with respect true strain.

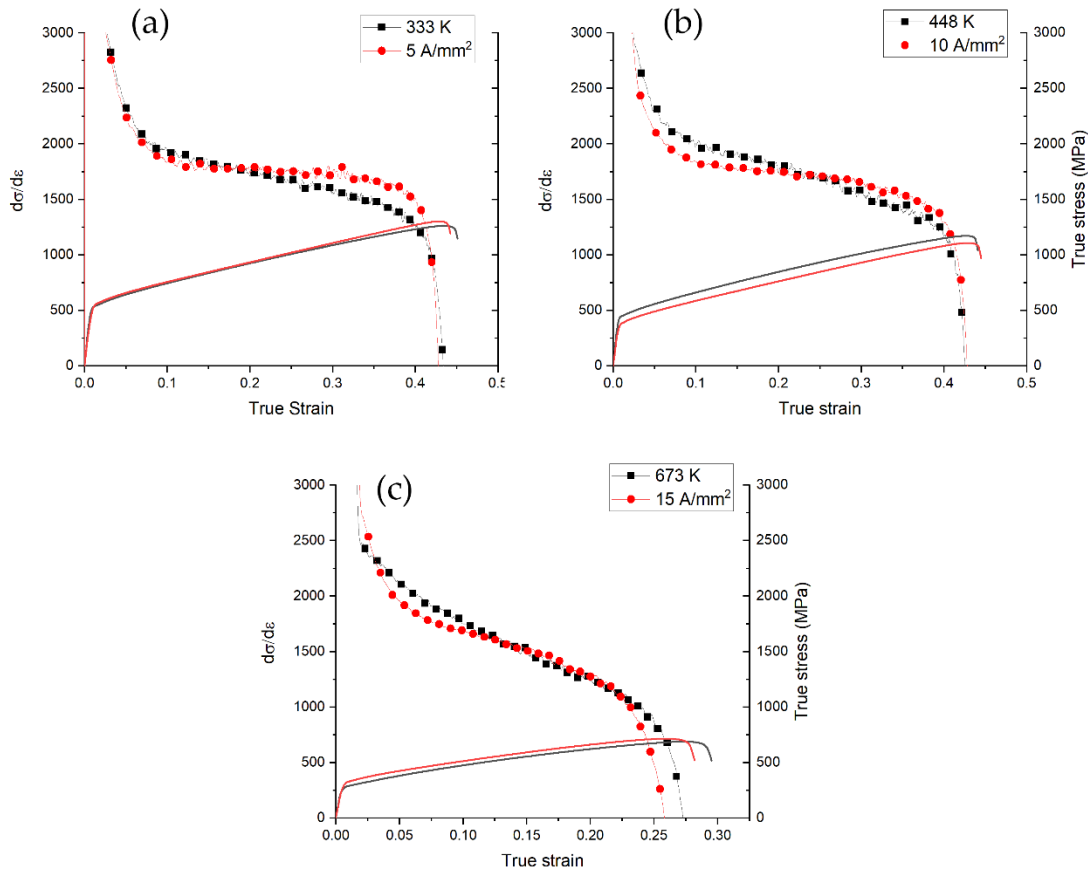


Figure 4.35 Strain hardening rate of the electrical and thermal tests together with the flow stress curves: (a) 5 A/mm² and 333 K, (b) 10 A/mm² and 448 K and (c) 15 A/mm² and 673 K.

As expected from the morphology of the true strain-stress curves of Figure 4.28 and Figure 4.29 and confirmed by the plot in Figure 4.35, no substantial differences can be observed on the strain hardening rate between the electrical tests and the related thermal tests. It can be noted that for the test conducted at lower temperatures and current densities, the strain rate is almost constant throughout the entire duration of the test, slightly decreasing until fracture. On the other hand, at higher temperature and current density, the strain hardening rate keep diminishing since the onset of plastic deformation, denoting higher

dislocation mobility and annihilation rate [24–26] (higher temperature increases SFE and favors dislocation climb easing annihilation of dislocations).

Microstructural investigation have been performed on the fractured specimens after electrolytic etching the polished surface with 10% oxalic acid at 6 V. The micrographs obtained are presented in Figure 4.36.

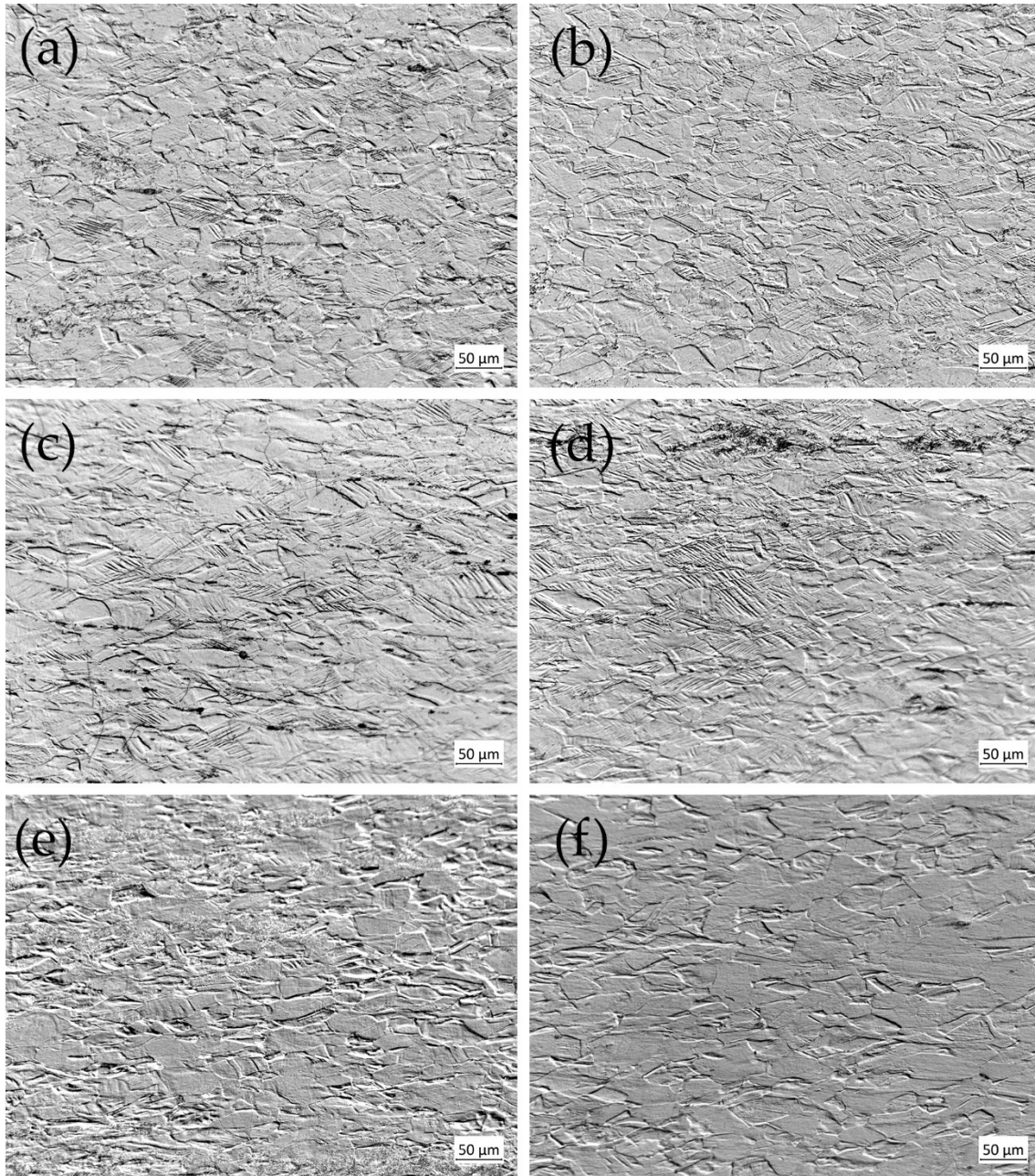


Figure 4.36 Micrographs of the tested samples after fracture: (a) 5 A/mm², (b) 333 K, (c) 10 A/mm², (d) 448 K, (e) 15 A/mm² and (f) 673 K.

Considering the pairs of micrograph relative to the electrical current test and the thermal counterpart, no differences can be observed in terms of volume

fraction of twins or extension of the slip bands within the grains, as expected from the almost identical tensile behaviour. The differences can be seen comparing samples strained at different current density and temperature. As the current density and the temperature increase, fewer grains show the presence of mechanical twins due to the higher SFE which reduces the extension of the stacking fault easing dislocation climb and consequent annihilation probability.

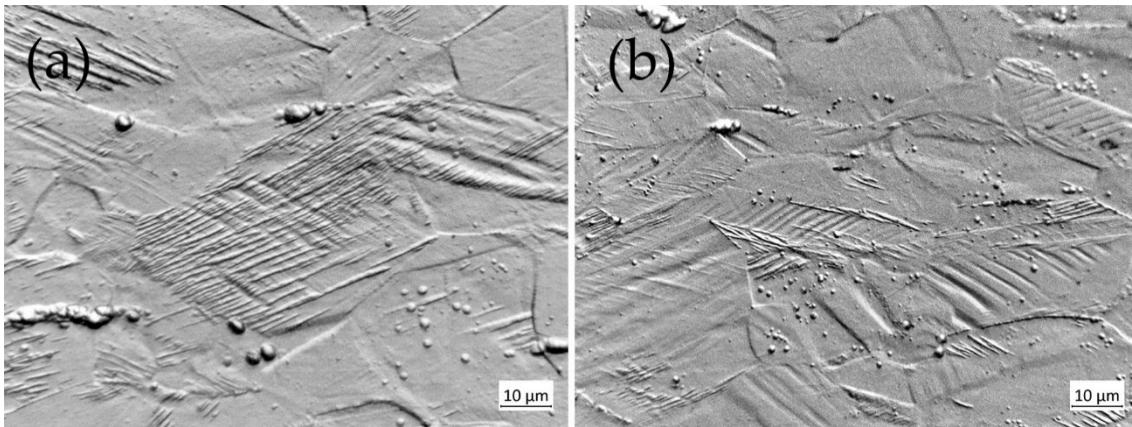


Figure 4.37 Deformation twins and dislocation bands within various grain: (a) 5 A/mm² and (b) 333 K.

Mechanical twins occur only in those grains that are favorable oriented with respect the load direction. Extended mechanical twins that occupy the whole grains can be observed (Figure 4.37) both for the material strained under electrical current and at the corresponding temperature. Sessile dislocations moves within the channel created by consequent stacking fault within the single grain [27] and the twin boundaries act as an impenetrable barrier for dislocations to overcome. Multiple twins system are activated as can be seen from Figure 4.37.

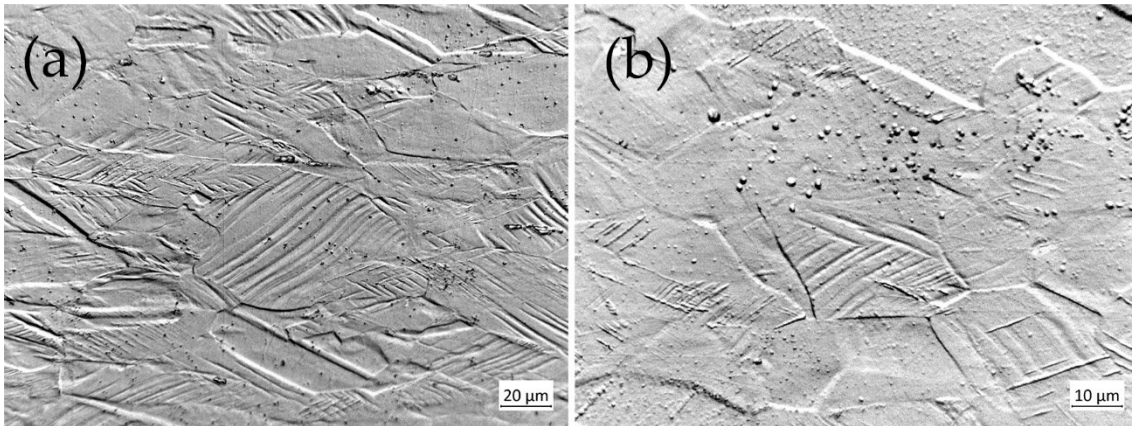


Figure 4.38 Deformation twins and dislocation bands within various grain: (a) 10 A/mm^2 and (b) 448 K.

As the temperature increases twins don't involve the whole grain anymore (Figure 4.38). The extension of the stacking fault that separate two partial dislocations is reduced as well due to the SFE being temperature dependent.

The extension of the mechanical twins for the material strained at higher temperature (673 K) is rather limited (Figure 4.39). Conversely to the lower temperature microstructures, multiple twin systems are difficult to resolve and probably are not activated reducing twins volume fraction hence lowering the strain hardening rate that leads into lower fracture and uniform strain.

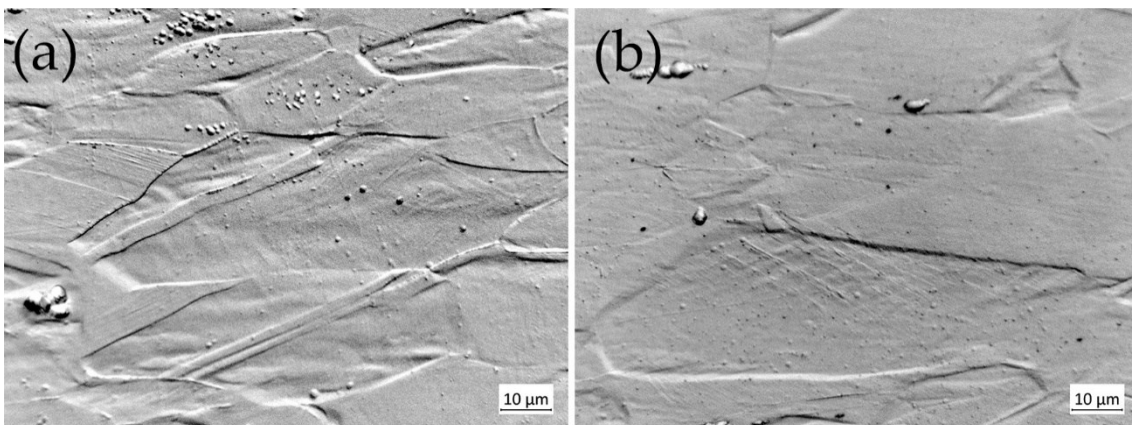


Figure 4.39 Deformation twins and dislocation bands within various grain: (a) 15 A/mm^2 and (b) 673 K.

X-ray diffraction measurements have been performed 5 mm from the fracture surfaces on the specimen strained at room temperature in order to check the possible presence of any TRIP effect.

TRIP effect can be seen through X-ray diffraction measurements because the formation of α' and ϵ -martensite have a different crystal structure (b.c.c. the former and h.c.p. the latter). α' and ϵ -martensite can be seen on an x-ray diffraction pattern of conventional steel at 2θ angle close to the first austenitic peak (Figure 4.40).

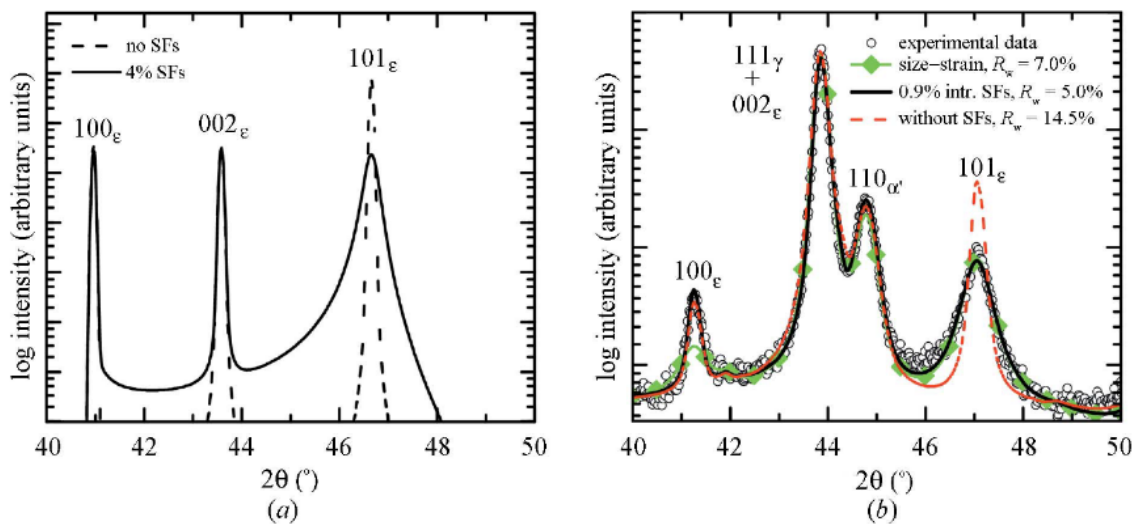


Figure 4.40 (a) A part of the XRD pattern of α' -martensite simulated using MAUD software, which illustrates the influence of 4% SFs on the broadening of the hexagonal XRD lines 100, 002 and 101. (b) Comparison of the experimental XRD pattern (open circles) with the XRD pattern calculated for a mixture of α' -martensite, austenite and ϵ -martensite (red dashed line) [28].

X-ray diffraction pattern of the room temperature tensile test is showed in Figure 4.41. Logarithmic intensity scale was used in order to enhance any possible low intensity peaks due to TRIP effect.

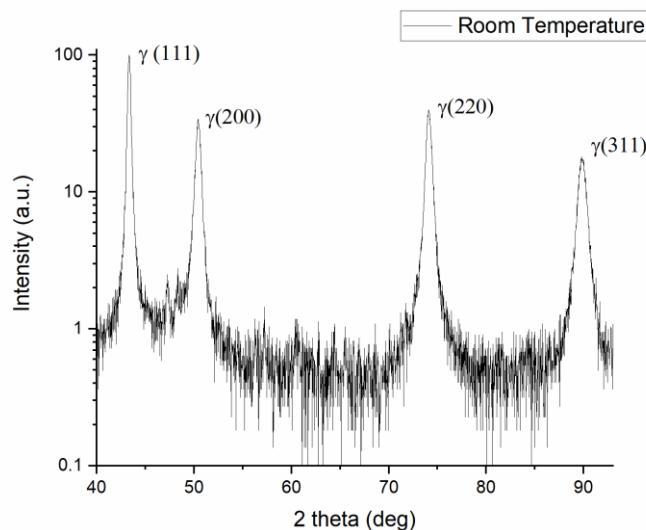


Figure 4.41 X-ray diffraction pattern of the room temperature tensile test.

No signal was detected in correspondence of 2θ angle relative to α' and ε -martensite. The absence of TRIP effect was expected since strain rate of 10^{-1} s^{-1} are high enough in order to hinder the cooling of the specimen during plastic strain, raising the temperature and hindering h.c.p. martensite or b.c.c. martensite precipitation.

4.3.6. *Concluding remarks*

Influence of continuous electrical current on the uniaxial tensile deformation have been investigated on an experimental TWIP steel formulation. Plastic deformation of TWIP steels involves different mechanisms, dislocation glide being the most important while mechanical twinning being responsible for the dynamic Hall-Petch effect, refining the grains as the deformation proceed. Thanks to its very high strain hardening rate, TWIP steels offer a very high uniform elongation which is very interesting in severe forming processes and due to the fact that they can absorb very high amount of energy during deformation (interesting from the automotive industry).

Electrically assisted tensile test showed no difference in terms of yield stress, ultimate tensile strength, uniform and fracture strain in comparison with the thermal counterpart. Strain hardening rate as well was the same for the electrical tensile tests and the thermal tests.

Electroplasticity have been hypothesized to work very well in depinning dislocation from weak obstacles enhancing their mobility hence increasing the probability of annihilation. The barriers that dislocations encounter during deformation in TWIP steels are twinning boundaries which don't pin the dislocations, rather they block their motion increasing the strain hardening coefficient (i.e., twin boundary are considered strong barrier to dislocation motion). Dislocations in TWIP steels are dissociated by wide stacking fault due to their low SFE, hence electrical current up to 15 A/mm^2 is probably not

enough to have any effect on deformation mechanism for TWIP steels. Further investigations with higher current density have to be performed. The only way possible being using pulsed current in order to limits or completely avoiding joule heating (depending on the pulse frequency and duration). Other researchers investigated the effect of continuous and pulsed electrical current on high manganese austenitic steels [29] finding that with current density lower than 30 A/mm² no EPE was observed and the lowering of the flow stress was only due to the increase in temperature. Higher current densities up to 55.4 A/mm² did not improve uniform elongation nor fracture strain but resulted just in the lowering of the ultimate tensile strength, fracture strain and uniform elongation as well. Investigation with higher current density must be performed along with TEM investigation in order to observe possible differences in dislocation dynamic mechanisms.

4.4. Aluminum AA1050 H24

Aluminum possesses an f.c.c. crystal structure with SFE of approximately 200 mJ/m² which is a great candidate to show a positive effect of the electrical current on plastic deformation [30]. Aluminum alloys are very interesting from a technological point of view because of their low density and high specific strength which is very attractive in the automotive and aerospace industries. Thanks to its low electrical resistivity, it is possible to investigate higher continuous current density in comparison to the other alloys previously tested.

From the encouraging results obtained in the preliminary tests it has been decided to investigate deeper the effect of electrical current on aluminum alloy AA1050 H24. This particular aluminum alloy is almost pure aluminum (99.5 wt.% aluminum with small amount of iron, silicon and traces of other elements) strain hardened and partially annealed. Investigation on the electroplastic effect on aluminum AA1050 H24 with respect different stress triaxiality have been made.

4.4.1. Materials and methods

In order to investigate different stress triaxiality, different specimen geometries have been used. Two commercially available *finite element* (FE) models were used to design the geometry and calculate the effective current density with respect the geometry of the specimens. An FE model in Ls-Dyna was used to design the specimen geometries to obtain five stress triaxiality condition: 0.10 for simple shear (chosen according to ASTM B831), 0.35 for smooth specimen, 0.40, 0.48 and 0.55 for notched specimens. Triaxiality was measured by means of the following equation:

$$\frac{\sigma_h}{\sigma_{eqv}} = TF = \frac{1/3 (\sigma_1 + \sigma_2 + \sigma_3)}{\frac{1}{\sqrt{2}} \sqrt{(\sigma_1 - \sigma_2)^2 + (\sigma_2 - \sigma_3)^2 + (\sigma_3 - \sigma_1)^2}} \quad (4.5)$$

which is the rate between the hydrostatic stress with respect the Von Mises stress.

The parameters for modeling the behaviour of the aluminum alloys utilized were determined on the basis of the room temperature test (Table 4.10) and modeled according to Hooke's law and Hollomon's equations 4.6.

$$\sigma = \begin{cases} E\varepsilon & \varepsilon \leq \varepsilon_y \\ \sigma_Y + K(\varepsilon - \varepsilon_y)^n & \varepsilon > \varepsilon_y \end{cases} \quad (4.6)$$

where E is the Young modulus, σ_Y is the yield stress, ε is the true strain, ε_y is the elastic strain and n is the strain hardening coefficient.

Table 4.10 Parameters utilized in the FE models.

E (MPa)	σ_Y (MPa)	K (MPa)	n
70000	124	140	0.0385

Specimen geometry utilized in the tests are showed in Figure 4.42

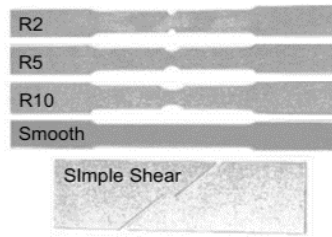


Figure 4.42 Specimen geometries.

Stress triaxiality was almost constant throughout the entire duration of the test, as can be seen from Figure 4.43, so the average was taken into account.

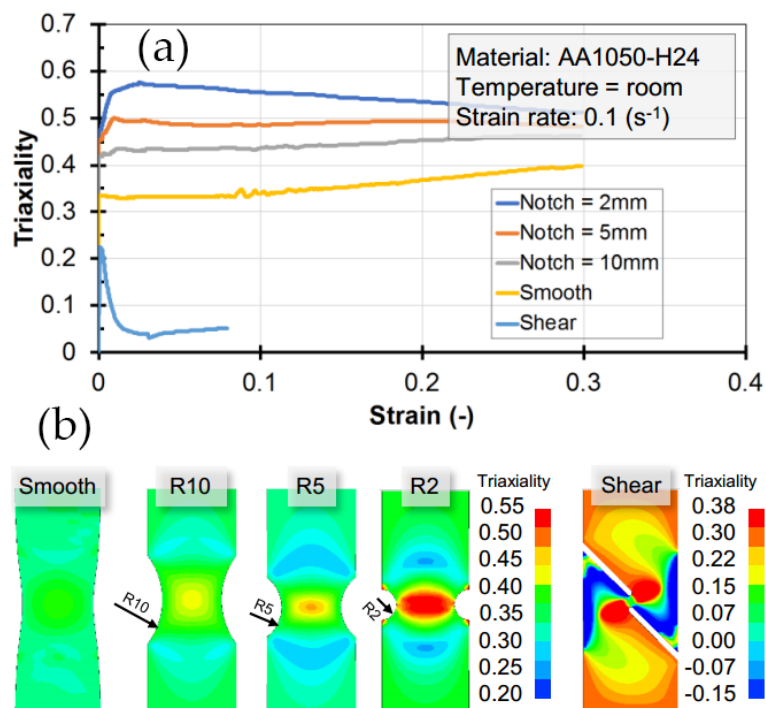


Figure 4.43 (a) Stress triaxiality FE simulation and (b) stress triaxiality as a function of strain and specimen geometries.

By mean of Ansys FE software, a multi physics FE model coupling thermal and electrical fields was utilized in order to identify the electrical current to be used for the notched specimens. In the case of all the notched specimens the current density was constant up to 85% of the width (Figure 4.44).

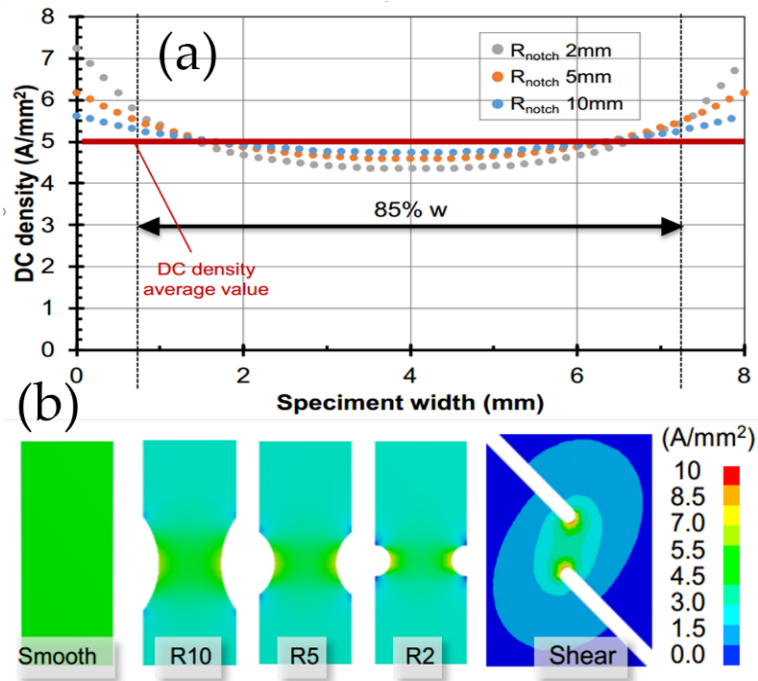


Figure 4.44 (a) Current density variation across specimen width and (b) current density along different specimen geometries.

In Figure 4.44b it is shown the current distribution along the specimen with different geometries obtained from the FE analysis.

Tensile test was carried out on an MTS 322 tensile test machine with a cell load of 50 kN equipped with self-designed copper jaws embedded in PEEK in order to isolate the specimen from the machine frame. Tensile test were conducted with a strain rate of $10^{-1}s^{-1}$ and with current densities ranging from 0 to 45 A/mm² depending on the geometry on specimens obtained along three directions with respect the rolling direction (Table 4.11 Experimental parameters).

Table 4.11 Experimental parameters.

Geometry	Current density [A/mm ²]	Direction
Smooth	0, 5, 10, 15, 20, 25, 30, 35, 40, 45	0, 45 90
2 mm notch	0, 5, 10, 15, 20, 25, 30	0
5 mm notch	0, 5, 10, 15, 20, 25, 30	0
10 mm notch	0, 5, 10, 15, 20, 25, 30	0
Simple shear	0, 5, 10, 15, 20, 25, 30	0

Each sample was painted on one side with an opaque lacquer in order to stabilize its emissivity and on the other side with a random pattern of black and white dot. The temperature of the tests was recorder by mean of a FLIR A40V infrared camera previously calibrated with a K-thermocouple pointed at the opaque side of the specimen. The other side was utilized to measure the strain with the help of a CCD camera connected to GOM Aramis software.

The electrical current was delivered by a Powerel power supply capable of delivering 6000 A at maximum 10 V with an accuracy of 1 A. Cooling was provided by two air nozzle pointed at the gauge length of the specimen during the tensile test connected to an 8 bar air pressure line.

Microstructural investigation were carried out by mean of a Leica DMRE optical microscopy operated in polarized light after polishing the surface to a mirror like finish and electrolytically etching with Barker's reagent. Disks of 3 mm diameter were then cut and electrolytically polished until perforation with a solution of 73% ethanol, 10% butoxyethanol, 9% distilled water and 8% of perchloric acid at 15 V and -10°C. The observations were made on a portion of the specimen gauge length parallel to the loading direction in bright field mode at 160 kV of accelerating voltage on a Jeol JEM 200CX transmission electron microscopy.

X-ray diffraction patterns have been performed by mean of a Bruker D8 diffractometer equipped with $\text{CuK}\alpha$ x-ray emission tube on samples strained to 0.05 at different current densities. Profile analysis on diffraction pattern were conducted using Panalytical HighScore Plus software.

4.4.2. As received material

The material was delivered in 1 mm thickness sheet form with declared composition summarized in Table 4.12.

Table 4.12 Nominal composition of the tested alloy.

Al	Cu	Fe	Mg	Mn	Si	Ti	V	Zn
99.5	0.05	0.4	0.05	0.05	0.25	0.03	0.05	0.05
	max	max	max	max	max	max	max	max

Microstructure of the as received material consisted of big elongated grains along the rolling direction due to the annealing treatment performed after the cold working process (Figure 4.45).

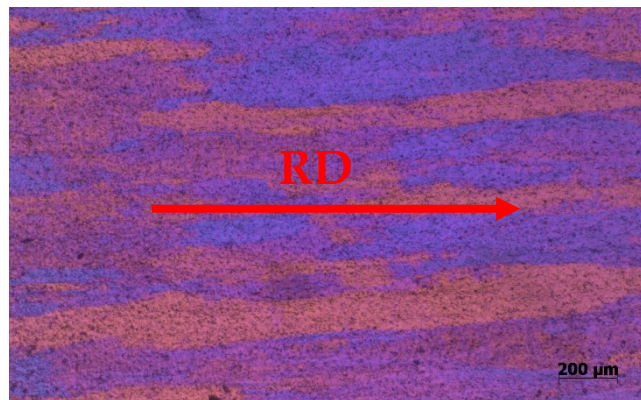


Figure 4.45 Microstructure of the as received material, RD rolling direction.

X-ray diffraction pattern were acquired in order to obtain the full width half maximum (FWHM) of the diffraction peaks as a reference (Figure 4.46)

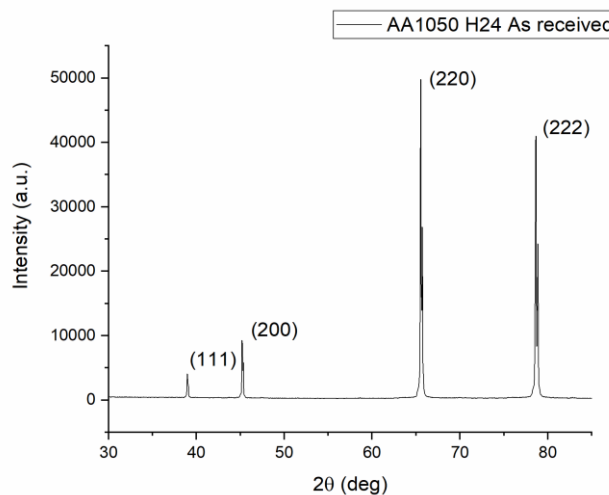


Figure 4.46 X-ray diffraction pattern along rolling direction of the as received material.

Very narrow peaks due to the big grain size can be seen from the diffraction pattern. A strong texture have been observed because rolling process on aluminum tends to orient the crystal structure, which leads to cube texture [31–33].

4.4.3. Thermal regimes

At current density lower than 20 A/mm² no sensitive joule heating was observed thanks to the very high conductivity of pure aluminum, it is in fact used as an electrical current conductor in power lines.

Increasing the current density the temperature did not increase uniformly across the length of the specimen, with a peak in the center of the specimen (Figure 4.47) as observed by other researchers [34]. This behaviour is due to the thermal equilibrium between the specimen and the grippers that act as a heat sink. It becomes more relevant when cooling isn't used and at the highest current densities tested.

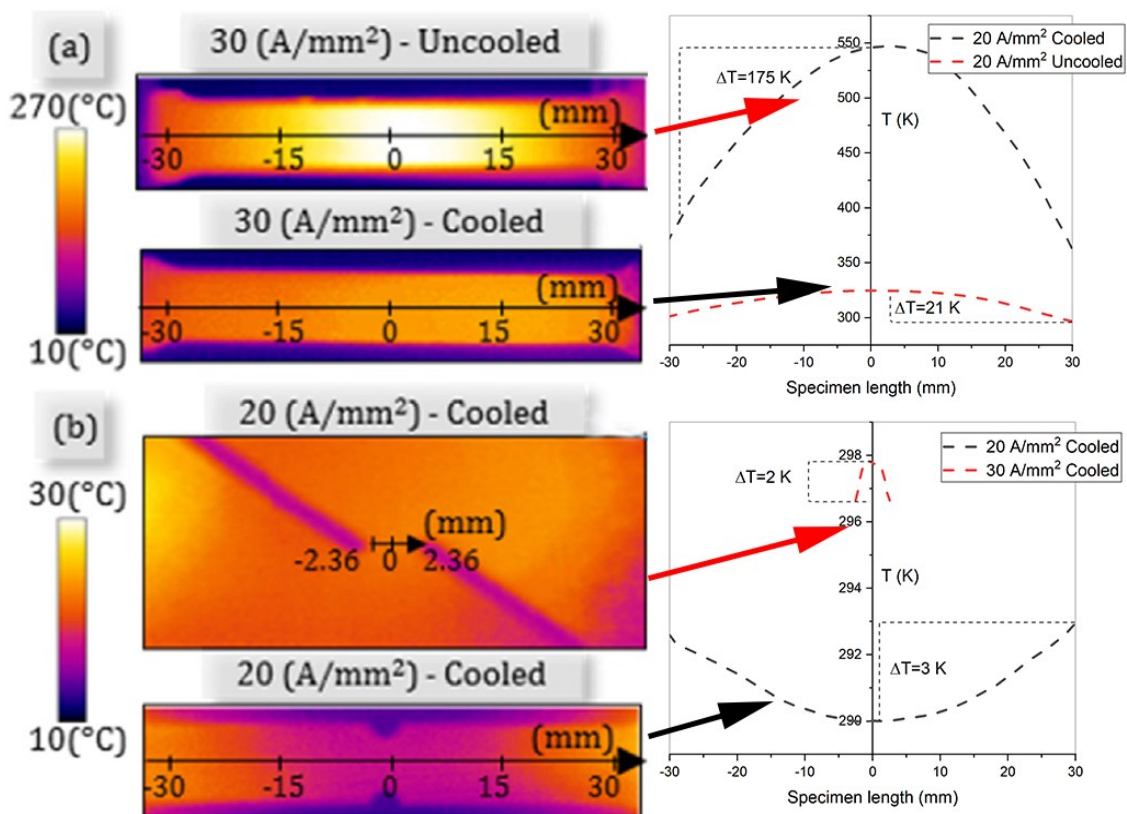


Figure 4.47 Temperature regimes of various specimen geometry under electrical current.

Current densities exceeding 30 A/mm² in uncooled condition caused local melting. On the other hand, under cooling, the temperature was much more uniform, with a peak of 324 K when 30 A/mm² were applied (Figure 4.48).

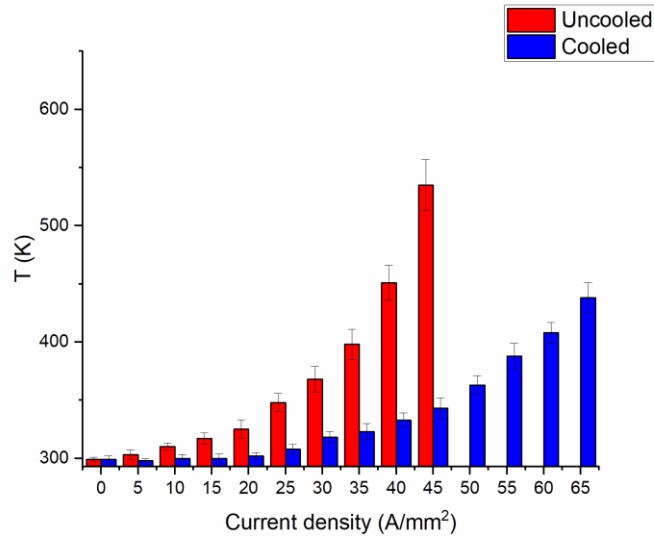


Figure 4.48 Temperature regimes with and without cooling of the smooth samples as a function of current density.

Current density of 30 A/mm² was set as the highest limit since local melting was observed for current exceeding that threshold.

4.4.4. Tensile tests

Tensile tests have been conducted in a wide range of current densities thanks to aluminum very low electrical resistivity and along three main directions with respect rolling direction (0° , 45° and 90°) in order to verify if there is any influence of anisotropy on the onset of EPE.

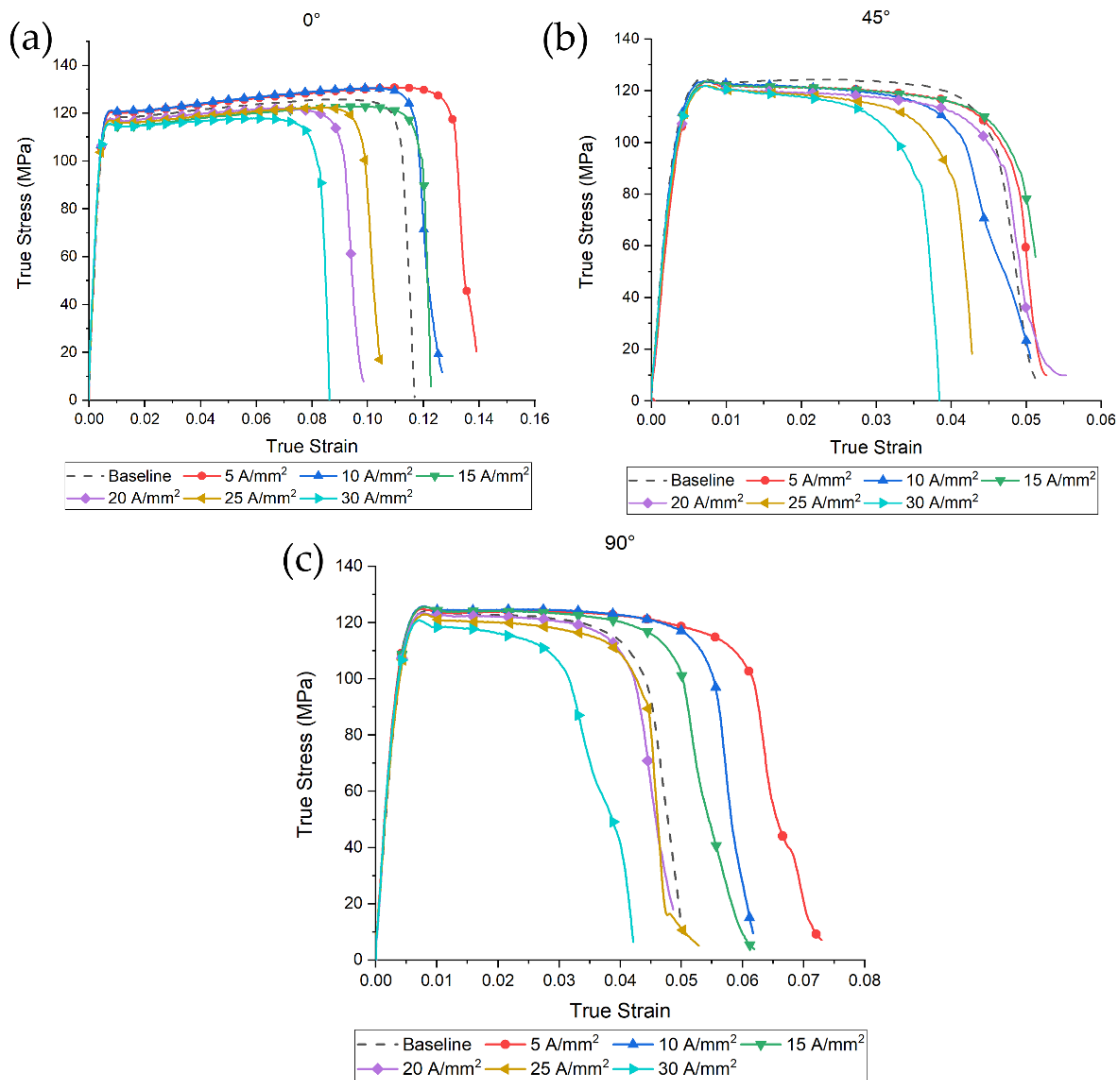


Figure 4.49 True stress-strain curves of AA1050H24 under various current density and along three directions with respect RD.

Focusing on Figure 4.49a it is clear an effect of the electrical current on the fracture strain. The test conducted at 5 A/mm^2 , 10 A/mm^2 and 15 A/mm^2 showed an increase in fracture strain in comparison with the room temperature test (black dashed line). On the other hand, as the current density and temperature increased as observed in Figure 4.48, a gradual decrease of the fracture strain is

evident. The increase in temperature was not high enough to justify the lowering of the fracture strain, hence the lower formability should be addressed only to the electrical current. From the test along the other two directions (Figure 4.49a and b) it can be seen a different morphology of the true stress-strain curve. This is because of the preferential grain orientation due to the rolling process as stated before. In the case of 45° very slight improvement on fracture strain can be observed for current densities of 5 A/mm², 15 A/mm² and 20 A/mm² even though those are within the experimental error. On the other hand, for the specimens at 90° with respect the rolling direction, a substantial increase in formability for the test conducted at 5 A/mm², 10A/mm² and 15 A/mm² is evident.

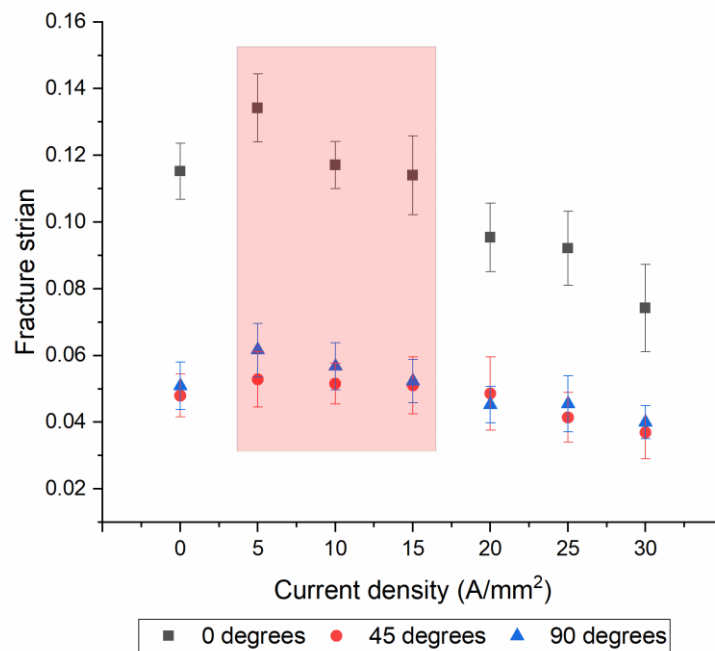


Figure 4.50 Fracture strain with respect current density.

From Figure 4.50 is clear the range of current density at which an increase in fracture strain was observed, while outside this region fracture strain decreased. Relative fracture strain is depicted in Figure 4.51. The dashed line represent the fracture strain of the baseline. It is much more evident that in the range between 5 A/mm² and 20 A/mm² depending on the specimen direction there is an increase in fracture strain only due to the electrical current.

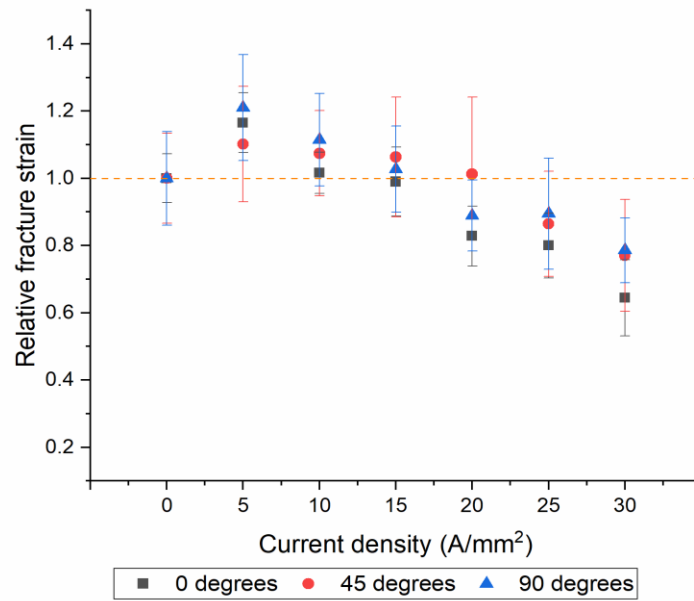


Figure 4.51 Relative fracture strain with respect current density.

To summarize, the smallest electroplastic effect was observed by the specimen oriented 45° from the RD, with only an increase of 10% of the fracture strain from that of the baseline. The samples at 90° from the RD showed the highest increase in formability (21%) compared to the baseline. However the highest absolute fracture strain was observed for the sample obtained along the RD, where the increase in formability for the test at 5 A/mm² was 16%.

The effect of electrical current with respect the triaxiality of the stress is presented in Figure 4.52.

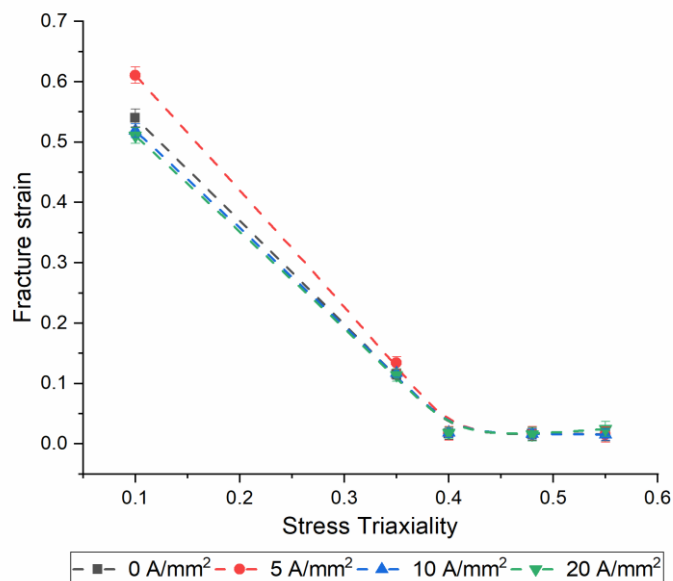


Figure 4.52 Stress triaxiality with respect fracture strain.

It can be seen that for all the current densities tested, the higher the stress triaxiality the lower the material formability. Furthermore, current density of 5 A/mm² is the one at which the electroplastic effect is more evident, regardless of the stress triaxiality. The increase in fracture strain is more significant at lower stress triaxialities, with a maximum influence in the case of simple shear condition.

4.4.5. X-ray diffraction and TEM

X-ray diffraction measurements were conducted on samples obtained along the rolling direction at 5 A/mm², 10 A/mm² and 30 A/mm². The specimens were strained to 0.05 in order to introduce a discrete amount of dislocations and observe how electricity interacts with them measuring the *full width half maximum* (FWHM) of the diffraction peaks. The broadening of the diffraction peaks is due to a lot of phenomena such as stacking faults, microstrain, increase in dislocation density, decrease of the crystallite size and so on. There are some methods that assign a contribution to the broadening of the peaks to each case [35–41], but some assumption have to be made. In this case it has been decided to report only the FWHM that takes into account all the above mentioned phenomena (Figure 4.53).

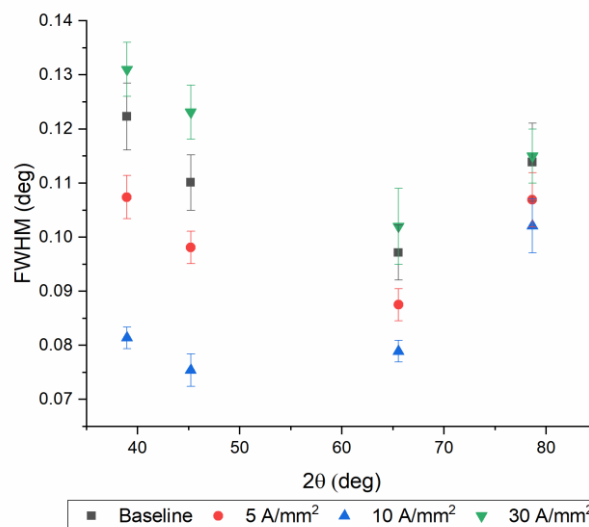


Figure 4.53 FWHM of the diffraction pattern for some samples.

FWHM of the specimens strained with 5 A/mm² and 10 A/mm² is lower compared to the baseline, meaning a lower dislocation density. The specimen strained with 30 A/mm² is the one which showed the lowest fracture strain and the highest FWHM in comparison with the baseline.

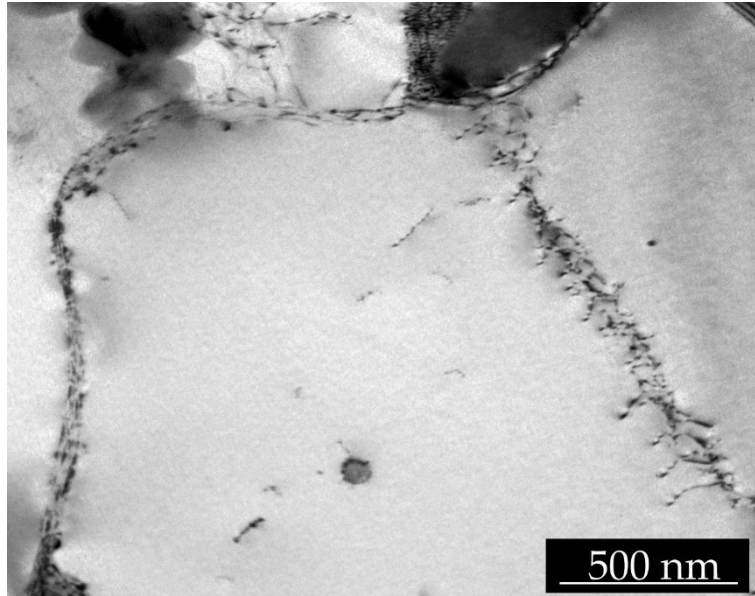


Figure 4.54 Transmission micrograph of 5 A/mm² sample strained at 0.05.

The transmission micrograph of Figure 4.54 shows the dislocation structure of the sample strained at 0.05 at 5 A/mm². It consists mainly of grains divided in sub cells with low dislocation density on the inside, separated by high dislocation density sub cell walls.

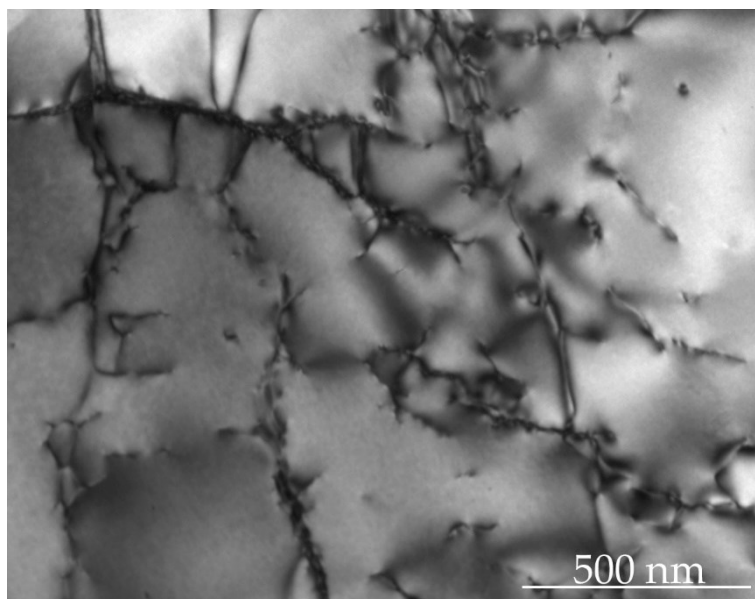


Figure 4.55 Transmission micrograph of 10 A/mm² sample strained at 0.05.

Comparing the micrograph of Figure 4.54 with that of Figure 4.55 it is clear the higher dislocation density of the latter, not to mention the smaller sub cell grain size. Nevertheless, the region within the single cell remains pretty much dislocation free, which could explain the increase in fracture strain due to the ability of the microstructure to generate new dislocations.

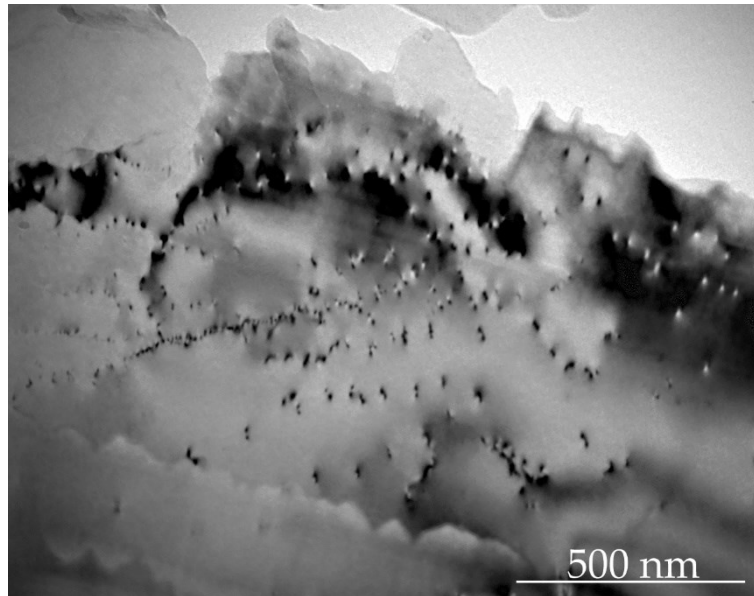


Figure 4.56 Transmission micrograph of 30 A/mm² sample strained at 0.05.

On the other hand, the specimen deformed under 30 A/mm² (Figure 4.56) shows a higher dislocation density, with dislocations present in the middle of the sub cell as well. Straining to 0.05 a specimen that showed fracture strain in the order of 0.08 from a microstructural point of view means that the sub cells are saturated with dislocations that interact with each other entangling themselves together. This will lead to fracture since the microstructure is not anymore able to accommodate more dislocations nor moving the ones that are already present since they form the so called “*dislocation forest*”.

4.4.6. *Concluding remarks*

Electrical current has been shown to influence in various extent the tensile behavior of AA1050 H24 under different stress triaxiality.

Increased fracture strain was observed in a very specific current densities range (up to 15 A/mm²), above which an unavoidable decrease in fracture strain occurred. Stress triaxiality had an effect on the occurrence of EPE as well. It has been more effective on sample tested under simple shear. EPE was also affected by the sample direction with respect RD: specimens orthogonal to RD showed the highest effect of electrical current, while along RD the EPE was the lowest. This effect is to ascribe to the texturization of the microstructure due to the rolling process. X-ray diffraction measurements confirmed that the specimens that showed the highest fracture strain possess the lowest dislocation density at a strain of 0.05. This fact was also confirmed by the transmission electron micrograph performed on the same samples, leading to the conclusion that a direct electron to dislocation interaction must have been taken place.

Electrical current probably acted increasing dislocation mobility, favoring its annihilation hence increasing the ability of the material to tolerate more strain.

4.5. Duplex stainless steels

Duplex stainless steels (DSSs) are a peculiar family of stainless steels characterize by their biphasic microstructure consisting of austenite dispersed in a ferritic matrix. They are widely used in a variety of industrial applications (i.e., pulp and paper industries, chemical and petrochemical industries, nuclear power plants, oil and gas offshore applications etc.), thanks to their high corrosion resistance and high mechanical properties in comparison to austenitic stainless steels [42–44].

Conversely to austenitic stainless steel, their formulation doesn't necessitate huge amount of nickel, so they got some attention in the last few decades due to the price increase of this element. Their composition must be very carefully controlled since the balanced microstructure depends on it. DSSs show the best combination of corrosion and mechanical properties when the volume fraction of austenite and ferrite is almost equal. Compositions of the main DSS grades are summarized in Table 4.13.

Table 4.13 Chemical composition of main DSS grades (wt.%).

Grade	UNS	EN	C	Cr	Ni	Mo	N	Mn	Cu	W
Lean										
2101	S32101	1.4162	0.04	21.0-22.0	1.4-1.7	0.1-0.8	0.20-0.25	4-6	0.1-0.8	-
-	S32202	1.4062	0.03	21.5-24.0	1.0-2.8	0.45	0.18-0.26	2.00		-
2304	S32304	1.4362	0.03	21.5-24.5	3.0-5.5	0.1-0.6	0.05-0.20	2.5	0.1-0.6	-
Standard										
2205	S31803	1.4462	0.03	21.0-23.0	4.5-6.5	2.5-3.5	0.08-0.20	2.00		-
2205	S32205	1.4462	0.03	22.0-23.0	4.5-6.5	3.0-3.5	0.14-0.20	2.00		-
Super										
2507	S32750	1.4410	0.03	24.0-26.0	6.0-8.0	3.0-5.0	0.24-0.32	1.20	0.5	-
-	S32760	1.4501	0.03	24.0-26.0	6.0-8.0	3.0-4.0	0.20-0.30	1.00	0.5-1.0	0.5-1
-	S32906	-	0.03	28.0-30.0	5.8-7.5	1.5-2.6	0.30-0.40	1-1.5	0.8	-
Hyper										
-	S32707	-	0.03	26.0-29.0	5.5-9.5	4.0-5.0	0.30-0.50	1.50	1.0	-
-	S33207	-	0.03	29.0-33.0	6.0-9.0	3.0-5.0	0.40-0.60	1.50	1.0	-

DSSs are also characterized by relatively high values of the *pitting resistance equivalent number* (PRE_N) which is an index that could be used to compare the pitting corrosion resistance of different stainless steels. It is calculated using the following equation:

$$PRE_N = Cr(\text{wt}\%) + 3.3[Mo(\text{wt}\%) + 0.5W(\text{wt}\%)] + kN(\text{wt}\%) \quad (4.7)$$

where k is a constant that is usually set at 16 but it can vary between 10 and 30. Cautions must be used when utilizing PRE_N because it takes into account just the chemical composition and not the actual physical state of the alloy which can suffer from localized pitting if secondary phases are present or if it is subjected to plastic deformation. *Critical pitting temperature* (CPT) is a more useful parameter that can be used to compare corrosion resistance to pitting of stainless steels because it is measured by means of a standardized corrosion test and it is affected by the metallurgical state of the alloy.

The peculiar microstructure is obtained through a solution annealing treatment conducted at a temperature that varies as a function of the chemical composition and at which equal amount of austenite and ferrite are present (Figure 4.57). The microstructure depends on the alloying elements which are divided into γ -forming elements and δ -forming elements depending on the ability to stabilize respectively austenite and ferrite. The contribution of each γ -forming element and δ -forming element is computed by means of the so called Nickel equivalent number in the first case and Chromium equivalent number in the latter. They are calculated with the following equations:

$$Ni_{eq} = Ni(\text{wt}\%) + 30C(\text{wt}\%) + 0.87Mn(\text{wt}\%) + a[N(\text{wt}\%) - 0.045] \quad (4.8)$$

$$Cr_{eq} = Cr(\text{wt}\%) + 1.5Si(\text{wt}\%) + Mo(\text{wt}\%) + 0.5Nb(\text{wt}\%) + 2Ti(\text{wt}\%) + 5V(\text{wt}\%) + 3Al(\text{wt}\%) \quad (4.9)$$

On the basis of chromium and nickel equivalent number, a section of the ternary phase diagram Fe-Cr-Ni with 70% Fe with respect Cr_{eq} and Ni_{eq} and temperature can be built (Figure 4.57).

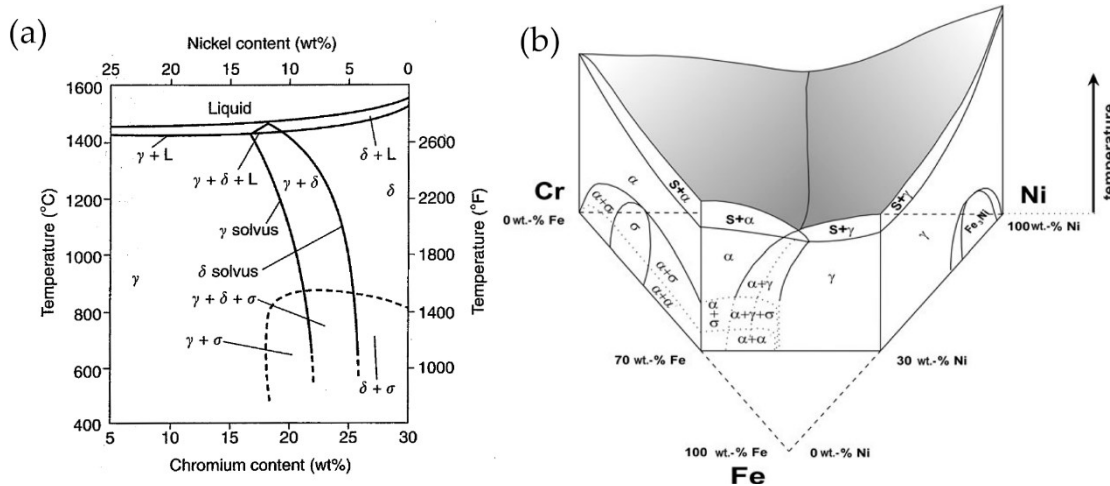


Figure 4.57 Pseudobinary section of Fe-Cr-Ni ternary system at (a) 70% Fe and (b) Quasi-binary section of Fe-Cr-Ni diagram at 70% Fe [45,46].

Upon cooling, DSSs solidify as fully ferritic and austenite starts to form after further cooling from a solid-state-diffusion-based transformation. Observing the phase diagram of Figure 4.57, at equilibrium and room temperature, austenite should not be present at room temperature. The duplex microstructure obtained at higher temperature is thermodynamically unstable at room temperature, but kinetically stable. Because of the thermodynamic instability of the microstructure at room temperature, DSSs suffers from secondary phase precipitation [44,47–50].

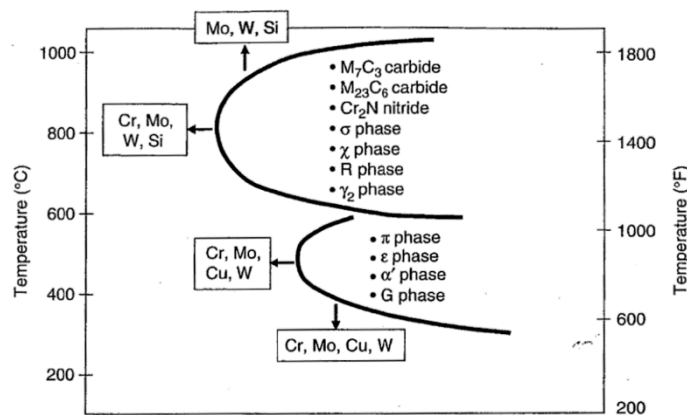


Figure 4.58 Time-Temperature-Precipitation diagram of secondary phases in DSSs with alloying elements [45].

Secondary phases can be subdivided into two categories depending on the temperature at which they form:

- Low temperature secondary phases (300-600 °C). In this range the main concern is the spinodal decomposition of ferrite in high-Cr

ferrite and high-Fe ferrite referred also as “475 °C embrittlement”. In this temperature range G-phase rich in Ni, Mo and Si can precipitate as well.

- High temperature secondary phases (600-1050 °C). Several secondary phases can precipitate in this temperature range. The most common and stable phase is the σ -phase but usually the first phase to precipitate is χ -phase due to its lattice compatibility to that of ferrite. Other phases that can precipitate are nitrides (mainly Cr_2N), carbides (M_{23}C_6 and M_7C_3 chromium carbides), π -phase, ε -phase, secondary austenite and R-phase. They precipitates starting from ferrite thanks to its eutectoidic decomposition.

Secondary phases precipitation kinetic mainly depends on the amount of alloying elements. The precipitation kinetic of lean DSSs is rather slow (in the order of 10 hours) in comparison to few minutes for the high alloyed DSSs (super DSSs or hyper DSSs). It is therefore important to perform a solution annealing heat treatment after the hot forming process step and ensure fast cooling rate in order to limits as much as possible the time within secondary phase precipitation stability range. The crystallographic information of the main secondary phases in DSSs are summarized in Table 4.14.

CHAPTER 4: Continuous and pulsed current

Table 4.14 Duplex stainless steels main secondary phases [48].

Phase	Chemical formula	Temperature [°C]	Space Group	Lattice parameter
α or δ Ferrite	-	-	<i>Im3m</i>	a=0.286-0.288
Austenite (γ)	-	-	<i>Fm3m</i>	a=0.358-0.362
σ	Fe-Cr-Mo	600-1000	<i>P4₂/mmm</i>	a=0.879, c=0.454
χ	Fe ₃₆ Cr ₁₂ Mo ₁₀	700-900	<i>I43m</i>	a=0.892
Chromium Nitride	Cr ₂ N	700-900	<i>P31m</i>	a=0.480, c=0.447
Chromium Nitride	CrN	-	<i>Fm3m</i>	a=0.413-0.447
R	Fe-Cr-Mo	550-650	<i>R3</i>	a=1.090, c=1.934
π	Fe ₇ Mo ₁₃ N ₄	550-600	<i>P4₁32</i>	a=0.647
Carbide	M ₇ C ₃	950-1050	<i>Pnma</i>	a=0.452, b=0.633, c=1.211
Carbide	M ₂₃ C ₆	600-950	<i>Fm3m</i>	a=1.056-1.065

Continuous Current

4.5.1. Materials and methods

Four grades of DSS provided by the Italian division of Outokumpu S.p.A., two lean duplex stainless steel grades (UNS S32101 and UNS S32304), a standard duplex stainless steel (UNS S32205) and a super duplex stainless steel (UNS S32750) have been tested. Their compositions are summarized in Table 4.15. All the materials were supplied in form of warm rolled sheets of 1 mm thickness except the UNS S32101 which was 3 mm thick. The specimens for the tensile tests were prepared according to ASTM E8/E8M 16a.

Table 4.15 Chemical composition of the investigated materials (wt.%).

	C	Si	Mn	Cr	Ni	Mo	N	P	S	Cu	Ti
UNS S32101	0.025	0.65	5.13	21.57	1.56	0.28	0.229	0.019	0.001	0.3	-
UNS S32304	0.03	0.56	1.43	23.17	4.29	0.18	0.13	0.027	0.001	0.16	-
UNS S32205	0.027	0.58	1.52	22.75	5.04	3.19	0.16	0.027	0.001	-	-
UNS S32750	0.014	0.35	0.68	24.99	3.63	6.41	0.253	0.021	0.001	0.06	0.002

Since UNS S32101 suffers from *Strain Induced Martensite* (SIM) formation [51] all tensile tests have been conducted at a strain rate of 10^{-1} s^{-1} to avoid *Transformation Induced Plasticity* (TRIP) effects. Direct current generator produced by Powerel S.r.l was able to deliver a maximum of 6000 A at 10 V. It was coupled with the tensile test machine through a self-made copper jaws embedded in PEEK, to electrically isolate the specimen with respect to the frame of the tensile test machine. The tensile tests were conducted on an MTS 322 tensile test machine modified as depicted in Figure 4.59. Tensile test machine was driven by a dedicated software, strain was evaluated by the crosshead movement while stress was collected by a load cell mounted on top of the MTS 322.

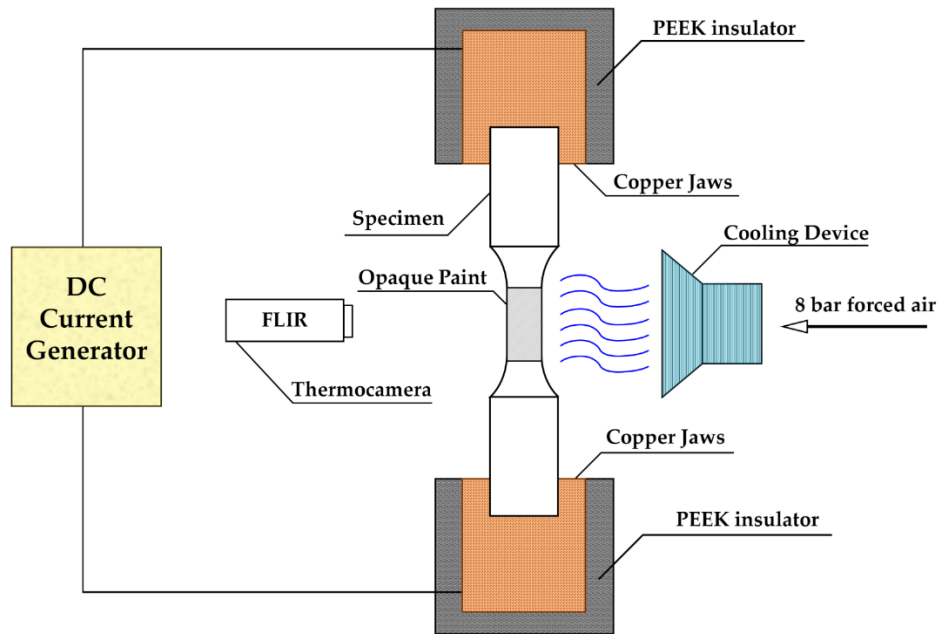


Figure 4.59 Schematic of tensile test machine setup for electroplastic tensile tests.

All steels were tested with three different continuous current densities (5 A/mm², 10 A/mm² and 15 A/mm²), the temperature was recorded for the total duration of the test by means of a FLIR A40 infrared thermal camera. The specimens were coated with a black heat resistant paint in order to stabilize its emissivity. The thermal tests were conducted at the same temperature and strain rate of the electrical ones. In order to reduce joule heating effect, air flow at 8 bar was blown through two nozzles during the electrical tensile tests. Current densities were chosen in order not to overcome 0.5 T_h which is the homologous temperature, defined as the ratio between the test temperature and the melting temperature of the alloy. Temperatures higher than 0.5 T_h can lead to secondary phase precipitation, enhance the diffusion process in the steel and introduce new dislocation dynamics which will be difficult to take into account to decouple the effect of electrical current from the that of temperature. Three tests per test condition have been conducted, the errors are presented as the standard deviation between the data collected for each test.

X-Ray Diffraction (XRD) measurements have been conducted along the rolling direction on the as received material by mean of a Siemens D500 x-ray

diffractometer using $\text{CuK}\alpha$ radiation with 2θ ranging from 30° to 100° (0.05° step and 5 s counting time per step). Rietveld analysis were conducted by mean of Maud[®] software in order to calculate the volume fraction of the different phases.

Microstructure of the as-received samples was analyzed on a Leica DMRE optical microscope after grinding up to 1200 grit SiC paper, mirror polishing with polycrystalline diamond suspension ($6\ \mu\text{m}$ and $1\ \mu\text{m}$) and etching with modified Beraha solution.

4.5.2. As received materials

The as received materials show a microstructure composed of austenite grains oriented along the rolling direction and dispersed in a ferrite matrix (Figure 4.60). The rolling process was conducted in the cold/warm regime as can be seen by the fragmented morphology of the austenite in Figure 4.60, as well as the modestly banded ferrite (Figure 4.60d).

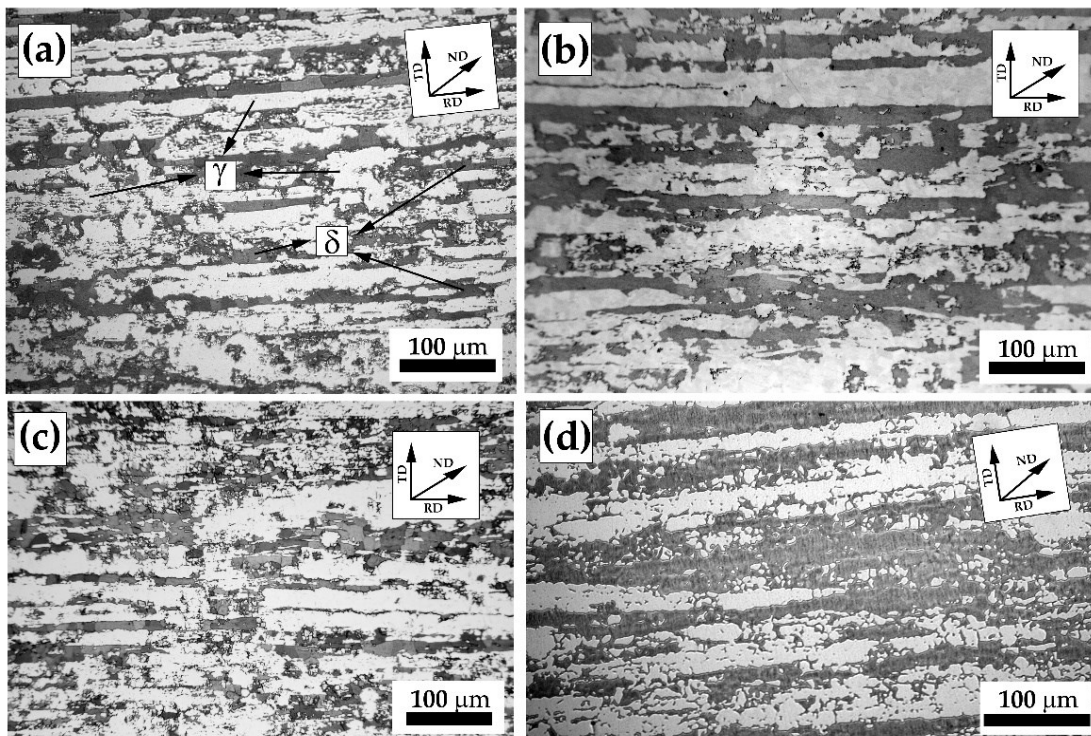


Figure 4.60 Microstructures of the as received materials: (a) UNS S32101, (b) UNS S32205, (c) UNS S32304 and (d) UNS S32750. Etching solution is modified Beraha. RD rolling direction, TD transversal direction, ND normal direction. Austenite and ferrite depicted as γ and δ respectively in micrograph (a).

XRD patterns of the as received materials have been acquired in order to verify the presence of secondary phases and to calculate the volume fraction of the constituents.

In Figure 4.61 are presented the normalized intensity XRD patterns with only the peaks of the two main constituents of DSSs, such as austenite and ferrite, depicted respectively as γ and δ . Firstly, secondary phases' peaks should be visible at lower diffraction angle because of their bigger crystalline cell compare to austenite and ferrite, secondly, since they grow inside the ferrite phase, the intensity of the ferrite peaks should also be reduced if secondary phases are present. It is therefore clear, that the as received materials is secondary phases free. Evidence of the rolling process can be observed in the XRD pattern: the peaks are much more broadened compared to a solution treated sample [51] and the height of the main peaks is different in comparison with a theoretical XRD pattern of austenite and ferrite which translates in a modestly texturized microstructure.

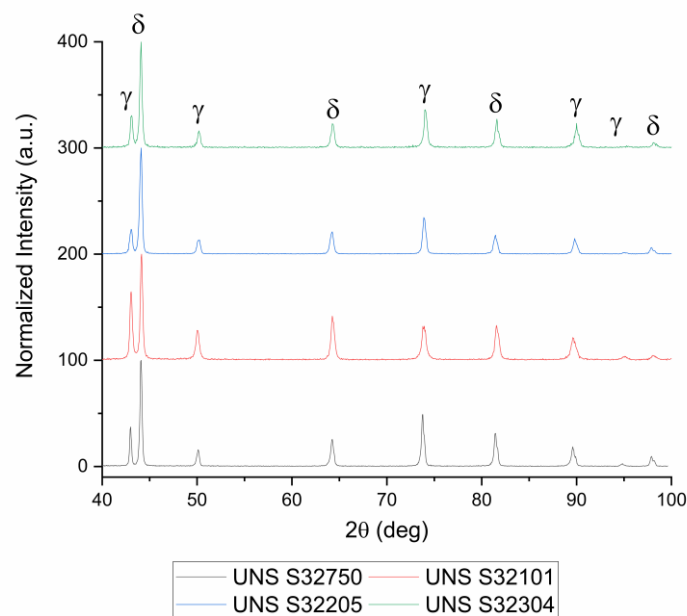


Figure 4.61 X-Ray Diffraction patterns of the investigated material.

Rietveld analysis on XRD patterns have been conducted to calculate the volume fraction of austenite and ferrite, the results are summarized in Table

4.16. The data confirm the results obtained with image analysis performed on optical microscopy micrographs. All the DSSs grades show a very well balanced microstructure with approximately equal volume fraction of austenite and ferrite.

Table 4.16 Austenite and ferrite volume fraction of the different DSS grades.

DSS Grade	Austenite	Ferrite
UNS S32101	0.51±0.02	0.49±0.03
UNS S32205	0.53±0.03	0.47±0.04
UNS S32304	0.51±0.01	0.49±0.02
UNS S32750	0.48±0.04	0.52±0.05

4.5.3. Temperature and current regimes

The increase in temperature during plastic deformation can be calculated with the following equation:

$$\Delta T(\bar{\varepsilon}^p) = \int_0^{\bar{\varepsilon}_{max}^p} \frac{\beta}{\rho C_p} \bar{\sigma}(\bar{\varepsilon}^p) d\bar{\varepsilon}^p \quad (4.2)$$

Where $\bar{\sigma}(\bar{\varepsilon}^p)$ is the evolution of stress during plastic deformation, ρ is the density of the material, C_p is the specific heat at constant pressure and β is the Quinner-Taylor parameter [52] that describes the fraction of energy that is converted into heat during plastic deformation. The Quinner-Taylor parameter can be considered constant even though it can vary during plastic strain. In the case that plastic flow is described using a power law, such as Hollomon formulation or Johnson Cook Model, β can be expressed as:

$$\beta(\bar{\varepsilon}^p) \approx 1 - n \left(\frac{\bar{\varepsilon}^p}{\varepsilon_0} \right)^{n-1} \quad (4.10)$$

Where n is the work hardening exponent of the material and ε_0 is the strain at yielding.

The tests were performed at a strain rate of 10^{-1} s^{-1} , hence heat exchange with the environment due to adiabatic heating is negligible because of the short

duration of the test. Overall, the increase in temperature calculated due to plastic deformation is between 70 °C and 150 °C depending on the fracture strain (Hollomon formulation has been used to describe the material behavior) which is consistent with the infrared camera measurements.

Figure 4.62 shows the thermal images of UNS S32101 before the tensile test (a) and just after fracture (b) under 5 A/mm² current density. The measurements of the temperature have been acquired along a line in the middle of the sample. In order to get a more precise temperature measurement for the lower current density test, the temperature range was limited via software up to 160.3 °C. It can be noted in Figure 4.62b that a peak temperature (white region) out of the measurement range in correspondence of the fracture surfaces is present because of the local plastic instability which decreases the cross section, hence increasing the local current density which translate in a higher joule heating of the region.

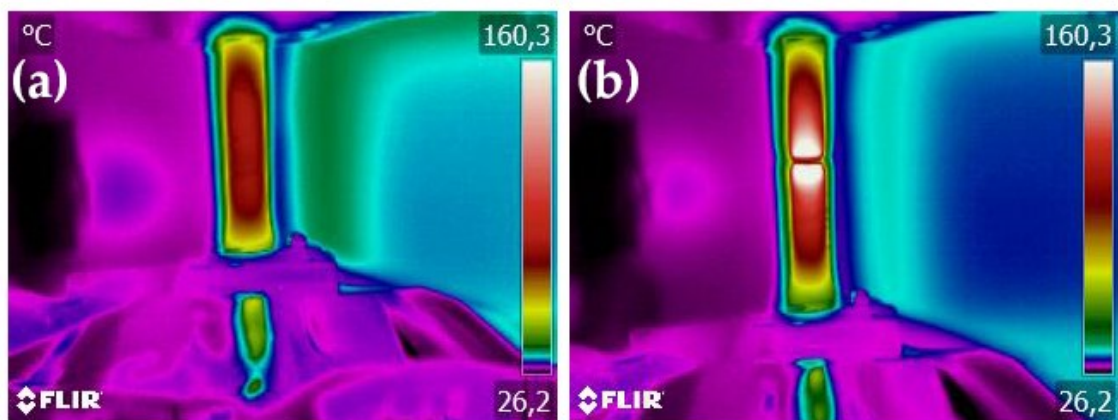


Figure 4.62 Thermal images of UNS S32101: (a) before the tensile test and (b) right after fracture. Tensile test conducted at 5 A/mm².

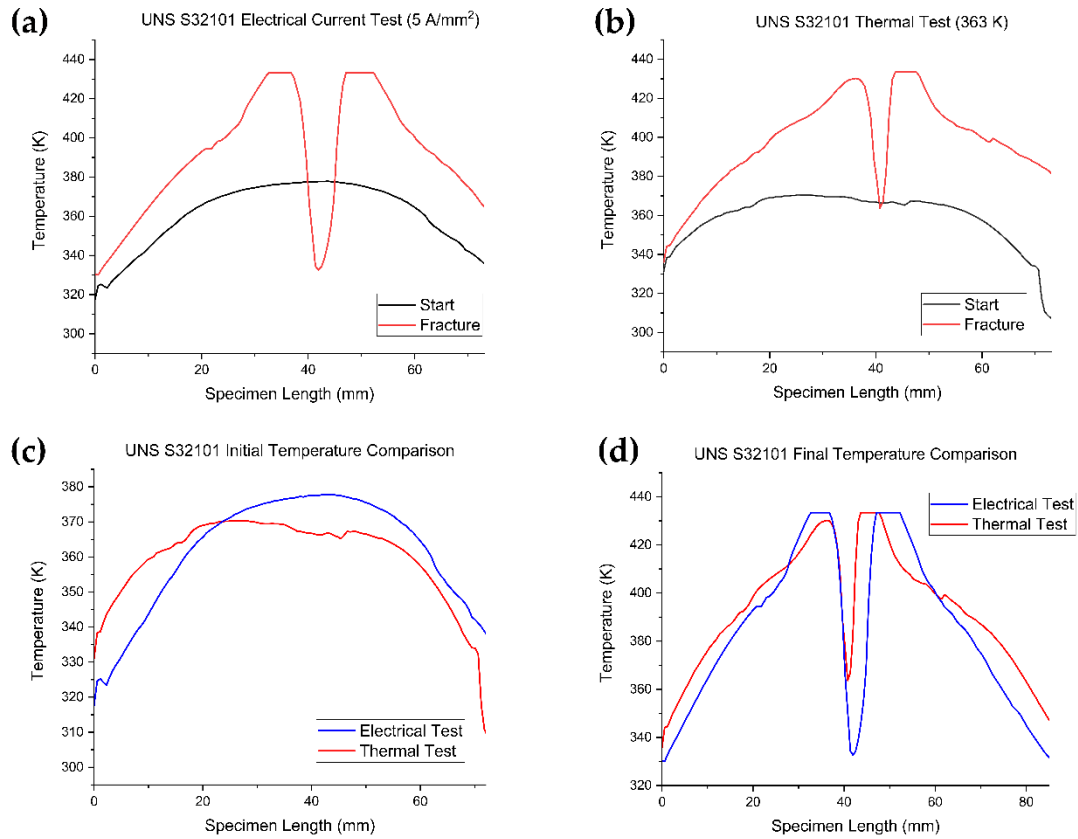


Figure 4.63 Evolution of temperature along the specimen length of UNS S32101: (a) tensile test at 5 A/mm², (b) tensile test at 363 K, (c) comparison between temperature regimes of specimen tested at 5 A/mm² and the corresponding thermal test at 363 K at the beginning of the tensile test and (d) comparison between temperature regimes of specimen tested at 5 A/mm² and the corresponding thermal test at 363 K right after fracture occurred.

Figure 4.63 shows the evolution of the temperature along the gauge length of the test conducted at 5 A/mm² and its thermal counterpart at the beginning of the tensile test and after reaching the fracture, in order to compare the imposed thermal regime with the one caused by the electrical current. It has been reported only the temperature regime of the test conducted at 5 A/mm² and its thermal counterpart for the UNS S32101 as an example since all the DSSs have shown the same trend.

Temperature along the specimen at the beginning of the test is not constant due to the copper jaws that act as a thermal sink. Nevertheless, the temperature regime imposed in the corresponding thermal test (Figure 4.63c and d) is in good agreement with the electrical current test.

As stated before, the higher joule heating of the necked region is much more evident in Figure 4.63d in which are compared the temperature regime of

the current test at 5 A/mm² and the corresponding thermal test. The two peaks in the graph describe the evolution of the temperature of the fracture surfaces: it can be noted that the peaks related to the 5 A/mm² test are clipped because of the software upper limit imposed during the recording of the temperature. For this reason, and because of the increased in current density after localized plastic instability, elongation at fracture is not a reliable parameter to consider in order to analyze the influence of electrical current during plastic deformation, nevertheless, some consideration can be made. Thermal regimes of the other DSS grades are not shown here but the same results have been obtained.

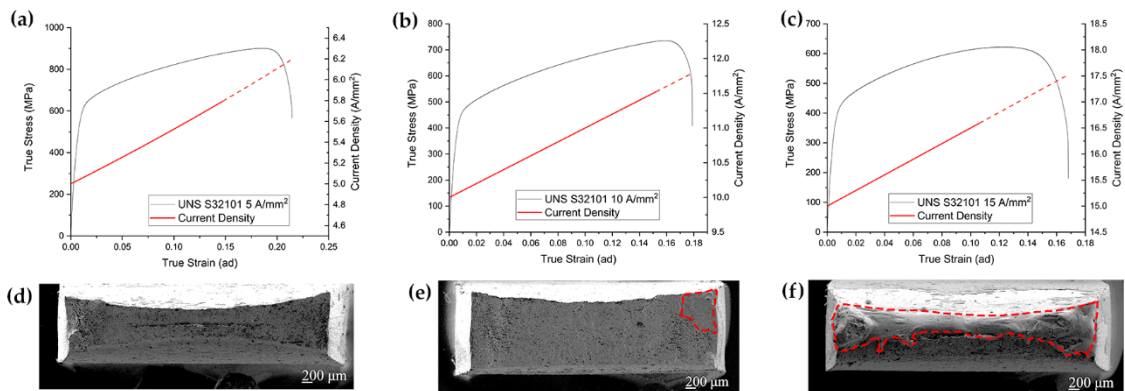


Figure 4.64 Current density evolution during the tensile test superimposed on the flow stress curve of the UNS S32101 and corresponding fractographies: (a, d) 5 A/mm² (b, e) 10 A/mm² (c, f) 15 A/mm².

The evolution of the current density during the tensile test has been calculated considering the diminishing of the cross section imposing the conservation of the volume. The true stress-strain curves at 5 A/mm², 10 A/mm² and 15 A/mm² together with the evolution of the current density during the test for UNS S32101 DSS grade, are showed in Figure 4.64 (a, b, c) as an example. It can be noted that the current density varies during the test from the nominal 5 A/mm² up to approximately 5.8 A/mm², from 10 A/mm² to 11.5 A/mm² and from 15 A/mm² to 16.6 A/mm² in correspondence with the maximum uniform elongation. The change from solid to dashed line denotes the insurgence of plastic instability in which the calculation for the current density evolution does not held because of necking. After uniform elongation, local plastic instability

causes an abrupt increase in current density due to necking, which can cause localized melting of the specimen (area between dashed red line Figure 4.64e and f). Some melted region have been observed in the fracture surfaces for the tests conducted at current densities of 10 A/mm² and 15 A/mm² as can be seen from Figure 4.64e and f.

The mean temperature reached by the different DSS grades subjected to the current densities used in the tests are summarized in Table 4.17.

Table 4.17 Current density, temperature and homologous temperature of the investigated DSSs.

DSS Grade	Current Density [A/mm ²]	Mean Temperature [K]	Homologous Temperature [ad]
UNS S32101	5	363	0.21
	10	603	0.35
	15	783	0.45
UNS S32205	5	333	0.19
	10	428	0.25
	15	623	0.36
UNS S32304	5	338	0.19
	10	448	0.26
	15	683	0.39
UNS S32750	5	338	0.19
	10	453	0.26
	15	713	0.41

It has been decided to limit the maximum temperature of the tested materials up to 0.5 T_h for various reasons: a) higher temperatures lead to different dislocation dynamics which are difficult to take into account and to separate the effect of the electrical current from that of the temperature, b) the influence of electrical current on secondary phase precipitation and spinodal decomposition of DSSs is not clear and no literature has been found regarding, c) at higher current densities the cooling device was not able to efficiently limit joule heating and finally d) higher temperature tensile tests were not possible. For more clarity, graphical transposition of Table 4.17 is shown in Figure 4.65. UNS S32101 stands out as its increase in temperature is definitely higher

compared to the other DSS grades. The composition of the tested DSS grades does not vary significantly enough to affect the specific heat at constant pressure, neither the electrical conductivity, hence the higher temperature reached by the UNS S32101 is because of the higher thickness of the sheet. Same geometry for all specimens has been used, except for the thickness. UNS S32101 has a lower surface to volume ratio since it is three times thicker than the other steels, hence a decrease in the efficiency of the cooling device is observed. Nevertheless, the temperature reached by the UNS S32101 was not high enough to fall into the secondary phases' temperature stability regime. An increase in temperature within the experimental error, with some differences due to the experimental set-up has been observed for the other three DSS grades.

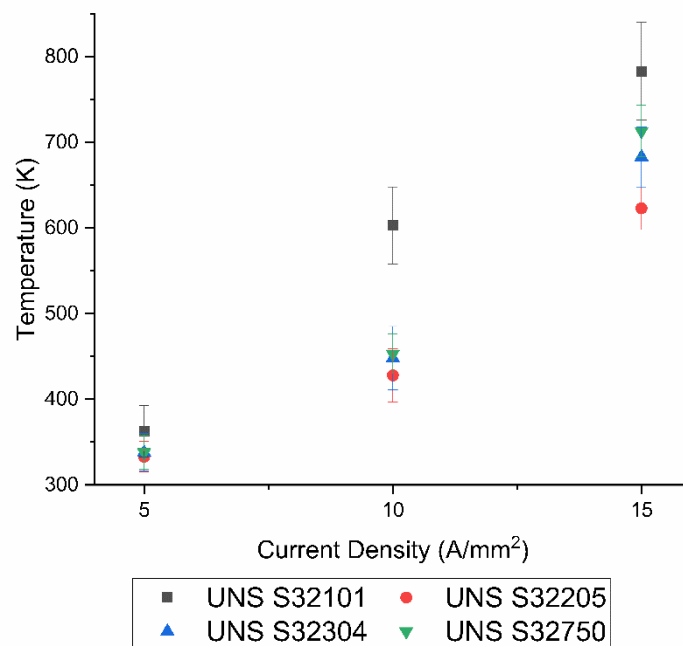


Figure 4.65 Average temperatures reached by DSS grades as a function of the current density.

4.5.4. *Tensile behaviour*

The flow stress curves obtained with the different current densities and the thermal counterparts of all the tested materials are showed in Figure 4.66. The Room Temperature (RT) tensile test is considered as the baseline (black flow stress curves in Figure 4.66). The electrical tests, as well as the thermal counterparts, showed a reduction in the total elongation as the temperature and the current densities increase, except for the UNS S32304 which showed an increase in fracture strain at 5 A/mm² compared to the baseline (Figure 4.66e red curve). Mechanical properties, such as yield stress and Ultimate Tensile Strength (UTS), have the same trend as the fracture strain, decreasing with increasing current density and temperature. A peculiar morphology of the flow stress curves for the tests conducted at 15 A/mm² along with the thermal counterpart can be noted for all the DSS grades, except for the UNS S32101. The segmentation of the flow stress curves is related to a phenomenon known as Dynamic Strain Aging (DSA) [53–55] which is an interaction between solid solution elements and the moving dislocations. UNS S32101, on the other hands, does not show DSA because the test temperature was high enough to facilitate the depinning of the dislocation from the solute atoms and because of the increased diffusion rate. The highest homologous temperature reached by the UNS S32101 is 0.45 (Table 4.17), which is very close to the threshold that separates the cold/warm deformation regime from the hot one. This is why the morphologies of the UNS S32101 higher temperature tests flow stress curves (electrical and thermal) are different from the others.

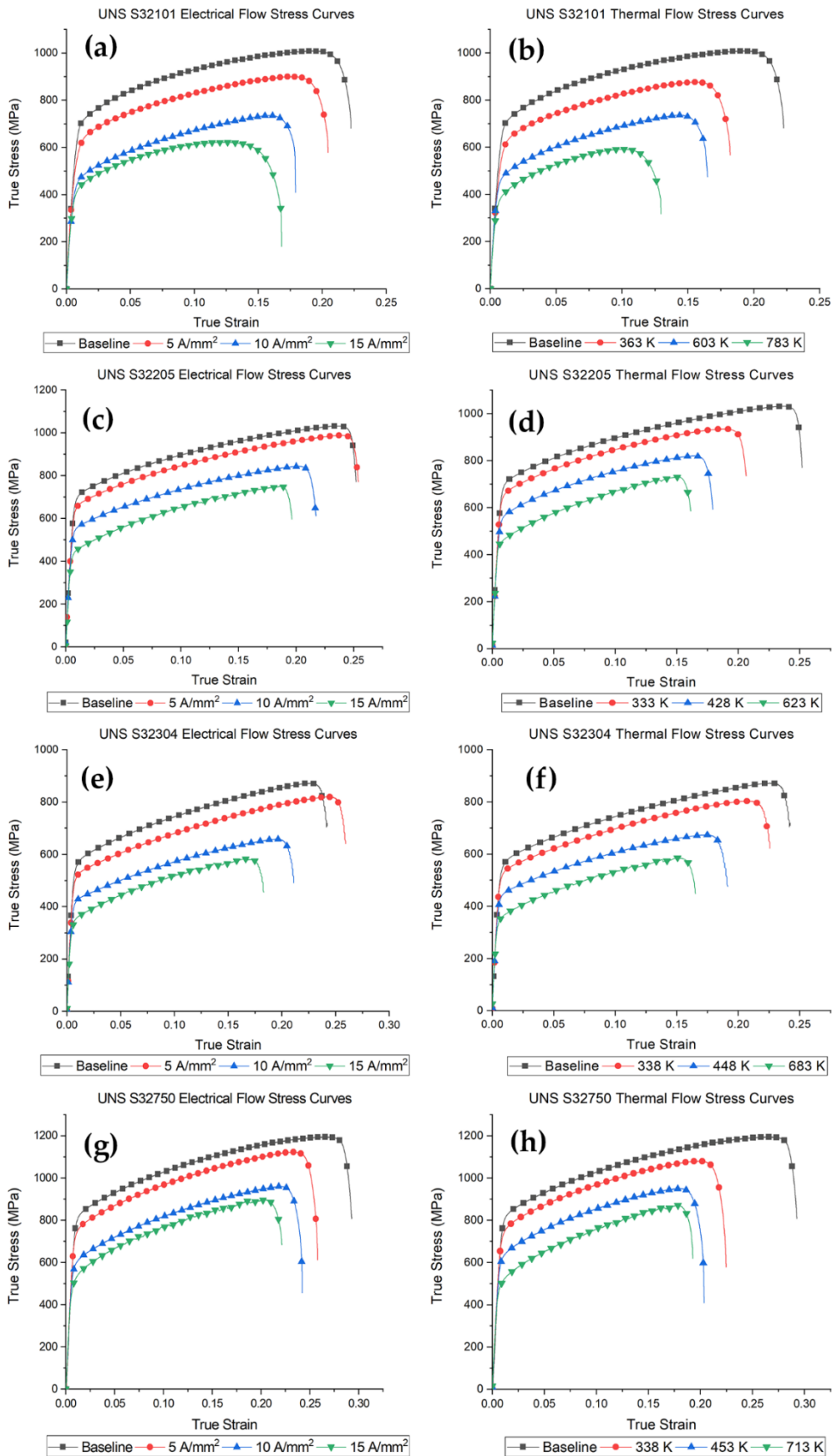


Figure 4.66 Flow stress curves with applied electrical current on the left side and the related thermal counterpart on the right side for the different DSS grades: UNS S32101 (a) and (b), UNS S32205 (c) and (d), UNS S32304 (e) and (f), and UNS S32750 (g) and (h).

To understand the influence of electrical current on these materials, the elongation in correspondence of UTS defined as uniform elongation was used to compare the behavior of the different DSS grades according to [56,57]. As up to this point the absence of necking effects does not lead to any considerable reduction of the sample cross section and so related temperature increases due to higher current density. At the same time, after necking occurrence, the stress distribution is no more uniaxial and the stress triaxiality is not constant.

Figure 4.67 shows the relative uniform elongation calculated with equation 4.4 of the electrical and thermal tensile tests of the DSS grades tested. It can be seen that the uniform elongation of the electrical tests is higher compared to that of the thermal counterparts for all the DSS grades. There is not a significative correlation between relative uniform elongation and test temperature for the different grades, moreover it can be seen an opposite trend for the electrical current test compared to the thermal ones both for UNS S32750 and UNS S32205.

A large uncertainty was calculated in relative uniform elongation for both the thermal and the electrical tests for all DSS grades except for the UNS S32101, because of the difficulty in measuring the uniform elongation in the case of insurgence of DSA phenomenon. Furthermore, it is interesting to note the positive effect of the electrical current on the uniform elongation compared to the thermal counterpart. Electrical tensile test for almost all the materials, except UNS S32304 at 10 A/mm² and 15 A/mm² and again UNS S32101 at 15 A/mm², show a uniform elongation higher than the baseline in contraposition with the thermal counterpart, denoting an effect of the electrical current. There is an evident correlation between the current density and the increase in relative uniform elongation. EPE seems to affect in less extent the uniform elongation of UNS S32101 and UNS S32304 compared to the other grades while the most prominent effect can be seen for the UNS S32750. UNS S32101 and UNS S32304 are known as lean duplex stainless steel because of the low amount of alloying

elements compared to the standard DSS UNS S32205 and the high alloyed DSS UNS S32750. The major effect of the electrical current on the uniform elongation was observed for the UNS S32750, which showed an increase of up to 17.5% compared to the baseline for the test conducted at 10 A/mm². The different behavior of the two lean DSSs compared to the other grades is probably because of the different work hardening rate due to the different alloying elements.

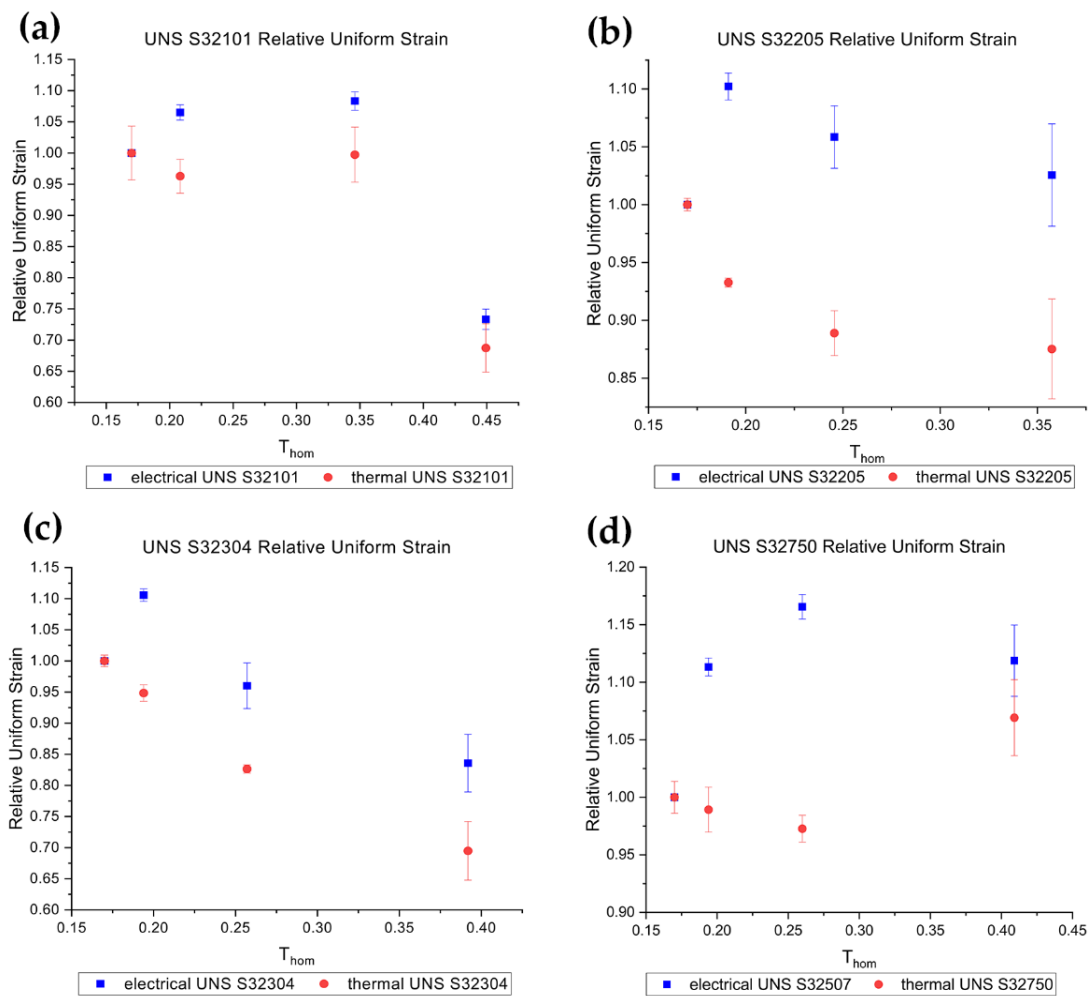


Figure 4.67 Relative uniform elongation of the different DSS grades. Red circles refer to the thermal test while the blue dots to the electrical test.

Figure 4.68 depicts the increase in uniform elongation of the electrical tests compared to the thermal counterparts computed as the difference between the relative uniform elongation of the electrical and the thermal tests. The highest increase in uniform elongation (19.3%) compared to the other DSS have been

observed for the test conducted on UNS S32750 at 10 A/mm². UNS S32205 and UNS S32304 reached almost the same increase in uniform elongation with respect to the current density while a gradual decrease can be observed for the UNS S32101. It has not been observed a particular trend within the tested materials, nevertheless all DSS grades showed an increase in uniform elongation approximately between 5% and 20% in the current density range tested.

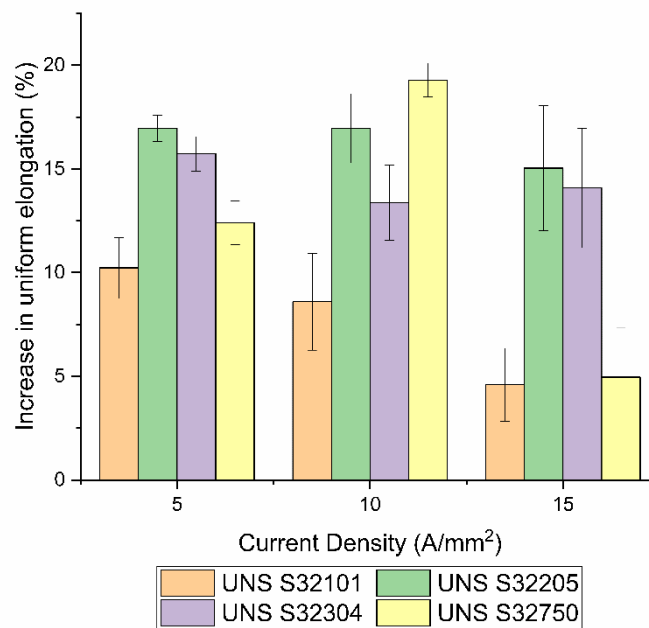


Figure 4.68 Uniform elongation percentage increase of electrical tests compared to the thermal counterpart with respect to current density.

4.5.5. Discussions

As mentioned in Chapter 2 an SFE dependence of electroplastic effect on the total elongation have been observed [30]. High SFE materials show a better formability compared to the low SFE ones.

The microstructure of DSS consists of a high SFE phase (ferrite) in which a low SFE phase (austenite) nucleates and grows lowering the temperature. In DSSs, a positive net effect of electrical current has been observed regardless the presence of a low SFE phase which should decrease the formability. Zhao et al.

[58] conducted some numerical simulation regarding the electrical potential inside a nanocrystalline material, taking into account non-homogeneities such as grain boundaries. They found out that there could be a non-uniform distribution of electrical potential which leads to an uneven distribution of electrical current inside the material. This means that in correspondence of regions of higher electrical resistivity, such as grain and phase boundaries and dislocation cell walls, it can be presumed a higher localized resistive heating. Same hypothesis have been made by Sánchez et al. [59] on an AISI 308L austenitic stainless steel subjected to electroplastic drawing and magnesium alloy AZ31 under uniaxial micro-tension. They observed a lower microhardness for the material subjected to electropulsing heat treatment after drawing in comparison with the conventional ones in the case of the AISI 308L and an increase in fracture strain of the AZ31. They concluded that a microscale hot spots should be present in both materials, reducing the hardness and changing the texture in the first case while arresting microcracks propagation and void initiation in the latter.

Current distribution inside DSS can be affected by the different electrical resistivity of ferrite and austenite due to their different crystal structure and alloying elements. As a matter of fact, ferrite matrix percolates the entire microstructure and has a lower electrical resistivity compared to austenite, hence an uneven distribution of the electrical current can be expected [60]. The different work hardening rate of the two phases has to be taken into account as well; austenite is subjected to higher deformation, hence higher work hardening rate owing to its low SFE compared to ferrite is expected [61]. Since ferrite has a higher yield stress than austenite, most of the plastic deformation initiates in the austenitic grains increasing the dislocation density of that phase which affects the resistivity as well. Inhomogeneities in the microstructure such as dislocations network, secondary phases precipitates, phase and grain boundaries could cause a stagnation of electrons in their proximity, as stated by

Ruszkiewicz et al. and as observed by Zhao et al. [58,62]. The local increase of electrons changes the electron to atom ratio which can lead to a decrease in the bond strength of the material easing the plastic deformation. The uneven distribution of electrical current through the microstructure and inside the grains can also lead to a localized resistive heating favoring the development of texture due to crystal rotation as observed by Rahnama et al. and by Sánchez et al. [59,63] and can also aid the diffusion rate because of an increase in atom flux due to the electrical current [64], a phenomenon known as electromigration. Even though some researchers claim that the athermal effect (i.e. electron wind force) plays an insignificant role in the EPE [65,66], the increase in current density in correspondence of the grain and phase boundaries can increase the effect of the electron wind force aiding the plastic flow of the material, confirmed by the lowering of the electrical resistivity.

The different effect of EPE on the DSSs is probably because of the different work hardening rate due to the different composition, as stated before, and also because of the different grain size distribution of the phase inside the material which can affect the amount of phase and grain boundaries.

To summarize the increase in uniform elongation with respect to the thermal test in duplex stainless steels can be related to the aforementioned phenomena, in particular we suggest that the uneven distribution of the electrical current throughout the microstructure plays a significant role in aiding the plastic flow, regardless of the presence of low SFE austenite which have been shown to reach fracture prematurely when deformed under applied continuous electrical current [30,67].

4.5.6. *Concluding remarks*

Tensile tests with the aid of electrical current and corresponding thermal tests have been conducted on four DSS grades, in order to investigate the influence of electrical current on materials that possess very different SFE phases. Comparisons between the mechanical properties of electrical tests and the thermal counterparts have been performed.

Thermal regimes reached by the DSS grades are within the cold/warm range and are comparable to each other except for the UNS S32101 because of its lower surface to volume ratio due its bigger thickness compare to the other DSSs.

No differences in terms of yield stress and ultimate tensile strength were found between the electrical and the thermal tests. On the other hand, a clear effect of the electrical current on the uniform elongation and on the total elongation has been observed.

All the tested material showed an increase in total uniform elongation compared to the thermal tests and to the room temperature tests (baseline) as well as the elongation at rupture.

Standard DSS UNS S32205 and Super DSS UNS S32750 showed the biggest increase in uniform elongation for the electrical tests compared both to the thermal tests and to the other DSS grades. The highest increase in uniform elongation is of approximately 20% for the UNS S32750 at 10 A/mm², nevertheless, all tested materials showed an increase in uniform elongation between 5% and 20%, the lowest for the UNS S32101 at 15 A/mm² because of its higher thermal regime due to specimen geometry.

Pulsed current

4.5.7. Materials and methods

The material was kindly supplied by the Italian division of Outokumpu S.p.A. in form of 2 mm thick warm rolled sheet. The composition of the investigated steel is reported in Table 4.18.

Table 4.18 Chemical composition of the investigated DSS (wt.%).

	C	Si	Mn	Cr	Ni	Mo	Cu	W	P	S	N
UNS S32750	0,018	0,26	0,84	25,08	6,88	3,82	0,17	-	0,019	0,0010	0,294

Specimens for the tensile tests were obtained along the transversal direction with geometry according to the ASTM E8 standard with length gauge reduced to 45 mm due to the small dimension of the sheet provided. Secondary phases and phase balance quantifications were conducted through X-ray diffraction with a Siemens D500 X-ray diffractometer equipped with copper X-ray tube and monochromator in front of the detector.

Tensile tests were conducted on an MTS 322 capable of 50 kN of force modified to conduct electroplasticity tests as showed in Figure 4.59. To isolate the machine from the current flow, special self-made isolated copper jaws were used.

The gage length of the specimen was painted with opaque heat resistive lacquer to get a uniform emissivity of 0.8 for the temperature reading through a FLIR A40 infrared thermal camera.

Pulsed continuous electrical current was provided by a Powerel generator capable of delivering 6000 A at 10 V. Temperature was recorded to perform the thermal test at the same temperature reached by the electrical current tests, to separate the contribution of joule heating from that of the electrical current. Pulsed tensile tests were conducted with a pulse duration of 2 ms and a frequency of 2 Hz at 50 A/mm², 100 A/mm², 150 A/mm², 200 A/mm² and

250 A/mm² at a strain rate of 10⁻² s⁻¹. For each condition three tests have been conducted to verify the repeatability.

Standard polishing procedure has been conducted with decreasing sandpaper grit from 500 to 1200 and final polish on rotating clothes with polycrystalline diamond suspension of 6 μm, 1 μm and finally with silica colloidal suspension of 200 nm.

Microstructure observation has been conducted on a LEICA DMRE optical microscope and a Leica Cambridge Stereoscan 440 scanning electron microscope operating at 29 kV in backscattered electron mode and at 15 kV in secondary electron mode.

4.5.8. *As received material*

The as received material shows a very well-balanced microstructure secondary phases free according to X-ray diffraction pattern with just the peaks of δ-ferrite and γ-austenite and to SEM-BSE investigations.

Phase balance was evaluated through Rietveld analysis on the X-ray diffraction pattern (Figure 4.69) which resulted in almost equal volume fraction of austenite and ferrite (0.48±0.04 and 0.52±0.05 respectively).

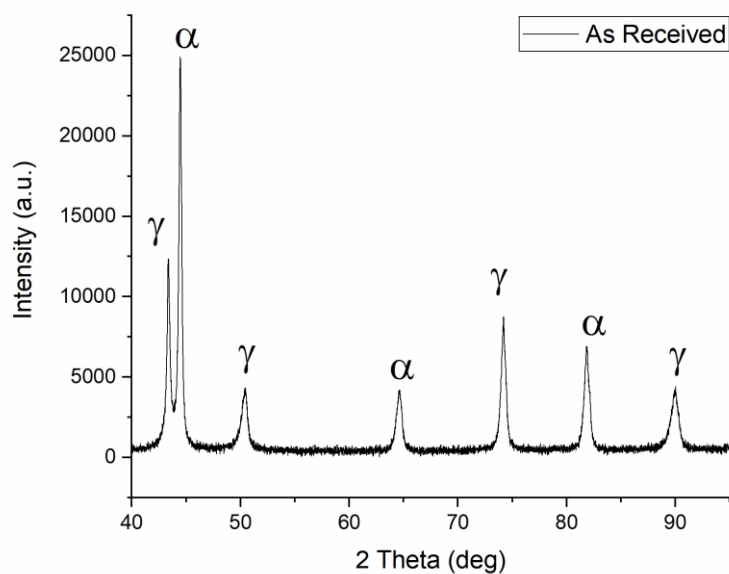


Figure 4.69 X-ray diffraction pattern of the as received material along rolling direction.

The as received material shows a microstructure consisting of fragmented austenite islands (bright grains) dispersed in a ferritic matrix (dark grains) as can be seen in Figure 4.70a. Rolling direction is highlighted by the black arrow. Austenite morphology is quite fragmented due to the last warm pass of the rolling process. Microstructure along the other dimension (transversal and normal) is shown in Figure 4.70b. The interphase space (space between austenite and ferrite) is smaller along the normal direction in comparison to that along the rolling direction.

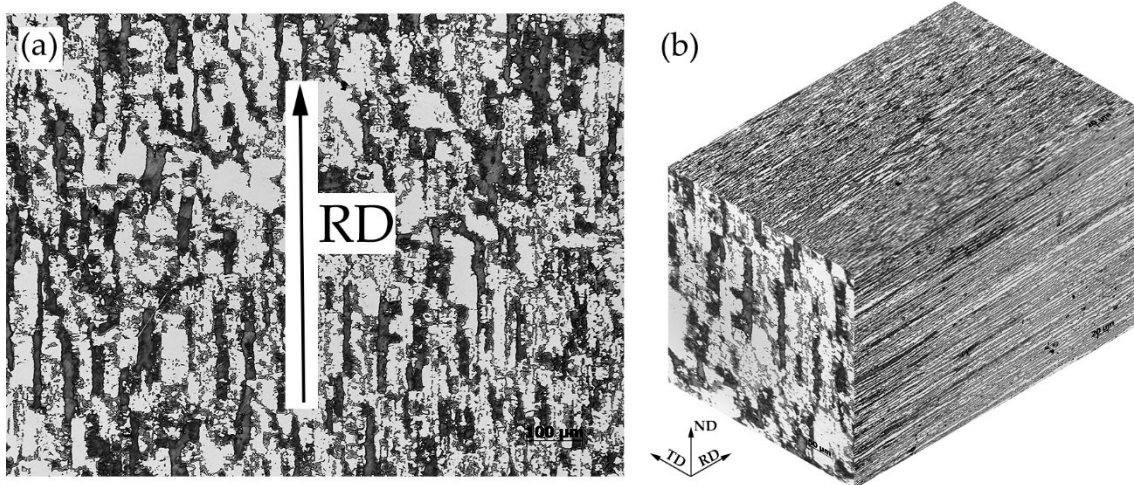


Figure 4.70 Microstructure of the as received materials: (a) along the rolling direction (RD) and (b) along the main three directions (b). Etching solution NaOH at 3 V and 5 s.

4.5.9. Thermal regimes

The parameters for the electrical current (i.e., pulse duration and frequency) were decided in order to reach the same temperature regime of the continuous current case (Figure 4.71) when utilizing the maximum electrical current the generator was able to deliver (6000 A). Due to the low pulse duration (2 ms) it was possible to achieve higher current densities maintaining the same maximum temperature in comparison to the continuous current case. The maximum current density was more than 15 times higher than the continuous current case.

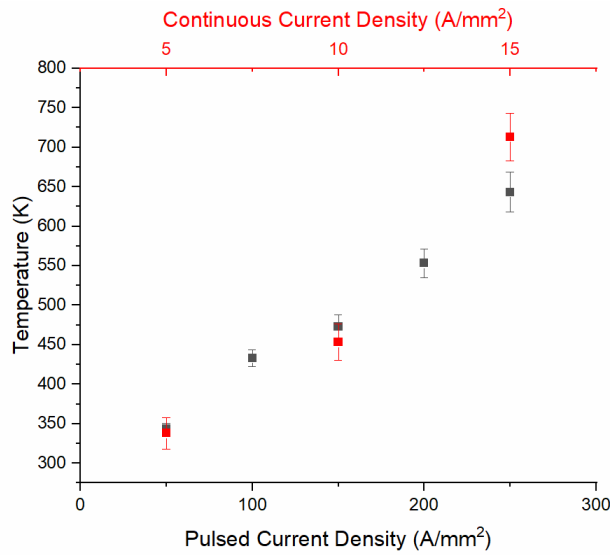


Figure 4.71 Temperature regime under pulsed electrical current (black dots) and under continuous electrical current (red dots).

As for the continuous current case, increase in temperature in correspondence of the fracture surfaces was observed as can be seen in Figure 4.72.

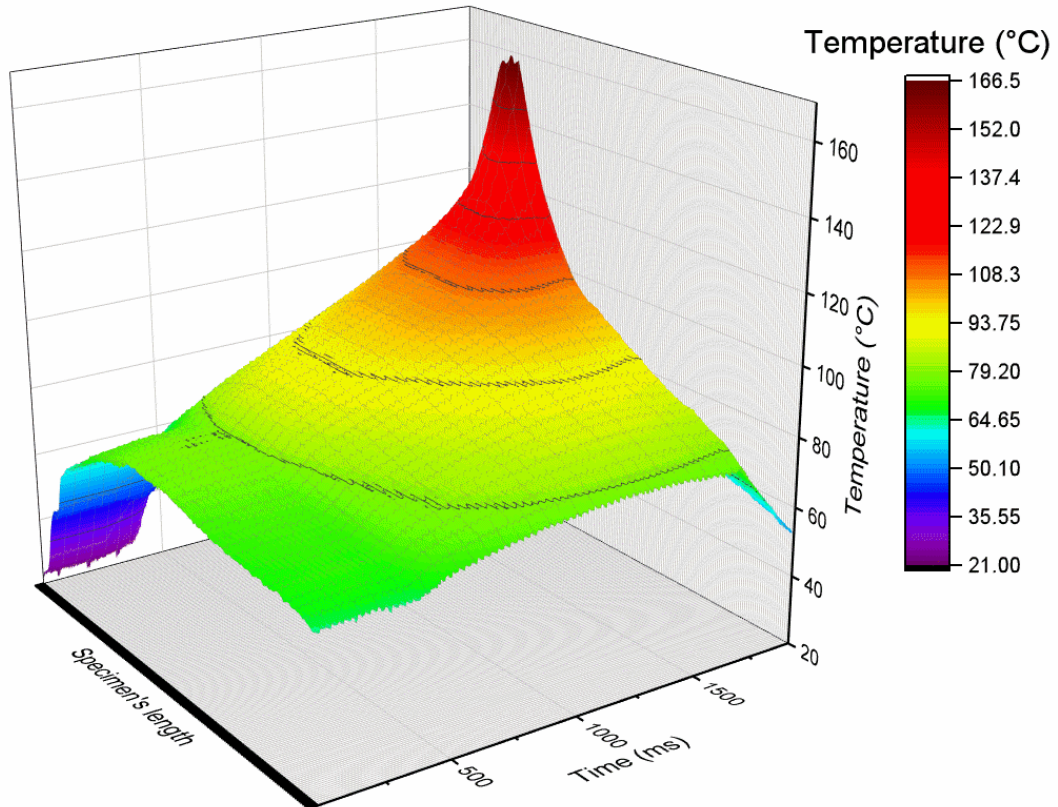


Figure 4.72 Temperature evolution during the test of the specimen strained under 50 A/mm².

In particular, the evolution of the temperature during the tensile test in correspondence of the fracture surfaces can be observed in Figure 4.73.

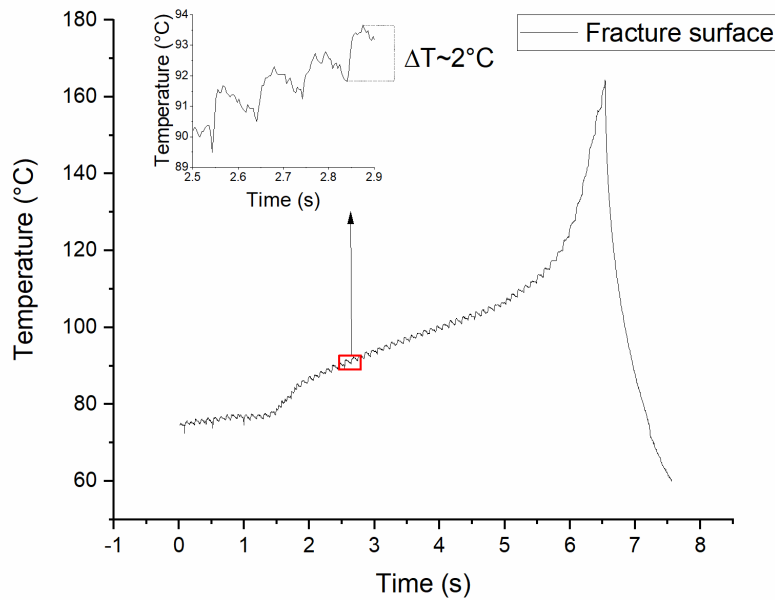


Figure 4.73 Evolution of fracture surface temperature during tensile test at 50 A/mm².

Current pulses are responsible for the serrations that can be seen in the curve. The increase in temperature is approximately 2 °C for each pulse, followed by a time period in which the specimen cools down thanks to the cooling apparatus.

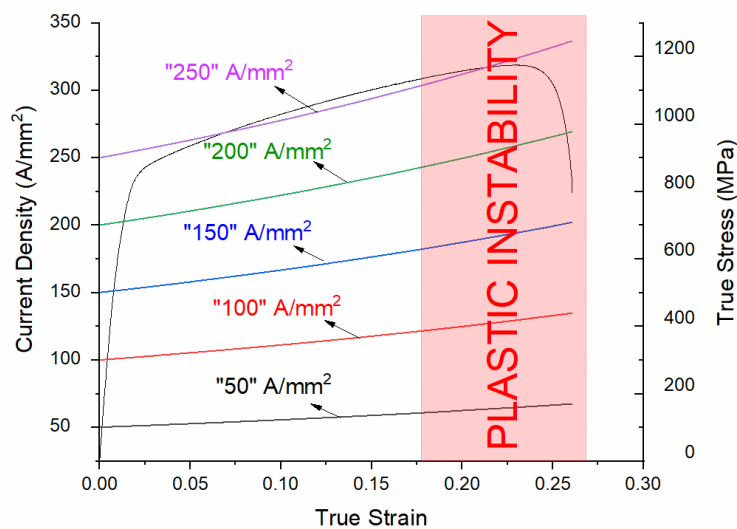


Figure 4.74 Current density evolution during the tensile test.

As for the continuous current case, the current density is not constant throughout the entire duration of the test. In Figure 4.74 it has been reported the current evolution during the tensile test for the various current density. Interesting to note that the higher the nominal current density the higher the its increase. Nevertheless, since post uniform elongation is not so pronounced for this type of DSSs, fracture strain can be taken as a parameter to compare the different current densities.

4.5.10. Pulsed current tensile tests

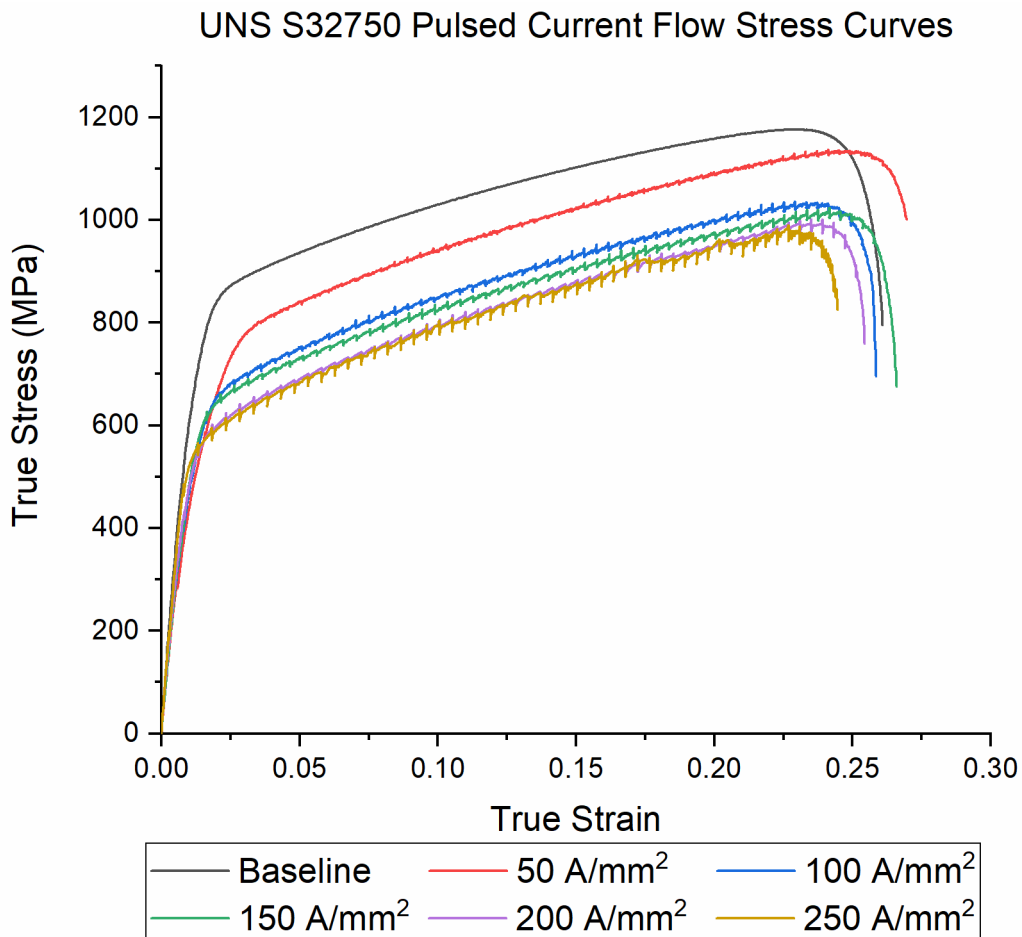


Figure 4.75 True stress-strain curve of the pulsed tensile tests.

The true stress-strain curves obtained with pulsed current density together with the room temperature test (baseline) are presented in Figure 4.75. The serrations on the stress-strain curves are not due to DSA but to the electrical

pulses. As mentioned in the previous paragraph, at each pulse a temperature increase of approximately 2 °C is observed in the specimen which causes an instantaneous thermal expansion. Since the tensile tests were conducted with constant displacement rate, the serrations on the stress strain curves are due to the instant increase in the force measured by the load cell. The “size” of the jump in the stress is directly linked with the intensity of the current density.

All the tests conducted under pulsed current showed similar fracture strain, yield stress and ultimate tensile strength except for the test at 50 A/mm² which has higher yield stress, ultimate tensile strength and fracture strain. No clear trend between fracture strain and current density is evident, moreover it is not observed the decrease in fracture strain with the increase in the thermal regime compared to the continuous current case. The test performed at 250 A/mm² showed the onset of DSA as in the continuous current case. Even though it seems that there could be an influence on the elastic behaviour of the material between the baseline and the pulsed tests, no extensometer has been used, so no consideration can be done on the elastic modulus of the material. All tests have comparable fracture strain, with no trend with respect to the current density.

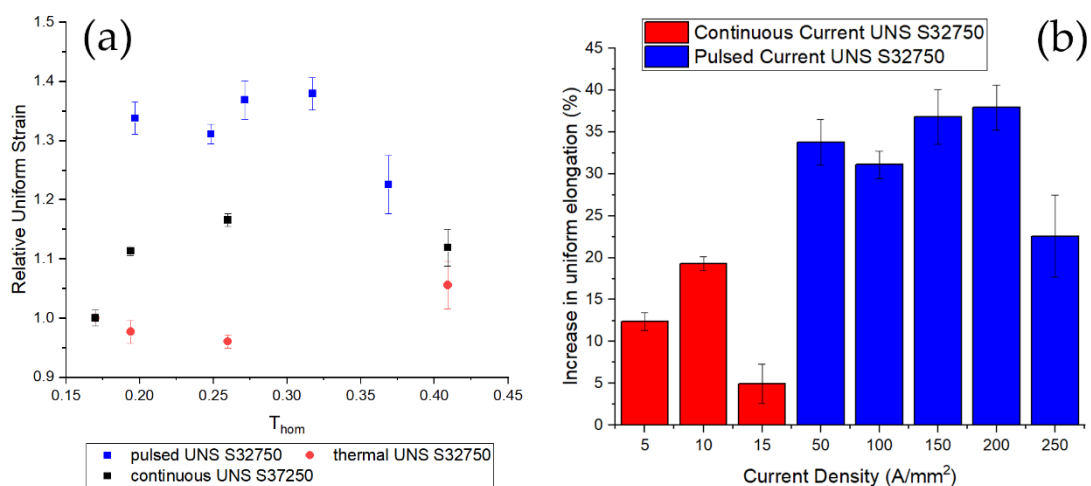


Figure 4.76 Relative uniform strain of pulsed current tensile tests compared to the thermal counterpart and the continuous current tensile tests (a) and percentage increase of uniform elongation (b).

Pulsed current tensile tests compared to the thermal counterparts showed an increase in uniform elongation much more evident compared to the continuous current case (Figure 4.76). All relative uniform strains were comparable except that of the test conducted at higher current density because of the higher temperature. The increase in uniform elongation with respect to the baseline was more than 35%, moreover it remained constant for all the current densities tested. It looks like the increase in current density compensate for the decrease in uniform elongation due to the mere joule heating conversely to the thermal tests. In this case, some considerations can be done on the fracture strain since localized plastic instability accounts for a very small duration of the test, and joule heating due to pulsed current is not so pronounced compared to the continuous current tests. Elongation at rupture was constant and comparable with that of the baseline despite the increase in the test temperature, as opposed to the continuous current case.

Overall, the effect of pulsed current was much more evident in comparison to the continuous current even though the electrical energy was much lower.

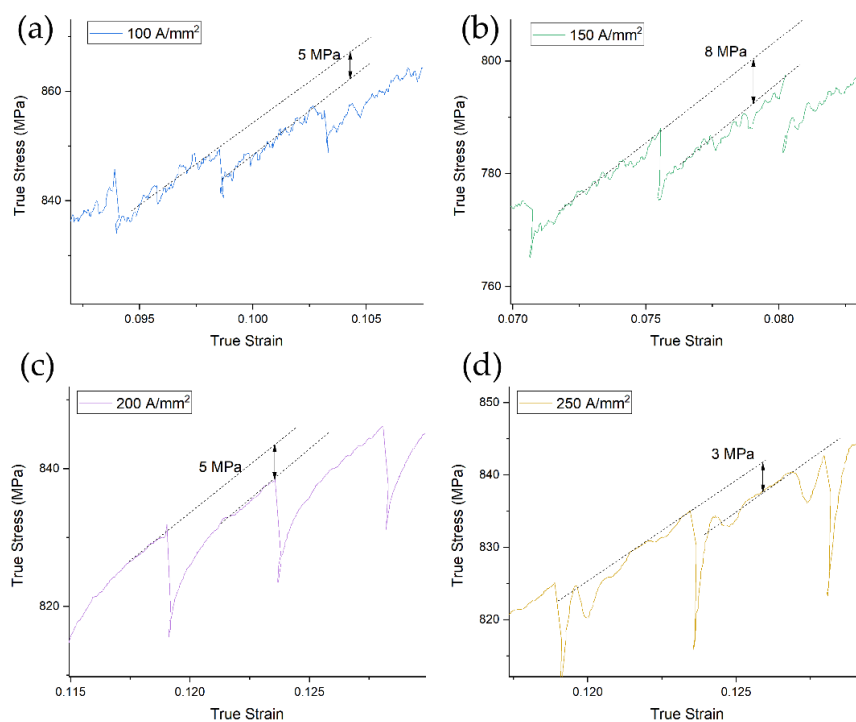


Figure 4.77 Serrations close up of the flow stress curves at various current densities.

With a closer look to the flow stress curves, the effect of one single current pulses can be observed (Figure 4.77). If thermal expansion would have been the only responsible for stress jumps on the flow stress curves, once the current was shut off the stress on the material should raise to before the application of the current pulse. Conversely, the stress was few MPa lower before the application of the n+1 pulse in comparison to the n pulse. This was probably due to some sort of current induced dislocation annealing due to higher dislocation mobility. Each current pulse partially annealed the material, reducing the dislocation density and increasing its ability to absorb more energy raising the fracture strain.

4.5.11. *Discussions*

The peculiarity of this material is the copresence of two phases with very different SFE: ferrite with high SFE and austenite with low SFE. In previous work it has been found that electroplasticity seems to be SFE-dependent [30], more precisely low SFE materials show a reduction in elongation at rupture when deformed under applied continuous current, conversely high SFE material such as ferritic stainless steels or aluminum show an increase in elongation at rupture.

The two phases have a different composition and because of the different SFE they work harden in a very different way, which leads to different resistivity of each phase. It has been hypothesized that the electrical current does not flow uniformly throughout each phase, it rather follows preferential paths, probably inside the ferritic matrix, that is why an overall positive effect of the current can be observed. Moreover, very extensive phase boundary due to the fragmented austenite grains because of cold rolling is present and acts as an additional barrier for the flow of electrons that get scattered and locally increase the temperature. Other researchers [62] explained the electroplastic

effect through heterogeneous joule heating developing a theory called *Electron Stagnation Theory*. They supposed that in correspondence of inclusions, defects, dislocation bundles, precipitates etc., there could be a stagnation of electrons that can change the electron to atom ratio leading to a weakening of the bonding energy of the atoms therefore, easing dislocations motion. This could be happening in this case in proximity of phase boundary and at ferrite/ferrite grain boundaries much more compared to austenite/austenite grain boundary causing an increase in temperature easing dislocation motion and facilitating annihilation of dislocations as well. It has to be mentioned that the different electrical resistivity of the two phases due to the chemical composition could also play an important role.

4.5.12. *Concluding remarks*

Relative uniform elongation of pulsed current tensile tests were significantly higher compared to the continuous current case (approximately 30% more compared to the baseline) while UTS and yield stress were not affected. Fracture strain for the pulsed tensile test was constant despite the increase in temperature of the material and comparable to that of the baseline, as opposed to the continuous current case.

An uneven distribution of current due to the presence of a ferrite matrix is the possible explanation as the occurrence of the electroplastic effect in a material presenting two different phases with opposite behaviour with respect the electrical current.

4.6. References

- [1] Froes, F.H. *Titanium: Physical Metallurgy Processing and Applications*; (1989); Vol. 53; ISBN 9788578110796.
- [2] Bhadeshia, H.K.D.H. *Metallurgy of Titanium and its Alloys* Available online: <https://www.phase-trans.msm.cam.ac.uk/2004/titanium/titanium.html> (accessed on Aug 7, 2019).
- [3] *Metallurgical Materials Science and Alloy Design - Titanium alloys* Available online: <http://www.dierk-raabe.com/titanium-alloys/> (accessed on Aug 8, 2019).
- [4] Hume-Rothery, W.; Powell, H.M. "On the Theory of Super-Lattice Structures in Alloys", **Zeitschrift für Krist. - Cryst. Mater.** (1935), Volume 91, pp.23–47.
- [5] Hume-Rothery, W. "The structure of metals and alloys", **Indian J. Phys.** (1969), Volume 11, pp.74.
- [6] Hume-Rothery, W. "Atomic theory for students of metallurgy", (1952).
- [7] Froes, F.H. "Titanium: Alloying", **Encycl. Mater. Sci. Technol.** (2004), pp.9361–9364.
- [8] Zhang, B.; Wang, J.; Wang, Y.; Wang, Y.; Li, Z. "Strain-rate-dependent tensile response of Ti-5Al-2.5Sn alloy", **Materials (Basel)**. (2019), Volume 12.
- [9] El-Domiaty, A. "The effect of strain, strain rate and temperature on formability of Ti-6Al-4V alloy", **J. Mater. Process. Tech.** (1992), Volume 32, pp.243–251.
- [10] Ross, C.D.; Kronenberger, T.J.; Roth, J.T. "Effect of dc on the Formability of Ti-6Al-4V", **J. Eng. Mater. Technol.** (2009), Volume 131, pp.031004.
- [11] Wang, Z. jin; Song, H. "Effect of high-density electropulsing on microstructure and mechanical properties of cold-rolled TA15 titanium alloy sheet", **J. Alloys Compd.** (2009), Volume 470, pp.522–530.
- [12] Park, J.-W.; Jeong, H.-J.; Jin, S.-W.; Kim, M.-J.; Lee, K.; Kim, J.J.; Hong, S.-T.; Han, H.N. "Effect of electric current on recrystallization kinetics in interstitial free steel and AZ31 magnesium alloy", **Mater. Charact.** (2017), Volume 133, pp.70–76.
- [13] Jiang, Y. bin; Guan, L.; Tang, G. yi; Cheng, B.; Liu, D. bo "Microstructure and

texture evolution of Mg-3Zn-1Al magnesium alloy during large-strain electroplastic rolling", **Int. J. Miner. Metall. Mater.** (2015), Volume 22, pp.411–416.

- [14] Jones, J.J.; Mears, L.; Roth, J.T. "Electrically-Assisted Forming of Magnesium AZ31: Effect of Current Magnitude and Deformation Rate on Forgeability", **J. Manuf. Sci. Eng.** (2012), Volume 134, pp.034504.
- [15] Wang, S.Z. Effect of Electric Pulses on Drawability and Corrosion Property of AZ31 Magnesium Alloy, Tsinghua University, (2009).
- [16] Chu, X.R.; Wang, L.; Lin, S.X.; Yue, Z.M.; Gao, J. "Experimental Investigation on Formability of AZ31B Magnesium Alloy V-Bending Under Pulse Current", **Acta Metall. Sin. (English Lett.** (2018), Volume 31, pp.1249–1257.
- [17] XIE, H.Y.; WANG, Q.; Peng, F.; LIU, K.; DONG, X.H.; WANG, J.F. "Electroplastic effect in AZ31B magnesium alloy sheet through uniaxial tensile tests", **Trans. Nonferrous Met. Soc. China (English Ed.** (2015), Volume 25, pp.2686–2692.
- [18] Magargee, J.; Fan, R.; Cao, J. "Analysis and Observations of Current Density Sensitivity and Thermally Activated Mechanical Behavior in Electrically-Assisted Deformation", **J. Manuf. Sci. Eng.** (2013), Volume 135, pp.061022.
- [19] Fonstein, N. "Advanced high strength sheet steels: Physical metallurgy, design, processing, and properties", **Adv. High Strength Sheet Steels Phys. Metall. Des. Process. Prop.** (2015), pp.1–396.
- [20] De Cooman, B.C.; Estrin, Y.; Kim, S.K. "Twinning-induced plasticity (TWIP) steels", **Acta Mater.** (2018), Volume 142, pp.283–362.
- [21] Kim, J.; Lee, S.J.; De Cooman, B.C. "Effect of Al on the stacking fault energy of Fe-18Mn-0.6C twinning-induced plasticity", **Scr. Mater.** (2011), Volume 65, pp.363–366.
- [22] De Cooman, B.C.; Kwon, O.; Chin, K.-G. "State-of-the-knowledge on TWIP steel", **Mater. Sci. Technol.** (2012), Volume 28, pp.513–527.
- [23] El-Danaf, E.; Kalidindi, S.R.; Doherty, R.D. "Influence of grain size and stacking-fault energy on deformation twinning in fcc metals", **Metall. Mater. Trans. A**

- (1999), Volume 30, pp.1223–1233.
- [24] De Cooman, B.C.; Kwon, O.; Chin, K.G. "State-of-the-knowledge on TWIP steel", **Mater. Sci. Technol.** (2012), Volume 28, pp.513–527.
- [25] Martin, S.; Wolf, S.; Martin, U.; Krüger, L.; Rafaja, D. "Deformation Mechanisms in Austenitic TRIP/TWIP Steel as a Function of Temperature", **Metall. Mater. Trans. A Phys. Metall. Mater. Sci.** (2016), Volume 47, pp.49–58.
- [26] De Cooman, B.C.; Chin, K.; Kim, J. "High Mn TWIP Steels for Automotive Applications", **New Trends Dev. Automot. Syst. Eng.** (2011).
- [27] Idrissi, H.; Renard, K.; Schryvers, D.; Jacques, P.J. "On the relationship between the twin internal structure and the work-hardening rate of TWIP steels", **Scr. Mater.** (2010), Volume 63, pp.961–964.
- [28] Martin, S.; Ullrich, C.; Imek, D.; Martin, U.; Rafaja, D. "Stacking fault model of martensite and its DIFFaX implementation", **J. Appl. Crystallogr.** (2011), Volume 44, pp.779–787.
- [29] Zimniak, Z.; Dobras, D. "Electroplastic effect of high manganese austenitic steel", **Arch. Metall. Mater.** (2019), Volume 64, pp.431–436.
- [30] Breda, M.; Calliari, I.; Bruschi, S.; Forzan, M.; Ghiotti, A.; Michieletto, F.; Spezzapria, M.; Gennari, C. "Influence of stacking fault energy in electrically assisted uniaxial tension of FCC metals", **Mater. Sci. Technol.** (2017), Volume 33, pp.317–325.
- [31] De Paula Martins, J.; De Carvalho, A.L.M.; Padilha, A.F. "Texture analysis of cold rolled and annealed aluminum alloy produced by twin-roll casting", **Mater. Res.** (2012), Volume 15, pp.97–102.
- [32] Li, S.; Zhao, Q.; Liu, Z.; Li, F. "A Review of Texture Evolution Mechanisms During Deformation by Rolling in Aluminum Alloys", **J. Mater. Eng. Perform.** (2018), Volume 27, pp.3350–3373.
- [33] Hirsch, J. "Texture evolution during rolling of aluminium alloys", **TMS Light Met.** (2008), pp.1071–1077.
- [34] Magargee, J.; Morestin, F.; Cao, J. "Characterization of Flow Stress for

Commercially Pure Titanium Subjected to Electrically Assisted Deformation", **J. Eng. Mater. Technol.** (2013), Volume 135, pp.041003.

- [35] Lutterotti, L. "Total pattern fitting for the combined size-strain-stress-texture determination in thin film diffraction", **Nucl. Instruments Methods Phys. Res. Sect. B Beam Interact. with Mater. Atoms** (2010), Volume 268, pp.334–340.
- [36] Mittemeijer, E.J.; Welzel, U. "The "state of the art" of the diffraction analysis of crystallite size and lattice strain", **Zeitschrift fur Krist.** (2008), Volume 223, pp.552–560.
- [37] Ferry, A.; Jacobsson, P. "Curve Fitting and Deconvolution of Instrumental Broadening: A Simulated Annealing Approach", **Appl. Spectrosc.** (2005), Volume 49, pp.273–278.
- [38] Ungár, T. "Microstructural parameters from X-ray diffraction peak broadening", **Scr. Mater.** (2004), Volume 51, pp.777–781.
- [39] Scardi, P.; Leoni, M. "Whole powder pattern modelling", **Acta Crystallogr. Sect. A Found. Crystallogr.** (2002), Volume 58, pp.190–200.
- [40] Williamson, G.; Hall, W.. "X-ray line broadening from filed aluminium and wolfram", **Acta Metall.** (1953), Volume 1, pp.22–31.
- [41] Williamson, G.K.; Smallman, R.E. "III. Dislocation densities in some annealed and cold-worked metals from measurements on the X-ray Debye-Scherrer spectrum", **Philos. Mag.** (1956), Volume 1, pp.34–46.
- [42] Gunn, R. *Duplex Stainless Steels*; (1997); ISBN 9781884207617.
- [43] Nilsson, J.O. "Super Duplex Stainless-Steels", **Mater. Sci. Technol.** (1992), Volume 8, pp.685–700.
- [44] Nilsson, J.O. "The physical metallurgy of duplex stainless steels", In Proceedings of the **Duplex stainless steels**; Nilsson, J.O., Ed.; KCI Publishing: Maastricht, Netherlands, (1997); pp. 73–82.
- [45] Lippold, J.C.; Savage, W.F. "Solidification of Austenitic Stainless Steel Weldments : Part I – A Proposed Mechanism The distribution and morphology of delta ferrite is dependent", **Weld. Res. Suppl.** (1979), pp.362s-374s.

- [46] Knyazeva, M.; Pohl, M. "*Duplex Steels: Part I: Genesis, Formation, Structure*", **Metallogr. Microstruct. Anal.** (2013), Volume 2, pp.113–121.
- [47] Gunn, R.N. *Duplex Stainless Steels: Microstructure, Properties and Applications*; Gunn, R.N., Ed.; 1st ed.; Woodhead: Sawston, United Kingdom, Cambridge, United Kingdom, (1997); ISBN 9781855733183.
- [48] Nilsson, J.O.O. "*Super duplex stainless steels*", **Mater. Sci. Technol.** (1992), Volume 8, pp.685–700.
- [49] Calliari, I.; Zanesco, M.; Ramous, E. "*Precipitazione di fasi secondarie in un acciaio duplex 2205 trattato isotermicamente*", **Metall. Ital.** (2004), Volume 96, pp.41–45.
- [50] Pérez, A.F.M.; Breda, M.; Calliari, I.; Medina, G.Y.P.; Sandström, R. "*Detrimental Cr-rich Phases Precipitation on SAF 2205 Duplex Stainless Steels Welds After Heat Treatment*", **Soldag. Inspeção** (2016), Volume 21, pp.165–171.
- [51] Breda, M.; Brunelli, K.; Grazzi, F.; Scherillo, A.; Calliari, I. "*Effects of Cold Rolling and Strain-Induced Martensite Formation in a SAF 2205 Duplex Stainless Steel*", **Metall. Mater. Trans. A Phys. Metall. Mater. Sci.** (2015), Volume 46, pp.577–586.
- [52] Taylor, G.I.; Quinney, H. "*The Latent Energy Remaining in a Metal after Cold Working*", **Proc. R. Soc. A Math. Phys. Eng. Sci.** (1934), Volume 143, pp.307–326.
- [53] Herenu, S.; Alvarez-Armas, I.; Armas, A.; Degallaix, S.; Condo, A.; Lovey, F. "*Microstructural changes in a Duplex stainless steel during low cycle fatigue*", **Mater. Test.** (2009), Volume 51, pp.359–364.
- [54] Herenu, S.; Alvarez-Armas, I.; Armas, A.F. "*The influence of dynamic strain aging on the low cycle fatigue of duplex stainless steel*", **Scr. Mater.** (2001), Volume 45, pp.739–745.
- [55] Fang, Y.L.; Liu, Z.Y.; Song, H.M.; Jiang, L.Z. "*Hot deformation behavior of a new austenite-ferrite duplex stainless steel containing high content of nitrogen*", **Mater. Sci. Eng. A** (2009), Volume 526, pp.128–133.
- [56] Bannister, A.C.; Ruiz Ocejó, J.; Gutierrez-Solana, F. "*Implications of the yield*

stress/tensile stress ratio to the SINTAP failure assessment diagrams for homogeneous materials", **Eng. Fract. Mech.** (2000), Volume 67, pp.547–562.

- [57] Ma, B.; Shuai, J. "*Influence of Plastic Deformation Capacity on Failure Behavior of Pipelines*", **J. Fail. Anal. Prev.** (2018), Volume 18, pp.508–518.
- [58] Zhao, J.; Wang, G.X.; Dong, Y.; Ye, C. "*Multiscale modeling of localized resistive heating in nanocrystalline metals subjected to electropulsing*", **J. Appl. Phys.** (2017), Volume 122.
- [59] Sánchez Egea, A.; Peiró, J.J.; Signorelli, J.W.; González Rojas, H.A.; Celentano, D.J. "*On the microstructure effects when using electropulsing versus furnace treatments while drawing inox 308L*", **J. Mater. Res. Technol.** (2019), Volume 8, pp.2269–2279.
- [60] Bohnenkamp, U.; Sandström, R.; Grimvall, G. "*Electrical resistivity of steels and face-centered-cubic iron*", **J. Appl. Phys.** (2002), Volume 92, pp.4402–4407.
- [61] Peng, R.L.; Gibmeier, J.; Eulert, S.; Johansson, S.; Chai, G.C. "*In Situ X-Ray Diffraction Study of Load Partitioning and Microyielding for the Super Duplex Stainless Steel SAF2507 (UNS S32750)*", **Mater. Sci. Forum** (2006), Volume 524–525, pp.847–852.
- [62] Ruskiewicz, B.J.; Mears, L.; Roth, J.T. "*Investigation of Heterogeneous Joule Heating as the Explanation for the Transient Electroplastic Stress Drop in Pulsed Tension of 7075-T6 Aluminum*", **J. Manuf. Sci. Eng.** (2018), Volume 140, pp.091014.
- [63] Rahnama, A.; Qin, R. "*Room temperature texturing of austenite/ferrite steel by electropulsing*", **Sci. Rep.** (2017), Volume 7, pp.1–6.
- [64] Zheng, Y.S.; Tang, G.Y.; Kuang, J.; Zheng, X.P. "*Effect of electropulse on solid solution treatment of 6061 aluminum alloy*", **J. Alloys Compd.** (2014), Volume 615, pp.849–853.
- [65] Molotskii, M.I. "*Theoretical basis for electro- and magnetoplasticity*", **Mater. Sci. Eng. A** (2000), Volume 287, pp.248–258.
- [66] Molotskii, M.I.; Fleurov, V. "*Magnetic effect in electroplasticity of metals*", **Phys.**

Rev. (1995), Volume 52, pp.829–834.

- [67] Breda, M.; Michieletto, F.; Beridze, E.E.E.; Gennari, C. "*Experimental Study on Electroplastic Effect in AISI 316L Austenitic Stainless Steel*", **Appl. Mech. Mater.** (2015), Volume 792, pp.568–571.

CHAPTER 5

Electropulsing treatment

5.1. INTRODUCTION

In contraposition to the previous chapter, where the influence of the electrical current was studied upon deformation of various metallic alloys, electropulsing treatments consist in applying the electrical current to a workpiece while it is not being deformed.

A thorough review of the electropulsing treatments have been done in subchapter 1.5. It has been observed that application of short pulse duration of high current density affected materials properties such as grain size and orientation, residual stresses, degree of work hardening, secondary phases precipitation, dissolution, morphology and distribution, phase transformations, microcracks healing etc. [1–19]. Predicting how the current pulses could affect the microstructure of the materials subjected to electropulsing treatments is quite hard and few theories have been proposed, dealing with local resistive heating, electron wind force, enhanced diffusion due to electromigration etc. In order to improve the knowledge of electropulsing treatments effect, more experiment on various metallurgical state of a lot of alloys have to be performed.

In this chapter, an investigation of the effect of electropulsing treatments applied to a work hardened super duplex stainless steel UNS S32750 have been performed.

5.2. Duplex stainless steel UNS S32750

UNS S32750 is a duplex stainless steel (DSS) that falls into the category of super-DSS because of its higher mechanical properties and higher corrosion resistance (in particular stress corrosion cracking and pitting corrosion) in comparison to the standard DSSs such as UNS S32205 and the lean DSS (UNS S32101 and UNS S32304). It lies in the category of super-DSS because of its higher amount of alloying elements, mainly Cr, Ni, Cu and W. In terms of PRE_N number, more specifically PRE_W because of the presence of tungsten, SDSS are equivalent to the super austenitic stainless steels that contains higher amount of Mo ($PRE_N=40/42$). As previously mentioned, since PRE_N depends only on the chemical composition, it does not give any information about the metallurgical state of the alloy. Critical pitting temperature (CPT), on the other hand is related to the microstructure of the alloy. CPT of UNS S32750 is very high in comparison to that of other DSSs and also to other class of stainless steel. A summary of the CPTs and PRE_N for the most used stainless steels are depicted in Figure 5.1.

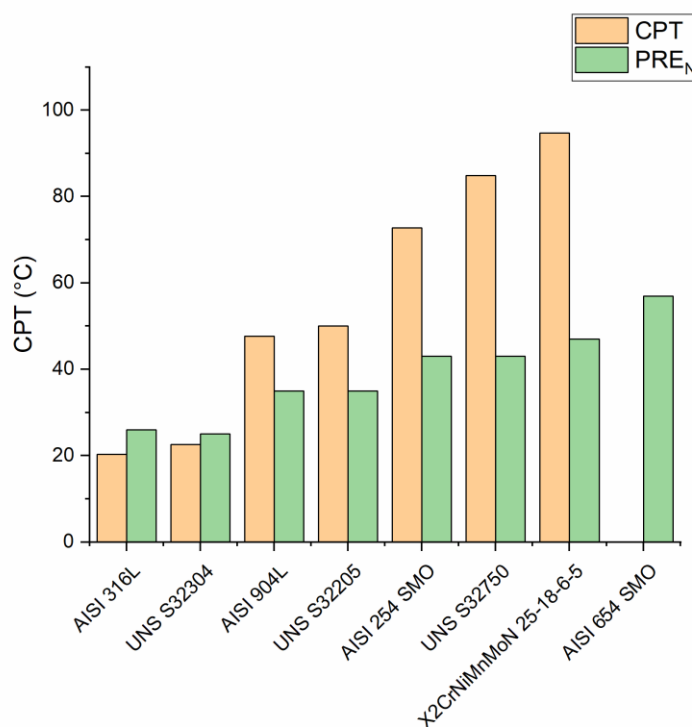


Figure 5.1 CPTs and PRE_N of some stainless steels [20].

Lean DSS have demonstrated to be pretty stable up to several hours of soaking time before any secondary phases particles started to precipitate (only nitrides without any σ or χ phase) [21]. On the other hand, for high alloyed DSS, secondary phases started to precipitate just after few minutes because of the higher Mo content and the lower stability of ferrite [22]. In Table 5.1 are summarized the volume fraction and type of secondary phases observed in various DSSs with respect the heat treatment [21].

Table 5.1 Heat treatment parameters and percentage of secondary phases observed [21].

DSS grade	Temperature [°C]	Soaking time	Secondary phases	% secondary phases
UNS S32101	750	90 min	Nitrides	0.62±0.05
	850	3 h	Nitrides	1.21±0.04
	850	20 h	Nitrides	1.25±0.05
	850	100 h	Nitrides	1.25±0.02
UNS S32304	750	1 h	Nitrides	0.65±0.03
	850	1 h	Nitrides	1.40±0.05
UNS S32205	850	10 min	Nitrides, σ , χ	1.01±0.12
	850	90 min	σ , χ	10.45±0.32
UNS S32750	850	5 min	σ , χ	0.97±0.08
	850	35 min	σ , χ	10.08±0.30

Even few minutes at 850 °C produced approximately 1% of σ and χ phase that have demonstrated to affect, even in this low amount, impact toughness and corrosion resistance [21,23–25]. It is therefore very important an accurate solution annealing treatment in order to dissolve any secondary phases present. The cooling rate is essential in order to limit the transit time in the secondary phases temperature region which cause a limitation in the maximum cross section of the manufactures obtainable with this DSS grade. Continuous-cooling-transformation (CCT) and transformation-time-temperature (TTT) diagrams for UNS S32750 are showed in Figure 5.2. Even a cooling rate of 10 °C/s is not enough to prevent precipitation of secondary phases.

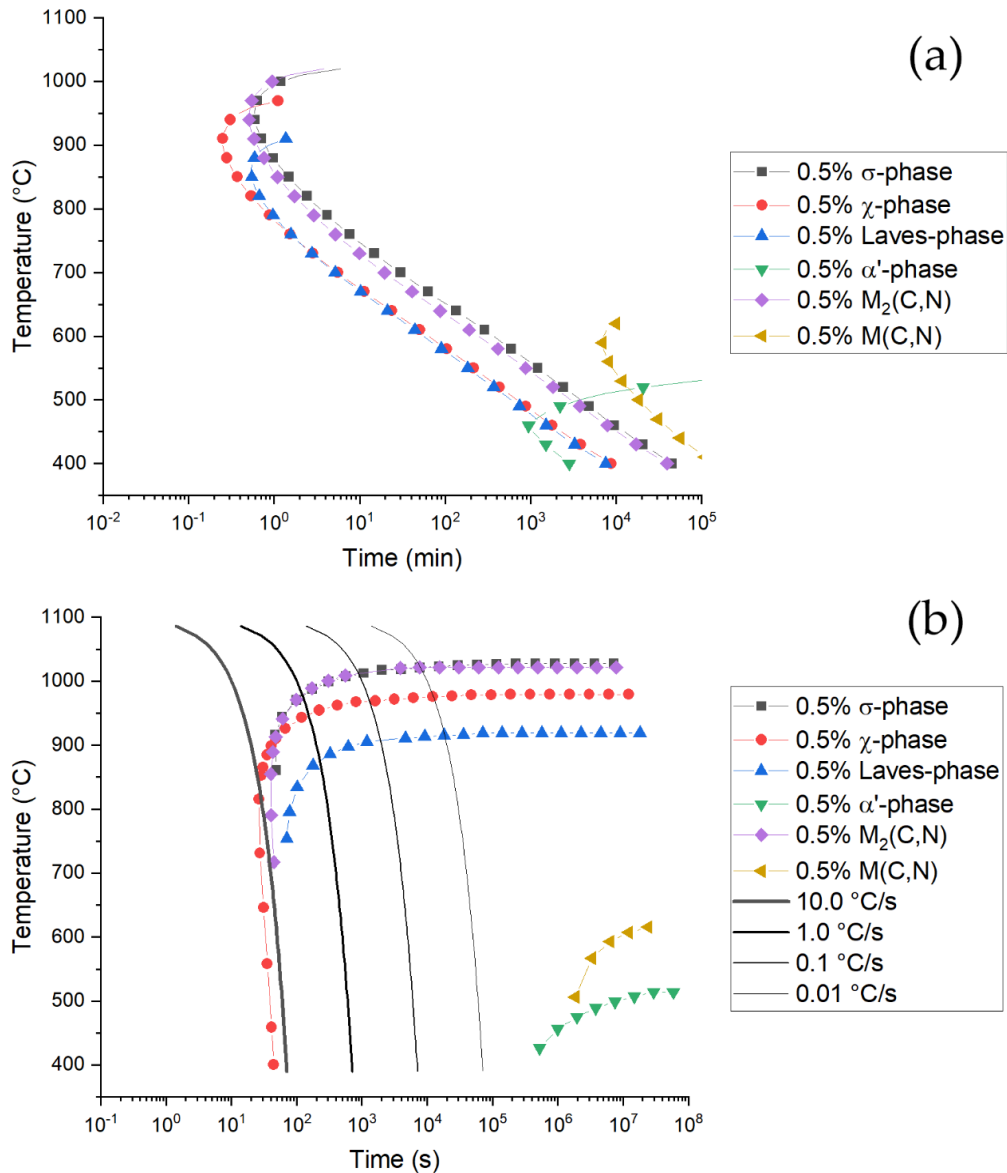


Figure 5.2 (a) Time-temperature-transformation diagram and (b) Continuous-cooling-transformation diagram for UNS S32750 computed with JMatPro software.

Super DSSs are much less sensitive to strain induced martensite (SIM) due to the fact that austenite is pretty stable and possesses higher stacking fault energy (SFE) in comparison to that of lean DSSs in which higher content in austenite stabilizing elements is present [26]. Nevertheless, SIM precipitation in higher alloyed DSSs have been observed in some cases and could lead to worse corrosion resistance and delayed cracking after forming processes [21,22,26–28].

5.2.1. Materials and methods

The material was supplied by the Italian division of Outokumpu S.p.a. in form of 2 mm thick warm rolled. The composition of the investigated steel is reported in Table 5.2.

Table 5.2 Chemical composition of the investigated DSS (wt.%).

	C	Si	Mn	Cr	Ni	Mo	Cu	W	P	S	N
UNS S32750	0,018	0,26	0,84	25,08	6,88	3,82	0,17	-	0,019	0,0010	0,294

Specimens for the tensile tests were obtained along the transversal direction with geometry according to the ASTM E8 standard with length gauge reduced to 45 mm due to the small dimension of the sheet provided. Secondary phases, phase balance quantifications and profile fitting were conducted through X-ray diffraction with a Bruker D8 X-ray diffractometer equipped with CuK α X-ray tube without monochromator on the detector side.

Tensile tests were conducted on an MTS 322 tensile test machine capable of 50 kN of force modified to conduct electroplasticity tests (Figure 5.3) at a strain rate of 10^{-2} s^{-1} .

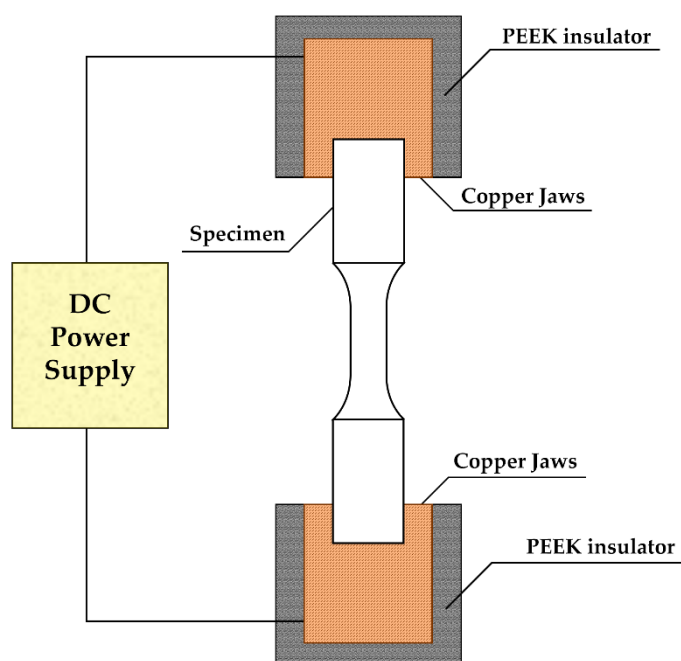


Figure 5.3 Experimental set up of the tensile test machine.

A self-designed power supply capable of producing up to 6 kA current pulses of approximately 110 μs duration with a maximum frequency of 50 Hz was employed. The wave form of the electrical current is showed in Figure 5.4.

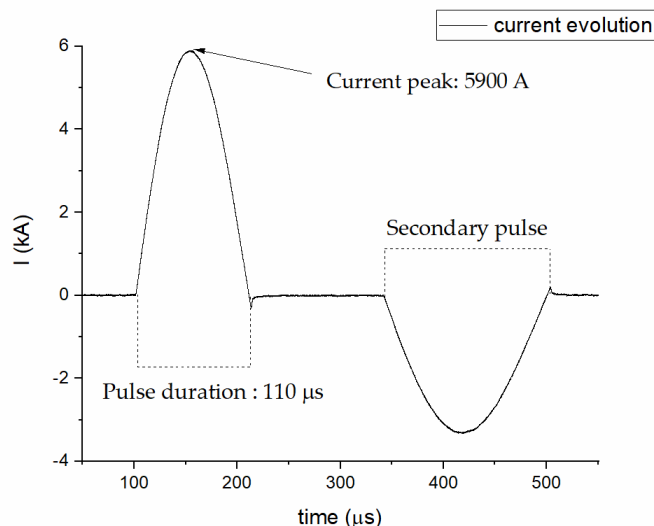


Figure 5.4 Wave form and duration of the electrical current.

Microhardness measurements were performed on a Leica microhardness tester with 500 g of weight for measuring the bulk hardness and 25 g for the hardness of each phase.

Residual stress measurements were performed by mean of a dedicated X-ray diffractometer equipped with $\text{CrK}\alpha$ radiation, along the rolling and transverse direction for each phase.

Potentiodynamic polarization tests were performed on an AMEL 2549 potentiostat at a scanning rate of 0.0005 V/s in a 0.01 M NaCl solution with a saturated calomel electrode according to standard ASTM G3-14.

Microstructural investigation were carried out through optical microscopy (Leica DMRE) and scanning electron microscopy (Leica Cambridge Stereoscan LEO 440).

5.2.1.1. Experimental procedure

The specimens were divided into two main categories. Room temperature tensile test was performed to obtain the main mechanical properties, with focus on the uniform strain. The specimens of the first category were strained to 5% while the ones of category number two were strained to 15%. After straining, residual stresses along the two directions and on the two phases, x-ray diffraction measurements, corrosion tests, microhardness measurements and microstructural analysis were conducted. A set of three specimen per categories were then strained until fracture in order to have a reference for the specimens strained after the electropulsed treatment.

Each categories were then subdivided into four groups depending on the electrical parameters:

- Group 1: 100 A/mm² 100 pulses
- Group 2: 100 A/mm² 500 pulses
- Group 3: 200 A/mm² 100 pulses
- Group 4: 200 A/mm² 500 pulses

As for the baseline, after each electropulsing treatment, residual stresses along the two directions and on the two phases, x-ray diffraction measurements, microhardness measurements and microstructural analysis were conducted.

At this point specimens of the two categories were strained until fracture and compared to the reference of each category. A schematic of the experimental procedure is showed in Figure 5.5.

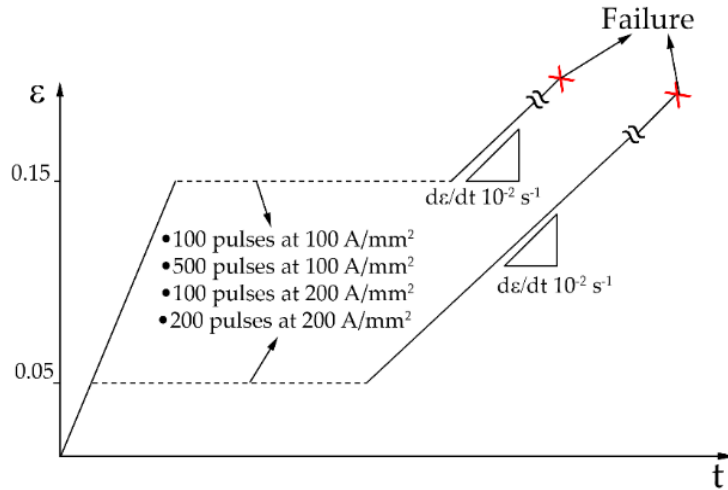


Figure 5.5 Schematic of the experimental procedure.

5.2.2. As received material

The as received material showed a very well-balanced microstructure secondary phases free according to X-ray diffraction pattern (only the peaks relative to δ -ferrite and γ -austenite were visible) and to SEM-BSE investigations.

Phase balance was evaluated through Rietveld analysis on the X-ray diffraction pattern of Figure 5.6 and resulted in almost equal volume fraction of austenite and ferrite (0.48 ± 0.04 and 0.52 ± 0.05 respectively).

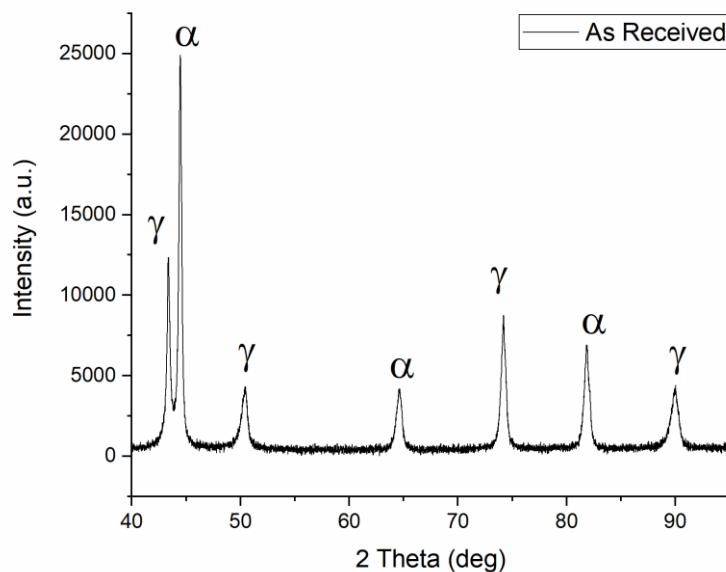


Figure 5.6 X-ray diffraction pattern of the as received material along rolling direction.

The as received material presented a microstructure consisting of fragmented austenite islands (bright grains) dispersed in a ferritic matrix (dark grains) as can be seen in Figure 5.7a. Rolling direction is highlighted by the black arrow. Austenite morphology was quite fragmented due to the last warm pass of the rolling process. Microstructure along the other dimension (transversal and normal) is shown in Figure 5.7b. The interphase space (space between austenite and ferrite) was smaller along the normal direction in comparison to that along the rolling direction.

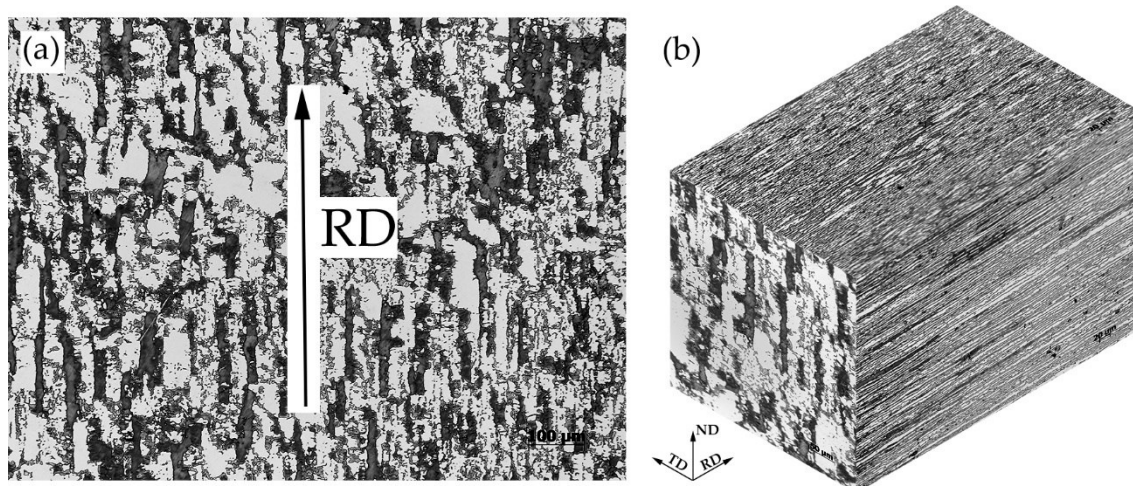


Figure 5.7 Microstructure of the as received materials: (a) along the rolling direction (RD) and (b) along the main three directions (b). Etching solution NaOH at 3 V and 5 s.

5.2.3. Results

5.2.3.1. Reference tensile tests

Tensile test on the as received material and on the specimens prestrained at 5% and 15% were conducted in order to have a reference (Figure 5.8).

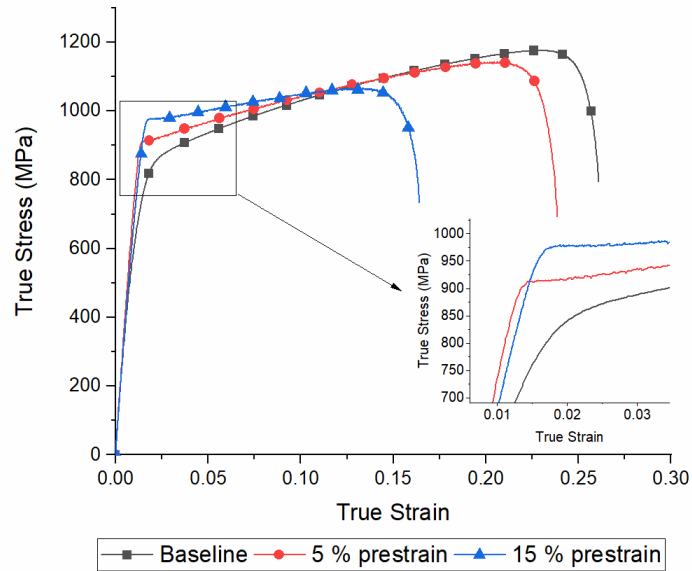


Figure 5.8 True stress-strain curves of the as received material and the two categories of specimens prestrained at 5% and 15%.

As the prestrain increased lower fracture strain, uniform elongation were observed, while yield stress (YS) and ultimate tensile strength (UTS) increased.

X-ray diffraction pattern of the three samples were collected before straining at fracture and FWHM are reported in Figure 5.9

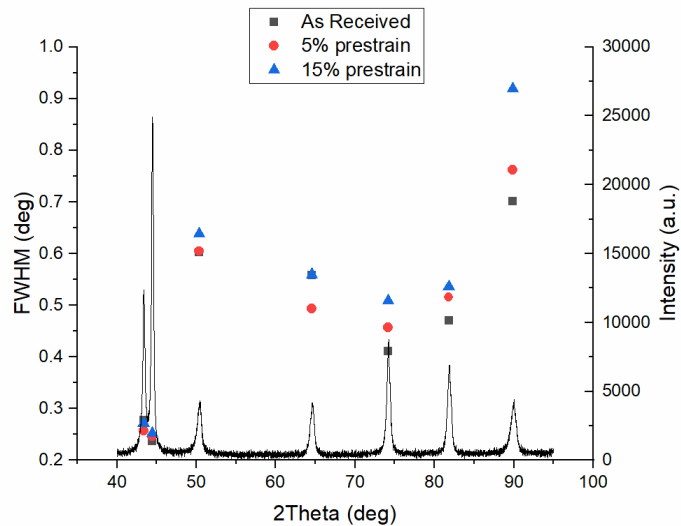


Figure 5.9 X-ray diffraction pattern together with full width half maximum for the three set of samples.

The broadening of the peaks is affected by dislocation density, microstrain, stacking fault, crystallite size and so on [29–35]. It is therefore very difficult to separate the contribution of each phenomenon, so raw FWHM

values of the peaks are considered. As expected, as the prestrain increased FWHM also increased because of the higher dislocation density, the generation of stacking fault in the austenitic phase, the evolution of the crystallite size due to dislocation network and so on. The higher the prestrain the higher the microhardness as well (Figure 5.10).

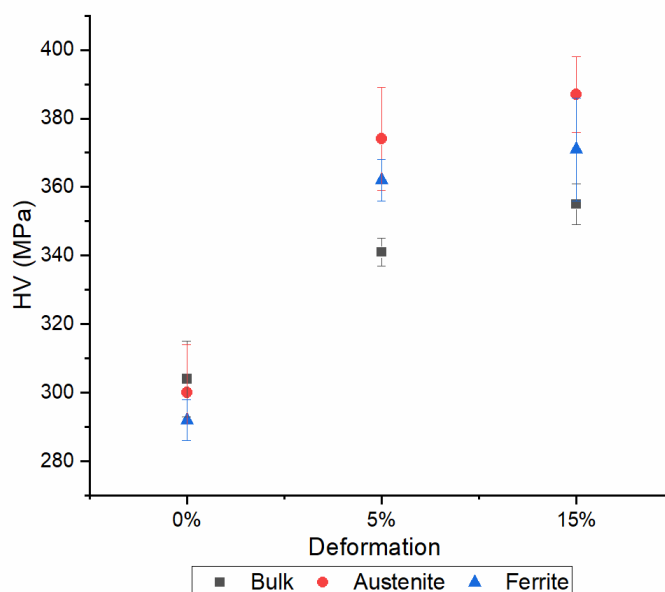


Figure 5.10 Microhardness evolution of as a function of the prestrain of the bulk material and of each phase.

Microhardness of the bulk material was lower compared to that of the single phases because it was measured using a bigger load. The smaller the load the more affected is the measure by the metallographic preparation of the surface that introduces a small work hardened layer on the surface. As the prestrain increased, microhardness of austenitic phase increased due to its higher strain hardening rate because of the lower YS in comparison to that of the ferrite.

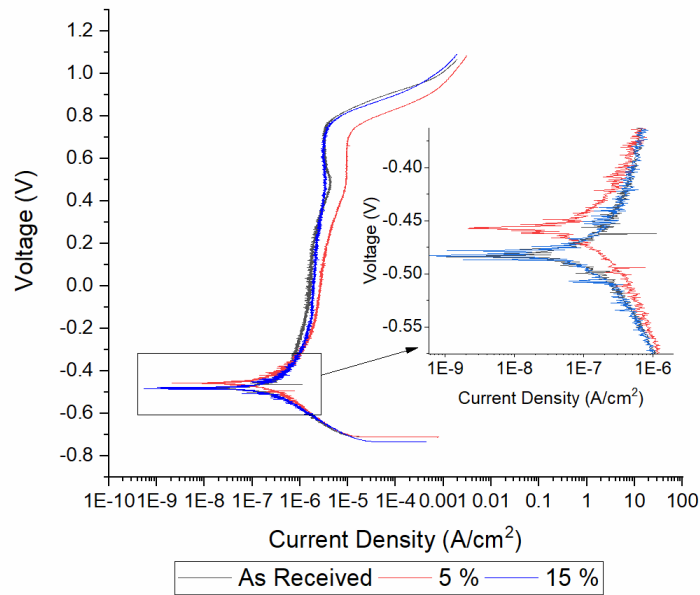


Figure 5.11 Polarization curves of the tested materials.

Corrosion properties were not substantially affected by the degree of prestrain as can be seen in Figure 5.11. The only observed effect was the raise in corrosion potential for the 5% prestrained specimens in comparison to the others. No effect on the corrosion current were observed.

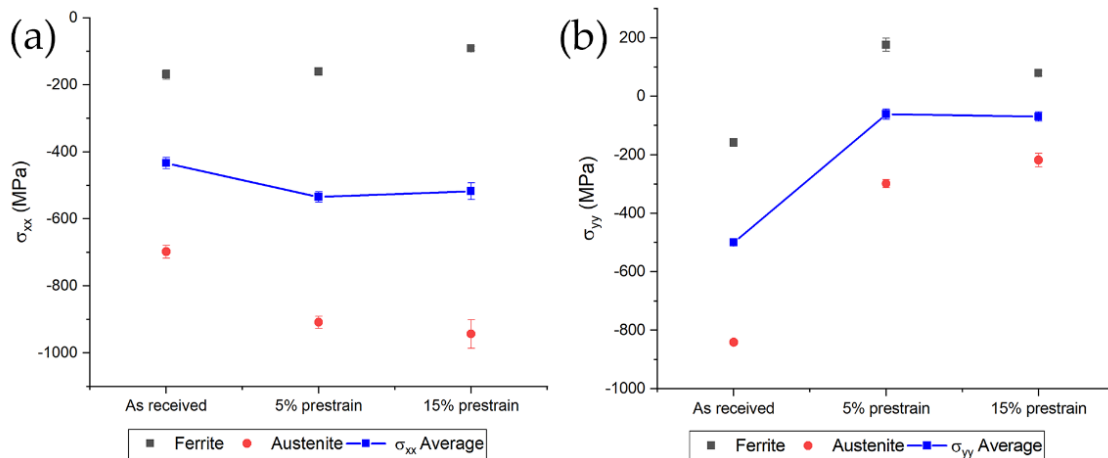


Figure 5.12 Residual stresses evolution on the single phases and the average along the rolling direction (a) and the transversal direction (b).

Compression stress state for each phases along the two direction was observed, conversely to what Johansson et al. found [36]. Since specimens were strained along the transversal direction, a decrease in the compression state for both phases was found (Figure 5.12b). The average stress was calculated with the rule of mixture according to [36]. Along the rolling direction, the average

residual stress remained almost constant while the compression state of the single phases increased for austenite and decreased for ferrite, as expected since tensile test provokes a uniaxial stress state in the specimen.

5.2.3.2. Tensile tests

Electropulsing treatments were conducted with 100 A/mm² and 200 A/mm² current density at 1 Hz for 100 s and 500 s. No increase in specimen temperature was observed during the electropulsing treatments due to the small duration and low frequency of the current pulses.

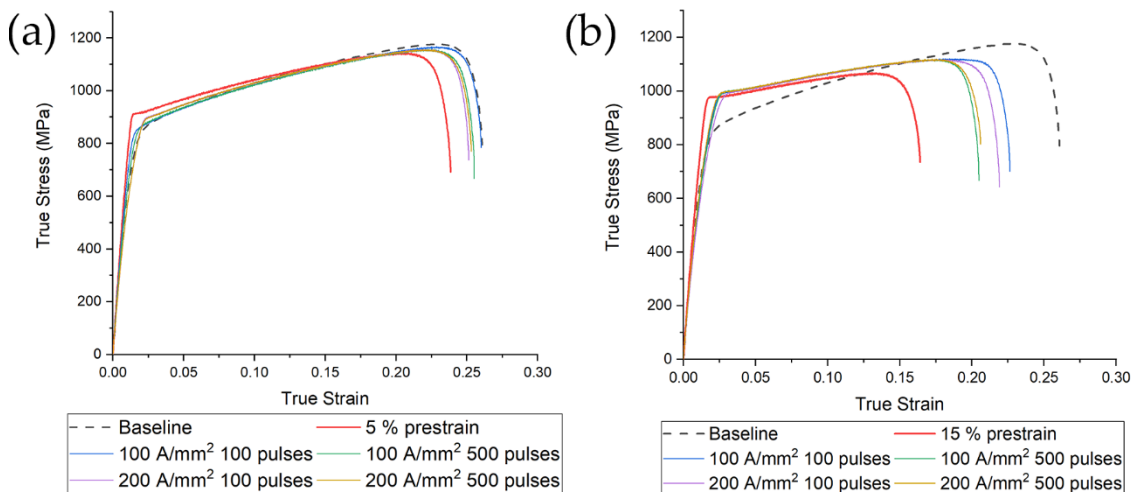


Figure 5.13 Tensile test of electropulsed specimen after prestrain of (a) 5% and (b) 15%. Dashed line is the room temperature test, while red line is the reference for each categories (5% tensile test (a) and 15% tensile test (b)).

After electropulsing treatments, tensile tests have been conducted and compared with the reference of each categories (namely 5% tensile test curve for category one and 15% tensile test curve for category two, together with the baseline). Overall improvement in mechanical properties have been observed for both categories. In the first category the best combination of current density and number of pulses was the lowest (100 A/mm² and 100 pulses). Nevertheless, all tested conditions affected the tensile response in a positive manner. In the case of the specimens prestrained at 15% a recovery of approximately 8% in fracture strain was observed for all tested conditions. The best combination of number of pulses and current density was the same

observed for the 5% case (100 A/mm² and 100 pulses). Interesting to note that the mechanical properties are more affected by the number of pulses rather than the current density. Fixing the current density, as the number of pulses increased smaller improvement in fracture strain were observed. The two current density tested affected in less extent the recovery of fracture strain in comparison to the number of pulses.

5.2.3.3. *Microhardness*

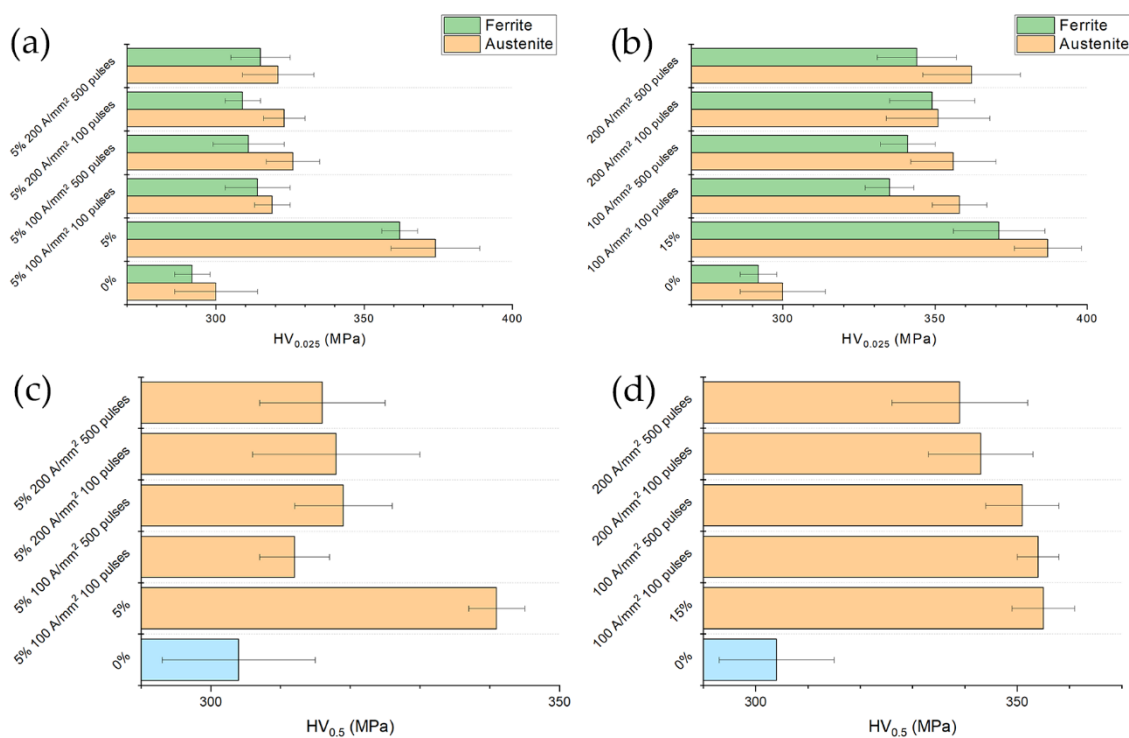


Figure 5.14 Single phases hardness and bulk hardness of specimens strained and electropulsed at (a) 5% and (b) 15% compared to the baseline (0%) and the related reference tests.

Bulk hardness of the electropulsed specimens of category one was slightly higher than that of the undeformed material (0%) while it was sensitively lower compared to the reference (Figure 5.14). Those results were expected on the basis of the true stress-strain curves of Figure 5.13a. Conversely, despite the substantial recovery of category two specimens in comparison to the reference tensile tests, no sensitive bulk hardness reduction was observed. Electropulsing treatments conducted at higher current density showed a lower bulk hardness

in contrast to what was expected on the basis of flow stress curve of Figure 5.13b. Microhardness of the single phases have the same trend as the bulk hardness. Austenite is the harder phase because of its higher work-hardening rate compared to ferrite. The reduction of hardness was almost the same for both phases.

5.2.3.4. Ultimate tensile strength and yield stress

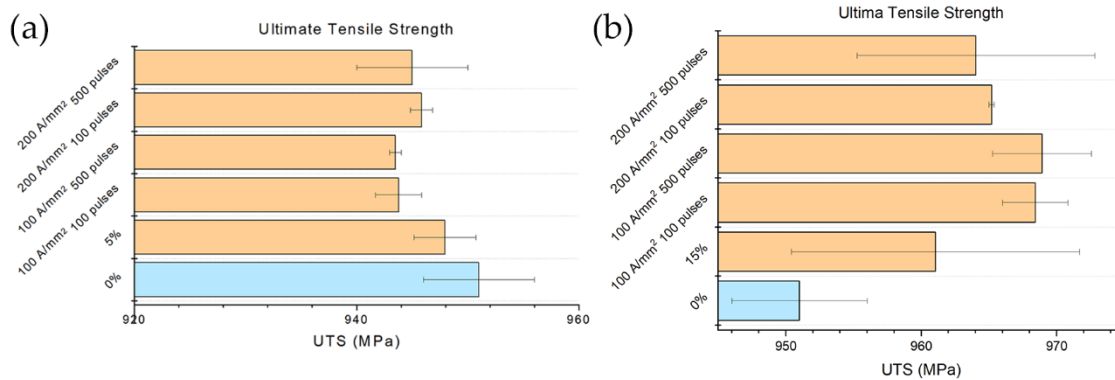


Figure 5.15 Evolution of UTS with respect to the different electropulsing treatments and references (a) 5% prestrained specimens and (b) 15% prestrained specimens.

Ultimate tensile strength was much less affected both by prestrain and by the electropulsing treatment. As can be seen from Figure 5.15a, 5% prestrain did not increase the UTS while the electropulsing treatments slightly decreased UTS in comparison to that of the prestrained material. As opposed to what expected, the electropulsing treatments increased UTS in the case of the sample strained at 15% (Figure 5.15b). This is because the uniform strain of the baseline ($\epsilon_u=0.184$) was very close to the value of the prestrain applied to the specimens of category two. Therefore, electropulsing treatments were able to recover a lot in terms of fracture strain, letting the material to deform more hence increasing its ability to work-harden which led to higher UTS.

Regarding the yield stress, in the case of 5% prestrain, the yield stress was higher in comparison to that of the baseline and the electropulsed specimens, as expected. Substantial reduction was observed for the electropulsing treatments conducted at lower current density, while small or even no reduction in the case

of the higher current density (Figure 5.16a). Strangely, yield stress increased in the case of the electropulsing treatments of the samples prestrained at 15% even in comparison to the reference value (Figure 5.16b).

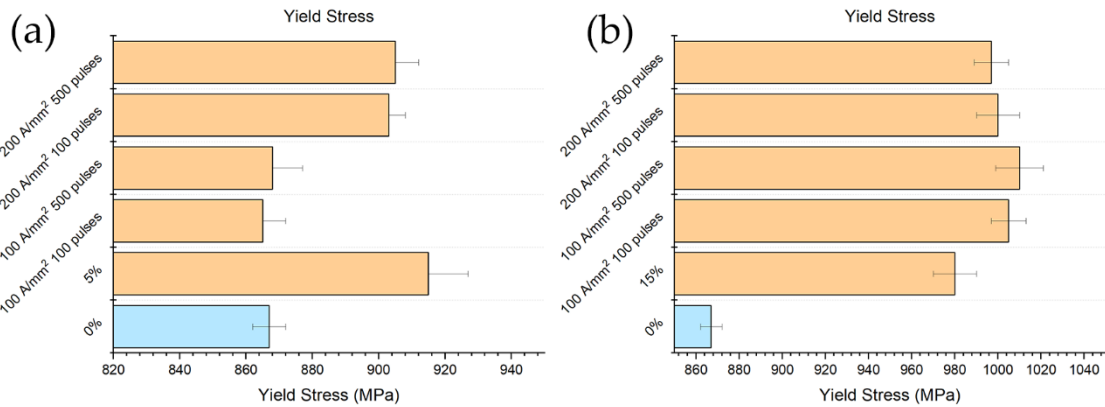


Figure 5.16 Evolution of YS with respect the different electropulsing treatments and references (a) 5% prestrained specimens and (b) 15% prestrained specimens.

The effect of the electropulsing treatments are much more evident in the case of uniform strain and fracture strain rather than UTS and YS (Figure 5.17 and Figure 5.18). In the case of the specimens prestrained at 5%, uniform strain was almost the same of the baseline for the electropulsing treatments conducted at the lower current density. Nevertheless, even at 200 A/mm² a substantial increase in uniform strain was observed in comparison to the untreated material. Much more evident the effect of the electropulsing treatments on the specimens prestrained at 15%. The relative recovery in uniform strain was higher in this case compared to the previous one, a slight constant increase of the uniform strain increasing the current density and the number of pulses was observed (Figure 5.17b).

5.2.3.5. Uniform and fracture strain

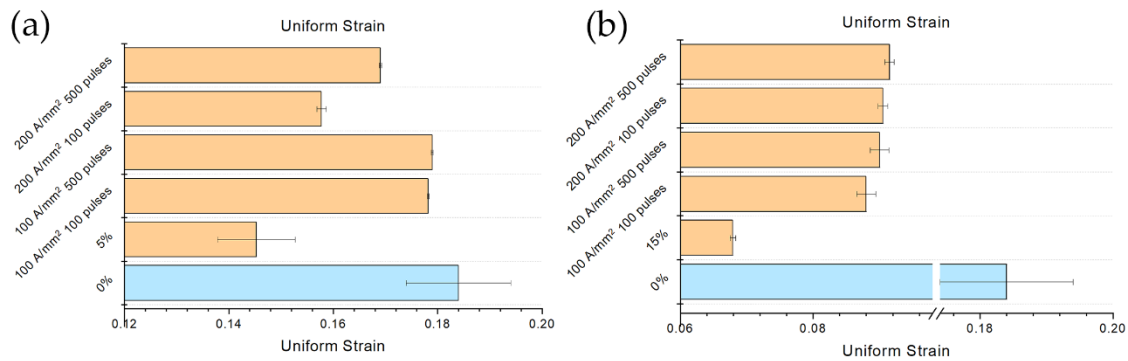


Figure 5.17 Evolution of uniform strain with respect to the different electropulsing treatments and references (a) 5% prestrained specimens and (b) 15% prestrained specimens.

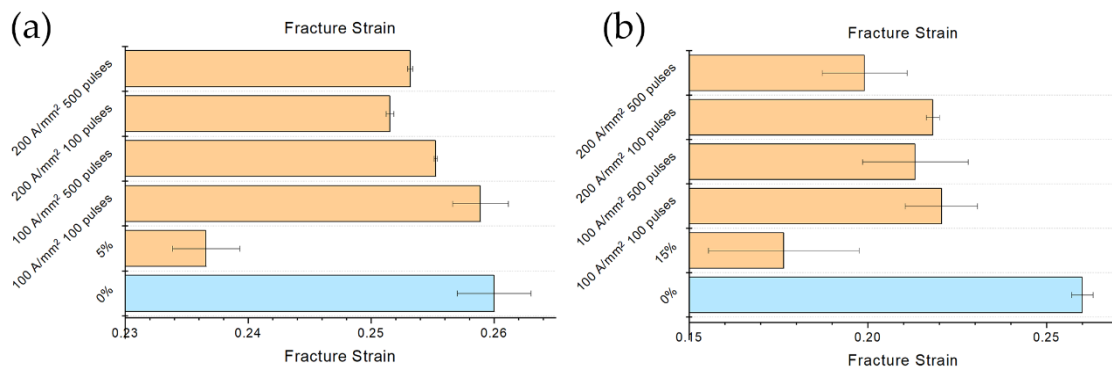


Figure 5.18 Evolution of fracture strain with respect to the different electropulsing treatments and references (a) 5% prestrained specimens and (b) 15% prestrained specimens.

In the case of the specimen prestrained at 5% fracture strain did not show any trend (Figure 5.18a). As said before, the treatment at lower current density and lower number of pulses showed a fracture strain comparable to that of the baseline. Fracture strain of the specimens treated at 200 A/mm², even if it was higher compared to the prestrained material, was slightly inferior to that of the 100 A/mm² treatment. It is clear from Figure 5.18b that, in the case of 15% prestrained specimens, the number of pulses affected in more extent the fracture strain rather than the current density. Treatments conducted with lower number of pulses showed the same increase in fracture strain. The most severe electropulsing treatment (200 A/mm² 500 pulses) increased fracture strain in comparison to the prestrained material but was the worst in terms of

absolute increase in fracture strain. It is worth noting the scattering of the data regarding the test conducted on the specimens prestrained at 15%.

5.2.3.6. *Residual stresses*

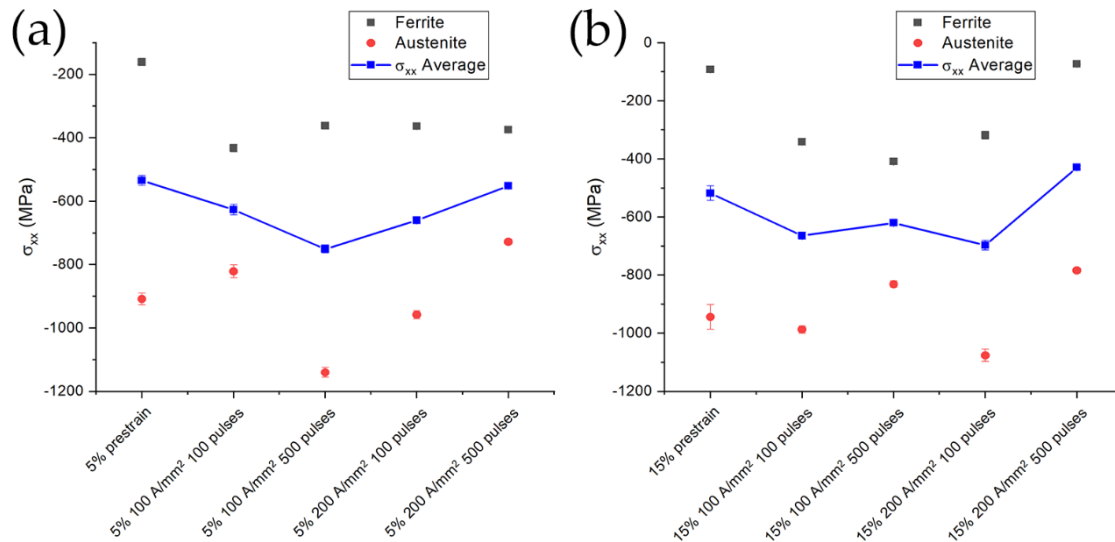


Figure 5.19 Evolution of transverse residual stresses in austenite (red circles), ferrite (black squares) and their average (blue thick line) for specimens prestrained and electropulsed at (a) 5% and (b) 15%.

The average transverse residual stresses for both the specimen showed almost the same values (Figure 5.19). Since the tensile test introduces uniaxial stress state in the specimen, no variation in the average residual internal stresses was expected. On the other hand, electropulsing treatments had shown to induce change in the grain orientation within the materials not to mention the change in the morphology of secondary low resistivity phases (i.e., cementite particles in perlite) hence, a change in the residual stresses of the single phase was expected [12,37–40]. Ferrite increased its compression stress state after the first electropulsing treatment and didn't change it even with the electropulsing treatments at higher current density and number of pulses (Figure 5.19a). In the case of the specimens prestrained at 15%, ferrite increased its compression state (approximately from -50 MPa to -400 MPa) for the low current density treatment. The higher current density treatment decreased the compression state in ferrite from -400 MPa to almost the same value as the

prestrained material (Figure 5.19b). Compression state in austenite was much sever in comparison to that of ferrite (Figure 5.19a) but no significant trend have been observed. Same considerations can be made in the case of the material prestrained at 15% (Figure 5.19b). On the other hand, the average residual stresses in both cases remained almost constant.

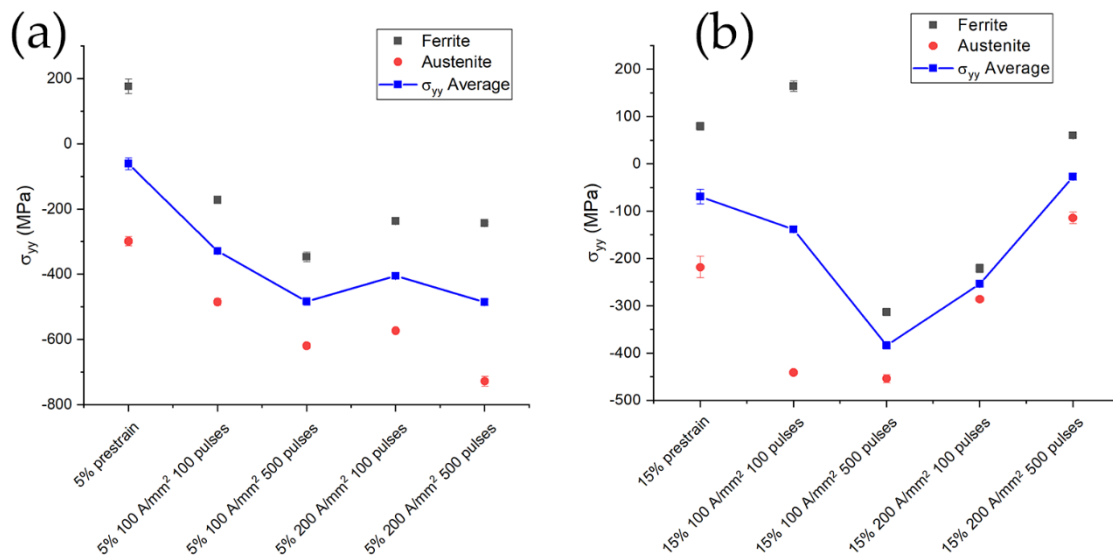


Figure 5.20 Evolution of longitudinal residual stresses in austenite (red circles), ferrite (black squares) and their average (blue thick line) for specimens prestrained and electropulsed at (a) 5% and (b) 15%.

Different evolution of the average residual stresses along the longitudinal direction can be seen in Figure 5.20. A gradual increase in the compression state in the case of the specimen prestrained at 5% was evident (Figure 5.20a) with a slight decrease for the electropulsing treatment of 100 pulses at 200 A/mm². Same trend was observed for the material prestrained at 15% under electropulsing treatment of 100 A/mm², while substantial decrease in the compressive stress state for the treatments conducted at 200 A/mm² were induced. Electropulsing treatments consisting of 500 pulses at 200 A/mm² presented a stress state comparable to that of the prestrained material. Residual stresses for the single phase followed the same trend of the average residual stress both for the specimen prestrained at 5% and 15% as can be seen in Figure 5.20. The only exception was the material prestrained at 15% treated with 100 pulses at 100 A/mm² in which ferrite jumped from a tensile stress state of

approximately 150 MPa to a compressive state of -300 MPa increasing the number of pulses.

5.2.3.7. *X-ray diffraction*

X-ray diffraction measurements were conducted in order to evaluate the evolution of the broadening of the peaks as a function of the specimen conditions.

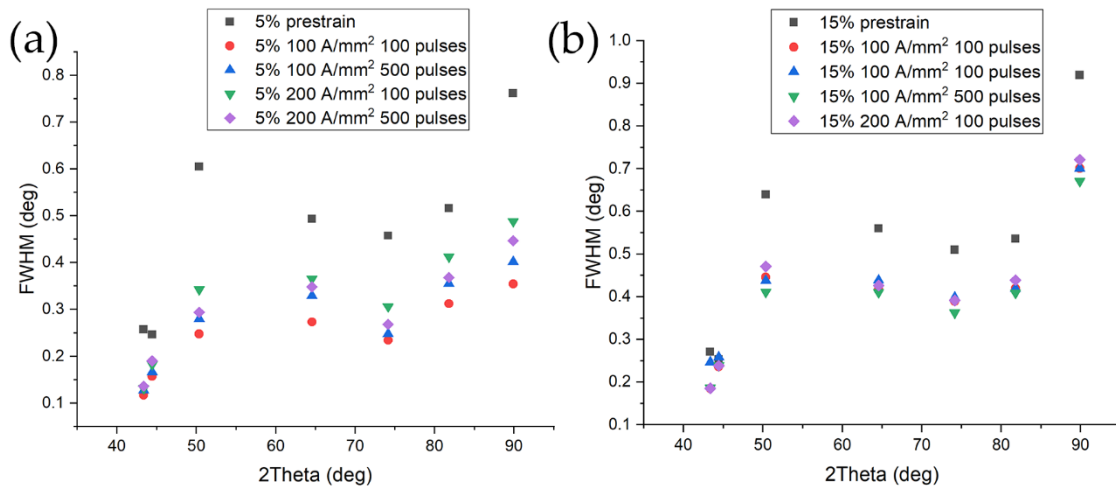


Figure 5.21 FWHM of the electropulsed specimens prestrained at (a) 5% and (b) 15%.

An overview of the evolution of the FWHM of the peaks related to the different treatment conditions is reported in Figure 5.21. Being the FWHM influenced by dislocations density, microstrain, stacking fault and so on, it is obvious that the higher value for the FWHM is that of the specimens prestrained at 5% and 15% (black squares of Figure 5.21). In order to enhance the differences in FWHM of each phase, a separate diagram have been built (Figure 5.22 and Figure 5.23).

As expected from the tensile test curves, the most significance decrease in FWHM for the samples prestrained at 5%, was observed in the case of the treatments that showed the highest recovery in fracture strain (100 pulses at 100 A/mm² in Figure 5.22). A slight increase in FWHM was observed with the other electropulsed treatment, with a subsequent reduction for the

electropulsing treatment at higher current density and number of pulses. It is interesting to note the higher reduction in terms of absolute values for the FWHM relative to the austenitic phase, due to its higher dislocation density because of the low yield point and high work hardening rate compared to ferrite.

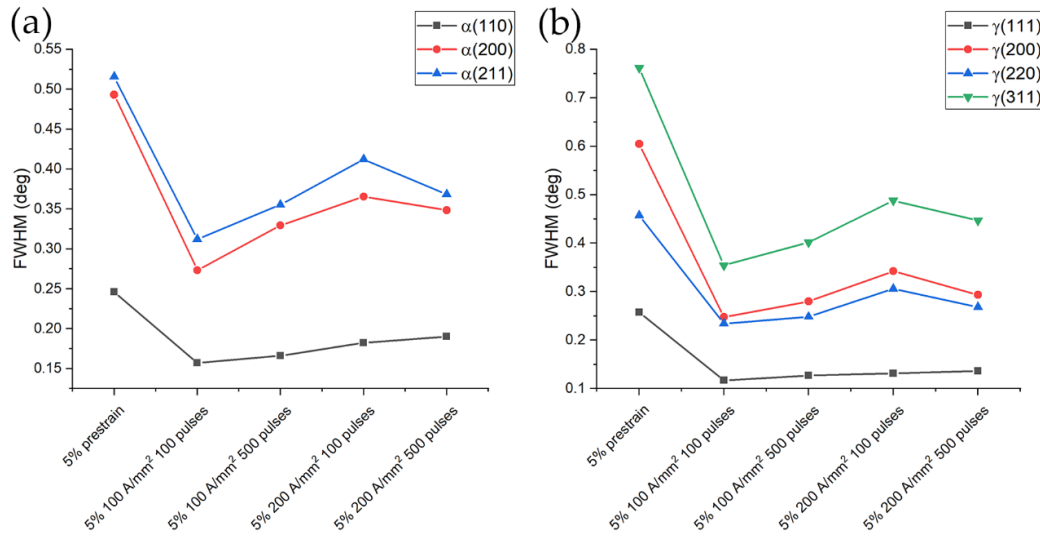


Figure 5.22 FWHM evolution of ferrite (a) and austenite (b) for the specimens prestrained at 5% and electropulsed

The reduction of FWHM in the case of the samples prestrained at 15% was lower in comparison to that prestrained at 5%. Same trend both for the ferritic and austenitic phase was observed (Figure 5.23). FWHM remained almost constant regardless the current density and number of pulses, except a slight increase after 500 pulses at 100 A/mm² (more evident in Figure 5.23a).

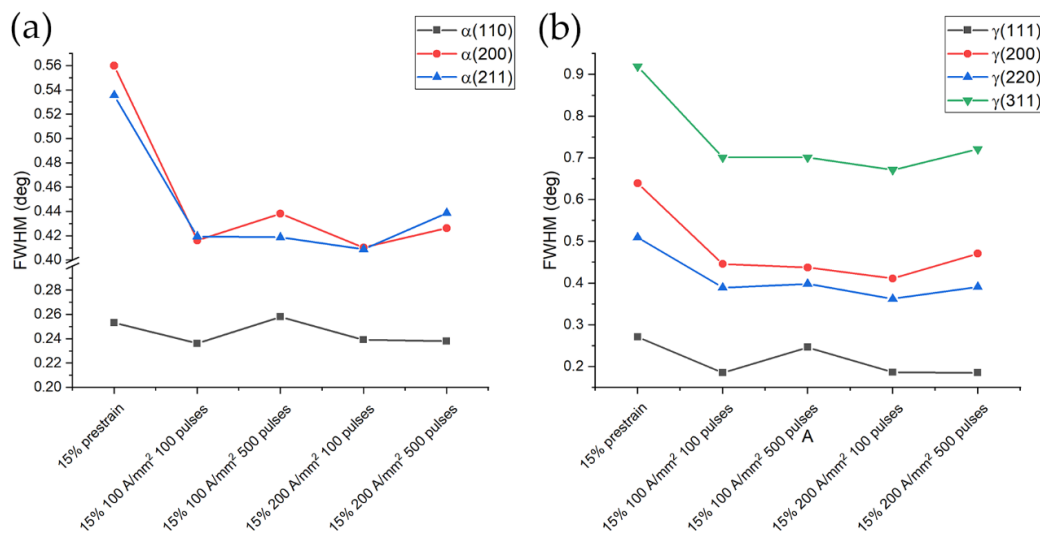


Figure 5.23 FWHM evolution of ferrite (a) and austenite (b) for the specimens prestrained at 15% and electropulsed.

5.2.4. *Discussions*

It is mandatory to understand how duplex stainless steels behave during a tensile test to understand the microscopic changes in dislocation distribution, strain and stress distribution that can affect current flow.

Due to the lower yield stress, austenite is the phase in which most of the strain is localized at the beginning of deformation. It absorbs much of the early stage of deformation because it possesses twelve closely packed slip systems and allows easy dislocation mobility in almost all crystallographic directions while the ferrite possesses less closely packed slip systems, which typically possess higher critically resolved shear stresses for their activation [41]. Even though ferrite has more slip system, its Peierls stress is higher compared to the yield stress of austenite, rendering austenite more ductile than ferrite. Ferrite starts to accommodate plastic deformation after the austenite has work-hardened enough to increase its yield stress above that necessary to overcome the Peierls barriers in ferrite. After that, ferrite starts to accommodate higher plastic strain than austenite, while some austenitic grains strain harden more depending on the orientation relationship between austenite and ferrite (Kurdjumov–Sachs orientation is the most favorable for the transfer of strain field between austenite and ferrite [42–45]). Direct dislocation transfer between austenite and ferrite is obviously impossible due to the phase boundary, but dislocations on the austenitic phase that keep packing on the phase boundary could generate dislocation sources in the adjacent phase. It is, therefore, clear that phase boundaries play an important role in governing the deformation mechanism in duplex stainless steels.

They are also inhomogeneities, saturated with dislocations and stacking faults which produce higher resistivity. When electrical current passes through the material, macro and microscopic effect occur. Bulk joule heating is a macroscopic effect, while at microscopic level electrons from electrical current

interacts with the inhomogeneities in the microstructure. As modeled by Zhao et al. [46], electrical current doesn't flow homogeneously inside the microstructure: in absence of secondary phases it is influenced by the grain boundary network. The grain boundary network will force the current to flow across the "easy-path" of the grain boundary network, such as the triple junctions. As a result, the current flow is distributed based on the angle between the macro current flow and the grain boundaries [46]. This uneven distribution of electrical current could cause local increase in current density which can enhance plastic deformation thanks to localized joule heating and the effect of a stronger electron wind force on dislocations.

In this specific case, on top of grain boundary network, another phase with different crystal structure, dislocation density and composition is present. It is therefore legit to hypothesize an uneven distribution of the current within the material. In correspondence of zones with different electrical resistivity (grain and phase boundary, dislocation tangles, dislocation sub cells walls and so on) there could be an electron stagnation as proposed by Ruszkiewicz et al. [47] and explained in chapter 1. Electron stagnation could cause local increase in electron to atom ratio, leading to lower bonding energy between the ions of the crystal structure therefore easing dislocation motion in the case of applied current during deformation. In this case the effect of the electrical current is in terms of recovery of the work-hardening state thanks to the localized joule heating effect, the reduction in bonding energy and the increase in atomic flux due to electromigration [48–50]. Electrical current will be unevenly distributed in a multiscale manner: at microscopic level dislocation tangles, sub cell walls, grain boundaries and so on affect the current distribution while at an intermediate scale the different resistivity, composition and work hardening state of the two phases could lead to partial redistribution of the current within one phase or the other. All the above mentioned phenomena are concurrent and caused the recovery of the work-hardened state observed in the specimen. On

top of that, possible room temperature grain rotation could have been taken place as observed by Rahnama et al. [11]. In order to investigate grain orientation, further *electron backscattered diffraction* (EBSD) analysis have to be performed and *kernel average misorientation* (KAM) measurements within single grain must be acquired.

5.2.5. *Concluding remarks*

The influence of electropulsing treatment has been investigated on UNS S32750 prestrained duplex stainless steel. It has been found that electropulsing treatment conducted on 5% and 15% prestrained specimens almost eliminate the work-hardening state in the first case, while partially recover the work-hardened state in the second. Interesting to note the increase in yield stress and ultimate tensile strength in the case of the electropulsed specimens prestrained at 15% coupled with the increase both in uniform and fracture strain.

Residual stresses did not show any particular trend: average transversal residual stress remained almost constant even though variation within the single phase was observed. Longitudinal compressive stress state increase in the case of the specimens prestrained at 5% and electropulsed, while in the case of the 15% prestrained samples the highest compressive state was found for the material electropulsed with 500 pulses at 100 A/mm².

The effect of the electropulsing treatment was observed in terms of reduction of FWHM of the peaks of the diffraction pattern. An effect in terms of recovering the work-hardened state thanks to uneven distribution and increased atomic flux due to the electrical current was hypothesized based on the data acquired and the literature.

5.3. References

- [1] Ye, X.; Wang, L.; Tse, Z.T.H.; Tang, G.; Song, G. "Effects of high-energy electropulsing treatment on microstructure, mechanical properties and corrosion behavior of Ti-6Al-4V alloy", **Mater. Sci. Eng. C** (2015), Volume 49, pp.851–860.
- [2] Jeong, H.J.; Park, J. won; Jeong, K.J.; Hwang, N.M.; Hong, S.T.; Han, H.N. "Effect of Pulsed Electric Current on TRIP-Aided Steel", **Int. J. Precis. Eng. Manuf. - Green Technol.** (2019), Volume 6, pp.315–327.
- [3] Sánchez Egea, A.; González Rojas, H.A.; Celentano, D.J.; Travieso-Rodríguez, J.A.; Llumà i Fuentes, J. "Electroplasticity-assisted bottom bending process", **J. Mater. Process. Technol.** (2014), Volume 214, pp.2261–2267.
- [4] Ma, B.; Zhao, Y.; Ma, J.; Guo, H.; Yang, Q. "Formation of local nanocrystalline structure in a boron steel induced by electropulsing", **J. Alloys Compd.** (2013), Volume 549, pp.77–81.
- [5] Ben, D.D.; Yang, H.J.; Ma, Y.R.; Shao, X.H.; Pang, J.C.; Zhang, Z.F. "Rapid hardening of AISI 4340 steel induced by electropulsing treatment", **Mater. Sci. Eng. A** (2018), Volume 725, pp.28–32.
- [6] Conrad, H. "Influence of an electric or magnetic field on the liquid–solid transformation in materials and on the microstructure of the solid", **Mater. Sci. Eng. A** (2000), Volume 287, pp.205–212.
- [7] Rahnama, A.; Qin, R.S. "Effect of electric current pulses on the microstructure and niobium carbide precipitates in a ferritic-pearlitic steel at an elevated temperature", **J. Mater. Res.** (2015), Volume 30, pp.3049–3055.
- [8] Jeong, H.J.; Kim, M.J.; Park, J.W.; Yim, C.D.; Kim, J.J.; Kwon, O.D.; Madakashira, P.P.; Han, H.N. "Effect of pulsed electric current on dissolution of Mg 17 Al 12 phases in as-extruded AZ91 magnesium alloy", **Mater. Sci. Eng. A** (2017), Volume 684, pp.668–676.
- [9] Xiao, H.; Zhang, K.; Shi, C.; Lu, Z.; Jiang, J. "Influence of electropulsing treatment combined with pre-deformation on ageing behavior and mechanical properties of 5A90

- Al-Li alloy*", **J. Alloys Compd.** (2019), Volume 784, pp.1234–1247.
- [10] Hosoi, A.; Nagahama, T.; Ju, Y. "Fatigue crack healing by a controlled high density electric current field", **Mater. Sci. Eng. A** (2012), Volume 533, pp.38–42.
- [11] Rahnama, A.; Qin, R. "Room temperature texturing of austenite/ferrite steel by electropulsing", **Sci. Rep.** (2017), Volume 7, pp.1–6.
- [12] Conrad, H. "Effects of electric current on solid state phase transformations in metals", **Mater. Sci. Eng. A** (2000), Volume 287, pp.227–237.
- [13] Xu, X.; Zhao, Y.; Wang, X.; Zhang, Y.; Ning, Y. "Effect of rapid solid-solution induced by electropulsing on the microstructure and mechanical properties in 7075 Al alloy", **Mater. Sci. Eng. A** (2016), Volume 654, pp.278–281.
- [14] Gallo, F.; Satapathy, S.; Ravi-Chandar, K. "Plastic deformation in electrical conductors subjected to short-duration current pulses", **Mech. Mater.** (2012), Volume 55, pp.146–162.
- [15] Du, X.N.N.; Yin, S.M.M.; Liu, S.C.C.; Wang, B.Q.Q.; Guo, J.D.D. "Effect of the electropulsing on mechanical properties and microstructure of an ECAPed AZ31 Mg alloy", **J. Mater. Res.** (2008), Volume 23, pp.1570–1577.
- [16] Zhu, R.; Jiang, Y.; Guan, L.; Li, H.; Tang, G. "Difference in recrystallization between electropulsing-treated and furnace-treated NiTi alloy", **J. Alloys Compd.** (2016), Volume 658, pp.548–554.
- [17] Guo, J.D.; Wang, X.L.; Dai, W.B. "Microstructure evolution in metals induced by high density electric current pulses", **Mater. Sci. Technol.** (2015), Volume 31, pp.1545–1554.
- [18] Qin, R.S.; Samuel, E.I.; Bhowmik, A. "Electropulse-induced cementite nanoparticle formation in deformed pearlitic steels", **J. Mater. Sci.** (2011), Volume 46, pp.2838–2842.
- [19] Luu, V.; Nguyen, T.; Hong, S.-T.; Jeong, H.-J.; Han, H. "Feasibility of a Two-Stage Forming Process of 316L Austenitic Stainless Steels with Rapid Electrically Assisted Annealing", **Metals (Basel)**. (2018), Volume 8, pp.815.
- [20] Lund, K.; Delblanc, A.; Iversen, A. "Comparing critical pitting temperatures of

- stainless steels measured electrochemically in NaCl and MgCl₂ solutions*", **Eur. Corros. Congr. EUROCORR 2016** (2016), Volume 3, pp.1934–1942.
- [21] Pezzato, L.; Lago, M.; Brunelli, K.; Breda, M.; Calliari, I. "Effect of the Heat Treatment on the Corrosion Resistance of Duplex Stainless Steels", **J. Mater. Eng. Perform.** (2018), Volume 27, pp.3859–3868.
- [22] Nilsson, J.-O. "Super duplex stainless steels", **Mater. Sci. Technol.** (1992), Volume 8, pp.685–700.
- [23] Gennari, C.; Breda, M.; Brunelli, K.; Ramous, E.; Calliari, I. "Influence of small amount of secondary phases on impact toughness of UNS S32205 and Zeron® 100 Duplex Stainless Steel", In Proceedings of the **ESSC and DUPLEX 2017 - 9th European Stainless Steel Conference - Science and Market and 5th European Duplex Stainless Steel Conference and Exhibition**; (2018).
- [24] Breda, M.; Calliari, I.; Ramous, E.; Pizzo, M.; Corain, L.; Straffelini, G. "Ductile-to-brittle transition in a Zeron© 100 SDSS in wrought and aged conditions", **Mater. Sci. Eng. A** (2013), Volume 585, pp.57–65.
- [25] Gennari, C.; Pezzato, L.; Piva, E.; Gobbo, R.; Calliari, I. "Influence of small amount and different morphology of secondary phases on impact toughness of UNS S32205 Duplex Stainless Steel", **Mater. Sci. Eng. A** (2018), Volume 729, pp.149–156.
- [26] Reick, W.; Pohl, M.; Padilha, A.F. "Determination of stacking fault energy of austenite in a duplex stainless steel", **Steel Res.** (1996), Volume 67, pp.253–256.
- [27] Chiu, P.K.; Wang, S.H.; Yang, J.R.; Weng, K.L.; Fang, J. "The effect of strain ratio on morphology of dislocation in low cycle fatigued SAF 2205 DSS", **Mater. Chem. Phys.** (2006), Volume 98, pp.103–110.
- [28] Breda, M.; Brunelli, K.; Grazzi, F.; Scherillo, A.; Calliari, I. "Effects of Cold Rolling and Strain-Induced Martensite Formation in a SAF 2205 Duplex Stainless Steel", **Metall. Mater. Trans. A Phys. Metall. Mater. Sci.** (2015), Volume 46, pp.577–586.
- [29] Williamson, G.K.; Smallman, R.E. "III. Dislocation densities in some annealed and cold-worked metals from measurements on the X-ray Debye-Scherrer spectrum",

- Philos. Mag.** (1956), Volume 1, pp.34–46.
- [30] Scardi, P.; Leoni, M. "Whole powder pattern modelling", **Acta Crystallogr. Sect. A Found. Crystallogr.** (2002), Volume 58, pp.190–200.
- [31] Ungár, T. "Microstructural parameters from X-ray diffraction peak broadening", **Scr. Mater.** (2004), Volume 51, pp.777–781.
- [32] Williamson, G.K.; Smallman, R.E. "X-ray extinction and the effect of cold work on integrated intensities", **Proc. Phys. Soc. Sect. B** (1955), Volume 68, pp.577–585.
- [33] Lutterotti, L. "Total pattern fitting for the combined size-strain-stress-texture determination in thin film diffraction", **Nucl. Instruments Methods Phys. Res. Sect. B Beam Interact. with Mater. Atoms** (2010), Volume 268, pp.334–340.
- [34] Balzar, D. "X-Ray Diffraction Line Broadening: Modeling and Applications to High-Tc Superconductors.", **J. Res. Natl. Inst. Stand. Technol.** (1993), Volume 98, pp.321–353.
- [35] Williamson, G.; Hall, W.. "X-ray line broadening from fided aluminium and wolfram", **Acta Metall.** (1953), Volume 1, pp.22–31.
- [36] Johansson, J.; Odén, M.; Zeng, X.-H. "Evolution of the residual stress state in a duplex stainless steel during loading", **Acta Mater.** (1999), Volume 47, pp.2669–2684.
- [37] Pan, L.; He, W.; Gu, B. "Non-uniform carbon segregation induced by electric current pulse under residual stresses", **J. Mater. Process. Technol.** (2015), Volume 226, pp.247–254.
- [38] Xiang, S.; Zhang, X. "Residual Stress Removal Under Pulsed Electric Current", **Acta Metall. Sin. (English Lett.** (2019).
- [39] Park, G.D.; Tran, V.L.; Hong, S.T.; Jeong, Y.H.; Yeo, T.S.; Nam, M.J.; Kim, M.J.; Jin, S.W.; Han, H.N. "Electrically assisted stress relief annealing of automotive springs", **J. Mech. Sci. Technol.** (2017), Volume 31, pp.3943–3948.
- [40] Sheng, Y.; Hua, Y.; Wang, X.; Zhao, X.; Chen, L.; Zhou, H.; Wang, J.; Berndt, C.C.; Li, W. "Application of High-Density Electropulsing to Improve the Performance of Metallic Materials: Mechanisms, Microstructure and Properties", **Materials**

(Basel). (2018), Volume 11, pp.185.

- [41] Bargel, H.-J.; Schulze, G. *Werkstoffkunde*; Springer-Verlag, (2008); ISBN 354079297X.
- [42] Serre, I.; Salazar, D.; Vogt, J.B. "Atomic force microscopy investigation of surface relief in individual phases of deformed duplex stainless steel", **Mater. Sci. Eng. A** (2008), Volume 492, pp.428–433.
- [43] Haghdadi, N.; Cizek, P.; Hodgson, P.D.; Tari, V.; Rohrer, G.S.; Beladi, H. "Effect of ferrite-to-austenite phase transformation path on the interface crystallographic character distributions in a duplex stainless steel", **Acta Mater.** (2018), Volume 145, pp.196–209.
- [44] Haghdadi, N.; Cizek, P.; Hodgson, P.D.; Beladi, H. "Microstructure dependence of impact toughness in duplex stainless steels", **Mater. Sci. Eng. A** (2019), Volume 745, pp.369–378.
- [45] Gunn, R.N. *Duplex Stainless Steels: Microstructure, Properties and Applications*; Gunn, R.N., Ed.; 1st ed.; Woodhead: Sawston, United Kingdom, Cambridge, United Kingdom, (1997); ISBN 9781855733183.
- [46] Zhao, J.; Wang, G.X.; Dong, Y.; Ye, C. "Multiscale modeling of localized resistive heating in nanocrystalline metals subjected to electropulsing", **J. Appl. Phys.** (2017), Volume 122.
- [47] Ruszkiewicz, B.J.; Mears, L.; Roth, J.T. "Investigation of Heterogeneous Joule Heating as the Explanation for the Transient Electroplastic Stress Drop in Pulsed Tension of 7075-T6 Aluminum", **J. Manuf. Sci. Eng.** (2018), Volume 140, pp.091014.
- [48] Ho, P.S. "Solute Effects on Electromigration", **Phys. Rev. B** (1973), Volume 8, pp.4534–4539.
- [49] Ho, P.S.; Kwok, T. "Electromigration in metals", **Reports Prog. Phys.** (1989), Volume 52, pp.301–348.
- [50] Lin, S.K.; Liu, Y.C.; Chiu, S.J.; Liu, Y.T.; Lee, H.Y. "The electromigration effect revisited: Non-uniform local tensile stress-driven diffusion", **Sci. Rep.** (2017),

Volume 7, pp.1-10.

CONCLUSIONS

This thesis investigated the electroplastic effect on a wide variety of metallic alloys, focusing mainly on the effect that the electric current had on a specific class of stainless steels.

From the preliminary studies it has been found a possible influence of stacking fault energy on the electroplastic effect. Materials that show the same crystal structure (i.e., f.c.c.) have shown to be influenced by electroplastic effect depending on their stacking fault energy. High stacking fault energy f.c.c. materials have shown to be positively affected by continuous electric current during tensile deformation. Increased fracture strain and uniform elongation whilst no sensitive effect on ultimate tensile strength nor yield stress on top of that of temperature have been observed. Ferritic stainless steel showed a better formability, but deformation on b.c.c. materials involves different dislocation mechanism in comparison to f.c.c.. Conversely low stacking fault materials showed a pejorative effect both in terms of fracture/uniform strain and ultimate tensile strength and yield stress.

Titanium grade five did not show positive nor negative effect when deformed under continuous electrical current during uniaxial tensile test. Higher current density is needed which could be possible only using pulsed current in order to limit joule heating. Almost same results were obtained for a lab-grade TWIP stainless steel. No effect at all on fracture strain, uniform strain, ultimate tensile strength and yield stress nor on the strain hardening coefficient was observed. This could be explained by the fact that in TWIP steels a dynamic Hall-Petch effect take place, by which grains get refined by the creation of mechanical twinning within, that acts as strong barrier to dislocation motion. In order for the electric current to interact with this mechanism higher current density could be needed as in titanium grade five case.

Triaxiality stress states have been shown to influence the occurrence of electroplastic effect on AA1050 H24 aluminum alloy. Increased fracture strain up to 15 A/mm² was observed with maximum effect in the case of simple shear. Transmission electron microscopy showed a gradual increase in dislocation density increasing the current density on specimen strained at 0.05. Increased annihilation probability due to higher dislocation mobility thanks to the electrical current was hypothesized.

Duplex stainless steels showed very interesting results during continuous current tensile tests, pulsed current tensile tests and during electropulsing treatment despite the presence of a low stacking fault energy phase dispersed in a high stacking fault energy ferritic matrix. All four grades tested showed increased uniform elongation and fracture strain while ultimate tensile strength and yield stress were not affected under continuous nor pulsed current. Moreover, pulsed current tensile tests showed fracture strain comparable to that of the baseline (room temperature test) despite the increase in temperature. Electropulsing treatment on prestrained duplex stainless steel have been shown to recover most of the work-hardened state (i.e., increasing fracture strain and uniform strain) maintaining higher yield stress and ultimate tensile strength in comparison to that of the prestrained material. An uneven distribution of the electrical current due to the different resistivity and strain hardening rate of the two phases together with stagnation of electron in correspondence of phase and grain boundaries and dislocation tangles could be the explanation for the effects observed in these type of steels. Decreased bonding energy due to localized joule heating, increase in the electron to atom ratio and higher effective electron wind force could be the causes for the positive electroplastic effect observed in duplex stainless steels.

Further investigations with higher current density on different metallic alloys and more in deep studies (i.e., transmission electron microscopy, electron

CONCLUSIONS

backscattered diffraction, etc.) are needed in order to understand how electrical current works and how to exploit this effect from a technological point of view.

APPENDIX A

Influence of small amount and different morphology of secondary phases on impact toughness of UNS S32205 Duplex Stainless Steel

INTRODUCTION

Duplex Stainless Steels (DSSs) are known for their high mechanical and corrosion resistance thanks to the biphasic ferritic-austenitic microstructure. In fact, DSSs are widely used in aggressive environments, like chemical, petrochemical and nuclear plants, oil and gas offshore applications, and pulp and paper industries, as an alternative to the austenitic grades [1–4].

Unfortunately, as compared to the austenitic grades, DSSs suffer from brittle to ductile transition behaviour because of ferrite in the microstructure. In fact, the presence of the BCC ferritic phase in DSSs enhances the tensile properties but decreases the impact toughness, which is directly linked to the ductile to brittle transition behaviour of the BCC crystal structure. On the other hand, as compared to the ferritic grades, the presence of the FCC austenitic phase increases the impact toughness because it accommodates plastic deformation retarding the cleavage fracture of the ferritic phase. The BCC crystalline structure suffers from ductile to brittle transition because the dislocation motion is a thermally activated phenomenon [5]. By contrast, the f.c.c. crystalline structure's dislocation motion is less temperature dependent [2,3].

The characteristic biphasic microstructure of DSSs is not thermodynamically stable; in fact, they are prone to secondary intermetallic phase precipitation. The most common secondary intermetallic phases are χ , σ and R phases along with carbides and nitrides. Secondary phases affect all mechanical and corrosion properties even in small amount, in particular

toughness [6–8]. The first phase to precipitate is an intermetallic metastable compound of iron, chromium and molybdenum ($\text{Fe}_{36}\text{Cr}_{12}\text{Mo}_{10}$), which is known as the χ phase. Its faster precipitation kinetic is due to its lower coherency strain to the cubic lattice as compared to the more thermodynamically stable σ phase [3,9,10]. In fact, the σ phase has a tetragonal closed pack structure of 32 atoms, mainly iron, chromium and molybdenum, varying in a range of compositions [11,12]. Those intermetallic phases are very brittle because of the absence of an easy slip system in their crystal structure. Moreover, owing to their high content in chromium, the surrounding matrix is impoverished in such element causing a drastic deterioration of the corrosion properties [13].

It was possible to change the morphologies and the distribution of secondary phases trimming the treatment temperature and the soaking time in order to precipitate small and fine dispersed particles in one specimen and localized and very coarse on the other [14,15]. This study investigates the influence of different secondary phase morphologies on the impact toughness of standard DSS UNS S32205.

Materials and methods

20 mm bars of DSS UNS S32205 provided by Acciaierie Valbruna S.p.a. were used for the study; the composition is summarized in Table 1.

The bars were solubilized at 1100 °C for 1 hour, water quenched to ensure a secondary phase free microstructure and then cut into 60 mm long pieces.

Two isothermal heat treatments (950 °C for 15 minutes and 850 °C for 5 minutes) were performed in order to obtain 0.02 volume fraction of secondary phases with different morphologies. The 60 mm heat-treated bars were then machined in the longitudinal plane direction by following ASTM A370 standard.

APPENDIX A

Table 1 Chemical composition of UNS S32205 Duplex Stainless Steel (wt.%).

	C	Cr	Ni	Mo	Cu	W	Mn	P	S	Si	N
UNS S32205	0.0223	22.38	5.80	3.15	0.26	0.026	1.44	0.0275	0.001	0.472	0.15

A Cambridge Stereoscan 440 scanning electron microscope (SEM) operating at 29 kV and at room temperature has been used. A backscattered electron detector was used to investigate the microstructure. In non-etched samples, the austenite appears lighter than ferrite due to the content being in high Z elements. The χ phase is brighter than the σ phase because of its high molybdenum content, while nitrides appear dark because of their very low atomic number due to the nitrogen.

Composition were measured by means of an EDS probe EDAX coupled with the SEM.

To measure the volume fraction of austenite, ferrite and secondary phases, an image analysis program on SEM micrographs was used (10 readings per specimen at 1500x), even though magnetic measurements are more accurate [16].

Impact toughness tests were conducted according to ASTM E23-16b standards on a Charpy Zwich/Roll PSW750 capable of producing 450 J.

The impact energy was evaluated in a temperature range between +20 °C to -196 °C for untreated samples and between 20 °C to -90 °C for the heat-treated ones. For each test temperature, three specimens were used, in accordance to the ASTM E23-16b standard. Error bars within Figure 4 and Figure 9 represent the standard deviation of the set of three specimens per test parameters.

The obtained values were then fitted mathematically by using the hyperbolic tangent function (tanh) for both the materials:

$$Y = A + B \cdot \tanh \left(\frac{T - T_0}{C} \right)$$

where Y is the KV energy, T is the test temperature and A , B , T_0 and C are adjustable parameters estimated by regression procedure [17]. T_0 is a location parameter, which provides the inflection point of the curve, and it was considered as the transition temperature from ductile to brittle behaviour even though the ductile to brittle transition occurs in a range of temperatures.

The fracture surfaces were then observed with the SEM Cambridge Stereoscan operating at 15 kV, a Leica DMRE optical microscope and a Zeiss stereo light microscope to better identify the fracture type, crack nucleation and propagation, all the observation were done at room temperature. The optical images of the fractures were taken with a Canon EOS 7D. Lateral expansion was measured to evaluate the plasticity behaviour following section 9.2 of ASTM E23-16b standard.

Results and discussions

Microstructure

Duplex stainless steel UNS S32205 shows a well-balanced microstructure, with $45 \pm 3\%$ of ferrite and $55 \pm 3\%$ of austenite and secondary phase free, as can be observed in Figure 1.

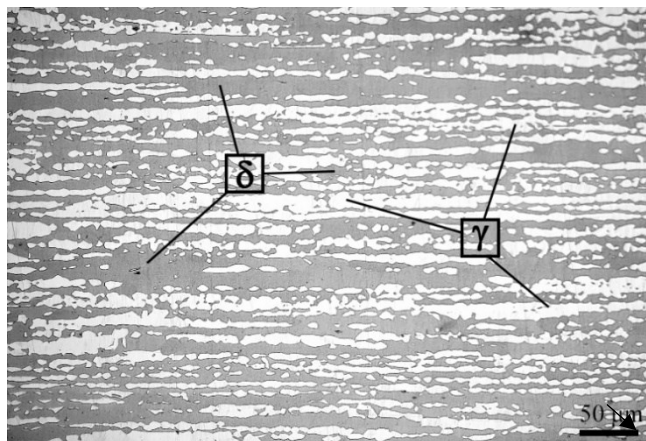


Figure 1 Microstructure of UNS S32205 as received: austenite (white) and ferrite (dark), optical microscope, etched with modified Beraha.

The heat-treated samples have about the same volume fraction of secondary phases with different morphologies and compositions.

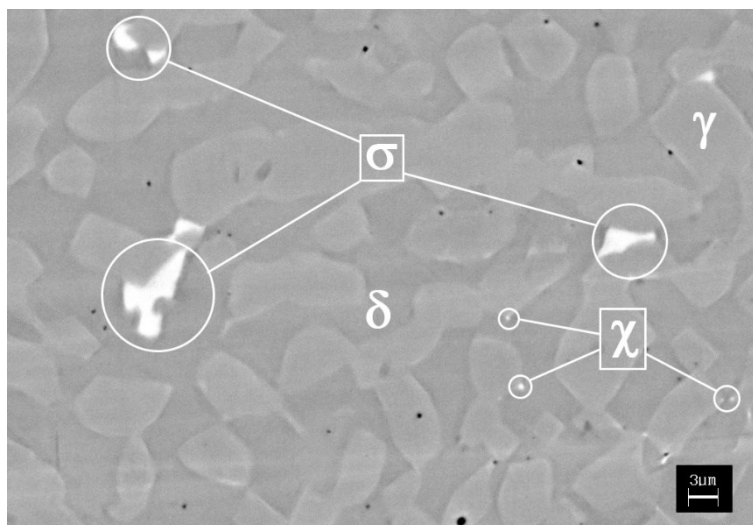


Figure 2 UNS S32205 aged at 950 °C for 15 minutes, small white spots are Chi particles, coarser particle is Sigma phase, austenite (light grey) and ferrite (dark grey).

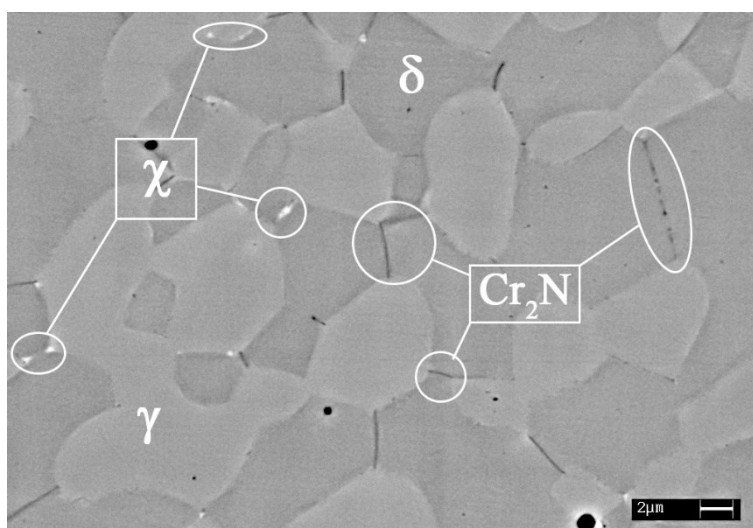


Figure 3 UNS S32205 aged 850 °C for 5 minutes, small white spots are Chi particles, dark networks in-between ferrite grains are nitrides, austenite (light grey) and ferrite (dark grey).

Thanks to its crystal structure coherency with the ferrite matrix, the χ phase is the first to precipitate, even though it is thermodynamically unstable. It precipitates mainly at triple points and at δ/γ interfaces as can be seen in Figure 3, while no χ phase at ferrite/ferrite grain boundary was detected. At longer treatment time, σ phase precipitates due to the eutectoidic decomposition of ferrite into σ phase and secondary austenite. As the temperature and soaking time increase, the σ phase consumes all χ phase and starts to grow as depicted

in Figure 2, even though some χ phase is left at the ferrite/austenite phase boundary.

At lower temperatures, nitrogen diffusion from ferrite to austenite during quenching is hindered. Ferrite/ferrite grain boundaries are preferential paths for diffusion because of the high density of defects. This fact and the decreasing of nitrogen solubility in ferrite during fast cooling are the basis of the chromium nitride precipitation at ferrite/ferrite grain boundaries, as reported in the micrograph. Figure 3 shows dark chains of chromium nitrides between ferrite grains. The overall composition of the σ phase and the χ phase observed in the UNS S32205 DSS are summarized in Table 2.

Table 2 Chemical composition (wt.%) of σ and χ phases in the UNS S32205 aged at 950 °C for 15 min.

	Fe	Cr	Ni	Mo
χ phase	Bal.	25.6	3.3	11.3
σ phase	Bal.	28.8	3.8	8.9

Volume fraction of secondary phases by means of image analysis were of the order of 0.02 ± 0.005 .

Impact toughness: ductile to brittle transition

Dislocation motion in the f.c.c. phase is less temperature dependent compared to b.c.c. phase in fact, austenitic stainless steels don't usually have a ductile to brittle transition temperature, conversely to ferritic stainless steels. Since DSSs microstructure consists of both phases it is expected a smoothed S-shaped curve, with a broader transition region compared to the ferritic stainless steels.

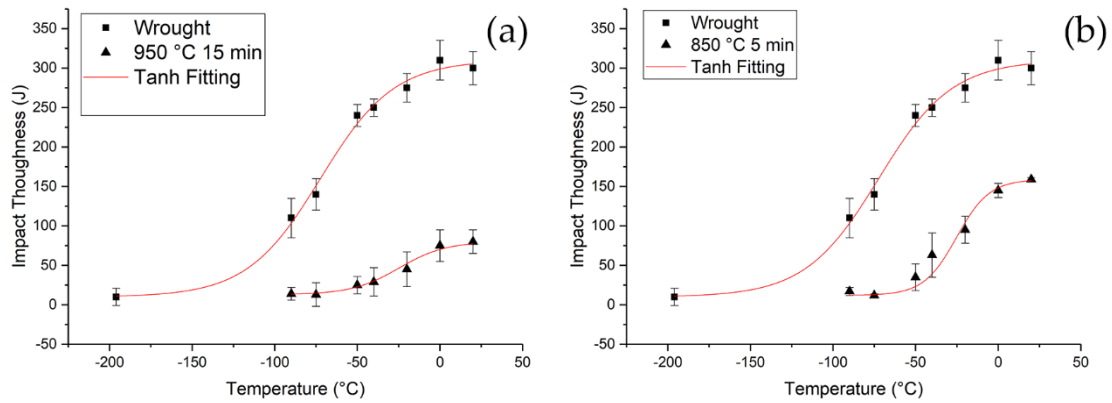


Figure 4 Ductile to brittle transition curves: a) wrought material and material aged at 950 °C for 15 minutes, b) wrought material and material aged at 850 °C for 5 minutes.

Figure 4 shows that the wrought material has an impact toughness of about 300 J at room temperature. Impact toughness starts to decline at -50 °C with a transition temperature of about -72.4 °C, as confirmed by the regression analysis. Nevertheless, the wrought material retains an impact energy higher than 100 J at -90 °C, which is quite good for this type of material. To reach brittle fracture it was necessary to lower the test temperature to -196 °C, which dropped the impact toughness below the brittle threshold of 27 J. The curves do not show a drastic decrease of toughness, as stated before, and the hyperbolic tangent function describes very well the behavior of all the materials, the wrought one and the aged ones.

At room temperature (RT), the wrought material has a very good impact toughness, but a small volume fraction of the order of 0.02 of secondary phases highly influences its value.

A drop of RT impact toughness of about 140 J for the material aged at 850 °C for 5 minutes and a massive drop of 220 J for the material aged at 950 °C for 15 minutes are evident. Both aged materials show a transition temperature derived from the hyperbolic tangent function fitting of about -25 °C, which implies that the ductile to brittle transition temperature is influenced just by the volume fraction of the secondary phases and not by its morphology. As other researchers confirmed [6] secondary phases are likely to act just as crack initiation rather than crack propagation, the last one governed by the duplex

matrix. In Table 3 the results from the hyperbolic tangent fitting function are summarized.

Table 3 Hyperbolic tangent fitting data.

Material	A	B	C	T₀[°C]	USE	X²	R²
Wrought	160	150	44.5	-72.4	310	0.26	0.996
850 °C 5 min	46.5	33.5	32.3	-25.2	80	0.67	0.999
950 °C 15 min	85.5	73.5	19.9	-24.8	159	0.05	0.988

Fracture behavior

The wrought material has an impact toughness of around 300 J at room temperature, while in the two aged samples the absorbed energy is lower because of the presence of brittle secondary phases, but they show as well ductile fracture, which is characterized by dimples and micro dimples depicted in Figure 5. In Figure 5b (upper right corner) and c) it can be seen that, even if the materials retain a good impact toughness at room temperature, there are microfacets and near-cleavage surfaces typical of a brittle fracture in correspondence with a small region close to some cracks. This is because the stress concentration overcame the capability of the steel to deform plastically resulting in a brittle region around those cracks. As stated before, secondary phase particles could have acted as preferential sites for crack initiation rather than preferential crack paths through the structure. A different dimension of the dimples of the aged materials as compared to the wrought one can be seen; this is due to the secondary phase particles, which permitted an easier micro void formation.

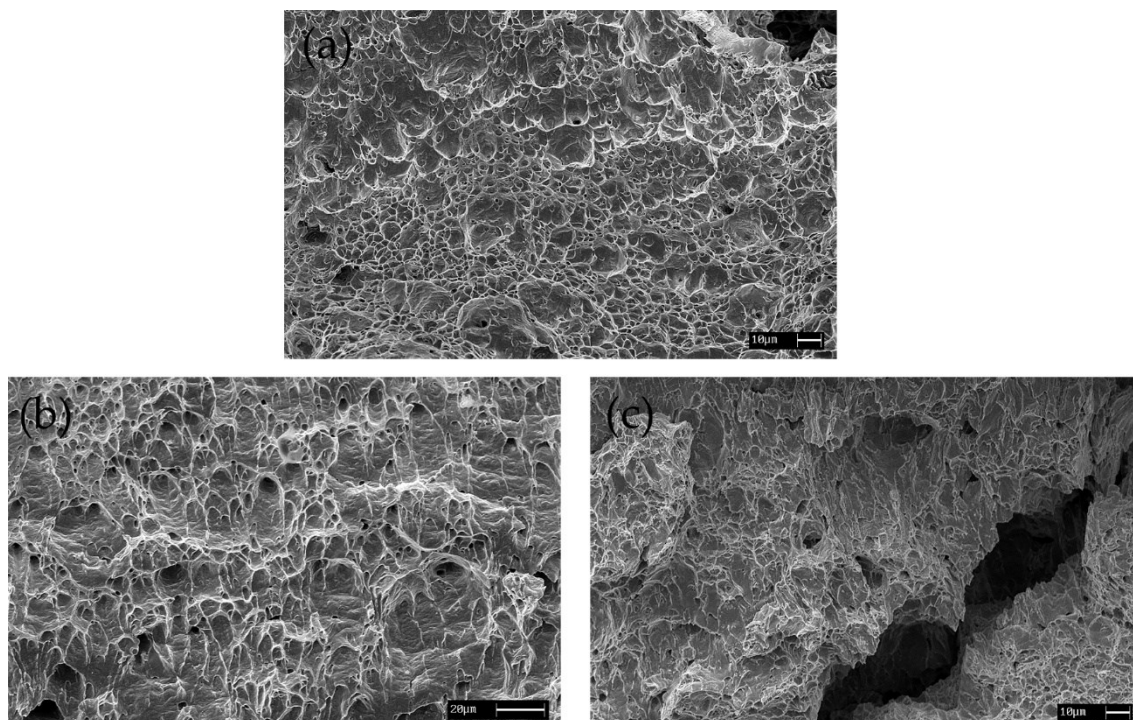


Figure 5 Secondary electron SEM images of fracture surface at 20 °C: a) wrought material, b) material aged at 950 °C for 15 minutes and c) material aged at 850 °C for 5 minutes.

Lowering the temperature down to -50 °C, the as-received materials retain an impact toughness of approximately 250 J, which is higher than those of the aged ones at room temperature. However, even if the absorbed energy is so high, small river patterns near microcracks (Figure 6a) can be observed denoting a change in the behavior of the material from completely ductile to ductile with a small brittle component. At these temperatures the transition from ductile to brittle behavior has already started. The material aged at 950 °C for 15 minutes has an impact toughness of 25 J, which is close to the brittle threshold of 27 J. In fact, there are no dimples or micro dimples, only cleavage surfaces that are characteristic of the brittle fractures, as can be seen in Figure 6b) along with small river patterns. The material aged for 5 minutes at 850 °C has a very low impact toughness at -50 °C (around 35 J), but higher than the brittle threshold. In fact, the fracture is characterized by dimples and micro dimples as well as cleavage surfaces, microfacets, river patterns and tongue (Figure 6c). The first two are typical of ductile fracture, while the others are an indication of the brittle ones, denoting its mixed nature. In addition, the micro

dimples density of the material aged at lower temperature is higher as compared to the wrought one for the same reason as stated before.

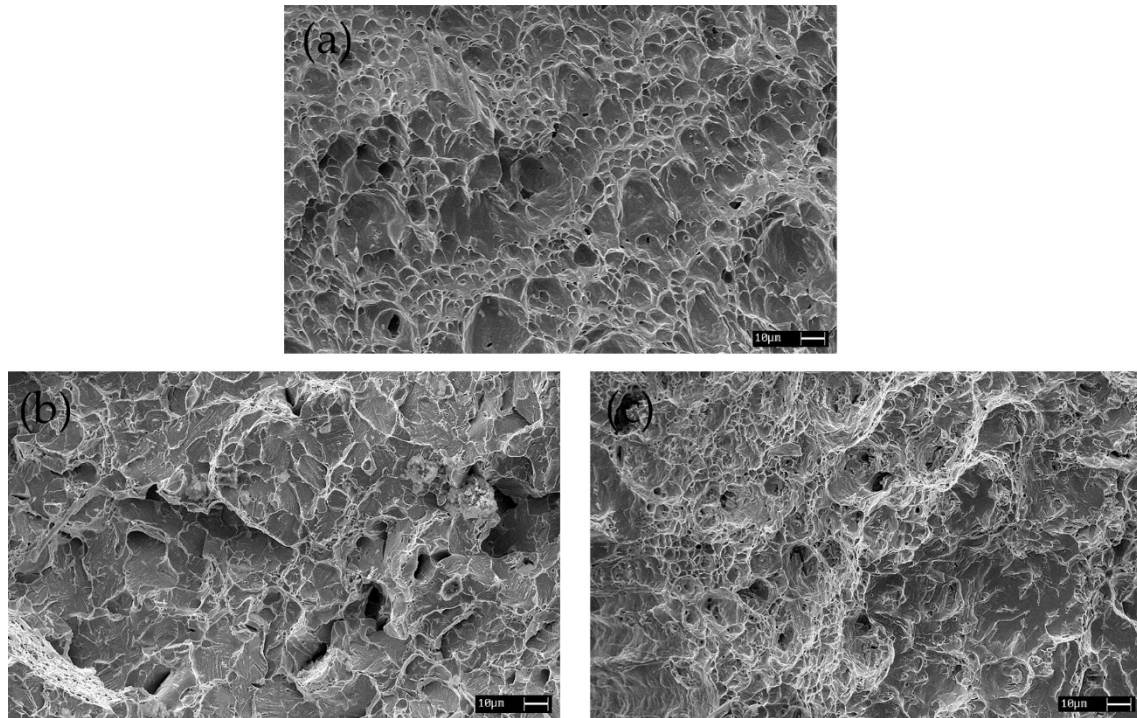


Figure 6 Secondary electron SEM images of fracture surface at $-50\text{ }^{\circ}\text{C}$: a) wrought material, b) material aged at $950\text{ }^{\circ}\text{C}$ for 15 minutes and c) material aged at $850\text{ }^{\circ}\text{C}$ for 5 minutes.

At the lowest temperatures ($-196\text{ }^{\circ}\text{C}$ for the wrought material and $-90\text{ }^{\circ}\text{C}$ for the others) all the materials present a brittle fracture showing quasi-cleavage surfaces, river pattern and tongue characteristic of brittle fracture. All three materials have an impact toughness around 10 J , significantly below the brittle threshold, and not so many differences can be observed between the three fractographies in Figure 7. The macrographs at lower temperature (Figure 7) suggest that the materials did not absorb much energy. In fact, there is no lateral expansion, and the surface is very shiny, typical of a brittle fracture.

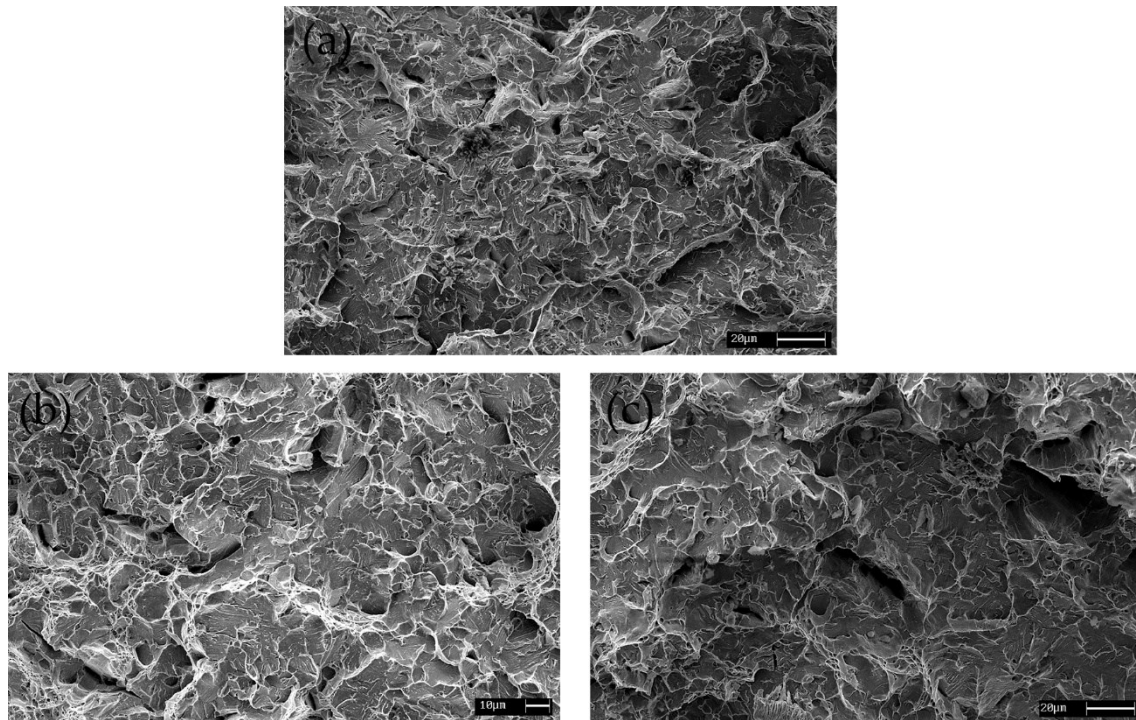


Figure 7 Secondary electron SEM images of fracture surface at lowest temperatures: a) at $-196\text{ }^{\circ}\text{C}$ for wrought material, b) at $-90\text{ }^{\circ}\text{C}$ for material aged at $950\text{ }^{\circ}\text{C}$ for 15 minutes and c) at $-90\text{ }^{\circ}\text{C}$ for material aged at $850\text{ }^{\circ}\text{C}$ for 5 minutes.

In Figure 8 the fracture surfaces of the samples tested at various temperatures are reported. Even if at room temperature all the materials showed a ductile fracture, the material aged at higher temperature and for longer time absorbed less energy as compared to the other one, and this can be seen from the low amount of the specimen's plastic deformation. Lowering the test temperature, the absorbed energy decreases, obviously, along with the plasticity. The specimens highlighted with red circles fell into the brittle region with an absorbed energy less than 27 J. Delamination walls are due to the unstable propagation of the crack along the austenite and ferrite grain boundary. Additionally, some delamination walls are present but in less extent as other researchers reported [6,18].

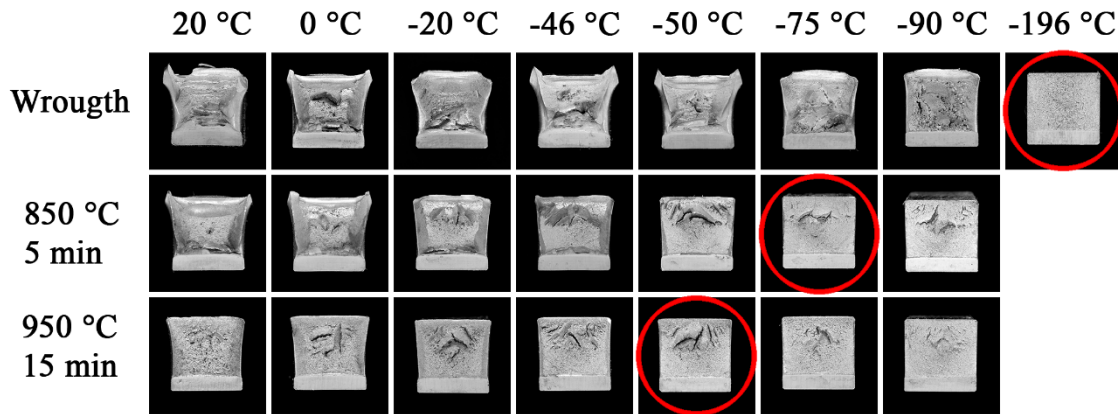


Figure 8 Fracture surfaces of the as-received material and the two materials aged at different temperatures.

Lateral expansion

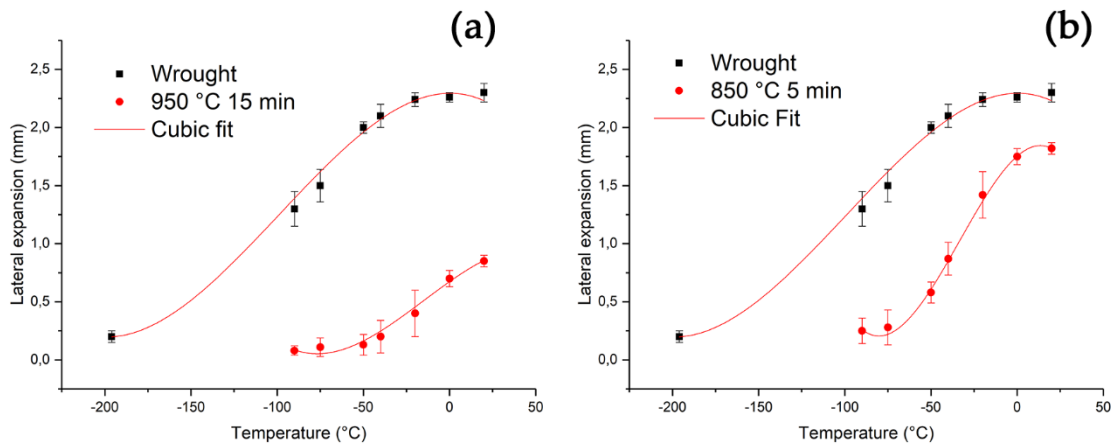


Figure 9 Lateral expansion with cubic fitting: a) wrought material and material aged at 950 °C for 15 minutes, b) wrought material and material aged at 850 °C for 5 minutes.

Lateral expansion is measured on the opposite side of the indentation after the specimen has undergone an impact test. It is a parameter that characterizes the toughness of the material along with the absorbed energy data. It is trivial that the higher the lateral expansion, the higher the ability of the material to plastically deform, which is strictly related to its strength and to the absorbed energy.

Figure 9 presents the evolution of the lateral expansion as a function of the temperature for the three tested materials, and the influence of the secondary phases on the plastic deformation is clear. Even at room temperature, secondary phases affect the plastic deformation of the material. A massive drop of the

lateral expansion with respect to the wrought material as compared to the one aged at higher temperature for a longer time can be observed. For the material aged at lower temperature, it can be seen that the drop of lateral expansion is not as high as in the material aged at 950 °C. Lateral expansion and absorbed energy during Charpy impact test are influenced by the test temperature because of the presence of the ferrite matrix in which dislocation motion is hindered as the temperature gets lower. A synergistic and detrimental effect of temperature along with precipitation of secondary phase intermetallic particles can be supposed. The difference in the drop of impact toughness of the two aged materials as compared to the wrought one can be attributed to the different morphologies of secondary phase particles and how they are involved in the crack nucleation process. Small and dispersed secondary phase particles generate a lot of short cracks, which has less influence on the lateral expansion, as observed in the material aged at 850 °C. Many short cracks are worse than few and longer ones, and the absorbed energy in the first case is much higher because of the new surface area that is formed. M. Scharnweber et al. reported that the work to propagate cracks is higher than that to nucleate them, not to mention the fact that with longer cracks the probability to have one longer than the minimum critical length is higher and that the average crack free path is lower [19].

Figure 10 and Figure 11 show that at the same temperature for all the materials the plastic behavior of the duplex matrix is quite the same, with elongated and deformed grains in correspondence with the notch root. It is therefore plausible to assert that the presence of the secondary phases facilitates the nucleation of cracks rather than their propagation. In particular, in Figure 11b can be seen a lot of cracks that cut through the secondary phase particles.

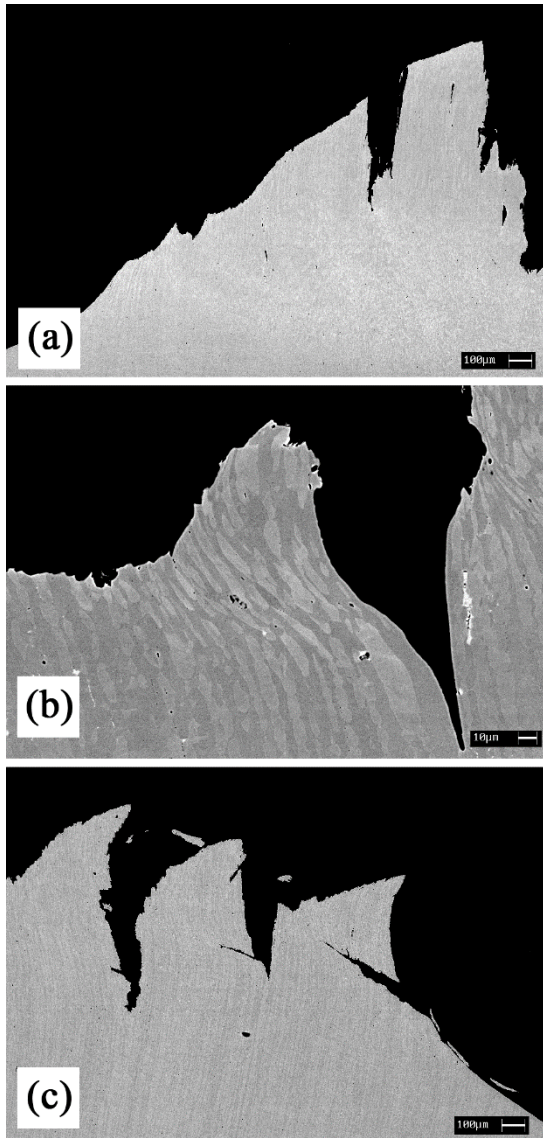


Figure 10 Fracture surfaces at 20 °C near the notch: a) wrought material, b) material aged at 950 °C for 15 minutes and c) material aged at 850 °C for 5 minutes.

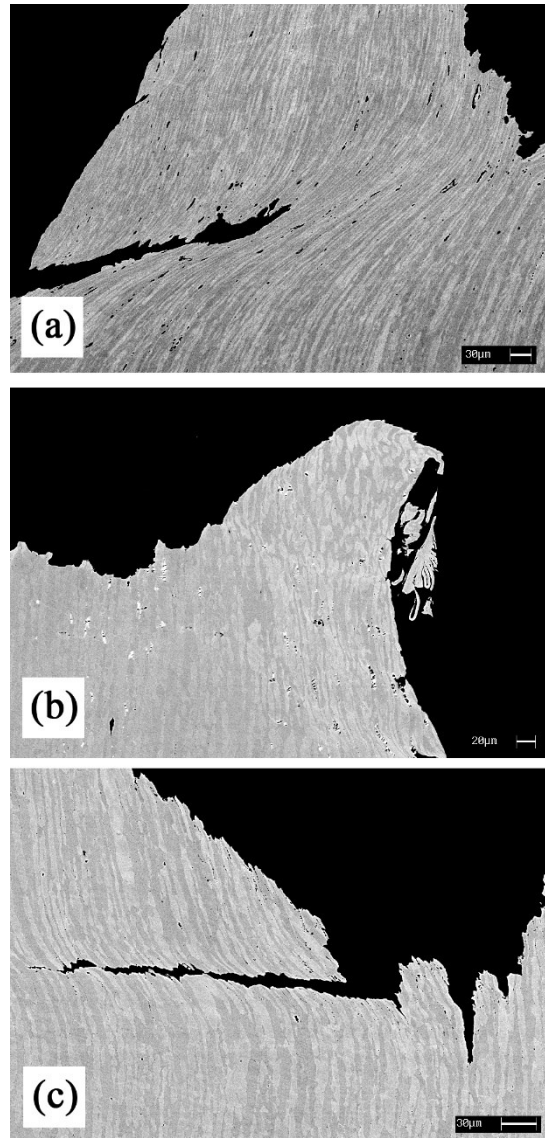


Figure 11 Fracture surfaces at -46 °C near the notch: a) wrought material, b) material aged at 950 °C for 15 minutes and c) material aged at 850 °C for 5 minutes.

Conclusions

The influence of different morphologies and compositions of secondary intermetallic phases in UNS S32205 duplex stainless steel was investigated. The wrought material exhibits a quite high impact toughness at room temperature, and the drop associated with the diminishing of temperature is halfway between austenitic and ferritic steels, with a very smooth S-shaped curve. Even at lower temperature the wrought material retains a very good impact toughness (more than 100 J at -90 °C); it was necessary to lower the temperature to -196 °C to reach brittle fracture. The impact toughness is very good but not as good as the UNS S32705 higher grade [6] .

The precipitation of approximately 0.02 volume fraction of secondary intermetallic phases lowered the absorbed energy starting from room temperature. A massive drop of 220 J was observed in the material with coarse secondary phase morphology and a temperature of ductile to brittle transition of about -25 °C. Finer and more dispersed particles of secondary phases affect the absorbed energy to a lesser extent, which is lowered to about 150 J at room temperature with a ductile to brittle transition temperature of about -25 °C. The ductility of the material aged at 850 °C for 5 minutes is higher as compared to the one aged at 950 °C for 15 minutes but much lower than the wrought material. As in Zeron[®] 100 [6], secondary phases act as preferential crack nucleation sites and lower the average crack free paths dropping the absorbed energy during the Charpy impact test but not affecting so much the ability of the matrix to plastically deform. A substantial difference was observed changing the morphology of secondary phases: smaller and more distributed particles are less detrimental rather than few and coarser ones. Probably, in the latter case the chance to create a crack bigger than the critical length is higher, and crack propagation is much more energy consuming than the nucleation process.

References

- [1] Iris Alvarez Armas, S.D.M. *Duplex Stainless Steels*; Iris Alvarez-Armas, S.D.M., Ed.; Wiley, (2009); ISBN 978-1-848-21137-7.
- [2] Gunn, R.N. *Duplex Stainless Steels: Microstructure, Properties and Applications*; Gunn, R.N., Ed.; 1st ed.; Woodhead: Sawston, United Kingdom, Cambridge, United Kingdom, (1997); ISBN 9781855733183.
- [3] Nilsson, J.O. "*The physical metallurgy of duplex stainless steels*", In *Proceedings of the Duplex stainless steels*; Nilsson, J.O., Ed.; KCI Publishing: Maastricht, Netherlands, (1997); pp. 73–82.
- [4] Nilsson, J.-O. "*Super duplex stainless steels*", **Mater. Sci. Technol.** (1992), Volume 8, pp.685–700.
- [5] Po, G.; Cui, Y.; Rivera, D.; Cereceda, D.; Swinburne, T.D.; Marian, J.; Ghoniem, N. "*A phenomenological dislocation mobility law for bcc metals*", **Acta Mater.** (2016), Volume 119, pp.123–135.
- [6] Breda, M.; Calliari, I.; Ramous, E.; Pizzo, M.; Corain, L.; Straffelini, G. "*Ductile-to-brittle transition in a Zeron© 100 SDSS in wrought and aged conditions*", **Mater. Sci. Eng. A** (2013), Volume 585, pp.57–65.
- [7] Calliari, I.; Ramous, E.; Rebuffi, G.; Straffelini, G. "*Investigation of secondary phases effect on 2205 DSS fracture toughness*", **Metall. Ital.** (2008), Volume 100, pp.5–8.
- [8] Pathak, C.S.; Navale, L.G.; Sahasrabudhe, A.D.; Rathod, M.J. *Analysis of HAZ Fracture Toughness of Duplex Stainless Steel Weldment* (2009), 427–435.
- [9] Chen, T.H.; Weng, K.L.; Yang, J.R. "*The effect of high-temperature exposure on the microstructural stability and toughness property in a 2205 duplex stainless steel*", **Mater. Sci. Eng. A** (2002), Volume 338, pp.259–270.
- [10] Marques, I.J.; Vicente, A. de A.; Tenório, J.A.S.; Santos, T.F. de A. "*Double Kinetics of Intermetallic Phase Precipitation in UNS S32205 Duplex Stainless Steels Submitted to Isothermal Heat Treatment*", **Mater. Res.** (2017), Volume ahead, pp.1–

7.

- [11] Hsieh, C.-C.; Wu, W. "Overview of Intermetallic Sigma Phase Precipitation in Stainless Steels", **ISRN Metall.** (2012), Volume 2012, pp.1–16.
- [12] Magnabosco, R. "Kinetics of Sigma Phase Formation In a Duplex Stainless Steel 2 . Experimental Procedure", **Mater. Res.** (2009), Volume 12, pp.321–327.
- [13] Breda, M.; Pezzato, L.; Pizzo, M.; Calliari, I. "Effect of cold rolling on pitting resistance in duplex stainless steels", **La Metall. Ital.** (2014), Volume 6, pp.15–19.
- [14] Calliari, I.; Zanesco, M.; Ramous, E. "Precipitazione di fasi secondarie in un acciaio duplex 2205 trattato isotermicamente", **Metall. Ital.** (2004), Volume 96, pp.41–45.
- [15] Calliari, I.; Pellizzari, M.; Zanellato, M.; Ramous, E. "The phase stability in Cr-Ni and Cr-Mn duplex stainless steels", **J. Mater. Sci.** (2011), Volume 46, pp.6916–6924.
- [16] Ginzler, J.; Mészáros, I.; Dévényi, L.; Hidasi, B.; Potgieter, J.H. "Magnetic investigations of stainless steels", **Int. J. Press. Vessel. Pip.** (1995).
- [17] Oldfield, W. "Fitting curves to Toughness data", **J. Test. Eval. ASTM Int.** (1979), Volume 7, pp.326–333.
- [18] Erauzkin, E.; Irisarri, A.M. "Influence of microstructure on the fracture toughness and fracture topography of a duplex stainless steel", **Fatigue Fract. Eng. Mater. Struct.** (1992), Volume 15, pp.129–137.
- [19] Scharnweber, M.; Tirschler, W.; Oertel, C.G.; Skrotzki, W. "Initiation and propagation of short cracks in austenitic-ferritic duplex steel", **Mater. Sci. Eng. A** (2013), Volume 583, pp.52–60.

APPENDIX B

Microstructural and corrosion properties of cold rolled laser welded UNS S32750 duplex stainless steel

INTRODUCTION

Duplex stainless steels (DSSs) are a family of steel with a biphasic microstructure consisting of ferrite and austenite. They are widely used in very aggressive environment like nuclear and petrochemical plants, oil and gas offshore applications, chemical plants, paper and pulp industries, food and beverages industries as an alternative to the austenitic stainless steels [1–4]. They have higher mechanical properties and corrosion resistance compared to the austenitic stainless steels but suffer from secondary phases embrittlement and cannot be used at temperature higher than 350 °C [5,6].

The optimum properties of super duplex stainless steels are achieved when approximately equal amount of ferrite and austenite are present in the microstructure. This balanced ratio between the two phases is obtained with a suitable combination of chemical composition and solution heat treatment [3,7]. However, during welding processes the microstructure can undergo detrimental transformations. DSSs solidifies starting from a fully ferritic microstructure and, as the material cools down to room temperature, the ferrite transforms into austenite through solid-state transformation [1–4,7,8]. With an improper cooling rate, two main problems may arise: an unbalanced austenite-ferrite ratio, and the precipitation of secondary phases in the weld zone (WZ) and heat-affected zone (HAZ) [9] which can both affect the mechanical properties, in particular impact toughness [10–13] and corrosion resistance [14,15].

Even though it is thermodynamically unstable, the first phase to precipitate is χ phase thanks to its lattice parameter close to three times that of ferrite, followed by σ -phase, both growing toward the ferrite phase, eventually consuming all of it [3,13,16]. Because of its higher content in high atomic number element (i.e. molybdenum and chromium) those secondary phases appear lighter in backscattered-electrons. Chromium nitrides, on the other hands, appear as a dark chain because of the lower atomic number of the constituent located at ferrite/ferrite grain boundary or ferrite/austenite phase boundaries. Nitrogen solubility in ferrite is considerably lower as compared to austenite, moreover it drops as the temperature decreases and nitrogen do not have enough time to diffuse in the austenite resulting in chromium nitrides precipitation [3].

Therefore, the study of weldability of super duplex stainless steels is a fundamental task for their proper industrial application. Previous investigation demonstrated that conventional welding processes as submerged arc welding (SAW) [17–19], plasma arc welding (PAW) [20–22], gas tungsten arc welding (GTAW) [23–25], and friction stir welding [26–28] highly affected the ratio between austenite and ferrite, promoting the precipitation of secondary harmful phases. For this reason, in recent years high power laser welding has seen a remarkable increase in research interest, due to its better precision, speed and versatility compared to traditional welding processes [29–31]. While earlier researchers studied the effect of laser beam parameters on microstructure and properties of DSSs [8,9,32,33], few focused on the change in ferrite-austenite ratio in SDSS welding [34–37].

In this work, the effects of Nd:YAG laser welding on microstructure and mechanical and corrosion properties of UNS S32750 SDSS samples with seven different grades of thickness reduction ($\epsilon = 0\%$, 9.6% , 21.1% , 29.6% , 39.4% , 49.5% , 60.3%) are studied.

Materials and methods

The UNS S32750 super duplex stainless steel were kindly supplied by Outokumpu S.p.a.. Its composition is reported in Table 1.

Table 1. Chemical composition (wt.%) of UNS S32750.

	C	Mn	P	S	Si	Cu	Ni	Cr	Mo	N
UNS S32750	0.021	0.822	0.0231	0.0004	0.313	0.178	6.592	24.792	3.705	0.2644

The as received material was a 15 mm thickness plate, previously solution annealed at 1100 °C for 1 hour and water quenched. Three sets of seven specimens 100 mm long and 10 mm wide were cut to undergo plastic deformation through cold rolling process. The samples were deformed along the hot rolling direction, using a double cylinder mill with a reduction per pass of 0.25 mm. The 9.6%, 21.1%, 29.6%, 39.4%, 49.9% and 60.3%. thickness reductions were applied, and the average strain rate was 0.15 s⁻¹.

To perform the laser beam welding, each specimen was milled to the dimension of 70 x 15 x 3 mm. The welds were performed with a 4 kW Rofin-Sinar DY 044 Nd:YAG laser assisted with a six-axis robot from ABB. To prevent distortion while welding, the samples were clamped to the workbench. The shielding gas used was argon with a purity of 99.995%.

All the specimens were butt-welded using the weld parameters summarized in Table 2 in order to achieve full penetration of the welds.

Table 2. Laser welding parameters.

Parameters	Value
Average power	1400 W
Welding speed	450 mm/min
Defocusing distance	0 mm
Spot Diameter	0.2 mm
Shielding gas flow rate	10 l/min

After the welding process, the specimens were cut transversal with respect to the weld direction for the metallographic analysis. Microhardness tests were performed in the cross surfaces of the welded samples following the ASTM E384 standard using a Buehler IndentaMet™ 1105, with a load of 300 g and an application time of 11 s. Corrosion resistance was evaluated on the surface of both welded and unwelded samples testing the weld bead surface and the longitudinal section of the unwelded sample. The content of ferrite in the weld bead was measured with Eddy's current test (ECT), a non-destructive electromagnetic test method, which uses electromagnetic induction to detect and characterize surface and sub-surface flaws, as well as ferromagnetic phase content in conductive materials.

To analyse the microstructure of the welds, all the samples were first mounted on a phenolic resin and then grinded to 1200 grit SiC paper and polished with diamond suspensions (6 µm and 1 µm) to a mirror like surface finish. After the polishing process, the samples were electrolytically etched at voltage ranging from 2 to 20 V with 20% sodium hydroxide to distinguish austenite from ferrite since this last one is preferentially etched.

The metallographic analysis was then performed with a Leica DMRE optical microscope and with a Leica Cambridge Stereoscan 440 scanning electron microscope, operating in secondary electron (15 kV) and backscattered electron (29 kV).

The corrosion resistance was evaluated by mean of the critical pitting temperature test (CPT) in order to correlate the microstructure modifications to the corrosion properties [15].

The CPT was determined following the ASTM G150 standard. A potentiostat AMEL 7060 was used, the equipment consisted of two cells, containing the same aqueous solution (1 M of NaCl), and electrically connected by a salt bridge; in the first cell, maintained at room temperature, the reference electrode (calomel) was immersed, whereas the counter electrode (platinum)

and the sample were placed in the second cell, where the temperature was controlled by a thermostatic bath.

The ASTM G150 standard involves the evaluation of the CPT by maintaining a constant anodic potential of 700 mV vs SCE and increasing the temperature of the thermostatic cell at the rate of 1°C/min. Before the test the open circuit potential (OCP) was evaluated letting the system stabilize for 60 min. The CPT is determined when the current density reaches 100 $\mu\text{A}/\text{cm}^2$ and remains above this level for a minimum of 60 s. The tests were conducted until the occurrence of stable pitting and then stopped to prevent excessive corrosion of the specimen.

The CPT determination was performed both for un-welded and welded samples, by exposing 1 cm^2 . In detail the samples were varnished with a thermal-resistant varnish letting exposed the selected area. This area include both the WZ and the HAZ due to the low dimensions of the HAZ in this type of welds. The corroded samples were then analyzed at the Stereomicroscope Zeiss Stereoscan Stemi C2000.

To determine the ferrite content on the welded samples, 13 ECT measurements were performed on the top section of each sample, starting from the middle of the joint. The distance between each detection point was 1 mm. The inspection was done at 4 different frequencies: 10,0 kHz, 40,0 kHz, 66,7 kHz and 100,0 kHz. The data acquisition, processing and the control of the set-up were done with ScanMax software.

Eddy-current testing (ECT) is a non-destructive electromagnetic test method, which uses electromagnetic induction to detect and characterize surface and sub-surface flaws, as well as ferromagnetic phase content in conductive materials. In an eddy current probe, a coil of conductive wire is excited with an alternating electrical current. This current produces an alternating magnetic field around the coil, which oscillates at the same frequency as the current. If the probe and its magnetic field are placed close to a

conductive material a circular flow of electrons, known as an eddy current, will begin to move through the metal. That eddy current flowing through the metal will, in turn, generate its own magnetic field, which will interact with the coil and its field through mutual inductance. Changes in metal thickness or defects, like near-surface cracking, will interrupt or alter the amplitude and pattern of the eddy current and the resulting magnetic field. This in turn affects the movement of electrons in the coil by varying its electrical impedance. Changes in the impedance amplitude and phase angle can be correlated with the volume fraction of magnetic phase in the material.

Results and discussions

Microstructure

The microstructure of the UNS S32750 SDSS base material is shown in Figure 1. The picture displays a biphasic microstructure with approximately equal volumes fraction of ferrite and austenite. Austenite phase (white) is orientated along the rolling direction (black arrow) dispersed in a ferrite matrix (blue-brown).

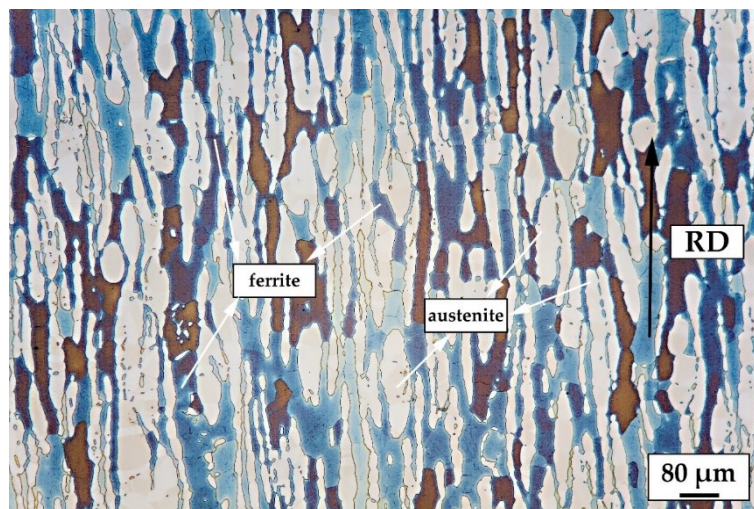


Figure 1 Microstructure of as received UN S32750 bar.

The microstructure of weld bead cross section (Figure 2) confirms the peculiarity of laser beam welding, where the development of the weld is

essentially symmetrical with respect to the axis of the laser beam [9]. The Y-type shape weld bead is because of the relatively low welding speed (450 mm/min) conversely to the classical V-type shape for welding speed greater than 2000 mm/min [38]. Elongated ferrite grains along the heat flux direction with austenite dispersed inside and along ferritic grain boundaries are evident. The highly oriented and elongated shape of ferritic grains is due to the high cooling rate, that in laser beam welding was estimated to be around 1000 °C/s [9,29,39]. Because of this remarkable cooling rate, the HAZ (region between dashed lines in Figure 3) was almost undetectable.



Figure 2 Overview of weld bead of the undeformed sample (electrolytic etching at 20 V with 20% NaOH).

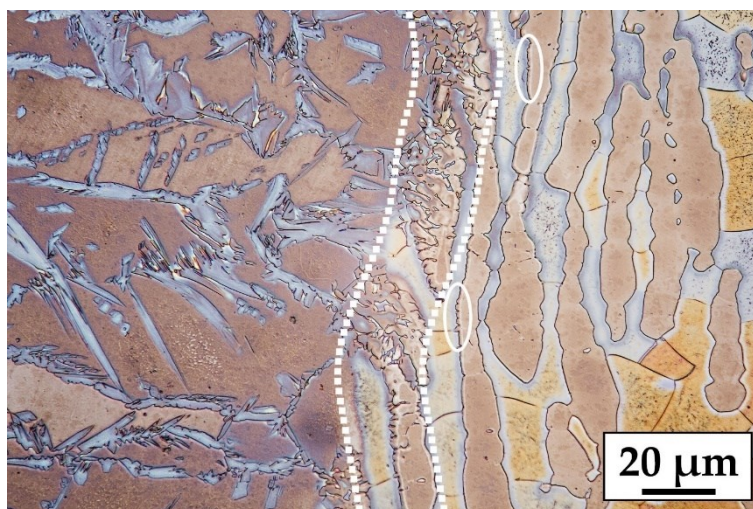


Figure 3 Heat Affected Zone (HAZ) of the sample deformed at 29.6%.

The fusion line is continuous and clear, with the ferritic grains emanated from the base material grains as well as the austenitic grains. The HAZ zone (between dashed lines) is very narrow due to the high heat input of the laser and its spot size. The temperature reached in the HAZ is not high enough to melt the material, but it is high enough to modify the phase balance towards ferrite (i.e. phase balance is temperature and composition dependent, for this DSS grade, a balanced microstructure is usually obtained at approximately 1150 °C). Fragmentation of austenite grains inside the dashed line is due to the temperature reached in this region which, as stated before, changed the phase balance of the base material toward ferrite since DSS starts to solidify from a fully ferritic microstructure. The segmentation of some austenitic-ferritic phase boundary (ellipses) is probably because the temperature reached in that region was high enough to start the dissolution of austenite inside the ferrite but not for long enough time to completely solubilize the austenite.

In agreement with the CCT diagram of σ -phase precipitation for a UNS S32750 [39], no precipitates were observed in this region, as can be seen from the scanning electron micrograph in backscattered electrons in Figure 4.

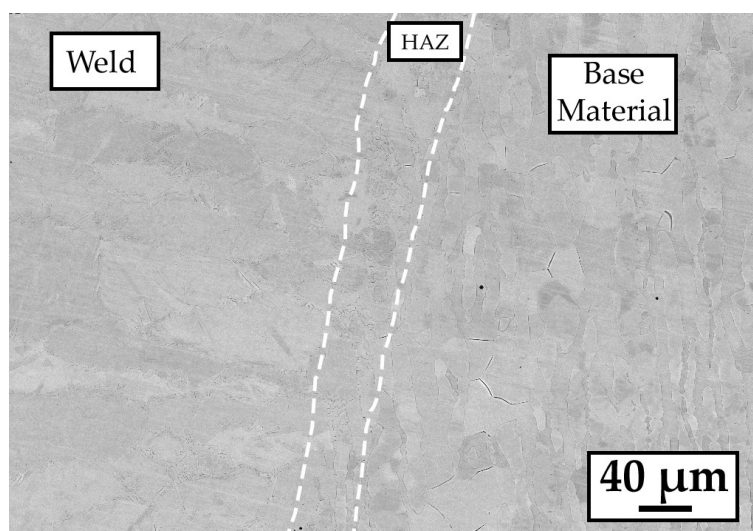


Figure 4 Back-scattered electron micrograph of the HAZ region (center), the weld bead (left) and the base metal (right).

Secondary phases should appear as a lighter spot located mostly at the triple points between ferrite grains and at the interphase boundary between

austenite and ferrite, while chromium nitrides should appear as dark chains at ferrite/ferrite grain boundaries. In this case the dark appearance of both austenite and ferrite grain boundaries of Figure 4 is due to the etching, it would not be possible otherwise to distinguish austenite from ferrite because of the similar composition that results in low contrast on backscattered electrons images. Previous SEM-WDS examinations have been performed without etching, asserting the absence of chromium nitrides. In the welded region, deformation does not influence the precipitation of secondary phases, in fact the results are similar to the one reported in Figure 4 for the undeformed sample with no secondary phases or chromium nitrides detected, due to high cooling rate for all the samples.

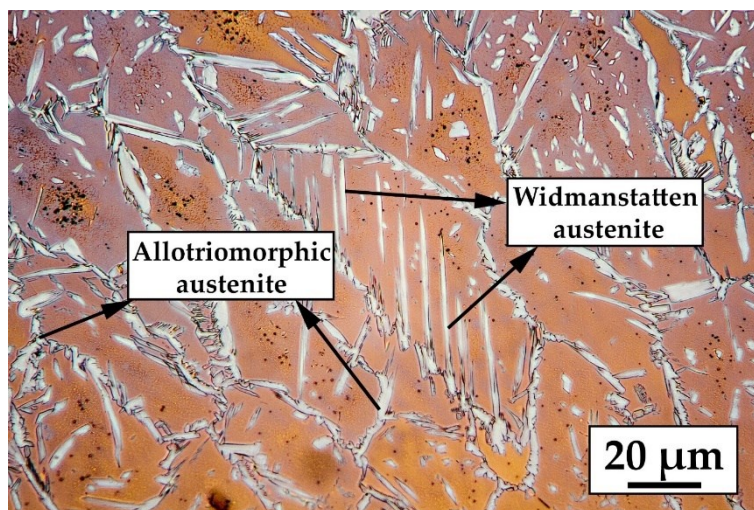


Figure 5 Microstructure of the welded zone showing austenite (light phase) and ferrite (brown matrix).

As previously mentioned, the weld zone initially solidifies into a fully ferritic microstructure, and later partially transforms into austenite through solid-state transformation. Because of the high cooling rate of laser welding, this transformation tends to be inhibited, resulting in a strongly unbalanced microstructure mostly consisting of ferritic phase [8,9,29]. It is clear from the micrographs in Figure 5 that the welded zone is mainly composed of massive ferrite grains, with a low volume fraction of austenite that grew both at ferrite grain boundaries and within the ferrite grains. Austenite nucleated at ferrite grain boundaries is allotriomorphic austenite while the elongate needle-like

grains that grows from the grain boundary inside the ferritic grains is Widmanstätten austenite (Figure 5). The polygonal grains of austenite inside ferrite grains could be isomorphous austenite, Widmanstätten austenite emanated from the grain boundary inside the material or fragmented Widmanstätten austenite due to the decomposition of the latter at lower temperatures as other researchers found [40,41].

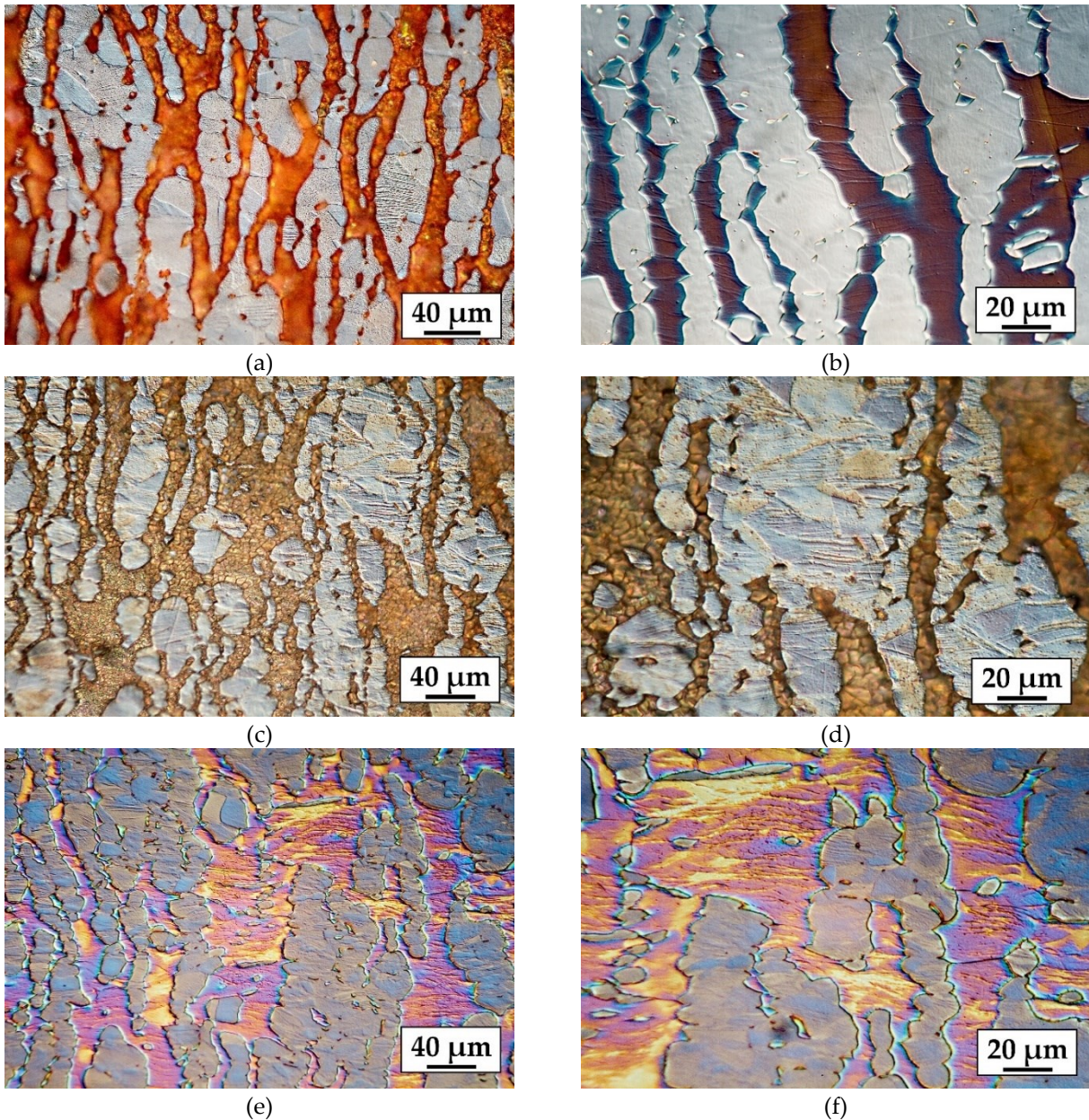


Figure 6 Deformation bands inside austenite and ferrite due to thickness reduction : (a) 29.6% thickness reduction, (b) 39.9% thickness reduction, (c,d) 49.9% thickness reduction, (e,f) 60.3% thickness reduction.

In order to observe the influence of the cold working on the austenite it was necessary to extend the etching time which caused the saturation of ferrite

with etching products. The higher the thickness reduction the higher the density of slip bands inside austenite and ferrite (Figure 6b, e, f). In low stacking fault energy phases, dislocations are split into partial, thus they can only move by gliding in its own crystal plane. This produces a planar distribution of dislocations among the same crystal. Slip bands are a direct consequence of this distribution, in which a lot of dislocation are piled up. Usually this does not happen in high stacking fault energy phases (i.e. ferrite), but due to the presence of austenite and its crystallographic compatibility with ferrite (Kurdjumov–Sachs crystallographic orientation) it is possible that piled up dislocation at austenite/ferrite interfaces will extend to the ferrite grains [42].

Microhardness

Microhardness evolution in the welded region, in the heat affected zone and in the base material is depicted in Figure 7. Regarding the microhardness of the base material (blue line) it is clear the ascending trend due to strain hardening which lead to generation and interaction of dislocations, causing an inevitable increase in hardness [30,43,44]. The microhardness in the welded region is approximately 300 HV and it is not related to the different thickness reduction. This is obviously due to the fact that the material melts, so the previous plastic deformation does not influence the hardness of the region. The hardness of the HAZ is slightly lower than that of the welded region because, even though the region is very narrow, the heat input due to the welding process fully recovers the plastic deformation (the hardness of the HAZ does not follow the trend of the base material) as well as partial dissolution of austenite which changes the phase balance toward ferrite occurs, as can be seen in Figure 3.

Overall the hardness of the welded region and the HAZ is higher compared to the un-deformed base material. This is related to the volume

fraction of ferrite which is higher in the HAZ and in the welded region compared to the base metal.

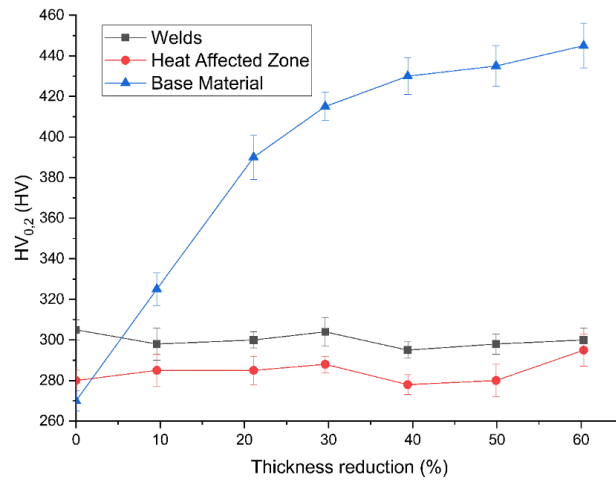


Figure 7 Evolution of hardness with respect to thickness reduction for the welds, the HAZ and the base material.

Corrosion pitting temperature (CPT)

The determination of the critical pitting temperature allows determining a very useful parameter in materials evaluation for applications in chlorinated environments.

The results of the CPT tests performed on the as received plate and on the cold rolled samples both welded and unwelded, are reported in Figure 8-9 and in Table 3-4. The results in the tables are the average obtained from three measurements for each sample.

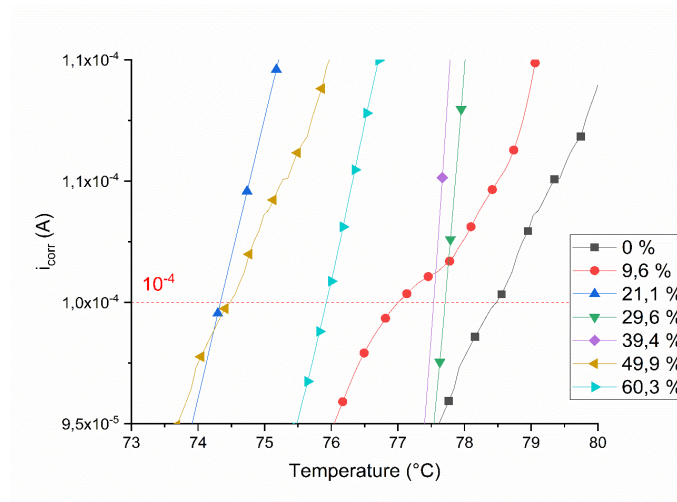


Figure 8 Close-up of the region of interest of the CPT curves of welded sheet metal.

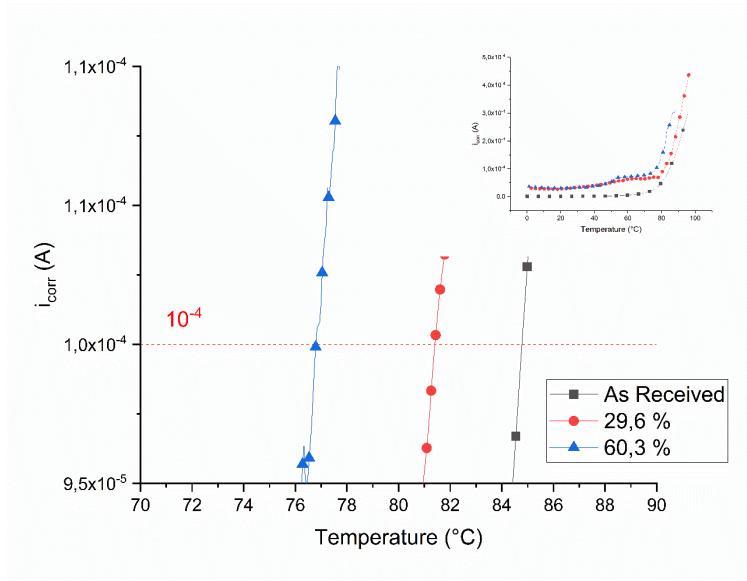


Figure 9 CPT curves of unwelded sheet metal.

Table 3 CPTs of the welded sheet metal.

Thickness reduction%	CPT [°C]
0	78±1.2
9.6	77±1.4
21.1	76±1.1
29.6	76±0.9
39.4	77±1.3
49.9	75±0.8
60.3	75±1.2

Table 4 CPTs of the unwelded sheet metal. For comparison is also reported the CPT of a bar of UNS S32750.

Thickness reduction%	CPT [°C]
0	84±1.4
29.6	81±1.1
60.3	77±0.9
Not rolled (bar)	88±1.8

The cold rolling process and the welding affect the corrosion resistance by lowering the CPT [14,45]. The increase in deformation causes a gradual drop of the CPT as can be observed in Table 4: the higher the thickness reduction the

lower the CPT as shown by the measurement done in the unwelded samples. CPT varies from a maximum of 88 °C for the bar to 77 °C for the maximum thickness reduction (60.3%).

The deformation process causes the modification of the microstructure: after cold working, the occurrence of residual stress and the formation of the Strain-Induced Martensite (SIM) from the metastable austenite can substantially affect the pitting resistance of duplex stainless steels, because the number of the active anodic sites in the surface are increased [46,47]. Thickness, composition and uniformity of the passive layer are modified in different extent by plastic deformation [48,49] and the increasing in dislocation density favors the film dissolution, due to the presence of lower binding energy regions, compared to a perfect crystal [50]. This may affect the formation of a less effective passive film on the steel surface; moreover, the presence of distorted high-energy interfaces may provide further trigger points for the localized attack [51,52]. This DSS grade is not prone to SIM precipitation in fact, it was not identified any SIM even though most accurate measurements and observations must be conducted (i.e., TEM and XRD).

CPTs range is between 78°C and 75°C so they can be considered constant with respect to reduction in coating thickness. Recrystallization phenomenon taking place during the welding process, delete the microstructural changes due to cold rolling. The weld process causes the fusion of the sheet metal with the consequent loss of effect of the cold hardening, so the CPT of the less deformed sample is basically the same of the 60.3% deformed sample among experimental error.

On the other hand, CPTs of the welded samples are lower than CPTs of the unwelded sheets due to the unbalance of ferrite and austenite that occurs during the welding process as shown by the ECT reported in Figure 12. This fact is also confirmed by the observation of the samples after the CPT tests, reported in Figure 11.

The trend of CPT for both welded and unwelded samples are reported in Figure 10.

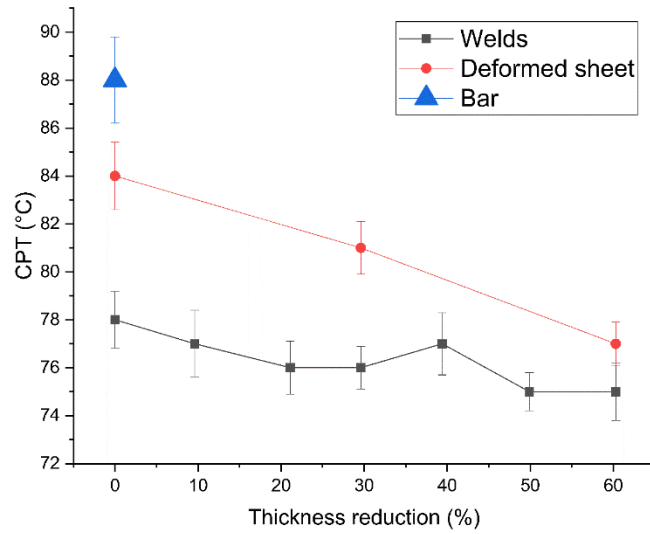


Figure 10 CPT trend of welded and unwelded sheets. For comparison is also reported the CPT of a bar of UNS S32750.

Macrographs in Figure 11 taken after the corrosion tests show that pits are mainly localized in the weld beads whilst base metal was left mostly unaffected, with some exceptions like the material which was subjected to the higher thickness reduction (60.3%). This clearly indicates that the corrosion phenomena can be ascribed to the unbalanced ferrite-austenite content in the welded zone.

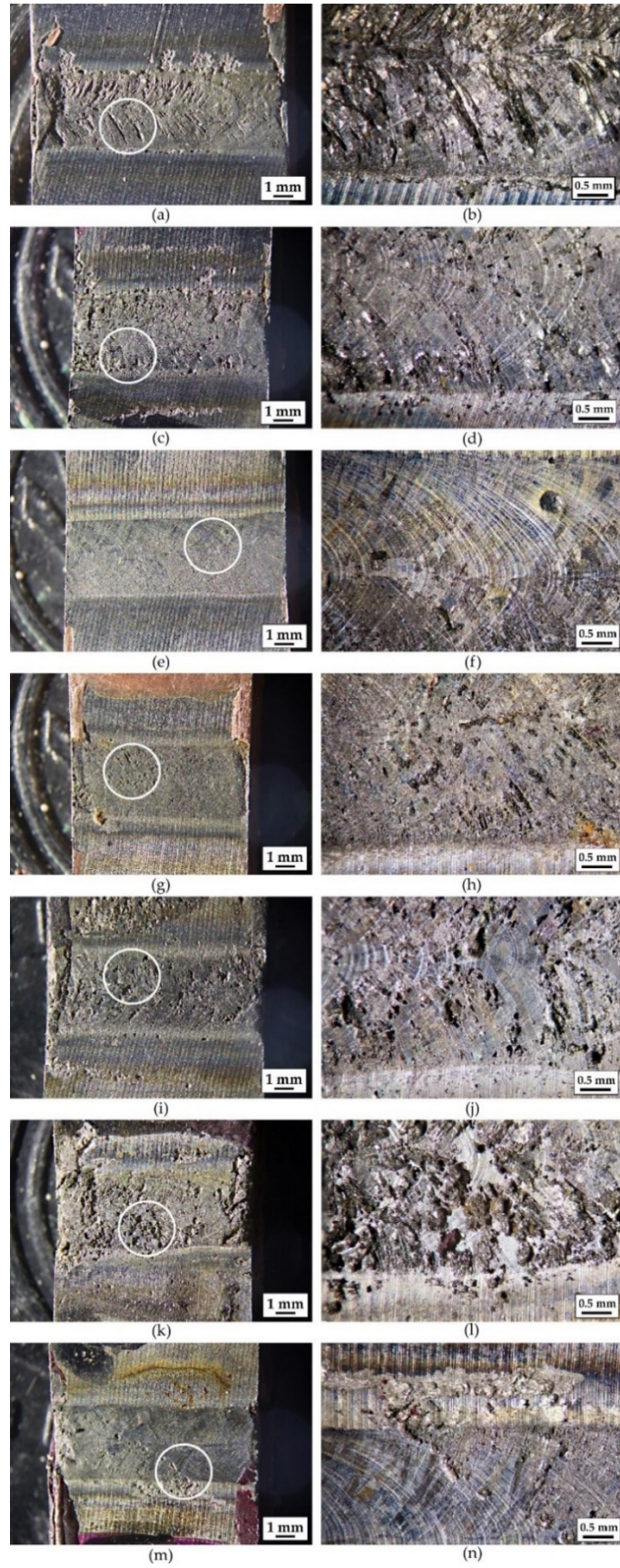


Figure 11 Pits location on the welded sample after CPT tests: (a,b) undeformed, (c,d) 9.6% thickness reduction, (e,f) 21.1% thickness reduction, (g,h) 29.6% thickness reduction, (i,j) 39.4% thickness reduction, (k,l) 49.9% thickness reduction, (m,n) 60.3% thickness reduction. Right column images are higher magnification of the highlighted area of the pictures on the left column.

Eddy currents

Eddy current tests were performed on the top section of the welded samples in order to analyse the change in ferrite content. Eddy's current results for the four frequencies used in the eddy current measurements (10 kHz – 40 kHz – 66.7 kHz – 100 kHz) are reported in Figure 12. A touch coil absolute probe was used to the measuring which diameter was about 1 mm. The probe was fixed in a holding device which ensured the perpendicular position of the probe and the measured surface of the sample. The sample was moveable in horizontal plane on a desk under the fixed probe.

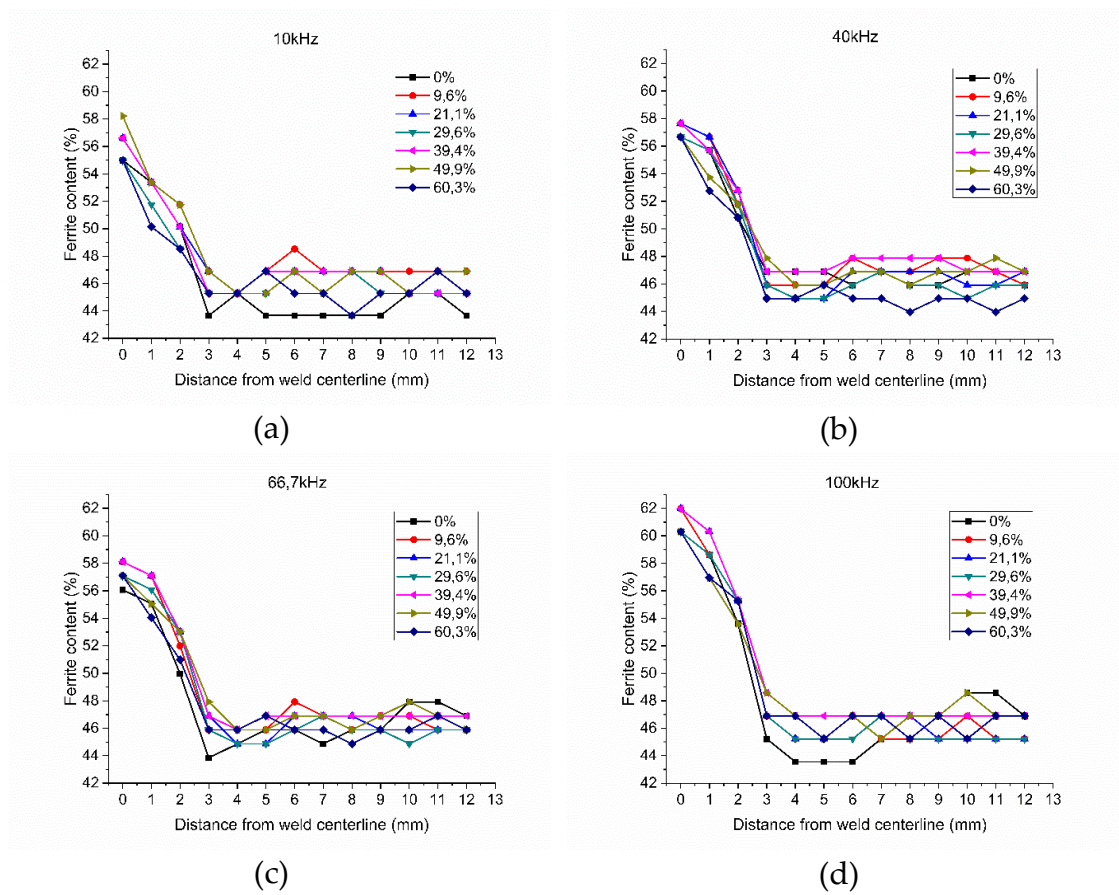


Figure 12 Evolution of the volume fraction of ferrite moving away from the weld centerline.

In accordance with previous studies [8,9,32,33], it can be seen that the amount of ferrite in the joint (~60%), due to the high cooling rate typical of the laser welding, is remarkably higher compared to the base material (46.9%). The precise ferrite content in the HAZ could not be measured because the

dimension of the eddy current probe was significantly bigger than the extension of the zone (~50 μm). However, the tendency of the ferrite content to decrease with increasing distances from the middle of the joint is quite clear for every frequency; the 40 kHz frequency was the most sensitive to the ferrite content variation. High heat input and small spot size of the laser combined with the fast welding process translates in narrow melted region (approximately 0.8 mm according to Figure 2) which limits the width of the HAZ thanks to the base material acting as a heat sink.

Conclusions

The main goal of this study was the investigation of cold rolling on the weldability of UNS S32750 duplex stainless steel. The importance of this problem arises from the fact that cold rolling before heat treatment can significantly increase the rate and decrease the starting temperature of the ferrite decomposition process. The mentioned phase transformation strongly influences phase balance and deteriorates mechanical properties and corrosion resistance of DSSs as well. Therefore, cold rolling prior to welding can be considered as an additional technological risk.

Three sets of seven different samples of UNS S32750 hot rolled and annealed with different thickness reduction up to 60.3% were laser welded and tested by mean of CPT tests, microhardness and eddy current tests. It has been found that:

- The higher the thickness reduction the lower the CPT for the base material
- Thickness reduction does not influence the CPT of the welded samples
- Most of the pits are located in the weld beads due to the unbalanced microstructure (higher ferrite volume fraction)
- The higher the thickness reduction the higher the microhardness on the base material due to strain hardening effects
- Microhardness of the welded region is not influenced by the prior plastic deformation
- Prior plastic deformation does not influence the phase balance on the weld beads
- Higher volume fraction of ferrite (60%) within the joint is responsible for the decrease in CPTs of the welds

References

- [1] Iris Alvarez Armas, S.D.M. *Duplex Stainless Steels*; Iris Alvarez-Armas, S.D.M., Ed.; Wiley, (2009); ISBN 978-1-848-21137-7.
- [2] Gunn, R.N. *Duplex Stainless Steels: Microstructure, Properties and Applications*; Gunn, R.N., Ed.; 1st ed.; Woodhead: Sawston, United Kingdom, Cambridge, United Kingdom, (1997); ISBN 9781855733183.
- [3] Nilsson, J.O. "*The physical metallurgy of duplex stainless steels*", In Proceedings of the **Duplex stainless steels**; Nilsson, J.O., Ed.; KCI Publishing: Maastricht, Netherlands, (1997); pp. 73–82.
- [4] Nilsson, J.-O. "*Super duplex stainless steels*", **Mater. Sci. Technol.** (1992), Volume 8, pp.685–700.
- [5] Li, S.L.; Wang, Y.L.; Wang, X.T. "*Effects of long term thermal aging on high temperature tensile deformation behaviours of duplex stainless steels*", **Mater. High Temp.** (2015), Volume 32, pp.524–529.
- [6] Gennari, C.; Pezzato, L.; Piva, E.; Gobbo, R.; Calliari, I. "*Influence of small amount and different morphology of secondary phases on impact toughness of UNS S32205 Duplex Stainless Steel*", **Mater. Sci. Eng. A** (2018), Volume 729, pp.149–156.
- [7] Calliari, I.; Pellizzari, M.; Zanellato, M.; Ramous, E. "*The phase stability in Cr-Ni and Cr-Mn duplex stainless steels*", **J. Mater. Sci.** (2011), Volume 46, pp.6916–6924.
- [8] Bolut, M.; Kong, C.Y.; Blackburn, J.; Cashell, K.A.; Hobson, P.R. "*Yb-fibre laser welding of 6 mm duplex stainless steel 2205*", **Phys. Procedia** (2016), Volume 83, pp.417–425.
- [9] El-Batahgy, A.-M.; Khourshid, A.-F.; Sharef, T. "*Effect of Laser Beam Welding Parameters on Microstructure and Properties of Duplex Stainless Steel*", **Mater. Sci. Appl.** (2011), Volume 02, pp.1443–1451.
- [10] Calliari, I.; Ramous, E.; Rebuffi, G.; Straffelini, G. "*Investigation of secondary phases effect on 2205 DSS fracture toughness*", **Metall. Ital.** (2008), Volume 100,

pp.5–8.

- [11] Gennari, C.; Breda, M.; Brunelli, K.; Ramous, E.; Calliari, I. "*Influence of small amount of secondary phases on impact toughness of UNS S32205 and Zeron® 100 Duplex Stainless Steel*", In Proceedings of the **ESSC and DUPLEX 2017 - 9th European Stainless Steel Conference - Science and Market and 5th European Duplex Stainless Steel Conference and Exhibition**; (2018).
- [12] Breda, M.; Calliari, I.; Ramous, E.; Pizzo, M.; Corain, L.; Straffelini, G. "*Ductile-to-brittle transition in a Zeron© 100 SDSS in wrought and aged conditions*", **Mater. Sci. Eng. A** (2013), Volume 585, pp.57–65.
- [13] Chen, T.H.; Weng, K.L.; Yang, J.R. "*The effect of high-temperature exposure on the microstructural stability and toughness property in a 2205 duplex stainless steel*", **Mater. Sci. Eng. A** (2002), Volume 338, pp.259–270.
- [14] Breda, M.; Pezzato, L.; Pizzo, M.; Calliari, I. "*Effect of cold rolling on pitting resistance in duplex stainless steels*", **La Metall. Ital.** (2014), Volume 6, pp.15–19.
- [15] Pezzato, L.; Lago, M.; Brunelli, K.; Breda, M.; Calliari, I. "*Effect of the Heat Treatment on the Corrosion Resistance of Duplex Stainless Steels*", **J. Mater. Eng. Perform.** (2018), Volume 27, pp.3859–3868.
- [16] Marques, I.J.; Vicente, A. de A.; Tenório, J.A.S.; Santos, T.F. de A. "*Double Kinetics of Intermetallic Phase Precipitation in UNS S32205 Duplex Stainless Steels Submitted to Isothermal Heat Treatment*", **Mater. Res.** (2017), Volume ahead, pp.1–7.
- [17] Luo, J.; Dong, Y.; Li, L.; Wang, X. "*Microstructure of 2205 duplex stainless steel joint in submerged arc welding by post weld heat treatment*", **J. Manuf. Process.** (2014), Volume 16, pp.144–148.
- [18] Nowacki, J.; Rybicki, P.P. "*The influence of welding heat input on submerged arc welded duplex steel joints imperfections*", **J. Mater. Process. Technol.** (2005), Volume 164–165, pp.1082–1088.
- [19] Sorrentino, S.; Fersini, M.; Zilli, G. "*Comparison between submerged arc (SAW) and laser welding applied to duplex stainless steel structures for bridges*", **Riv. Ital. della**

Saldatura (2008), Volume 60, pp.487–498.

- [20] Taban, E.; Kaluc, E. "Welding behaviour of duplex and superduplex stainless steels using laser and plasma arc welding processes", **Weld. World** (2011), Volume 55, pp.48–57.
- [21] Bharathi, R.S.; Shanmugam, N.S.; Kannan, R.M.; Vendan, S.A. "Studies on the Parametric Effects of Plasma Arc Welding of 2205 Duplex Stainless Steel", **High Temp. Mater. Process.** (2018), Volume 37, pp.219–232.
- [22] Šimeková, B.; Kovaříková, I.; Ulrich, K. "Microstructure and Properties of Plasma Arc Welding with Depth Penetration Keyhole SAF 2205 Duplex Stainless Steel", **Adv. Mater. Res.** (2013), Volume 664, pp.578–583.
- [23] Eghlimi, A.; Shamanian, M.; Raeissi, K. "Effect of current type on microstructure and corrosion resistance of super duplex stainless steel claddings produced by the gas tungsten arc welding process", **Surf. Coatings Technol.** (2014), Volume 244, pp.45–51.
- [24] Neissi, R.; Shamanian, M.; Hajhashemi, M. "The Effect of Constant and Pulsed Current Gas Tungsten Arc Welding on Joint Properties of 2205 Duplex Stainless Steel to 316L Austenitic Stainless Steel", **J. Mater. Eng. Perform.** (2016), Volume 25, pp.2017–2028.
- [25] Mourad, A.-H.I.; Khourshid, A.; Sharef, T. "Gas tungsten arc and laser beam welding processes effects on duplex stainless steel 2205 properties", (2012), Volume 549, pp.105–113.
- [26] Chen, W.; Wang, J.; Li, J.; Zheng, Y.; Li, H.; Liu, Y.; Han, P. "Effect of the Rotation Speed during Friction Stir Welding on the Microstructure and Corrosion Resistance of SAF 2707 Hyper Duplex Stainless Steel", **Steel Res. Int.** (2018), Volume 89.
- [27] Santos, T.F. de A.; Torres, E.A.; Ramirez, A.J. "Friction stir welding of duplex stainless steels", **Weld. Int.** (2018), Volume 32, pp.103–111.
- [28] Saeid, T.; Abdollah-zadeh, A.; Assadi, H.; Malek Ghaini, F. "Effect of friction stir welding speed on the microstructure and mechanical properties of a duplex stainless steel", **Mater. Sci. Eng. A** (2008), Volume 496, pp.262–268.

- [29] Keskitalo, M.; Mäntyjärvi, K.; Sundqvist, J.; Powell, J.; Kaplan, A.F.H. "*Laser welding of duplex stainless steel with nitrogen as shielding gas*", **J. Mater. Process. Technol.** (2015), Volume 216, pp.381–384.
- [30] de Lima Milton Sergio Fernandes, de Carvalh Sheila Medeiros, Teleginski Viviane, P.M. "*Mechanical and Corrosion Properties of a Duplex Steel Welded using Micro-Arc or Laser-2015*", **Mater. Res.** (2015), Volume 18, pp.723–731.
- [31] Quiroz, V.; Gumenyuk, A.; Rethmeier, M. "*Laser beam weldability of high-manganese austenitic and duplex stainless steel sheets*", **Weld. World** (2012), Volume 56, pp.9–20.
- [32] Saravanan, S.; Raghukandan, K.; Sivagurumanikandan, N. "*Pulsed Nd: YAG laser welding and subsequent post-weld heat treatment on super duplex stainless steel*", **J. Manuf. Process.** (2017), Volume 25, pp.284–289.
- [33] Sivakumar, G.; Saravanan, S.; Raghukandan, K. "*Investigation of microstructure and mechanical properties of Nd:YAG laser welded lean duplex stainless steel joints*", **Optik (Stuttg.)** (2017), Volume 131, pp.1–10.
- [34] Arabi, S.H.; Pouranvari, M.; Movahedi, M. "*Pathways to improve the austenite–ferrite phase balance during resistance spot welding of duplex stainless steels*", **Sci. Technol. Weld. Join.** (2018), pp.1–8.
- [35] Yasuda, K.; Gunn, R.N.; Gooch, T.G. "*Prediction of austenite phase fraction in duplex stainless steel weld metals*", **Yosetsu Gakkai Ronbunshu/Quarterly J. Japan Weld. Soc.** (2002), Volume 20, pp.68–77.
- [36] Varbai, B.; Pickle, T.; M´jlinger, K. "*Development and comparison of quantitative phase analysis for duplex stainless steel weld*", **Period. Polytech. Mech. Eng.** (2018), Volume 62, pp.247–253.
- [37] Baughn, K.; Ahmed, N.; Jarvis, L.; Viano, D. "*Tailoring the phase balance during laser and GTA keyhole welding of SAF 2205 duplex stainless steel*", **ASM Proc. Int. Conf. Trends Weld. Res.** (2002), pp.11–16.
- [38] Meng, W.; Li, Z.; Huang, J.; Wu, Y.; Chen, J.; Katayama, S. "*The influence of various factors on the geometric profile of laser lap welded T-joints*", **Int. J. Adv.**

- Manuf. Technol.** (2014), Volume 74, pp.1625–1636.
- [39] Mirakhorli, F.; Malek Ghaini, F.; Torkamany, M.J. "*Development of weld metal microstructures in pulsed laser welding of duplex stainless steel*", **J. Mater. Eng. Perform.** (2012), Volume 21, pp.2173–2176.
- [40] Menezes, A.J.W.; Abreu, H.; Kundu, S.; Bhadeshia, H.K.D.H.; Kelly, P.M. "*Crystallography of Widmanstätten austenite in duplex stainless steel weld metal*", **Sci. Technol. Weld. Join.** (2009), Volume 14, pp.4–10.
- [41] Ohmori, Y.; Nakai, K.; Ohtsubo, H.; Isshiki, Y. "*Mechanism of Widmanstätten Austenite Formation in a .DELTA./GAMMA. Duplex Phase Stainless Steel.*", **ISI Int.** (1995), Volume 35, pp.969–975.
- [42] Serre, I.; Salazar, D.; Vogt, J.B. "*Atomic force microscopy investigation of surface relief in individual phases of deformed duplex stainless steel*", **Mater. Sci. Eng. A** (2008), Volume 492, pp.428–433.
- [43] Amigó, V.; Bonache, V.; Teruel, L.; Vicente, A. "*Mechanical properties of duplex stainless steel laser joints*", **Weld. Int.** (2006), Volume 20, pp.361–366.
- [44] Köse, C.; Kaçar, R. "*Mechanical Properties of Laser Welded 2205 Duplex Stainless Steel*", **Mater. Test.** (2014), Volume 56, pp.779–785.
- [45] Elhoud, A.M.; Renton, N.C.; Deans, W.F. "*The effect of manufacturing variables on the corrosion resistance of a super duplex stainless steel*", **Int. J. Adv. Manuf. Technol.** (2011), Volume 52, pp.451–461.
- [46] Matting, A.; Koch, H.; Dorn, L. "*Einfluß des Elektronenstrahl- und Schutzgasschweißens auf das Korrosionsverhalten von X5 CrNiMo 18 10*", **Mater. Corros.** (1970), Volume 21, pp.94–97.
- [47] Elayaperumal, K.; De, P.K.; Balachandra, J. Passivity of Type 304 Stainless Steel-Effect of Plastic Deformation. *Corrosion* (1972), 28, 269–273.
- [48] Phadnis, S. V.; Satpati, A.K.; Muthe, K.P.; Vyas, J.C.; Sundaresan, R.I. "*Comparison of rolled and heat treated SS304 in chloride solution using electrochemical and XPS techniques*", **Corros. Sci.** (2003), Volume 45, pp.2467–2483.

- [49] Navai, F. "*Effects of tensile and compressive stresses on the passive layers formed on a type 302 stainless steel in a normal sulphuric acid bath*", **J. Mater. Sci.** (1995), Volume 30, pp.1166–1172.
- [50] Greene, N.D.; Saltzman, G.A. "*Effect of Plastic Deformation On the Corrosion of Iron and Steel*", **Corrosion** (1964), Volume 20, pp.293t-298t.
- [51] Serna, M.M.; Jesus, E.R.B.; Galego, E.; Martinez, L.G.; Corrêa, H.P.S.; Rossi, J.L. "*An Overview of the Microstructures Present in High-Speed Steel -Carbides Crystallography*", **Mater. Sci. Forum** (2006), Volume 530–531, pp.48–52.
- [52] Chiu, P.K.; Wang, S.H.; Yang, J.R.; Weng, K.L.; Fang, J. "*The effect of strain ratio on morphology of dislocation in low cycle fatigued SAF 2205 DSS*", **Mater. Chem. Phys.** (2006), Volume 98, pp.103–110.